Probing of Electron and Nuclear Spin Properties in Strain Engineered GaAs/AlGaAs Quantum Dots

Harry E. Dyte

A thesis submitted in partial fulfilment of the requirements for the degree of Doctor of Philosophy

Supervisor: Dr. Evgeny Chekhovich & Prof. Jenny Clark

October 2025



Low Dimensional Structures and Devices Group
School of Mathematical and Physical Sciences
University of Sheffield

Abstract

This thesis presents experimental measurements on externally uniaxially strained nanohole infilled III-V GaAs/AlGaAs quantum dots (QDs). A combination of optical and nuclear magnetic resonance (NMR) techniques are used to probe and study the nuclear spin system. We perform a series of investigations demonstrating how the nuclear spins can be harnessed to probe electron spin relaxation, and function as a long lived quantum memory.

First we examine the nuclear spin system in these strained QDs using inverse NMR. Measuring the strain-induced quadrupolar effect we obtain a value for the peak applied strain as well as the value of S_{44} for GaAs.

Current techniques for performing electron spin state readout, such as resonance fluorescence, have limited fidelity due to unwanted spin flips caused by the high energy measurement. We demonstrate that high fidelity, single-shot, quantum non-demolition (QND) measurements can be performed by using detuned radio frequency (RF) pulses on the QDs nuclear spin bath, achieving readout fidelities of $F \approx 99.85\%$. Additionally the nature of the measurement poses questions about quantum measurements, wavefunction collapse, and other interpretations of quantum mechanics.

We use the nuclear spins to probe the spin dynamics of multi-electron states. We perform measurements on the electron's Knight field and relaxation rate, obtaining a maximum spin lifetime of $T_{1,e} \approx 50$ ms.

Finally we present work on extending the nuclear spin coherence time using dynamical decoupling Combined Hahn and Solid Echo (CHASE) sequences. The low internal sample strain combined with strain engineering provides an ideal nuclear spin system for dynamical decoupling sequences. This, combined with new CHASE sequences, allows an extension of $T_{2,N}$ to over 100 milliseconds. Due to the excellent optical properties of QDs, these nuclei would be an ideal candidate for a quantum memory in optical quantum communication.

Acknowledgements

I would like to start this thesis by thanking the numerous people who have supported me during my PhD. Working on this thesis has consumed most of the last three and a half years of my life, and I know it would not have been possible without help from my colleagues, friends and family.

First I would like to thank **EPSRC** for providing the funding needed to make this PhD possible. I would like to give my thanks to my supervisor **Evgeny Chekhovich** for giving me the opportunity to work in his lab and for the endless hours of support he provided during my PhD, his work ethic is truly something to aspire to and I thank him for continuing to supervise me remotely after moving universities. I would also like to thank **Jenny Clark** for taking over as my supervisor during my final year. I would additionally like to thank **Santanu Manna**, **Saimon Covre da Silva** and **Armando Rastelli** who grew the GaAs/AlGaAs sample that I studied for the duration of my PhD.

Next I would like to thank my colleagues in the C11 lab. An enormous thank you first goes to **George Gillard** who taught me how to operate the equipment in the lab, skills that continued to serve me well throughout my PhD. Second, I would like to thank **Peter Millington-Hotze** for providing hours of advice and listening to my frustrations regarding experiments, many hours of work were saved through avoided mistakes based on your help. Next I wish to thank everyone in the E46 office for putting up with my frequent and vocal frustration with work as well as providing a friendly working atmosphere, I hope you can enjoy the reduced office noise levels in my absence.

A wider thanks to members in the broader LDSD group. I thank **Chris Vickers** and **Thomas Ball** for ensuring that liquid helium was always available for the incredibly thirsty C11 lab. I would also like to thank **Mark Fox** for his leadership of the LDSD group as well as for ensuring my PhD

remained on track during my final year.

Lastly, I would like to thank my family and friends for their support. A massive thank you goes to my parents **Robert Dyte** and **Sara Dyte** who's never ending support has been crucial for me to reach where I am today (and yes this does now mean I need to get a real job). I would like to thank my sisters **Lily Dyte** and **Ruby Dyte** who I have had many laughs with over the last few years, even if my physics bores them. Additionally their continued 'interest' in my work has really helped to keep me grounded and ensure that I remember how little it actually matters. I wish to thank both of my nan's **Diane Dyte** and **Valerie Croucher** for their continued interest in my studies and I give many thanks to my other family members for the good times that we've shared. I would also like to thank my friends for their support as well as my appreciation for the hard earned money they paid in taxes to fund my PhD, I am sure you think it was worth it.

Publications and Conferences

Publications

P. Millington-Hotze, **H. E. Dyte**, S. Manna, S. F. Covre da Silva, A. Rastelli, E. A. Chekhovich. "Approaching a fully-polarized state of nuclear spins in a solid". *Nat. Commun.* **15**, 985 (2024). DOI: https://doi.org/10.1038/s41467-024-45364-2

H. E. Dyte, G. Gillard, S. Manna, S. F. Covre da Silva, A. Rastelli, E. A. Chekhovich. "Is wave-function collapse necessary? Explaining quantum nondemolition measurement of a spin qubit within linear evolution". *Phys. Rev. Lett.* **132**, 160804 (2024). DOI: https://doi.org/10.1103/PhysRevLett.132.160804

H. E. Dyte, S. Manna, S. F. Covre da Silva, A. Rastelli, E. A. Chekhovich. "Storing quantum coherence in a quantum dot nuclear spin ensemble for over 100 milliseconds". *arXiv:2502.11092* (2025). DOI: https://doi.org/10.48550/arXiv.2502.11092

P. Millington-Hotze, P. Klenovsky, **H. E. Dyte**, G. Gillard, S. Manna, S. F. Covre da Silva, A. Rastelli, E. A. Chekhovich. "Few-electron spin qubits in optically active GaAs quantum dots". *arXiv:2504.19257* (2025). DOI: https://doi.org/10.48550/arXiv.2504.19257

Conference talks

H. E. Dyte, G. Gillard, S. Manna, S. F. Covre da Silva, A. Rastelli, E. A. Chekhovich. "Quantum non-demolition measurement of an electron spin qubit through its low-energy many-body spin environment". *GaAs Workshop*. Oxford, UK. May 2023.

H. E. Dyte, G. Gillard, S. Manna, S. F. Covre da Silva, A. Rastelli, E. A. Chekhovich. "Quantum non-demolition measurement of an electron spin qubit through its low-energy many-body spin environment". *Quantum dot day 2023*. Manchester, UK. September 2023.

H. E. Dyte, S. Manna, S. F. Covre da Silva, A. Rastelli, E. A. Chekhovich. "Storing quantum coherence in a quantum dot nuclear spin ensemble for over 100 milliseconds". *QD2024*. Munich, Germany. March 2024.

H. E. Dyte, S. Manna, S. F. Covre da Silva, A. Rastelli, E. A. Chekhovich. "Storing quantum coherence in a quantum dot nuclear spin ensemble for over 100 milliseconds". *2nd International GaAs Quantum Dot Workshop*. Traunkirchen, Austria. April 2024.

Conference posters

H. E. Dyte, S. Manna, S. F. Covre da Silva, A. Rastelli, E. A. Chekhovich. "Storing quantum coherence in a quantum dot nuclear spin ensemble for over 100 milliseconds". *Quantum dot day 2023*. Manchester, UK. September 2023.

H. E. Dyte, S. Manna, S. F. Covre da Silva, A. Rastelli, E. A. Chekhovich. "Storing quantum coherence in a quantum dot nuclear spin ensemble for over 100 milliseconds". *Materials for Quantum Network - Horizon Scanning UK Conference (M4QN)*. Cambridge, UK. November 2023.

H. E. Dyte, S. Manna, S. F. Covre da Silva, A. Rastelli, E. A. Chekhovich. "Storing quantum coherence in a quantum dot nuclear spin ensemble for over 100 milliseconds". *Physics of Excitons and Polaritons in Semiconductors (PEPS)*. Reykjavík, Iceland. August 2024.

List of Acronyms

AC alternating current

AFM atomic force microscopy

Al aluminium

AlGaAs aluminium gallium arsenide

AOM acousto-optic modulator

As arsenic

BE bright exciton

BNC Bayonet Neill-Concelman radio frequency connector/cable

BS beam splitter

C carbon

CB conduction band

CCD charge-coupled device

CHASE Combined Hahn and Solid Echo

CP Carr-Purcell

CPMG Carr-Purcell-Meiboom-Gills

CT central transition

CuCl copper chloride

CVD chemical vapour deposition

CW continuous wave

DC direct current

DE dark exciton

DNP dynamical nuclear polarisation

EFG electric field gradient

EOM electro-optic modulator

ESR electron spin resonance

FvdM Frank-van der Merve

FWHM full width half maximum

Ga gallium

GaAs gallium arsenide

HWP half-wave plate

InGaAs indium gallium arsenide

LDE local droplet etching

MAS magic-angle spinning

MBE molecular-beam epitaxy

MER Merkulov-Efros-Rosen

MOVPE metalorganic vapour phase epitaxy

MRI magnetic resonance imaging

NMR nuclear magnetic resonance

ODNMR optically detected nuclear magnetic resonance

PL photoluminescence

QCSE quantum confined Stark effect

QD quantum dot

QND quantum non-demolition

QWP quarter-wave plate

QW quantum well

QWR quantum wire

RF radio frequency

RHEED reflection high-energy electron diffraction

Si silicon

SK Stranski-Krastanow

ST satellite transition

UHV ultra high vacuum

VB valence band

VW Volmer-Weber

WL wetting layer

Contents

1 Introduction **1**

2 Background **5**

2.1 Quantum Dots 5

2.1.1 Semiconductor and Quantum Dot Growth 6

2.1.2 Semiconductor Band Structures 10

2.1.3 QD Confinement of Charge Carriers 12

2.2 Optical Properties of Quantum Dots 15

2.2.1 Charged Excitons and Charge Tuning 18

2.2.2 Fine Structure 21

2.2.3 External Fields 24

2.3 Quantum Dot Spin System 27

2.3.1 Carrier Spins 27

2.3.2 Nuclear Spins 29

2.3.3 Hyperfine Interaction 36

2.4 Spin Control in Quantum Dots 41

2.4.1 State Initialisation 41

2.4.2 Spin Control 44

2.4.3 Relaxation 47

2.4.4 State Readout 51

3 Experimental Techniques **52**

3.1 Sample . . . 52

3.2 Bath Cryostat Setup . . . 55

3.3 Optical Spectroscopy . . . 57

3.4 Dynamic Nuclear Polarisation . . . 60

3.4.1 Optical Pumping . . . 61

3.4.2 Optical Probing . . . 64

3.4.3 Nuclear Polarisation Bistability . . . 65

3.5 Nuclear Magnetic Resonance . . . 66

3.5.1 NMR Setup . . . 66

3.5.2 Inverse NMR . . . 69

3.5.3 Pulsed NMR . . . 71

3.5.4 Population Transfer . . . 73

3.5.5 Optically Detected Nuclear Magnetic Resonance . . . 75

4 Low-field Quadrupolar Effects in Uniaxially Strained GaAs QDs **77**

4.1 Introduction . . . 77

4.2 Methods . . . 78

4.3 NMR on GaAs . . . 81

4.4 Derivation of Strain . . . 84

4.5 Sample Strain Analysis . . . 88

4.6 Comparison Between Unstrained and Strained Samples . . . 93

4.7 Summary . . . 96

5 Is Wavefunction Collapse Necessary? Explaining Quantum Nondemolition Measurement of a Spin Qubit Within Linear Evolution **97**

6 Electron Spin Lifetimes in GaAs QDs **94**

6.1 Introduction . . . 94

6.2 Methods 95
6.3 Deterministic Generation of Charged QD States 99
6.4 Probing the Knight Field 101
6.5 Electron Spin Lifetimes 103
6.6 Summary 108

7 Storing Quantum Coherence in a Quantum Dot Nuclear Spin Ensemble for over 100 Milliseconds **110**

8 Conclusions **112**

List of Figures

2.1 Density of states for different nanostructures 6
2.2 Schematic diagram of different heteroepitaxial growth modes 8
2.3 Band structure for an unstrained and strained zincblende crystal 11
2.4 GaAs QD energy level diagram 14
2.5 Resonant and off-resonant optical excitation schemes for QDs 17
2.6 Common exciton charge configurations 19
2.7 QD charge tuning by an applied bias V_{Gate} 20
2.8 Exciton fine structure energy level diagram 22
2.9 Central spin system of a QD 28
2.10 Schematic diagram of the QD nuclear spin bath 31
2.11 Energy level diagram for a quadrupolar nucleus in an external magnetic field 35
2.12 Experimental observations of the hyperfine interaction on electrons and nuclei . . . 39
2.13 Optical initialisation of spins in a QD 43
2.14 Spin relaxation processes 49

3.1 Schematic diagram of the GaAs/AlGaAs QD sample structure. 53
3.2 Schematic diagram of the GaAs/AlGaAs sample mounted in the stress bracket . . . 54
3.3 GaAs/AlGaAs sample PL spectra 55
3.4 Schematic of bath cryostat and sample insert 56
3.5 Diagram of setup for optical experiments 59
3.6 Optical pumping calibration measurements 62

3.7 Calibration of optical probe duration 65
3.8 Schematic of NMR experimental setup 67
3.9 Frequency spectra of shunt stub reflection 68
3.10 Schematic of CW NMR techniques. 70
3.11 Pulsed NMR calibration 72
3.12 Schematic of pulsed NMR and population transfer techniques. 74
3.13 Measurement of hyperfine shift via ODNMR 76

4.1 Inverse NMR measurement timing diagram 79
4.2 Inverse NMR experimental parameters 80
4.3 NMR spectra for ^{75}As, ^{69}Ga, and ^{71}Ga 82
4.4 Waterfall plot of NMR spectra at different external magnetic fields 89
4.5 External magnetic field dependence of first-order quadrupolar splitting 90
4.6 External magnetic field dependence of $\Delta\nu_Q^{(2)}$ 92
4.7 Comparison of QD NMR spectra for strained and unstrained samples 94
4.8 Maximum DNP dependence on externally applied magnetic field 95

6.1 Electron spin readout measurement timing diagrams 96
6.2 Calibration of optical electron spin pumping 98
6.3 Dependence of the nuclear spin relaxation time on the applied sample bias 100
6.4 Heat map of single shot readouts showing the effect of the 1e and 3e Knight field . 102
6.5 Different methods of measuring the electron spin lifetime 104
6.6 Magnetic field dependence of the electron spin lifetime 107

List of Tables

2.1 Exciton eigenstates and energy levels 26
2.2 Properties of GaAs QD nuclear spins 33

Chapter 1

Introduction

At the start of the 20th century, observations of phenomena such as black body radiation and the photoelectric effect were puzzling physicists as they could not be explained within the framework of what would become 'classical' physics. A solution for these problems came in a new form of physics, where energy was transmitted as discrete packets (quanta). This new framework would come to be known as quantum mechanics [1]. Quantum mechanics has continued to be developed over the past century leading to numerous discoveries and new technologies such as transistors, lasers and magnetic resonance imaging (MRI). Yet still the counter-intuitive properties of quantum mechanics continues to challenge researchers to this day.

One potential way to improve our understanding of quantum systems would be to simulate them. It began to emerge in the 1980s that trying to do this with classical computers would be impractical. Instead physicists such as Benioff, Feynmann and Deutch (and the works of many others) would propose that a new type of computer would be needed, one that exploits the quantum mechanical properties of nature [2–6]. These new computers would be called quantum computers. Further work would lead to the development of quantum algorithms such as Deustch-Jozsa's algorithm [7], Grover's list search [8], and Shor's prime factorisation [9] all theoretically showing that quantum computers can solve certain problems significantly faster than a classical computer. With demonstrations of quantum computing software, all that is now needed is hardware to implement them on. Unfortunately this has been a trickier problem though current quantum computers are approaching the point where they can compute problems faster than their classical competitors, a point that has been named quantum advantage [10].

The fundamental component for a classical computer is a bit, which can exist in two states 'on' $|1\rangle$ and 'off' $|0\rangle$. Through the manipulation of the states of numerous bits computations can be carried out. Likewise the fundamental hardware of a quantum computer is a quantum bit, or qubit. Again at minimum this is a two state system e.g. a spin 1/2 particle placed in a magnetic field. The difference is the qubit can exist in a superposition of states which in turn means that phenomena

such as quantum entanglement can be exploited, a property that allows quantum computers to outpace classical computers. Such a system is described by a wavefunction of the form:

$$|\psi\rangle = \alpha|0\rangle + \beta|1\rangle, \tag{1.1}$$

where $|\psi\rangle$ is the wavefunction, and α and β are the probability amplitudes of the states $|0\rangle$ and $|1\rangle$ respectively. When the system is measured the wavefunction 'collapses' and it is projected into one of the two states. The likelihood of it being projected into a state is given by the states corresponding probability amplitude squared ($|\alpha|^2$ or $|\beta|^2$).

The above description gives the minimum requirement to have a qubit. However for actual practical applications the requirements are more stringent. While these requirements have not been universally defined, there are generally accept properties that qubits should possess, such as those proposed by DiVincenzo [11] and later refined by Ladd [12] which we restate here:

Scalability: The physical system used to build the quantum computer should be able to grow exponentially without an exponential cost in resources (time, energy, space, etc.). This can be realised through entanglement of qubits.

Universal logic: The system must be controllable by a finite set of control operations. The resources required for these operations must also not scale exponentially.

Correctability: There must be a way to extract entropy introduced from the environment from the computer, i.e. it must be possible to initialise the computer into a desired state and also perform a measurement (readout) of the computers state.

Numerous systems are now being investigated as potential qubits [12], such as trapped atoms and ions [13–16], superconductors [10, 17–20], doped crystal impurities in silicon [21–23], the well-known nitrogen-vacancy centre in diamond [24, 25], and epitaxial quantum dots [26–28]. All of these systems have various strengths and weaknesses in satisfying the above criteria [12]. Another system to consider are photons, which are free from the coherence time issues that plague many of the above materials [12], but are unable to be confined to a fixed location making them unsuitable for a quantum computer. However it would ideally be desired to connect spatially separated quantum computers much like how classical computers are connected [29]. Their properties mean that photons will be the ideal building blocks of such quantum networks, meaning it becomes desirable for a 'stationary' qubit to be able to interface directly with these 'flying' optical photon qubits [11, 12].

In this thesis we focus on quantum dots (QDs), which are 3D nanostructures that form at the boundary of two semiconductors during heteroepitaxial growth. QDs can confine charged particles such as electrons which, due to the electrons spin angular momentum, can form a two level system when placed in a magnetic field, giving a qubit. Initialisation, control and readout of the electron spin qubit has already been demonstrated [30, 31]. Additionally, QDs are able to strongly couple to photons and are excellent sources of single [32] and entangled photons [33], while also possessing high entanglement generation rates between electron qubits [34]. Additionally, semiconductor fabrication techniques allow QDs to be placed into optical cavities or diode structures, further enhancing their optical properties and allowing simple control over the confinement of electrons.

However the random nature of QD growth currently limits their scalability. While work has been directed to developing controlled QD growth, it is still not sufficient to enable a QD to be grown in a specific position. Additionally, coupling to phonons significantly limits QD optical properties requiring cryogenic ($T \approx 4$ K) temperatures for operation. Another issue with QD electron spin qubits is the surrounding nuclei. In III-V semiconductor materials all of the nuclei possess nuclear spin dipole moments. This generates a randomly fluctuating nuclear spin magnetic field that couples to the electron spin, driving decoherence. However, much like the electron, it is possible to perform initialisation and readout of the nuclei optically, while control can be achieved using NMR techniques. This means that the nuclei may be an alternative or additional route to QD spin qubits.

The work in this thesis is directed to studying the electron and nuclear spins in strain engineered gallium arsenide (GaAs)/aluminium gallium arsenide (AlGaAs) QDs. We study the affects of externally applied stress on the nuclear spin system before demonstrating how it can be harnessed either as a probe of a confined electron's spin state or as a long-lived quantum memory. The contents of this thesis are:

Chapter 2: An introduction to QDs. We begin with a description of QD growth, before discussing the quantum mechanics and optical properties of these nanostructures. We then introduce the nuclear spin system and discuss the interactions between electron and nuclear spins. Finally we introduce how the spins of electrons and nuclei can be initialised, controlled and measured in the context of QDs.

Chapter 3: A summary of the experimental setup and techniques used to conduct measurements in this thesis including the sample structure, bath cryostat, and optical system. We also introduce the inverse and pulsed NMR techniques and the equipment used to implement them.

Chapter 4: Discusses a series of inverse NMR measurements used to probe the nuclear spins

under externally applied uniaxial stress. We then use perturbation theory to measure the magnitude of the applied stress via the quadrupolar interaction as well as obtain independent measurements of the S_{44} value for GaAs. Finally, we present a discussion of the advantages and disadvantages of strain engineering in the context of nuclear spin qubits.

Chapter 5: A published paper where the nuclei are used as a low-energy probe of the spin state of a confined electron, enabling high fidelity ($F \approx 99.85\%$), single-shot QND measurements of the electron spin state. We investigate the source of observed electron spin flips, ruling out the nuclei and predicting that thermal phonons are the cause. Finally we discuss this measurement technique in the context of the quantum mechanics measurement problem, suggesting the lack of any need of a wavefunction collapse to describe the measurements presented here may provide evidence for other interpretations of quantum mechanics, such as Quantum Darwinism.

Chapter 6: An extension on the work in Chapter 5 where we use the electron spin readout method to measure the electron spin lifetime of the one and three electron states, where we measure a maximum $T_{1,e} \approx 50$ ms. We also discuss the causes for electron spin relaxation and perform initial probing of the multi-electron spin interactions using nuclear spin relaxation measurements.

Chapter 7: A pre-submission manuscript discussing work extending the nuclear spin coherence time. New dynamical decoupling RF pulse sequences combined with strain engineered QDs allows extension of the nuclear spin coherence time to over 100 ms. Combined with the excellent optical properties of QDs, these nuclear spin qubits combined with dynamical decoupling are an attractive quantum memory candidate for quantum communication.

Chapter 8: Summary of the findings of the work in this thesis and a discussion of future work.

Chapter 2

Background

2.1 Quantum Dots

QDs are 3D nanostructures that can form in semiconductor materials. Historically, nanostructures have been exploited to produce stained glass, as the optical properties of the glass could be altered by introducing metallic impurities [35]. However development of specific nanocrystal structures and their uses beyond aesthetic applications would not occur until more recently, where it was discovered that nanostructures could be used to trap and study charge carriers (electrons, holes and excitons).

Semiconductor nanostructures are formed during the growth of heteroepitaxal materials, where the material used is varied during the layer-by-layer growth of the substrate. Development of improved growth techniques, like molecular-beam epitaxy (MBE), in the 1960s meant that complex structures could be developed to confine charges in the potential wells formed due to differences in the material band structures. In early works, such as those on superlattices [36] and single potential wells [37], 1D confinement effects could be observed in the measured optical properties. Since then further research has led to the development of more complex structures with greater confinement effects, as shown in Fig. 2.1.

QDs, originally observed by Ekimov *et al.* [38] in copper chloride (CuCl) nanocrystals and independently a year later by Brus *et al.* [39] in collidal suspensions, extended these confinement effects to 3-dimensions, causing a reduction of the density of states to 0-dimensions. In QDs, confined charge carriers can be described by the particle-in-a-box model and display clear quantised energy levels much like those of atoms. As a result, QDs are commonly nicknamed artificial atoms. QD confinement effects were demonstrated by a clear blue-shift in optical emission as the size of the dot decreased [40, 41]. With simultaneous development of QD growth techniques allowing them to be accurately grown to a desired size [42], it was realised that the properties of QDs

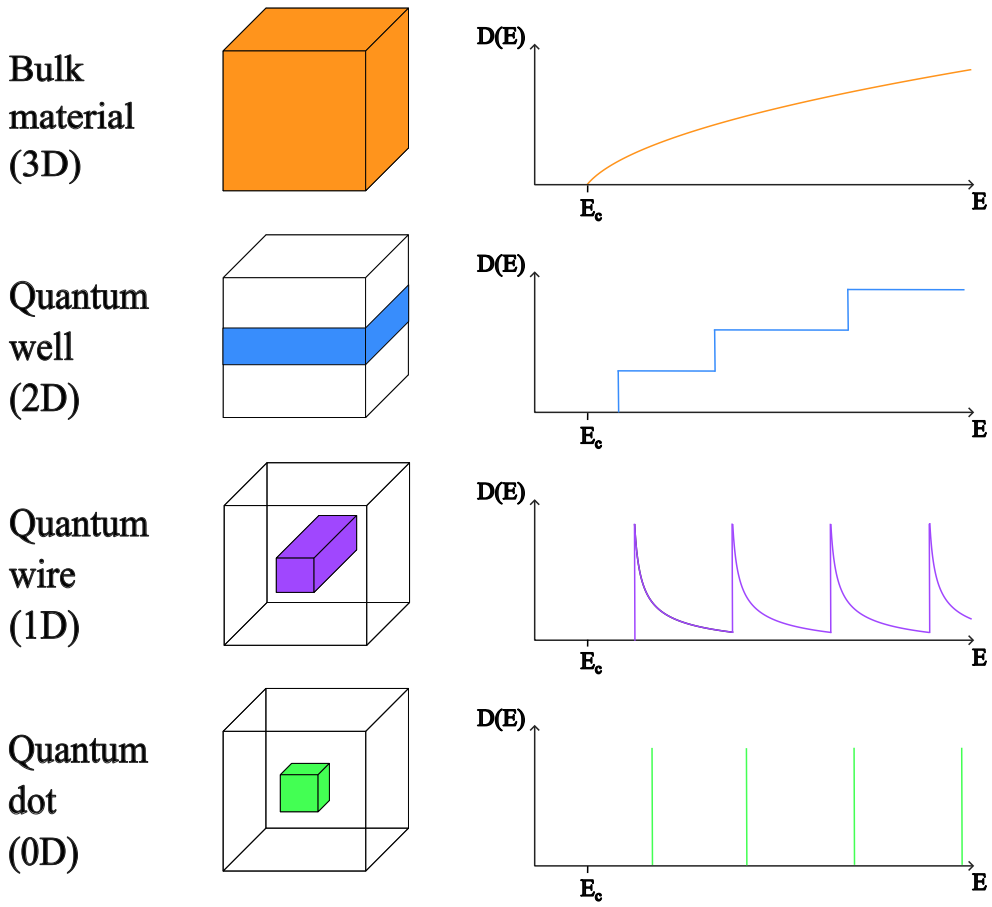


Figure 2.1: Schematic representation of electronic confinement effects in various nanostructures as well as their respective density of states D(E) plotted against energy E. This image has been adapted from [44].

could be tuned and have since be used in a wide range of applications in biology, solar cells, high-efficiency LED displays, and are an attractive candidate for quantum computing and information technologies [35, 43].

The work included in this thesis was carried out on optically-active III-V semiconductor QDs. In the following sections we discuss the growth and properties of these QDs.

2.1.1 Semiconductor and Quantum Dot Growth

The work in this thesis was conducted on individual GaAs QDs. Over the years, various methods for growing heterostructures have been developed for wide range of materials. For III-V semiconductors, such as GaAs, the most common are chemical vapour deposition (CVD), metalorganic vapour phase epitaxy (MOVPE) and MBE [44]. The samples used in this work were grown using

MBE.

MBE operates on the principle of evaporation and deposition of the desired materials under high vacuum conditions. The process is carried out in an ultra high vacuum (UHV) chamber, where source materials are heated and evaporated. The evaporated material is then directed towards the heated sample where they then diffuse onto the surface. Because of the UHV chamber, the evaporated materials have a high-mean travel distance and are described as a beam. Once diffused on the surface, the materials either desorb and leave the sample or they are chemisorbed and incorporated into the sample. The absorption rate can be controlled precisely by controlling the temperature and orientation of the sample. Sample growth is monitored using reflection high-energy electron diffraction (RHEED) which, combined with computer control of the furnaces, enables single-atomic layer control allowing for fabrication of structures such as quantum wells (QWs), quantum wires (QWRs) and QDs [44].

In heteroepitaxy, differences between the chemical and structural properties of the deposited and substrate materials means QD growth can occur via three modes. The three modes Frank-van der Merve (FvdM), Volmer-Weber (VW) and Stranski-Krastanow (SK) are shown in Fig. 2.2. Which mode occurs is determined by the balance between the surface and strain energies. The FvdM and VW growth modes occur when the crystal structure and lattice constants of the deposited and substrate materials are near identical. In this low strain regime, material growth is controlled by the balance between the sum of the surface (α_2) and interface (β_{12}) energies, and the surface energy of the substrate (α_1). In the case where $\alpha_2 + \beta_{12} < \alpha_1$ the deposited material forms a continuous layer above the substrate and proceeds to grow layer-by-layer (FvdM) [45]. If the system instead satisfies the condition $\alpha_2 + \beta_{12} > \alpha_1$ the deposited material forms islands on top of the substrate (VW) [46]. In strained systems, where the crystal structure and lattice constants of the deposited and substrate materials are different, SK growth occurs [47]. First the deposited material forms a highly strained 2D wetting layer (WL) where elastic energy accumulates. Once a critical thickness is reached, the deposited material begins to form islands to reduce the strain energy of the material. The formation of new surfaces causes an increase in the surface energy, but the resulting decrease in elastic energy means the total free energy of the crystal decreases [48].

Typically, QDs are grown via the SK growth mode as they reliably self-assemble. However, this only works for materials that are not lattice-matched meaning the QDs are highly strained [49]. Inhomogeneous strain causes significant broadening of the NMR transitions due to the quadrupolar nuclear spins coupling to strain induced electric field gradients (EFGs). This broadening limits the fidelity of controlling the nuclear spin system, which we discuss in more detail in Chapter 7. To reduce broadening of the nuclear spin NMR frequencies we require dots with low internal strain.

Using local droplet etching (LDE), it is possible to produce strain-free self-assembling QDs made from lattice matched materials. LDE first involves etching away at the substrate to form

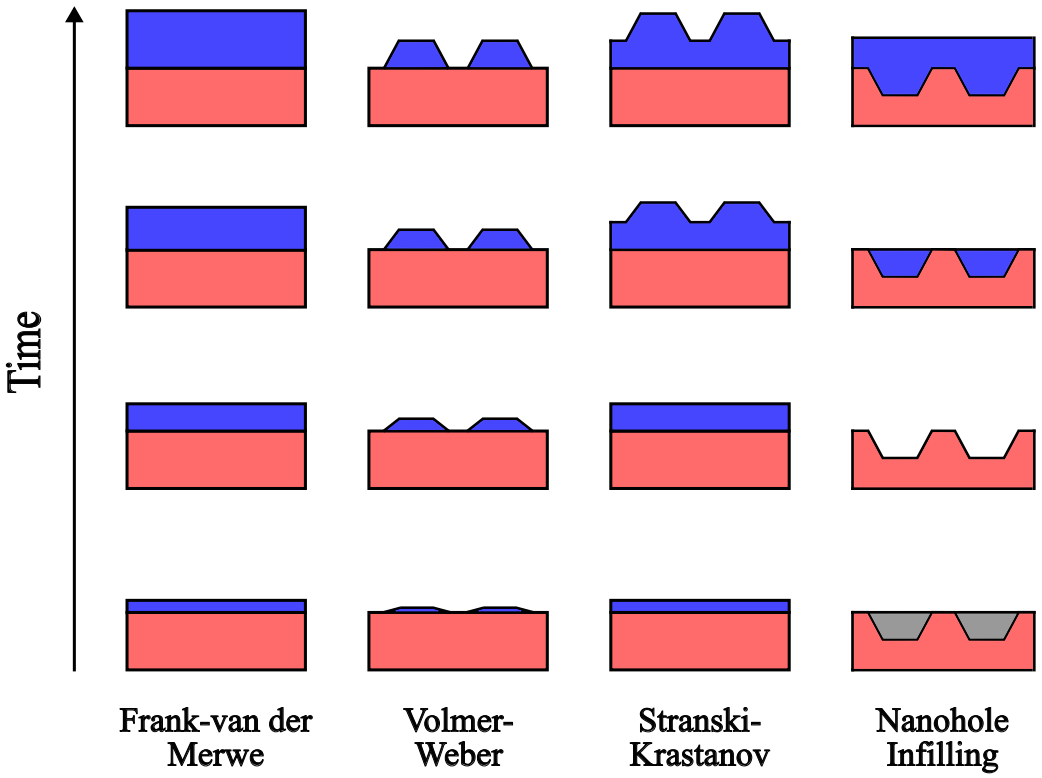


Figure 2.2: Diagram showing different heterostructure growth modes (from left to right) FvdM, VW, SK, and nanohole infilling. The substrate (red) is used as a base to grow the new material on (blue), as material is added it forms structures depending on the given growth mode (going bottom to top). For nanohole infilling the substrate is first etched away using droplets of a different material (grey) before the QD material is deposited. For SK growth the two materials are lattice mismatched while for nanohole infilling the two materials have matching (or nearly matching) lattice structures.

nanoholes on the surface before filling them, forming QDs inside the nanoholes. For the samples used in this thesis, a layer of AlGaAs is first grown on a GaAs substrate. Aluminium (Al) flux is applied briefly to the sample and forms Al droplets on the AlGaAs surface. The high Al concentration at the boundary between the droplet and sample causes arsenic (As) in the sample to desorb into the droplet, causing a hole to be etched into the AlGaAs [50].

Nanohole depth is found to be spread as a bimodal distribution forming either 'flat' holes (depth < 5 nm) or 'deep' holes (depth > 5 nm). The formation of flat holes can be suppressed by using high temperatures during etching, allowing for the reliable and consistent formation of deep holes [51]. Additionally the hole depth, width and density can be controlled by the etching material, the deposition rate, and temperature allowing for tuning of the QD's properties via the nanoholes [52, 53]. GaAs is then deposited to fill the nanoholes forming QDs and a QW layer above them in what looks like an 'inverted' SK grown sample as shown in Fig. 2.2. The QDs have an inverted cone

shape. The height of the QD can be controlled by the amount of GaAs deposited and can be used to tune the energy levels due to quantum confinement effects as seen in the photoluminescence (PL) spectra for different QDs, while PL linewidths down to ≈ 40 μeV have been demonstrated [49, 53].

The optical properties of LDE QDs are significantly better, owing to the higher temperatures used during QD growth, than those produced by previous droplet based growth techniques. This means they have similar optical properties to SK QDs, which was a serious limiting factor in the usefulness of these techniques in the past [54]. The optical properties can be improved further by introducing a Bragg reflector into the sample structure. The Bragg reflector is made by growing layers of AlGaAs and alternating the ratio of Al and gallium (Ga) in each layer and hence their refractive index. When light is shined on the sample, there is partial reflection of the light at each layer of the reflector due to the changing refractive index, the reflected light then interferes constructively leading to a significant enhancement in the PL emission strength from the QDs.

It is often desirable to be able to control the occupation of the QDs with charge carriers, enabling the emission of different exciton states to be investigated or, in the case of spin qubits, a single charge carrier needs to be confined within a given QD to form the spin qubit [55–57]. Such charge tuning can be done by incorporating the sample into a *p*-*i*-*n* diode structure. This is achieved simply by doping a layer below the QD layer with an electron donor material to form a *n*-doped layer, while the *p*-doped layer is formed above the sample by incorporating an electron accepting material. This means the QDs are in-between the two ends of the diode. By applying a positive bias across the sample electrons will tunnel from the *n*-doped layer into the QDs, while the application of a negative bias will cause an electron to tunnel from the QD to *p*-doped layer, forming a hole in the QD. Incorporation of a diode helps to further optimise QD optical properties and suppress charge noise [58]. Suppression of the tunnelling of electrons and holes can be achieved by increasing the depth of the tunnelling barrier layer between the doped layers and the QDs.

To realise usable quantum devices, it will be necessary for QDs to be incorporated into more complex structures, such as wave-guides. This means that QDs need to be growable in specific locations. For self-assembled QDs achieving site-control has been allusive due to the random nature in which QDs nucleate. This means that QDs must be located on a sample before device fabrication around the QD, which can be achieved for LDE grown dots by locating the nanoholes formed by etching using atomic force microscopy (AFM). Work has been done to make site-controlled SK grown dots by using pre-patterned substrates, though the dot optical properties show significantly broader line widths [59]. For the newer strain-free QDs site control is still in its infancy, limited to using droplet epitaxy with pre-patterned substrates [60].

2.1.2 Semiconductor Band Structures

The optical properties of QDs are dependent on the behaviour of charge carriers, such as electrons. In bulk semiconductors charge carriers are not free. They experience a periodic potential due to the regular lattice structure of charged nuclei, giving rise to an altered dispersion relation [44]. Due to the dependence on the periodic potential the dispersion relation varies for different semiconductors and is called the band structure. These dispersion relations can be determined using Bloch's theorem [61] which, for a free electron (periodic potential $U = 0$), the dispersion relation has the form [44]:

$$E(\boldsymbol{k}) = \frac{\hbar^2 \boldsymbol{k}^2}{2m_e}, \tag{2.1}$$

where $\boldsymbol{k}$ is the crystal momentum (an arbitrary vector in reciprocal space) and m_e is the electron mass. It can be shown that m_e is inversely proportional to the curvature of the band, meaning it will change when a potential is introduced by a crystal lattice. It is then referred to as the effective mass m^*_α, with α being used to denote the carrier (e for electrons, h for holes) [44, 48]. Another property of semiconductors is that there exists a relatively large energy range with no carrier states, which is called the band gap E_g. This separates the dispersion relation into two distinct bands above and below the band gap called the conduction band (CB) and valence band (VB) respectively.

GaAs and AlGaAs are III-V semiconductors meaning they have a zincblende crystal structure [62]. The CB and VB can be approximated as parabolic for small $\boldsymbol{k}$ around the Γ point (the origin in reciprocal space, $\boldsymbol{k} = 0$) and are given by [48, 63]:

$$E_c(\boldsymbol{k}) \approx E_g + \frac{\hbar^2 \boldsymbol{k}^2}{2m^*_\alpha} \tag{2.2}$$

$$E_v(\boldsymbol{k}) \approx -\frac{\hbar^2 \boldsymbol{k}^2}{2m^*_\alpha}, \tag{2.3}$$

where E_c and E_v are the conduction and valence band energies respectively, E_g is the band gap energy, $\hbar$ is the reduced Plank constant and m^*_α is the effective carrier mass. Due to the VB maxima and CB minima both being at the Γ point, carriers can be excited between the bands with no need for additional momentum to be supplied via an intermediate state. Therefore, GaAs and AlGaAs are both direct band gap semiconductors meaning they are significantly more optically active than indirect band gap semiconductors like silicon (Si). Band gap energies vary between semiconductors and in alloys are dependent on the fraction of each species [44]. At room temperature GaAs has a band gap energy of $E_g \approx 1.42$ eV [62, 64] while for $Al_{0.3}Ga_{0.7}As$ $E_g \approx 1.81$ eV [65]. The difference in band gaps causes confinement effects in QDs. The band gap is also dependent on temperature [66] and for this work, it is more relevant to discuss band gap energies at liquid helium

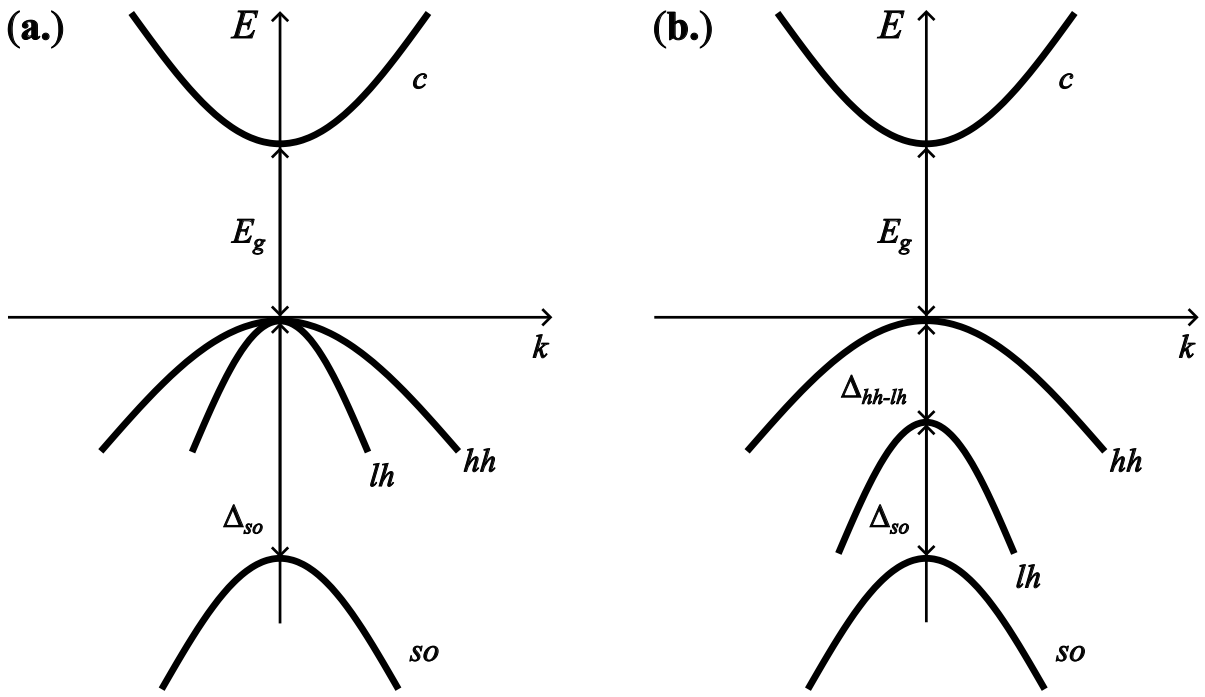


Figure 2.3: (a.) Schematic diagram of the band structure of a zincblende semiconductor. There are two bands, the CB and VB, which are separated by the band gap energy, E_g. The conduction band consists of one sub-band c, while the valence band has three sub-bands. lh and hh are degenerate at the Γ point ($\boldsymbol{k} = 0$) but differ at other values of $\boldsymbol{k}$ due to different effective carrier masses. The so band is separated by large energy Δ_{so} due to the spin-orbit interaction. All bands are approximated to be parabolic in the region around the Γ point. (b.) Schematic diagram of a uniaxially compressively strained QD sample focused on the Γ point, meaning band warping due to shear strain is not shown. A combination of strain and confinement effects causes a splitting Δ_{hh-lh} between the lh and hh bands meaning they are no longer degenerate at the Γ point, leaving the hh band as the highest energy VB state. Figure based on figure found in [48].

temperatures ($T \approx 4.2$ K), where $E_g \approx 1.53$ eV for GaAs and $E_g \approx 1.88$ eV for $Al_{0.3}Ga_{0.7}As$ [64, 67].

For semiconductors the Fermi level lies within the band gap meaning the VB is fully occupied with electrons while the CB is empty. In experiments an electron is typically excited optically to the CB leaving an electron vacancy in the VB. As this excited system is more relevant to experiments we will consider this in the following.

The band structure for GaAs is shown in Fig. 2.3a. There is a single CB where the electron is while the VB contains a hole, a quasi-particle with positive charge that represents the electron vacancy, and is split into three bands. These bands originate from the spin of the charge carriers. In semiconductors carriers experience a relativistic effect, called the spin-orbit interaction, where charge carriers feel a magnetic field as they travel through the periodic potential of the lattice [48].

This magnetic field couples the carriers spin angular momentum $\hat{\mathbf{S}}$ to its orbital angular moment $\hat{\mathbf{L}}$, meaning the total momentum $\hat{\mathbf{J}}$ must be considered:

$$\hat{\mathbf{J}} = \hat{\mathbf{L}} + \hat{\mathbf{S}}. \tag{2.4}$$

The CB is like an *s*-type atomic orbital with orbital angular momentum $\hat{\mathbf{L}} = 0$, so only the electron's spin $\hat{\mathbf{S}} = \frac{1}{2}$ needs to be considered. This gives two CB states corresponding to the two electron spin states $s_z = \pm\frac{1}{2}$. For the VB the orbitals are like *p*-type atomic orbitals, with $\hat{\mathbf{L}} = 1$. This gives rise to holes with total momentum $\hat{\mathbf{J}} = \frac{1}{2}, \frac{3}{2}$. For the case where $\hat{\mathbf{J}} = \frac{1}{2}$ there are only two states, similar to the CB, for the two hole spin states $J_z = \pm\frac{1}{2}$ which are separated from the other VBs by a large energy splitting Δ_{so}, meaning they can be typically ignored. This is called the split-off band (*so*). For the $\hat{\mathbf{J}} = \frac{3}{2}$ case there are four states $J_z = -\frac{3}{2}, -\frac{1}{2}, +\frac{1}{2}, +\frac{3}{2}$ which form an additional two sub bands. The light hole (*lh*) band is formed from the $J_z = \pm\frac{1}{2}$ states while the $J_z = \pm\frac{3}{2}$ states form the heavy hole band (*hh*). At the Γ point the heavy and light hole energy is degenerate but differs as the magnitude of $\boldsymbol{k}$ increases. This is due to differences in the hole effective masses (seen in the band curvatures), which is where the bands get their names [44, 48]. As mentioned, electrons can be excited into the CB optically where they become free to move through the material. This, however, limits their uses in quantum technology applications, meaning we need to be able to localise carriers in order to be able to use them as a quantum resource.

2.1.3 QD Confinement of Charge Carriers

QDs are structural defects and, as such, they disrupt the band structure of the bulk semiconductor in two ways. The first is the introduction of strain, caused by stretching or compression of atomic bonds due to differences in the two materials lattice structures. The band structure of a bulk crystal can be determined using the Luttinger model where strain effects are described by the Pikus-Bir Hamiltonian [68]. For a direct band gap zincblende crystal structure, such as GaAs, it is found that the CB is primarily sensitive to hydrostatic strain while the VB is sensitive to both hydrostatic and shear strains. Hydrostatic strain shifts the energy of the CB and VB causing the band gap to change in magnitude. Comparatively, shear stain alters the symmetry of the bulk crystal which has two affects. First it lifts the degeneracy of the *hh* and *lh* bands at the Γ point causing an energy splitting Δ_{hh-lh}. Second, it causes them to mix leading to the CB and VB becoming warped [69]. The resulting change in the band structure is dependent on if the strain is compressive or tensile. Under compressive strain the hydrostatic component causes the CB to increase in energy, while the VBs will decrease in energy leading to an increase in the band gap. The opposite occurs for tensile strain [44, 69]. The magnitude and sign of Δ_{hh-lh} is dependent also on which crystallographic axis the strain is applied along and the type of strain applied (biaxial, uniaxial etc.) but often breaks the

symmetry of the band structure along the different crystallographic axes. This can lead to either the *hh* character (not a fully *hh* band due to *hh*-*lh* mixing) or *lh* character band being the highest energy VB state [48, 69].

For the lattice matched GaAs/AlGaAs samples used in this thesis the strain caused by the formation of quantum dots is small, which can be seen from the narrower NMR linewidths observed in experiments compared to lattice mismatched indium gallium arsenide (InGaAs)/GaAs QDs ($\approx$ 1-10 kHz compared to $\approx$ 1 MHz) [70, 71]. Instead the externally applied uniaxial compressive strain applied along the [110] crystallographic axis will dominate. The in plane (*x*-*y* plane) compression increases the bandgap and means that the *lh* band is the highest VB state in plane while the *hh* band is the highest out of plane (along *z*) VB state. Additionally there is a strong mixing of the all of the bands [69]. A simplified version of the out of plane altered band structure is shown in Fig. 2.3b [44, 69], where we have neglected band warping which occurs far from the Γ point by focusing on the Γ point, which is where the most relevant physics for this work occurs. An important consequence of strain effects for QD optical properties is that it causes quantisation based on the spin states of carriers [48].

The second alteration of the bulk band structure caused by QDs is the quantisation of carrier states due to confinement effects. The QD creates a potential well which, due to its small size, is enough to cause confined charge carriers to exhibit quantum behaviour, such as discrete quantised states in comparison with the bulk semiconductor dispersion relation. The origin of the potential is differences in the band gap E_g between the QD material and the surrounding material. Therefore, the materials used are important when calculating the strength of the confinement and the corresponding energy levels. To determine the carrier energy states the shape of the potential must also be considered. For the QDs used in this thesis the dots are not spherical, they tend to be shallower along the growth direction (*z*) and wider in the *x*-*y* plane meaning a simpler spherical potential is not applicable, and a more complex system is needed. Instead it has been shown that a valid approximate solution is to consider the system as two separate problems: A 1D potential well to simulate confinement along the *z* axis, and a 2D parabolic potential for confinement in the *x*-*y* plane.

The potential well for a GaAs/AlGaAs QD would be $V(z) \approx 0.35$ eV at 4.2 K and, due to the small dot depth, introduces a strong confinement along the *z*+ direction, causing large splitting between the different carrier energy levels. This further increases splitting between the *lh*, *hh* and *so* bands [48]. This splitting is large enough that we can assume that only the ground states are relevant in the following, as the energy required for a carrier to occupy a higher level would be sufficient to excite the carrier out of the QD. Considering this system, we would expect there to be a single state at each value of n where n is the principal quantum number with values $n = 0$, 1, 2 etc. However, this does not provide the full picture: we now need to consider the 2D parabolic

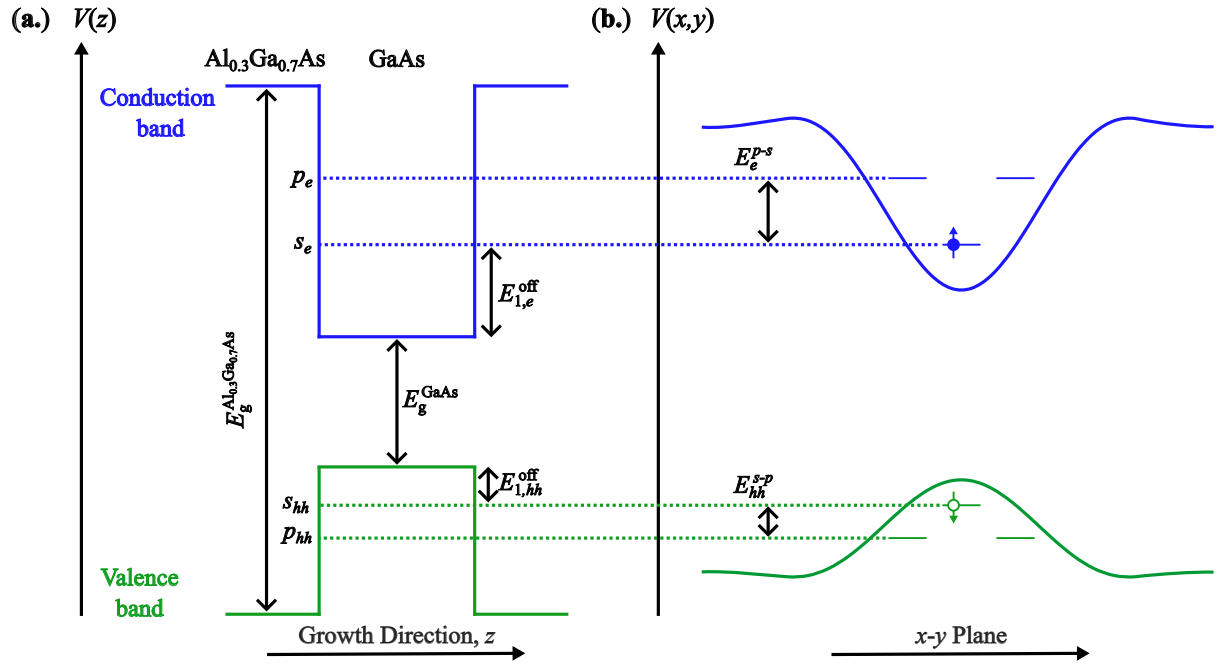


Figure 2.4: (a.) Diagram of QD energy levels caused by confinement along the z axis (growth direction). A potential well is formed by the difference in band gap energies inside (E_g^{GaAs}) and outside ($E_g^{\mathrm{Al_{0.3}Ga_{0.7}As}}$) of the QD. The potential well splits the carrier bands meaning the *hh* band becomes the highest energy VB. There are additional energy offsets for the lowest (highest) CB (VB) states $E_{1,e}^{\mathrm{off}}$ ($E_{1,hh}^{\mathrm{off}}$), meaning the energy needed to excite an electron into the CB is equal to $E_{1,hh}^{\mathrm{off}} + E_g^{\mathrm{GaAs}} + E_{1,e}^{\mathrm{off}}$. (b) Diagram of the confinement due to the parabolic potential in the x-y plane. The confinement splits the band into distinct quantised energy levels labelled s and p like those found in atomic orbitals which are separated by energy E_e^{p-s} and E_{hh}^{s-p} for the CB and VB respectively. The 2D confinement also introduces degenerate states for energy levels above the ground state (s).

potential across the x-y plane, which takes the form:

$$V(x,y) = \frac{1}{2} m_\alpha^* \omega_\alpha^2 (x^2 + y^2), \tag{2.5}$$

where m_α^* is the effective carrier mass and ω_α is an offset frequency. The confinement effects are significantly weaker for this potential due to the broadness of the dot in the x-y plane, yet it does introduce additional states. If we consider the eigenvalues for Eq. 2.5 [63]:

$$E_{n_x,n_y}^{\alpha} = \hbar\omega_\alpha (n_x + n_y + 1). \tag{2.6}$$

We now have energy levels dependent on n_x and n_y, with the condition that $n = n_x + n_y$ this introduces a $n + 1$ degeneracy. This means for states $n = 0$, 1, 2, etc. we have a corresponding

number of degenerate states 1, 2, 3, etc. at each level, while the z confinement is treated simply as an offset. This offset further separates the CB and VB ground states by energies $E^{\text{off}}_{1,e} \approx 168$ meV and $E^{\text{off}}_{1,hh} \approx 43$ meV respectively [72]. However, it should be noted that the values will vary significantly from dot to dot due to the strong dependence of the QD size and shape on the confinement. The energy level structure of QDs are therefore very similar to those of 3D atomic orbitals, with clear orbital shells s, p, d, f, etc. separated by energy $\hbar\omega_\alpha$, as shown by Eq. 2.6. It is worth mentioning that the above is a simplification because we have assumed that the dot is perfectly circular in the x-y plane which is almost never the case. For realistic dots the confinement varies with the dot's own geometry where perturbations in the confining potentials can introduce a mixing of states, such as mixing of the *lh* and *hh* states, requiring significantly more complex solutions [48]. Critically, unlike CB electrons in bulk semiconductors, electrons confined to QDs are no longer free to move. They are instead localised, meaning it is simpler to manipulate them. This is what makes QDs useful for quantum technology applications.

2.2 Optical Properties of Quantum Dots

For the experimental work in this thesis, nuclear spin measurements were performed optically via charge carriers, meaning the optical properties of QDs need to be considered. As mentioned in the previous chapter, electrons, using energy supplied by a photon, can be excited from the VB to the CB leaving behind an electron vacancy in the VB. The remaining VB electrons and the vacancy can then be treated as a single quasi-particle called a hole, which has the same charge as an electron but with different sign ($+e$). This process must conserve crystal momentum ($\boldsymbol{k}$) which, because photons do not carry crystal momentum, a purely optical excitation requires the electron and hole have the same $\boldsymbol{k}$ value. If this condition is not met, due to the CB minima and VB maxima not being at the same $\boldsymbol{k}$ value, then a phonon is additionally required to supply the missing crystal momentum. This significantly reduces how optically active these materials, referred to as indirect band gap semiconductors, are. As mentioned, GaAs and AlGaAs are direct band gap semiconductors with the CB minima and VB maxima both located at the Γ point ($\boldsymbol{k} = 0$), meaning state transitions can be driven purely by optical photons making them optically active, a big advantage for these kinds of QDs.

In order to conduct optically detected nuclear magnetic resonance (ODNMR) measurements, we need to be able to resolve the Zeeman split PL lines corresponding to the two electron spin states. Additionally measurements need to be sensitive to small energy shifts in the PL induced by the hyperfine interaction between the nuclear and electron spins, requiring the dot's PL to be bright and possess a small linewidth. At high temperatures, the optical properties of QDs are severely limited by lattice vibrations (phonons) caused by the thermal energy. This causes a broadening of

PL lines as electrons can be excited to higher states and can even be excited out of the dot, leading to an additional loss in brightness [73–76]. We therefore use liquid helium to cool the sample down to $T \approx 4.2$ K which reduces the number of thermal phonons so that spin interaction induced PL changes can be resolved.

Optical excitation occurs when the QD absorbs a photon of the correct energy to excite an electron from the VB to the CB which, is an energy given by:

$$E_{\text{photon}} = \hbar\omega_{\text{photon}} \geq E_{1,hh}^{\text{off}} + E_g^{\text{GaAs}} + E_{1,e}^{\text{off}}, \tag{2.7}$$

where ω_{photon} is the photon frequency, E_g^{GaAs} is the GaAs band gap energy and $E_{1,e}^{\text{off}}$ and $E_{1,hh}^{\text{off}}$ are the electron and heavy hole offset energies. When the electron is excited into the CB a hole is created in the VB. The two particles then begin to interact via the Coulomb interaction between their charges:

$$V_{\text{Coul}}(\mathbf{r}_1, \mathbf{r}_2) = \frac{q_1 q_2}{4\pi\varepsilon} \frac{1}{|\mathbf{r}_1 - \mathbf{r}_2|} = -\frac{e^2}{4\pi\varepsilon} \frac{1}{|\mathbf{r}_1 - \mathbf{r}_2|}, \tag{2.8}$$

where q_1 and q_2 are the two particles charges which, for an electron and hole, are $-e$ and $+e$ respectively, $\mathbf{r}_1$ and $\mathbf{r}_2$ are the positions of the two particles and $\varepsilon = \varepsilon_0\varepsilon_r$, where ε_r is the relative dielectric constant. As electrons and holes possess charges of opposite sign, they are attracted to each other, and this interaction causes them to become bound together as a single state called an exciton with a binding energy dependent on the strength of the Coulomb interaction between them. The exciton binding energy complicates the optical emission from the dot. Under confinement effects alone we would expect the carrier energies to increase with decreasing dot size, yet the binding energy acts against this reducing the carrier energies. In fact, the binding energy is actually increased by confinement effects as the carriers are forced closer together causing their wavefuctions to overlap increasing the strength of their Coulomb interaction [77, 78]. This creates two distinct regimes for exciton behaviour. If the confinement is larger than the Coulomb induced coupling then the exciton is said to be in the strong confinement regime, if instead the strength of the Coulomb interaction is stronger than the confinement effects the exciton is said to be weakly confined. For the scope of this work we deal only with excitons in the strong confinement regime, meaning we can simply treat the Coulomb interaction as a perturbation on the already discussed confinement effects [48, 79].

Not all transitions are allowed in QDs due to the selection rules imposed by conservation laws. Photons possess a parity of -1 and a spin angular momentum of 1. Parity is a fundamental property describing the symmetry of a particle under spatial inversion, a photon is said to have odd parity. The CB and VB states are *s*-like and *p*-like respectively meaning that equivalent sub-bands have opposite parity. Likewise different sub-bands have alternating parity (s_e, p_e, d_e, etc.). In order to

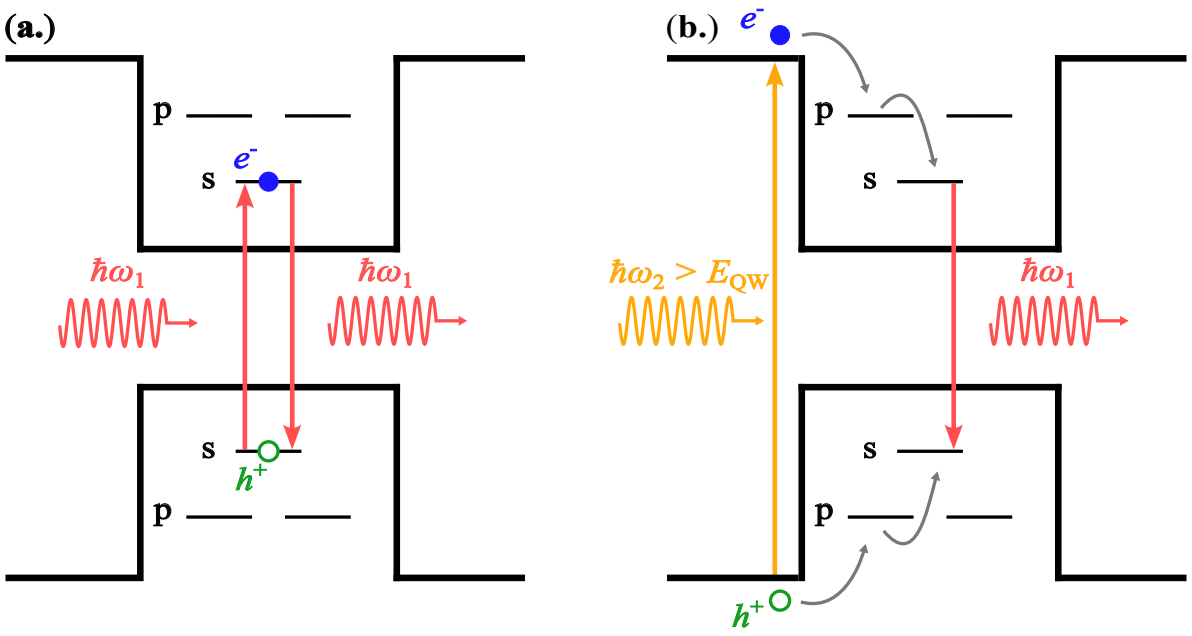


Figure 2.5: (a.) Schematic diagram of resonant excitation. A photon of energy $\hbar\omega_1$ is absorbed by an electron (e^-) in the VB s state exciting it to the CB s state, leaving a hole (h^+) in the VB and forming an exciton. After radiative lifetime τ_R the exciton recombines and a photon is emitted with energy $\hbar\omega_1$. The excitation and emitted photons have identical energy. (b) Schematic diagram of non-resonant excitation. A photon with energy $\hbar\omega_2 > E_{QW}$ excites an electron into the CB QW states; a hole is also created in the VB. The carriers relax through a series of intraband transitions and are recaptured by the dot before recombining, emitting a photon of energy $\hbar\omega_1$. The excitation and emitted photons have different energies.

conserve parity it is required that the starting and final states have opposite parity, this imposes the restriction that optical transitions must be interband ($s_e \leftrightarrow s_{hh}$, $p_e \leftrightarrow p_{hh}$, etc.). The transitions are also spin conserving in order to conserve the total momentum. This is important as it influences which transitions between different carrier spin orientations are optically active, which will be discussed in the next section [48].

As shown by Eq. 2.7 there are two photon energy conditions where optical transitions can be driven. The first, in the case where the photon energy is exactly equal to the energy between the two states, is resonant excitation. Here the photon causes an interband transition ($s_e \leftrightarrow s_{hh}$) forming an exciton. After a short time, termed the radiative lifetime τ_R, the electron and hole recombine and emit a photon of the same energy as the excitation photon. This method is outlined in Fig. 2.5a. This process is difficult to measure optically as the wavelength of the excitation and PL light are identical, meaning the scattered excitation light cannot be simply filtered out to observe light from the dot. Instead, cross polarisation techniques [80] can be used to achieve this. Despite the added experimental complexity, this technique is beneficial as using resonance florescences reduces PL

line widths, preserves coherence and gives more indistinguishable photons, which is significant for the development of single-photon sources and optical spin control [81–83]. This technique is not limited to the transition between the *s* shells. The same process, termed quasi-resonant excitation, can be applied to the higher energy shells.

An alternative to this is to use off-resonant excitation which is shown in Fig. 2.5b. Photons of higher energy than the ground state energy are used, exciting electrons into higher CB states or even out of the dot and into the QW layer; a hole is generated in the equivalent VB state. Non-radiative processes then allow the carriers to decrease in energy through intraband transitions, becoming recaptured by the QD before reaching the ground state. As before with resonant excitation, the exciton then undergoes recombination emitting a photon. The benefit of this approach is that it is extremely simple to isolate the emitted dot PL from the excitation laser light as they are different wavelengths, meaning optical filters can be used. For the work is this thesis we use non-resonant excitation for ODNMR.

2.2.1 Charged Excitons and Charge Tuning

In the previous section we discussed the optical generation of excitons formed from an electron-hole pair. Due to the opposing charge of the two carriers, these excitons have a net charge of 0 and are termed neutral excitons (X^0). However, this is not the only type of exciton: it is possible for additional carriers to become confined within a QD. The interactions between all of the confined carriers must then be considered forming different types of excitons. The most common of these would be trions composed of three carriers meaning they are charged as one of the carriers will be unpaired. For example the negative exciton (X^-) is formed from a pair of electrons and a single hole, giving a net charge of $-e$. Similarly, the positive exciton (X^+) consists of a single electron and a pair of holes. It is possible to form excitons with larger charge magnitudes by confining additional unpaired carriers ($X^{2\pm}$, $X^{3\pm}$, etc). Another common exciton is the biexciton, which is comprised of two electrons and two holes, that forms by chance when two electron-hole pairs are excited into the dot at the same time. These four common charge configurations are shown in Fig. 2.6.

The addition of more carriers alters the energy of different excitons compared to the neutral exciton: this is due to additional interactions via the Coulomb interaction. For example, in the negative exciton there is an additional attraction between the second electron and the hole as well as repulsion between the two electrons. The net result is there is a decrease in exciton energy as additional electrons are added, the opposite is true for adding holes. This means that electron-electron repulsion is weaker than the electron-hole attraction, a result of holes being more localised [55, 79, 84, 85]. In the case of the biexciton two PL lines are observed, which correspond to the recombination of the two electron-hole pairs. The PL line corresponding to the first recombination

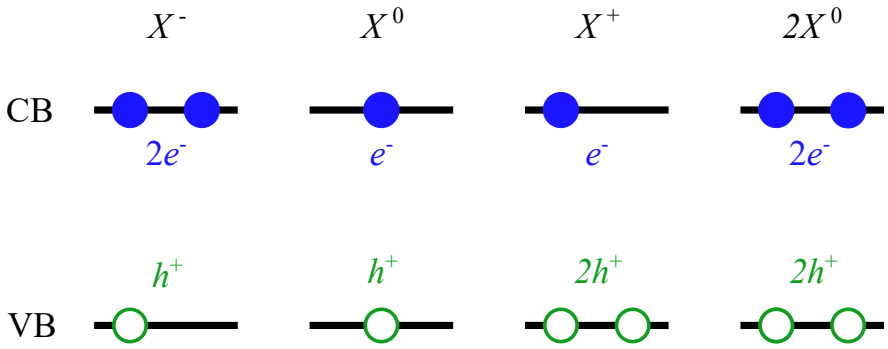


Figure 2.6: Diagram of the four most common excitons and the carriers they are composed of. Moving from left-to-right: negative exciton (X^-), neutral exciton (X^0), positive exciton (X^+) and the biexciton ($2X^0$).

is found at lower energies than the X^0 line due to the additional Coulomb interactions between the four carriers; after this the second recombination emits at the same energy as X^0 as the systems are identical [48].

Generation of more complex excitons can be achieved either by using high optical powers or by the application of an electric potential across the dot, which is the method we use for this thesis. When there is no potential across the sample, excitons are formed by chance when high power photons generate carriers in states above those of the QD; these carriers then relax into the dot states as discussed previously. However, there is a chance that this can lead to two exciton pairs being confined within the dot at the same time forming a biexciton. Likewise, there is a chance for individual carriers to tunnel out of the dot, leaving an unpaired electron or hole in the dot to form a X^- or X^+ exciton respectively [48, 86].

In the case where a bias is applied across the sample, which we do by incorporating a *p-i-n* diode into our samples, the generation of charged excitons can be done deterministically. Fig. 2.7a shows a schematic energy level diagram for our samples. The Fermi level lies below the QD ground state and the free CB electrons in the *n*-doped material are separated from the QD by a barrier layer of thickness t_B. By applying a positive bias the QD ground state is brought into resonance with the Fermi level allowing electrons to tunnel into the dot and become trapped. This electron can then be used as a spin qubit or, by combining it with an optically excited exciton, generate charged excitons (X^-). Similarly using a negative bias it is possible to tune the QD VB into resonance with the Fermi level, allowing electrons to tunnel out of the dot and into the *n*-doped layer. This leaves trapped holes in the QD meaning positively charged excitons can be formed. A thick tunnelling barrier between the QD layer and the *p*-doped layer suppresses the tunnelling of holes. It is possible using a larger positive bias to tunnel additional electrons into the QD and in previous works this

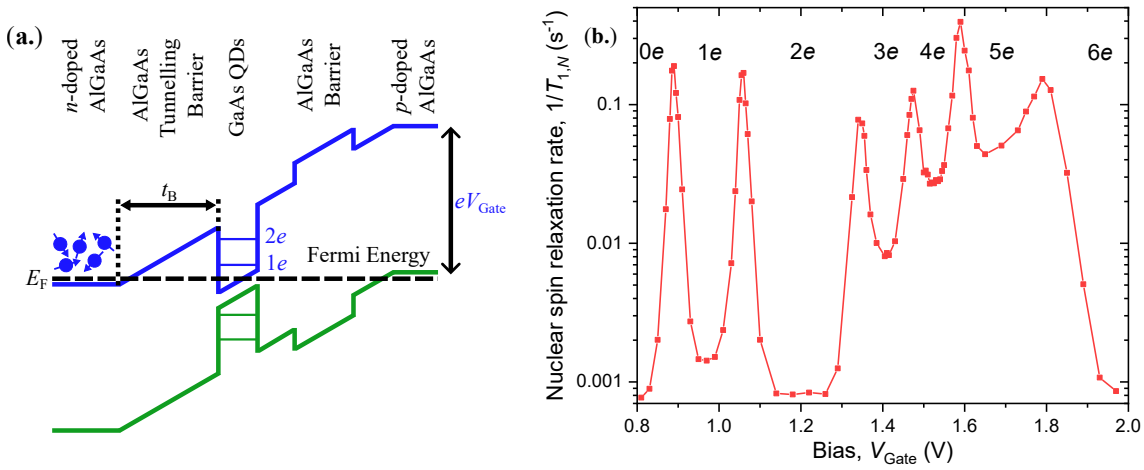


Figure 2.7: (a) Energy level diagram of a QD sample with an incorporated *p-i-n* diode. When the bias $V_{\text{Gate}} = 0$ V the QD CB ground state lies above the Fermi level meaning here are no electrons in the QD CB. By increasing V_{Gate} the QD CB states can be brought into resonance with the Fermi level allowing electrons to tunnel into the dot. Further increasing the bias allows progressively more electrons to tunnel into the QD. The tunnelling of holes from the *p*-doped layer is suppressed by the inclusion of a thick tunnelling barrier. (b) Dependence of nuclear spin relaxation rate ($1/T_{1,N}$) on the applied bias V_{Gate}. The relaxation rate increases significantly when an electron is tunnelling into the dot, due to interactions between the electron and nuclear spins. Therefore, the plateaus are regions where the electron occupation of the dot is stable, allowing the dot charge states to be mapped. This graph is from work in Chapter 6 and will be discussed in more detail there.

can be observed by measuring either the capacitance or the PL from the dot [55, 79, 84, 85]. Here we instead infer the charging state of the QD through changes in the nuclear spin relaxation rate ($1/T_{1,N}$) due to interactions with the electron spins, which will be discussed in more detail in Chapter 6 [87]. In Fig. 2.7b we see that changing the bias across the sample changes the nuclear spin relaxation rate. We observe regions where the relaxation rate sharply increases separated by flat regions where the relaxation rate is stable. These regions of increased relaxation are a result of an electron tunnelling in and out of the dot rapidly, which has a knock on effect of increasing the nuclear spin relaxation rate due to the randomly oriented electron spin. Therefore, the plateau regions must mean the dot is in a stable charged state. These charge states have been labelled in Fig. 2.7b. We can therefore see that electron states are occupied in QDs similarly to Hund's rule in atomic physics. The first electron is added as described above but, despite the two *s*-states being degenerate, more energy is required to add a second electron due to the electric charge of the electron trapped in the dot repelling electrons trying to tunnel in, increasing the energy needed. This is called the Coulomb blockade. After a second electron is added there is a large stable region. This is because the *s*-shell is full and the next electron must occupy a *p*-shell state, requiring additional energy. After this, additional electrons are added to the *p*-shell following a pattern similar to filling the *s*-shell states. By choosing a bias in one of these plateau regions we can select and ensure the

generation of a negatively charged exciton.

2.2.2 Fine Structure

Confinement and Coulomb interactions are not the only effects that must be considered when determining QD optical properties. The interactions between carrier spins can break energy level degeneracies, giving rise to the exciton fine structure.

First, considering the X^0 exciton, we must consider the different orientations of the electron and heavy hole spin. We have four different spin configurations arising from the electron spin $\hat{\mathbf{S}} = \frac{1}{2}$, $s_z = \pm\frac{1}{2}$ ($\uparrow/\downarrow$) and the heavy hole angular momentum $\hat{\mathbf{J}} = \frac{3}{2}$, $J_{h,z} = \pm\frac{3}{2}$ ($\Uparrow$ / $\Downarrow$), which we will refer to from now on as the hole spin. Considering the total exciton spin, defined as $M = s_z + J_{h,z}$, there are two states where the spins are parallel ($|\uparrow\Uparrow\rangle$,$|\downarrow\Downarrow\rangle$) with total spin $|M| = 2$ and two where they are anti-parallel ($|\uparrow\Downarrow\rangle$,$|\downarrow\Uparrow\rangle$) with total spin $|M| = 1$. This has two consequences, the first of these being that only two of the states are optically active. As photons carry angular momentum $L = 1$ only the states with $|M| = 1$ ($|\uparrow\Downarrow\rangle$,$|\downarrow\Uparrow\rangle$) can be excited optically and are referred to as the bright excitons (BEs). The other two states ($|\uparrow\Uparrow\rangle$,$|\downarrow\Downarrow\rangle$) with total momentum $|M| = 2$ are optically forbidden and are referred to as the dark excitons (DEs) [86, 88, 89].

Secondly, the four exciton states are not degenerate owing to the electron-hole exchange interaction. This is a coupling between the electron and hole spins arising due to symmetry requirements. The strength is enhanced by confinement effects due to the electron and hole wavefunctions being closer together or overlapping [89–91]. The exchange interaction is given by [48, 88]:

$$H_{\text{exchange}} = -\sum_{i=x,y,z} (a_i J_{h,i} S_{e,i} + b_i J_{h,i}^3 S_{e,i}), \tag{2.9}$$

where a_i and b_i are coupling constants and are linked to the QD geometry, $J_{h,i}$ (J = $\frac{3}{2}$) is the hole spin and $S_{e,i}$ (S = $\frac{1}{2}$) is the electron spin. As mentioned, due to strain, the energy splitting between the *hh* and *lh* states (Δ_{hh-lh}) means we can neglect the *lh* states in the following. Taking the four exciton spin states as a basis, it can be shown that Eq. 2.9 can be written as the matrix:

$$H_{\text{exchange}} = \frac{1}{2}\begin{pmatrix} \Delta_0 & \Delta_1 & 0 & 0 \\ \Delta_1 & \Delta_0 & 0 & 0 \\ 0 & 0 & -\Delta_0 & \Delta_2 \\ 0 & 0 & \Delta_2 & -\Delta_0 \end{pmatrix}. \tag{2.10}$$

Here Δ_0 are energy shifts on the four exciton states while Δ_1 and Δ_2 couple the bright and dark

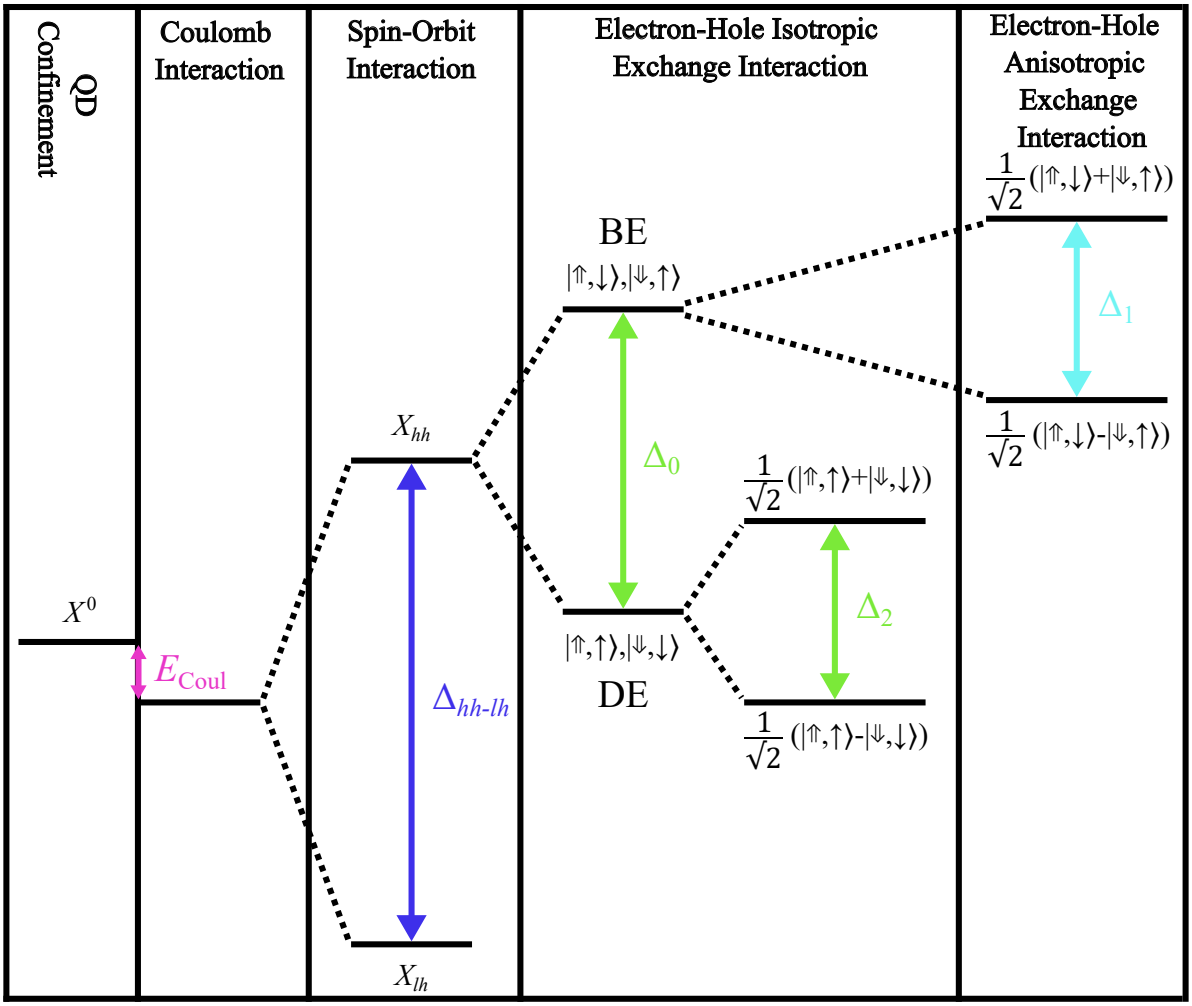


Figure 2.8: Energy level diagram for the neutral exciton states. The Coulomb interaction between the electron and hole reduce the confined exciton energy by E_{Coul}. The states are then split in energy due to the strain induced *hh*-*lh* splitting. Finally, the four heavy hole excitons are split in energy by the exchange interaction between the electron and hole spins. The isotropic exchange interaction splits the BE ($|M| = 1$) and DE ($|M| = 2$) states by energy Δ_0, and additionally it mixes and splits the two DE states by energy Δ_2. If the dot is not symmetric the anisotropic exchange interaction splits the two BE states by energy Δ_1, and also causes them to mix.

excitons respectively. The energies are given by:

$$\Delta_0 = \frac{3}{2}(a_z + \frac{9}{4}b_z) \tag{2.11}$$

$$\Delta_1 = -\frac{3}{4}(b_x - b_y) \tag{2.12}$$

$$\Delta_2 = -\frac{3}{4}(b_x + b_y). \tag{2.13}$$

From Eqs. 2.10-2.13 the fine structure emerges. First we see that the bright states are shifted in energy by $\frac{1}{2}\Delta_0$ while the dark states are shifted by energy $-\frac{1}{2}\Delta_0$, this causes an energy splitting between the BE and DE states of Δ_0, dependent only on the dot's geometry along the z axis.

The states are further split by the coupling between the two bright and dark states, however from Eq. 2.12 and Eq. 2.13 we see that there are two different types of fine structure splitting which are dependent on the dot geometry. The first is the case where the dot is symmetric ($b_x = b_y$), meaning $\Delta_1 = 0$ and there is no splitting between the BEs, only the dark states are split by Δ_2. This means that the energy splittings Δ_0 and Δ_2 are present regardless of the dot's geometry, and are called the isotropic exchange interaction. The BEs can be split under the condition the dot is not symmetric ($b_x \neq b_y$) with energy splitting Δ_1; this is termed the anisotropic exchange interaction. The terms Δ_1 and Δ_2 also cause a mixing of the two bright and dark states respectively, resulting in them becoming linearly polarised [92]. This means, for a non-symmetric QD, the exchange interaction fully breaks the degeneracy of the exciton states, giving a four level system with two bright states ($\frac{1}{\sqrt{2}}(|\uparrow\Downarrow\rangle + |\downarrow\Uparrow\rangle), \frac{1}{\sqrt{2}}(|\uparrow\Downarrow\rangle - |\downarrow\Uparrow\rangle)$) and two dark states ($\frac{1}{\sqrt{2}}(|\uparrow\Uparrow\rangle + |\downarrow\Downarrow\rangle), \frac{1}{\sqrt{2}}(|\uparrow\Uparrow\rangle - |\downarrow\Downarrow\rangle)$) [86, 88, 89]. The fine structure energy level diagram is shown in Fig. 2.8. While we have ignored the *lh* states, the exchange interaction causes similar splitting between them and can cause mixing between the *hh* and *lh* states [89].

The above behaviour disappears in the case of a charged exciton due to spin pairing. Take the X^- exciton composed of two electrons and a hole. Here, the two electron spins are anti-parallel due to Kramer's degeneracy theorem and therefore the net electron spin is 0. This just leaves the hole spin giving rise to two degenerate states corresponding to the hole spin up ($\Uparrow$) and spin down ($\Downarrow$) states. The states are degenerate as there is no other spins to couple with and hence no exchange interaction. The degeneracy can however still be lifted by introducing an external magnetic field, which causes Zeeman splitting of the two states [86]. We will discuss this in the next section.

2.2.3 External Fields

Electric Fields

As already discussed in Section 2.2.1, external electric fields can be used to allow deterministic charging of a QD owing to the Coulomb blockade. Electric fields also play an important role in determining the exciton binding energy, which is reduced by the attraction between the electron and hole charges. In a similar manner an external field can be used to tune exciton emission energies.

In the presence of an external electric field the electron and hole in an exciton will become slightly displaced creating an electric dipole. This dipole will then couple to the external field, causing an energy shift given as [48]:

$$\Delta E_{\text{Stark}} = -\mathbf{p} \cdot \mathbf{F}. \tag{2.14}$$

Here, $\mathbf{p}$ is the exciton dipole moment (going from positive to negative), $\mathbf{F}$ is the external field and ΔE_{Stark} is the shift in exciton energy caused by the external electric field. The effect of static electric fields on quantum states is called the Stark effect, though in the case of nanostructures the effect is largely driven by the the confinement and it is called the quantum confined Stark effect (QCSE). ΔE_{Stark} is called the Stark shift.

From Eq. 2.14 we see that the QCSE should always lower the exciton energy. However, even if the external field is zero the electron and hole will still be displaced by distance $\mathbf{s}_0$. There will therefore be a zero-field dipole moment $\mathbf{p}_0 = e\mathbf{s}_0$, and the electric field then induces a small dipole moment:

$$\mathbf{p} = -\beta \mathbf{F} + \mathbf{p}_0, \tag{2.15}$$

where β is the exciton polarisability. Consequently, the exciton dipole moment is split into two dipoles: an intrinsic dipole $\mathbf{p}_0$, and one controlled by the external field $\beta\mathbf{F}$. Substituting this back into Eq. 2.14 we obtain the Stark shift:

$$\Delta E_{\text{Stark}} = -\mathbf{p}_0 \cdot \mathbf{F} - \beta F^2, \tag{2.16}$$

and finally the Stark shifted exciton energy:

$$E_0 = E_0 + \Delta E_{\text{Stark}} = E_0 - \mathbf{p}_0 \cdot \mathbf{F} - \beta F^2, \tag{2.17}$$

with $F = |\mathbf{F}|$ and E_0 is the zero-field exciton energy. From Eq. 2.17 we see the QCSE gives a parabolic dependence to the exciton energy, with an additional linear term arising from the intrinsic dipole. Confinement effects are again important in determining the exciton behaviour. In QDs the confinement causes the electron and hole wavefuction to localise away from each other ensuring

that $\mathbf{s}_0 \neq 0$ and there is always an intrinsic dipole component. Secondly, the confinement limits the maximum electron-hole separation causing the Stark shift to become linear at large electric fields [48, 93]. Electric fields can therefore be used to control QD optical properties allowing for tuning PL brightness and emission wavelength. Additionally QDs can be tuned into resonance with one another or an optical cavity allowing for the development of photonic devices [94–99]. Here we have only discussed the direct current (DC) QCSE which describes the effects of static fields on excitons. There is also the alternating current (AC) QCSE describing exciton behaviour under an oscillating external field. For the work in this thesis we only use the DC QCSE to optimise QD PL brightness and to enable charge tuning. Therefore the AC QCSE is not discussed further.

Magnetic Fields

Externally applied magnetic fields are also able to alter exciton state energies due to interactions with the carrier spins. The orientation of the magnetic field is an important factor that determines the subsequent behaviour. There are two commonly used geometries. The first orientation has the field aligned parallel to the optical axis (z) and is referred to as Faraday geometry. The second has the field aligned in the x-y plane perpendicular to the optical axis, and is called Voigt geometry. The work in this thesis is carried out using Faraday geometry, specifically with the field pointed along the growth direction ($+z$). Interactions between magnetic fields and carrier spins causes an energy splitting between different spin states, referred to as Zeeman splitting. For an exciton we must consider the interaction of both the electron ($S_{e,i}$) and hole ($J_{h,i}$) spins giving the Zeeman Hamiltonian [88, 90, 91]:

$$H_{\text{Zeeman}}(B) = -\mu_B \sum_i (g_{e,i} S_{e,i} - g_{h,i} J_{h,i}) B_i. \tag{2.18}$$

Here, μ_B is the Bohr magneton, $g_{e,i}$ and $g_{h,i}$ are the electron and hole g-factors respectively and B is the applied field. Again we are neglecting the lh contribution and Eq. 2.18 has been simplified such that $J_{h,i} = \pm\frac{1}{2}$ is the effective heavy hole spin. As we work in Faraday geometry, $B = (0,0,B_z)$ and Eq. 2.18 is simplified significantly as all terms other than $i = z$ become zero giving:

$$H_{\text{Zeeman}}(B_z) = -\mu_B (g_{e,z} S_{e,z} - g_{h,z} J_{h,z}) B_z, \tag{2.19}$$

State	Eigenstate	Energy
B^+	$N_{B^+}\left(\lvert\Uparrow\downarrow\rangle+\left(\frac{\beta_1}{\Delta_1}+\sqrt{1+\frac{\beta_1^2}{\Delta_1^2}}\right)\lvert\Downarrow\uparrow\rangle\right)$	$E=E_0+\frac{1}{2}\left(\Delta_0+\sqrt{\Delta_1^2+\beta_1^2}\right)+\gamma_2 B_z^2$
B^-	$N_{B^-}\left(\lvert\Uparrow\downarrow\rangle+\left(\frac{\beta_1}{\Delta_1}-\sqrt{1+\frac{\beta_1^2}{\Delta_1^2}}\right)\lvert\Downarrow\uparrow\rangle\right)$	$E=E_0+\frac{1}{2}\left(\Delta_0-\sqrt{\Delta_1^2+\beta_1^2}\right)+\gamma_2 B_z^2$
D^+	$N_{D^+}\left(\lvert\Uparrow\uparrow\rangle+\left(\frac{\beta_2}{\Delta_2}+\sqrt{1+\frac{\beta_2^2}{\Delta_2^2}}\right)\lvert\Downarrow\downarrow\rangle\right)$	$E=E_0-\frac{1}{2}\left(\Delta_0-\sqrt{\Delta_2^2+\beta_2^2}\right)+\gamma_2 B_z^2$
D^-	$N_{D^-}\left(\lvert\Uparrow\uparrow\rangle+\left(\frac{\beta_2}{\Delta_2}-\sqrt{1+\frac{\beta_2^2}{\Delta_2^2}}\right)\lvert\Downarrow\downarrow\rangle\right)$	$E=E_0-\frac{1}{2}\left(\Delta_0+\sqrt{\Delta_2^2+\beta_2^2}\right)+\gamma_2 B_z^2$

Table 2.1: Table outlining the four exciton eigenstates and their corresponding energies arising from the combined exchange and Zeeman interactions. Here the terms from Eq. 2.20 have been simplified with $\beta_1=\frac{\mu_B B_z}{2}(g_{e,z}+g_{h,z})$ and $\beta_2=-\frac{\mu_B B_z}{2}(g_{e,z}-g_{h,z})$. N_{B^+,B^-,D^+,D^-} are normalisation constants that are dependent on the external field B_z. Terms obtained from [88].

where B_z is the magnetic field magnitude along the z axis. Similarly to the exciton fine structure we can construct a matrix from Eq. 2.19 [88]:

$$H_{\text{Zeeman}}=\frac{\mu_B B_z}{2}\begin{pmatrix} g_{e,z}+g_{h,z} & 0 & 0 & 0 \\ 0 & -g_{e,z}-g_{h,z} & 0 & 0 \\ 0 & 0 & -g_{e,z}+g_{h,z} & 0 \\ 0 & 0 & 0 & g_{e,z}-g_{h,z} \end{pmatrix}. \tag{2.20}$$

As H_{Zeeman} is diagonal there is no additional mixing of states; mixing only arises due to the exchange interaction. To obtain the total energy shifts of the four states we must consider both the exchange and Zeeman interactions $H = H_{\text{exchange}}+H_{\text{Zeeman}}$. The four resulting states and their corresponding energies are shown in Table 2.1. β_1 and β_2 are terms introduced by the Zeeman interaction and are dependent on the externally applied magnetic field. Due to the exciton fine structure, at small B_z the splitting follows a quadratic dependence on the applied field. As the field strength increases, such that $B_n \gg \Delta_n$, the dependence becomes linear. This has the additional effect of enabling the states to couple to circularly polarised light. At low fields, due to the exchange interaction, the eigenstates are linear combinations of the exciton states meaning they couple only to linearly polarised light. As B_z is increased the rotational symmetry is restored allowing coupling to circularly polarised light again [88, 91]. For oddly charged excitons (X^-, X^+, etc.) due to the lack of fine structure the energy states splitting is linearly dependent on the external field and no loss in circular polarisation is observed at weak fields [100]. Additionally, from Table 2.1 we

see that there is an additional term $\gamma_2 B_z^2$ which increases quadratically with the external field. This additional energy arises due to squeezing of the exciton wavefunction due to the strong confinement and is characterised by the diamagnetic constant γ_2 which, for GaAs/AlGaAs QDs, has typical value $\gamma_2 = 5.8\ \mu eVT^{-2}$ [101].

Comparatively using Voigt geometry, where the field is oriented in the *x*-*y* plane, the external field instead causes a mixing of the bright and dark exciton states allowing the dark exciton states to be observed optically [102]. However, as we only used Faraday geometry for this work we will not discuss this further.

2.3 Quantum Dot Spin System

2.3.1 Carrier Spins

In previous sections, we have discussed the optical properties of QDs and how we are able to tune these properties both through control of the dot's growth and by using external fields. We have also seen how QDs allow the confinement of individual charge carriers, meaning their spins can be manipulated and controlled. The carriers can also be added or removed from the QD simply using a diode structure. We now move on to discuss the spins of single carriers confined in a QD and how they are usable as a qubit. The work in this thesis is primarily focused on electrons, though holes have also been investigated as spin qubits. We also avoid discussing cases where multiple carriers are present as they either cause the overall states to have a net spin of zero, and are therefore useless as a qubit, or they add additional interactions which are discussed in Chapter 6.

Electrons possess spin angular momentum $\hat{\mathbf{S}} = \frac{1}{2}$, which means they form a two state system owing to the two electron spin states: $s_z = +\frac{1}{2}$ is the spin-up state ($|\uparrow\rangle$) and $s_z = -\frac{1}{2}$ is the spin-down state ($|\downarrow\rangle$). The names up and down originate from the direction of the spin along the principal axis. The states are degenerate unless an external field is applied. Spin qubits ideally would retain information indefinitely. Unfortunately, in all quantum systems interactions with the environment provide relaxation pathways that can alter a qubit's state. At $T \approx 4.2$ K many of these pathways are suppressed, such as spin-orbit interaction or phonon driven processes [103, 104]. Relaxation at low temperatures is instead driven by interactions with the QD's nuclear spin bath. As the electron states are degenerate, the electron spin can be flipped by exchanging its spin with one of the nuclear spins, termed spin flip-flops, giving electron fluctuation time scales of $\approx$ 1 ns [48, 105, 106]. By applying an external magnetic field, the electron spin state degeneracy is broken and the states are split by energy ΔE_{Zeeman}. This reduces the spin flip-flop rate as the interaction is dominated by the external field, subsequently decreasing the relaxation rate [106, 107]. It also means the system becomes a two-level system usable as a qubit. The orientation of

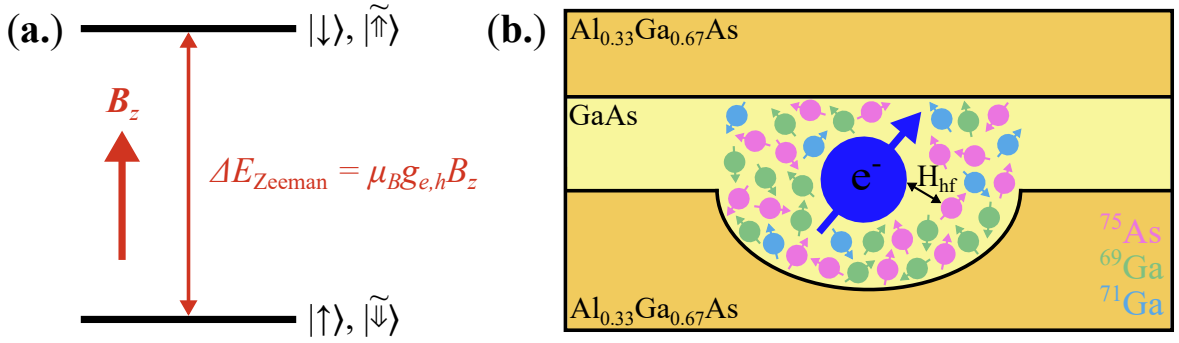


Figure 2.9: (a.) Energy levels and corresponding spin states for a single carrier in a quantum dot with an externally applied magnetic field, B_z. The field is applied in Faraday geometry, splitting the states by energy ΔE_{Zeeman} and leaving them pure. (b.) Schematic representation of the full spin system of a GaAs/AlGaAs QD. An electron (Blue) is confined within the QD where its spin becomes coupled to the spins of the surrounding nuclear spin bath (^{75}As - pink, ^{69}Ga - green, ^{71}Ga - light blue) through the hyperfine interaction H_{hf}. This 'setup' is commonly referred to as the central spin problem.

the field again is important for the final states. For Faraday geometry the states are split and remain pure (Fig. 2.9a), yet in Voigt geometry the final states are a mix of the up and down states.

In comparison to electrons, the interaction between holes and the surrounding nuclei should be negligible. This is because the hole wavefunction possesses *p*-symmetry and thus has small overlap with the nuclear wavefunctions [103, 107]. However, works have shown that this is not the case and that interactions between holes and nuclei do occur, though the mechanism differs compared to electrons. For electrons, flip-flops with the nuclei are driven by the Fermi-contact hyperfine interaction. This term is negligible for holes owing to their *p*-symmetry; instead flip-flops occur via the dipole term. As discussed, for QDs strain causes a splitting between the *hh* and *lh* states leaving the ground state as a *hh*. Due to momentum conservation, the dipole interaction can only occur with *lh* states, which are inaccessible by the *hh* as the *hh*-*lh* splitting prevents energy conservation. Therefore, the strength of this process is entirely dependent on the strength of valence band mixing between the *hh* and *lh* states [108, 109], characterised by the term β_h. This means the hole relaxation rate varies considerably between different dots as different strain environments influence β_h. Generally, the strength of the hole-nuclear hyperfine interaction is found to be ≈ 10 times smaller than for electrons [110], meaning relaxation times are increased by a similar factor [103, 107, 111]. Similar to electrons, the hole states are split in energy if an external field is applied. In Faraday geometry, the states are not pure they are instead a mixed *hh*-*lh* state:

$$|\tilde{\Uparrow}\rangle = |+3/2\rangle + \beta_h|-1/2\rangle \tag{2.21}$$

$$|\tilde{\Downarrow}\rangle = |-3/2\rangle - \beta_h|+1/2\rangle \tag{2.22}$$

while in Voigt these two states are mixed further [103]. Fig. 2.9b shows a schematic diagram of the full QD spin system.

Finally, the g-factor of both types of carriers are altered in semiconductor QDs compared to the in vacuum value of $g_e \approx 2$. This change is caused both by the bulk semiconductor and by the QD confinement. In bulk semiconductors it can be shown that the g-factor is dependent on the both the band gap energy E_g and the spin orbit splitting Δ_{so} [112, 113]. In bulk semiconductors the spin-orbit interaction is positive and it becomes energetically favourable for the orbital and spin momenta to align anti-parallel. This causes a reduction in the g-factor in bulk semiconductors [113]; with the magnitude of the decrease being dependent on the type of crystal. For large spin orbit coupling this decrease can be sufficient to cause the g-factor to become negative as is the case for electrons in bulk GaAs $g_e \approx -0.44$ [48, 113]. The discrete carrier energy states due to QD confinement effects further modify the carrier g-factors. The confinement modifies the lowest energy carrier state leading to a significant reduction in the resulting angular momentum. This causes the g-factor to increase towards the vacuum value as the dot size decreases (confinement increases) [113]. An additional increase is expected for small QDs due to the electron wavefunction penetrating into the surrounding AlGaAs, causing the g-factor to increase toward the bulk AlGaAs g-factor $g_e \approx 0.4$ [114, 115]. Due to symmetry breaking caused by strain and variations in the dot's dimensions the g-factor is anisotropic along the different crystallographic axes, but for the purposes of this work only the value along the z axis (growth direction) is relevant as we work in Faraday geometry, we therefore only quote these values in the following. For the measured GaAs/AlGaAs QDs the electron g-factor is found to be $g_e \approx -0.1$ [116, 117]. While for a heavy hole in the presences of two electrons $g_h \approx 1.68$ [116].

2.3.2 Nuclear Spins

As discussed, the performance of electron spin qubits in QDs is limited due to interactions between the carrier spin and surrounding nuclear spin bath. These nuclear spins are an intrinsic problem of the III-V semiconductor spin system where all present nuclei possess spin angular momentum. Alternative systems, such as NV centres in diamond avoid this issue by either having a low number of spin possessing nuclei near the electron spin, or possessing nuclei with no spin [118, 119]. Yet these materials do not possess the fantastic optical properties of III-V semiconductor QDs.

The spin bath of GaAs QDs, shown schematically in Fig. 2.10, contains $N \approx 5 \times 10^4$ nuclei. It is comprised of three nuclear species ^{75}As, and two isotopes of Ga, ^{69}Ga and ^{71}Ga. The ratio of ^{69}Ga to ^{71}Ga is approximately 1:0.664 [120]. All three of these nuclear species possess spin angular momentum $I = \frac{3}{2}$. Consequently, each nuclei acts as magnetic dipole with magnetic moment μ_i

(where i is used to denote the ith spin). The dipoles create an overall magnetisation $\mathbf{M}$ given by:

$$\mathbf{M} = \sum_i \mu_i. \tag{2.23}$$

At thermal equilibrium, and in the absence of an external field, each μ_i is randomly distributed among the four nuclear spin states $I_z = \pm\frac{1}{2}, \pm\frac{3}{2}$. If the nuclear spin bath contained an infinite number of nuclei the dipoles will cancel out due to averaging, giving a net magnetisation of $\mathbf{M} = 0$. However, as there is a finite number of nuclei, statistical variation will result in some small fluctuating value of $\mathbf{M}$, which consequently will interact with any trapped carrier spin in the QD. On the other hand, the large number of nuclei make them difficult to control reliably due to, as we will discuss in the following, interactions between the $N \approx 5 \times 10^4$ nuclear spins introducing further noise to the system. The nuclear spin system is both too small to be ignored while simultaneously too large to be reliably controlled [107].

The work in this thesis is dedicated to trying to turn the complex dynamics of QD nuclear spin systems into a reliable and usable resource for quantum information and computing. In the following sections we discuss the interactions between the nuclear spins of a QD's spin bath in the absence of a carrier spin, before we reintroduce carriers and consider the spin interactions between them and the surrounding nuclei.

External Magnetic Fields

Much like carriers, the spins of the nuclei will interact with an externally applied magnetic field. As we work in Faraday geometry, with field B_z, the nuclei experience Zeeman splitting given by:

$$H_{\text{Zeeman}}(B) = -\mu_N g_N I_z B_z = -\hbar \gamma_N I_z B_z. \tag{2.24}$$

Here, μ_N is the nuclear magneton and g_N is the nuclear g-factor. We also introduce the gyromagnetic ratio defined as $\gamma_N = \frac{g_N \mu_N}{\hbar}$ which varies between different types of nuclei. The Zeeman splitting breaks the degeneracy of the four nuclear spin states and causes them to become evenly split in energy. Additionally, as different nuclei have different gyromagnetic ratios, the magnitude of the energy spacing will vary between different nuclear species.

Nuclear Dipolar Interaction

The interactions between nuclei are primarily carried out through the dipole interaction and can couple nuclei both within the dot and the surrounding material. For two nuclear spins $\mathbf{I}_i$ and $\mathbf{I}_j$,

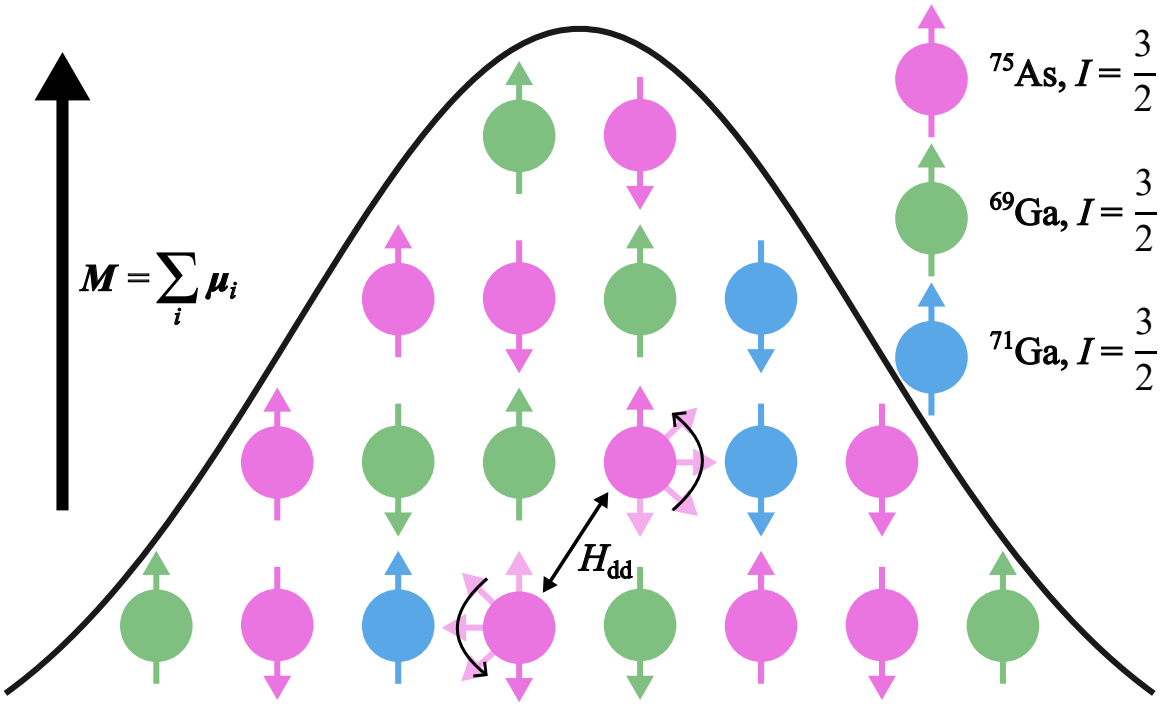


Figure 2.10: Schematic diagram of the nuclear spin bath in a GaAs QD. At thermal equilibrium, the nuclear spin orientations are randomly distributed but, due to statistical variations, there will be a net magnetisation **M**. Couplings between the nuclear dipoles H_{dd} allows spin momentum to be exchanged between nearby nuclei via spin flip-flops.

separated by a distance $\mathbf{r}_{ij}$ the dipolar interaction between them is given by [121]:

$$H_{dd} = \frac{\mu_N^2}{2} \sum_{i \neq j} \frac{g_i g_j}{r_{ij}^3} \left(\mathbf{I}_i \mathbf{I}_j - 3 \frac{(\mathbf{I}_i \mathbf{r}_{ij})(\mathbf{I}_j \mathbf{r}_{ij})}{r_{ij}^2} \right), \tag{2.25}$$

where μ_N is the nuclear magneton and $g_{i,j}$ are the g-factors of the nuclei at sites i and j respectively. In the case of a system with N nuclei, each of the individual nuclei couples with the other $N-1$ nuclei in the surrounding spin bath, though the strength of the interaction with distant nuclei is significantly reduced owing to the $1/r_{ij}^3$ term. Effectively, each nucleus experiences a magnetic field generated by the surrounding nuclei. As the nuclei are randomly distributed between the nuclear spin states, the local field varies significantly between each nuclear site causing a broadening of the nuclear energy levels.

There are two terms in Eq. 2.25. The first simply causes an energy shift in the nuclear states. The second term enables spin flip-flops between like nuclei, allowing nearby nuclei to exchange spin with one another. It is therefore called the flip-flop term. This leads to a phenomenon known as spin diffusion where polarised nuclei can transfer their polarisation to the other nearby nuclei

[122]. This is an important process as it drives a loss of polarisation of the nuclei in a QD to the environment (i.e. the surrounding nuclei in the bulk material), limiting the maximum achievable optically generated dynamical nuclear polarisation (DNP) as well as driving nuclear spin relaxation [116, 123]. The flip-flop term induced diffusion can be suppressed in QDs significantly by both quadrupolar interactions and the strong coupling to the Knight field of trapped electrons [124], yet fundamentally nuclear spin polarisation will eventually be lost to the surrounding crystal via the non-secular (non-spin conserving) part of the nuclear dipolar interaction [103, 121].

Nuclear Quadrupolar Interaction

The nuclei in QDs do not couple to homogeneous electric fields as a consequence of them possessing no electric dipole moment. However, all of the nuclear species present in GaAs/AlGaAs QDs are spin $I = \frac{3}{2}$ particles meaning they possess a nonspherical (prolate) charge distribution, creating a quadrupolar moment which can couple to EFGs. In bulk materials, the cubic symmetry causes the electric field to vanish preventing quadrupolar coupling. In QDs, the bulk cubic symmetry is broken and EFGs can be generated by strain caused either due to lattice mismatch or external application [103]. The resulting EFG is then generated along one of the crystallographic axes. In the case of lattice mismatch induced strain, the strain (and hence, EFG) at each lattice site is different, meaning the strength of each nuclei's quadrupolar interaction varies. The EFG is given by:

$$V_{ij} = \sum_{k,l} S_{ijkl}\varepsilon_{kl}, \tag{2.26}$$

where ε_{kl} is the symmetric strain tensor, and S_{ijkl} is the gradient field tensor defined such that Eq. 2.26 is valid. We then define the Hamiltonian H_{Q} that describes the coupling of the nuclear quadrupole to the EFG V_{ij} in the principal axis reference frame $+z$ [121, 125]:

$$H_{\mathrm{Q}} = \frac{eQ}{4I(2I-1)}(V_{zz}(3\hat{I}_z^2 - \hat{I}^2) + (V_{xx} - V_{yy})(\hat{I}_x^2 - \hat{I}_y^2)). \tag{2.27}$$

Here, e is the elementary charge and Q is the quadrupolar moment for a given nucleus. It is common to simplify the EFG by introducing an asymmetry parameter $\eta = (V_{xx} - V_{yy})/V_{zz}$ as well as a field gradient parameter $q = V_{zz}/e$. It is also common to assume axial symmetry meaning that $V_{xx} = V_{yy}$. Therefore, $\eta = 0$ and Eq. 2.27 becomes:

$$H_{\mathrm{Q}} = \frac{e^2qQ}{4I(2I-1)}(3\hat{I}_z^2 - \hat{I}^2). \tag{2.28}$$

The quadrupolar moments for the nuclei present in GaAs/AlGaAs QDs are shown in Table 2.2.

We have now discussed the three primary interactions for nuclear spins in QDs and can con-

Isotope	Nuclear Spin, I	Nuclear Magnetic Moment, μ_i/μ_N	Hyperfine Constant, A_i (μeV)	Quadrupolar Moment (Q fm^{-2})	Gyromagnetic Ratio, γ (rad MHz T^{-1})	Natural Abundance (%)
^{75}As	3/2	1.858	43.5	31.4	45.962	100
^{69}Ga	3/2	2.603	43.1	17.1	64.389	60.108
^{71}Ga	3/2	3.308	54.8	10.7	81.812	39.892
^{27}Al	5/2	4.309		14.7	69.763	100

Table 2.2: Properties of ^{75}As, ^{69}Ga, ^{71}Ga and ^{27}Al nuclear spins. Values for hyperfine constants were obtained from [103], other values were found in [120]. ^{27}Al is only present within the QD in small amounts near the dot-substrate boundary where it can replace a Ga atom.

struct an energy level diagram. The dipolar interaction between the nuclei is relatively small and does not significantly contribute to the energy level spacing. Instead it contributes a broadening of the energy levels. Therefore, the full Hamiltonian is constructed from the Zeeman interaction between the nuclear spin dipole moments and an external magnetic field, and the interaction between the nuclear quadrupolar moments and strain induced EFGs:

$$H = H_{\text{Zeeman}} + H_{\text{Q}}. \tag{2.29}$$

For the majority of work in this thesis, the magnetic field is large enough that H_{Zeeman} dominates over H_{Q}, meaning H_{Q} can simply be considered as a perturbation [121]. Cases where this assumption begins to break down are discussed in Chapter 4. We are therefore able to describe the resulting nuclear energy levels as:

$$E_m = E_m^{(0)} + E_m^{(1)} + E_m^{(2)}, \tag{2.30}$$

where $E_m^{(0)}$ is the splitting due to the Zeeman interaction, which from Eq. 2.24, we obtain $E_m^{(0)} = \hbar\omega_L I_z$, where ω_L is the Larmor precession frequency for the nuclei. In Fig. 2.11 we see the four nuclear energy levels are evenly split due to H_{Zeeman}.

The terms $E_m^{(1)}$ and $E_m^{(2)}$ are the first-order and second-order perturbations due to the quadrupolar interaction (we do not consider higher order terms in this work). To obtain these energies we consider axially symmetric strain as laid out in Eq. 2.28. Consequently, only the angle θ between the growth direction z and the electric field gradient z' influences the strength of quadrupolar interaction. It becomes possible, without a loss of generality, to write [121]:

$$I_{z'} = I_z \cos(\theta) + I_x \sin(\theta). \tag{2.31}$$

Substituting into Eq. 2.28 and solving using second order perturbation theory the energies are obtained:

$$E_{I_z}^{(0)} = \hbar\omega_L I_z \tag{2.32}$$

$$E_{I_z}^{(1)} = \frac{\hbar\omega_Q}{4}\left(3\cos^2(\theta)-1\right)\left(I_z^2 - \frac{1}{3}(I(I+1))\right) \tag{2.33}$$

$$\begin{aligned} E_{I_z}^{(2)} = \frac{-\hbar\omega_Q^2}{12\omega_L} I_z \Bigg(& \frac{3}{2}\cos^2(\theta)(1-\cos^2(\theta))(8I_z^2 - 4I(I+1)+1) \\ & + \frac{3}{8}(1-\cos^2(\theta))^2(-2I_z^2 + 2I(I+1)-1)\Bigg). \end{aligned} \tag{2.34}$$

Where we define $\omega_Q = \frac{3e^2qQ}{\hbar 2I(2I-1)}$ as the quadrupolar coupling strength. $I = \frac{3}{2}$ is the nuclear spin and $I_z = \pm\frac{1}{2},\ \pm\frac{3}{2}$ are the spin projections along the z axis. From the above equations, we can calculate the energy shift between two nuclear spin states with spin projection I_z and $I_z - 1$:

$$\Delta E_{I_z}^{(0)} = E_{I_z-1}^{(0)} - E_{I_z}^{(0)} = \hbar\omega_L \tag{2.35}$$

$$\Delta E_{I_z}^{(1)} = E_{I_z-1}^{(1)} - E_{I_z}^{(1)} = \frac{\hbar\omega_Q}{2}\left(I_z - \frac{1}{2}\right)\left(3\cos^2(\theta)-1\right) \tag{2.36}$$

$$\begin{aligned} \Delta E_{I_z}^{(2)} = E_{I_z-1}^{(2)} - E_{I_z}^{(2)} = \frac{\hbar^2\omega_Q^2}{32\omega_L}\sin^2(\theta)(2I(I+1) - 6I_z(I_z-1) - 3 \\ -3\cos^2(\theta)(6I(I+1) - 34I_z(I_z-1) - 13)). \end{aligned} \tag{2.37}$$

From Eqs. 2.35-2.37 the nuclear spin energy diagram shown in Fig. 2.11 emerges. Assuming $B_z > 0$ the degeneracy of the four nuclear spin states is lifted and they become equally split by $\Delta E_{I_z}^{(0)} = \hbar\omega_L$. Introducing the quadrupolar interaction causes a perturbation to the energy level shifts, meaning that they are no longer even. First, in the case of first-order interactions, it can be seen from Eq. 2.36 that for the central transition (CT), where $I_z = \frac{1}{2}$, that the $(I_z - \frac{1}{2})$ term becomes 0 and so the transition is unaffected by first-order effects. Comparatively, the other two shifts $I_z = +\frac{3}{2},\ -\frac{1}{2}$ are non-zero and are both shifted in frequency by $\pm\omega_Q^{(1)}$ respectively. Typically, $\Delta E_{I_z}^{(1)} \gg \Delta E_{I_z}^{(2)}$ and the satellite transitions (STs) can be said to be unaffected by second-order quadrupolar interactions. Consequently, due to the lack of first-order splitting, the CT becomes shifted by frequency $\omega_Q^{(2)}$.

In real QDs, the nuclei are not evenly shifted by quadrupolar couplings to the strain-induced EFG. Due to local variations in the strain, the strength of the EFG will vary between each nuclear

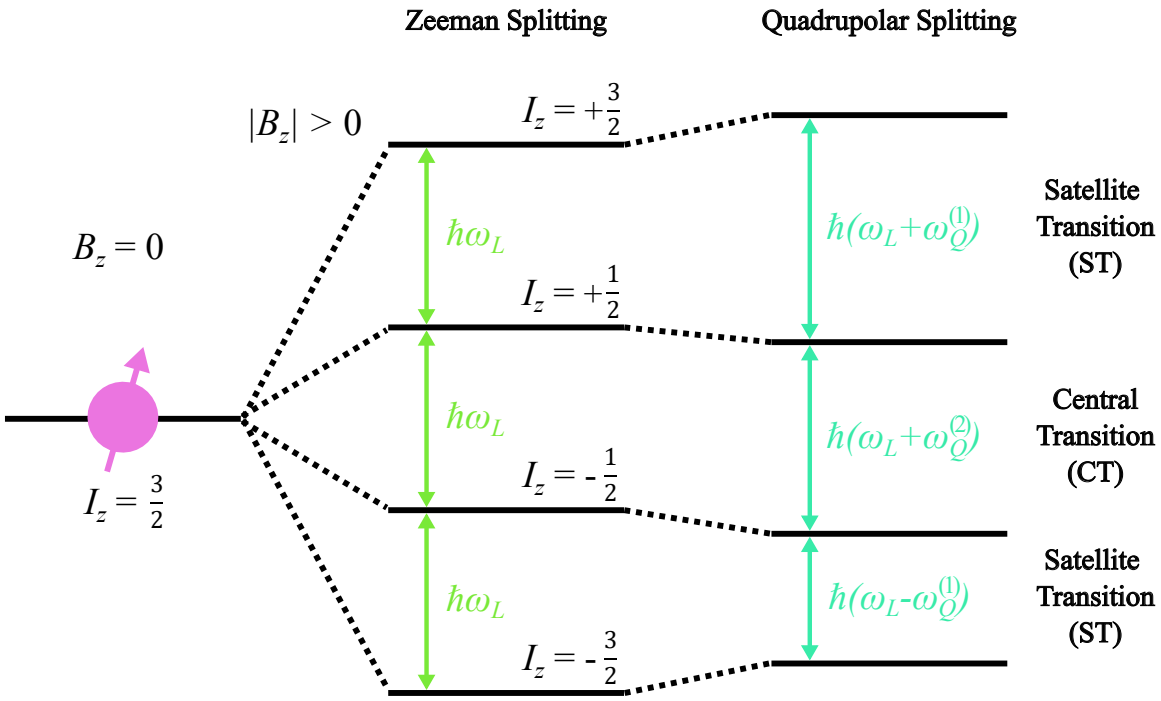


Figure 2.11: Energy level diagram for a spin $I = \frac{3}{2}$ nucleus in the presence of external magnetic field B_z and quadrupolar interaction. The application of B_z lifts the degeneracy of the four nuclear spin states, which become equally spaced in energy. The addition of the quadrupole interaction introduces a frequency shift of $\pm\omega_Q^{(1)}$ to the transition frequencies between the $+\frac{1}{2} \leftrightarrow +\frac{3}{2}$ and $-\frac{3}{2} \leftrightarrow -\frac{1}{2}$ states due to first-order effects. These two transitions are referred to as the higher ST and lower ST respectively. The $-\frac{1}{2} \leftrightarrow +\frac{1}{2}$ transition is called the CT and is unaffected by first-order effects. Instead, it is shifted by frequency $\omega_Q^{(2)}$ due to second-order effects. The sign of $\omega_Q^{(1)}$ and $\omega_Q^{(2)}$ may be positive or negative which changes the order of states in terms of energy. The final spin $\frac{3}{2}$ system has four non-degenerate energy levels separated by three energy transitions of different magnitude, meaning they can be resolved separately in NMR measurements.

site, leading to an effective broadening of the NMR transitions. Consequently, the NMR linewidths are determined both by the inhomogeneous strain and the strength of the nuclear dipole-dipole couplings. In self-assembled SK grown QDs, the lattice mismatch between the substrate and QD material means the inhomogeneous strain is large and there is a significant ≈ 1 MHz broadening of the NMR transitions as a result, particularly for the STs as they are sensitive to first-order quadrupolar effects [71]. The sample used in this work has several key differences. First, as the QDs are lattice matched, the overall inhomogeneous strain is significantly reduced, resulting in much narrower NMR linewidths ($\approx 1-14$ kHz) [70, 117]. This is most visible for the CT, where the broadening becomes comparable to the dipolar couplings owing to the lack of first-order quadrupolar effects. Second, we apply compressive uniaxial stress along the [110] direction perpendicular to the [001] growth direction which dominates $\omega_Q^{(1)}$ and leads to a significant increase in the frequency separation between the three NMR transitions ($\omega_Q^{(1)} \approx 250$ kHz for ^{75}As and $\omega_Q^{(1)} \approx 130$ Hz for ^{69}Ga), allowing each of them to be resolved individually by applied RF pulses, enabling high levels of control over the nuclear spin system [70]. The effect of the applied strain is discussed further in Chapter 4. More recent analysis of the nuclear spin system in GaAs/AlGaAs QDs has revealed that the above description only accounts for $\approx 65\%$ of the nuclei in the STs, the other $\approx 35\%$ forms a broad (≈ 200 kHz) peak that is not visible in typical NMR measurements. This broad peak arises due to strain cause by the random positioning of Ga and Al [126].

Finally, we will briefly discuss cases where the energy level diagram shown in Fig 2.11 is no longer valid. The simplest case is where the EFG is oriented along the sample growth direction ($\theta = 0$). Due to the $\sin^2(\theta)$ term $E_{I_z}^{(2)}$ becomes zero, and the second order shift vanishes. A second case is where the magnetic field is oriented such that $\theta \approx 54.7^\circ$ which causes the first-order term to vanish and the three transitions occur at the same frequency. This is used in magic-angle spinning (MAS) NMR to improve the measurement resolution [127]. Finally, as mentioned already, at low magnetic fields $\Delta E_{I_z}^{(0)} \leq \Delta E_{I_z}^{(1)}$ the quadrupolar interaction is no longer a perturbation but dominates the energy splitting, resulting in degenerate $I_z = \pm\frac{1}{2}$ states.

2.3.3 Hyperfine Interaction

We have now discussed the two types of spins present in III-V semiconductor QDs. Unfortunately, the two systems are not independent as the spin of a confined electron couples to the spins of the surrounding nuclei through the hyperfine interaction. The coupling works in both directions; the electron spin is exposed to the net magnetic field created by the nuclear spins, while the nuclei are influenced by the field generated by the electron's spin magnetic dipole moment. The two magnetic fields are named the Overhauser [128] and Knight [129] fields respectively.

Consequently, the nuclei act as a noisy spin bath for a confined electron spin, accelerating its

relaxation rate and limiting the ability to exploit the electron as a spin qubit [103, 105, 130]. Similarly, the presence of an electron significantly reduces the lifetimes and coherence times of the nuclei [87, 131]. Despite these issues, the hyperfine interaction also enables one system to be accessed via the other. For example, the work in this thesis makes extensive use of optically generated DNP to create initial nuclear spin bath states. This is achieved through hyperfine interaction driven spin flip-flops between optically excited electrons and the nuclei [103, 124, 128, 132, 133]. Similarly ODNMR is possible because the electron's energy levels are sensitive to the magnetic field generated by the nuclear spins [134]. More recently, the hyperfine interaction has been exploited to allow driving of the nuclear spins optically via an electron [135], and even enable transfer of information between the two systems [136]. The work in Chapter 5 demonstrates an experimental technique where the hyperfine interaction allows the nuclear spin bath to be exploited as a probe which can perform high-fidelity readout of the electron spin state [137].

The strength of the nuclear dipoles are typically on the order of 1000 times smaller than those of electrons, owing to the higher nuclear mass [103]. Yet there are approximately $N \approx 5\times10^4$ nuclei in GaAs/AlGaAs QDs, all of which possess non-zero spin. Subsequently, due to the large number of nuclei present, the strength of the interaction with the electron is still significant. Additionally the confinement induced localisation of the electron wavefunction in QDs further enhances the strength of the electron-nuclear spin coupling. The hyperfine interaction between the electron and a single nuclear spin is given by the Hamiltonian [121]:

$$H_{\text{hf}} = 2\mu_B\gamma\hbar\mathbf{I}\left(\frac{\mathbf{l}}{r^3} - \frac{\mathbf{s}}{r^3} + \frac{3\mathbf{r}(\mathbf{s}\cdot\mathbf{r})}{r^5} + \frac{8}{3}\pi\mathbf{s}\delta(\mathbf{r})\right), \tag{2.38}$$

where μ_B is the Bohr magneton, γ is the nuclear gyromagnetic ratio, $\mathbf{I}$ is the nuclear spin operator, $\mathbf{l}$ and $\mathbf{s}$ are the carrier orbital and spin angular momentum operators respectively and finally $\mathbf{r}$ is the separation distance between the electron and the nucleus. There are three components to the hyperfine interaction, which we separately define as [123]:

$$H_{\text{hf}} = H_{\text{hf}}^{\text{FC}} + H_{\text{hf}}^{\text{Dip}} + H_{\text{hf}}^{\text{Orb}} \tag{2.39}$$

$$H_{\text{hf}}^{\text{FC}} = 2\mu_B\gamma\hbar\mathbf{I}\left(\frac{8}{3}\pi\mathbf{s}\delta(\mathbf{r})\right) \tag{2.40}$$

$$H_{\text{hf}}^{\text{Dip}} = 2\mu_B\gamma\hbar\mathbf{I}\left(\frac{3\mathbf{r}(\mathbf{s}\cdot\mathbf{r})}{r^5} - \frac{\mathbf{s}}{r^3}\right) \tag{2.41}$$

$$H_{\text{hf}}^{\text{Orb}} = 2\mu_B\gamma\hbar\mathbf{I}\left(\frac{\mathbf{l}}{r^3}\right). \tag{2.42}$$

The first term $H_{\text{hf}}^{\text{FC}}$ is the Fermi-contact hyperfine interaction. It is caused due to the overlap

between the carrier's wavefunction and the nucleus. It is therefore only relevant for electrons owing to their s-type wavefunction. Comparatively for holes, there is no overlap between the nucleus and the p-type wave function and so $H_{\text{hf}}^{\text{FC}} = 0$ meaning the other two terms become relevant. For electrons, the Fermi-contact interaction dominates the hyperfine interaction. For an electron interacting with N number of nuclear spins, $H_{\text{hf}}^{\text{FC}}$ is given by [103, 123, 133, 138]:

$$H_{\text{hf}}^{\text{FC}} = \frac{v_0}{2}\sum_i A^i |\psi(\mathbf{r}_i)|^2 (2\hat{I}_z^i \hat{s}_z^{\,e} + (\hat{I}_+^i \hat{s}_-^{\,e} + \hat{I}_-^i \hat{s}_+^{\,e})), \tag{2.43}$$

where v_0 is the unit cell volume, $\psi(\mathbf{r}_i)$ is the electron density at the nucleus, $\hat{I}_z^i$ and $\hat{s}_z^{\,e}$ are the z projections of the ith nucleus and the electron respectively, and $\hat{I}_\pm^i$, $\hat{s}_\pm^{\,e}$ are the raising and lowering ladder operators for the nuclear and electron spin respectively. The term A^i describes the strength of the interaction between the electron and the ith nuclear isotope and is called the hyperfine interaction constant [139]:

$$A^i = \frac{2\mu_0}{3}\hbar\gamma_N g_e \mu_B |\psi(0)|^2, \tag{2.44}$$

where μ_0 is the vacuum permeability.

The electron therefore interacts with the sum of the magnetic fields produced by the N nuclear spins in the QD. The contribution of each nuclear dipole is weighted through A^i. Also the precession of the nuclear moments are generally orders of magnitude smaller than the electrons. Therefore, the electron spin effectively 'sees' a static average magnetic field produced by the nuclei. This is called the mean field approximation and causes Eq. 2.43 to become [138]:

$$\langle H_{\text{hf}}^{\text{FC}} \rangle = \frac{1}{2} A \langle I_z \rangle \hat{s}_z^{\,e}, \tag{2.45}$$

where $A = \sum_i A^i$ and $\langle I_z \rangle$ is the average nuclear spin. The strength of A^i varies between different nuclear isotopes and also with the overlap of the electron wavefunction at the nuclear site. Therefore, the contribution of each nucleus to the hyperfine interaction is dependent on the isotope and its position within the QD. The resulting magnetic field B_{OH} can be obtained from Eq. 2.43 and is given by [103]:

$$B_{\text{OH}} = \frac{v_0}{\mu_B g_e}\sum_i A^i |\psi(\mathbf{r}_i)|^2 \langle \hat{\mathbf{I}}^i \rangle. \tag{2.46}$$

Consequently, the electron experiences a total magnetic field, $B_{\text{Tot}} = B_z + B_{\text{OH}}$ generated by the combined external field and the nuclear Overhauser field resulting in a Zeeman splitting $H_{\text{Zeeman}} = \mu_B g_e B_{\text{Tot}}$. This means that QD PL lines have an energy splitting that is sensitive to the nuclear spin polarisation, allowing for optical measurements of the nuclear spin polarisation (see Section. 3.13). An example of changing PL line splitting under different nuclear spin polarisations is shown in Fig. 2.12a.

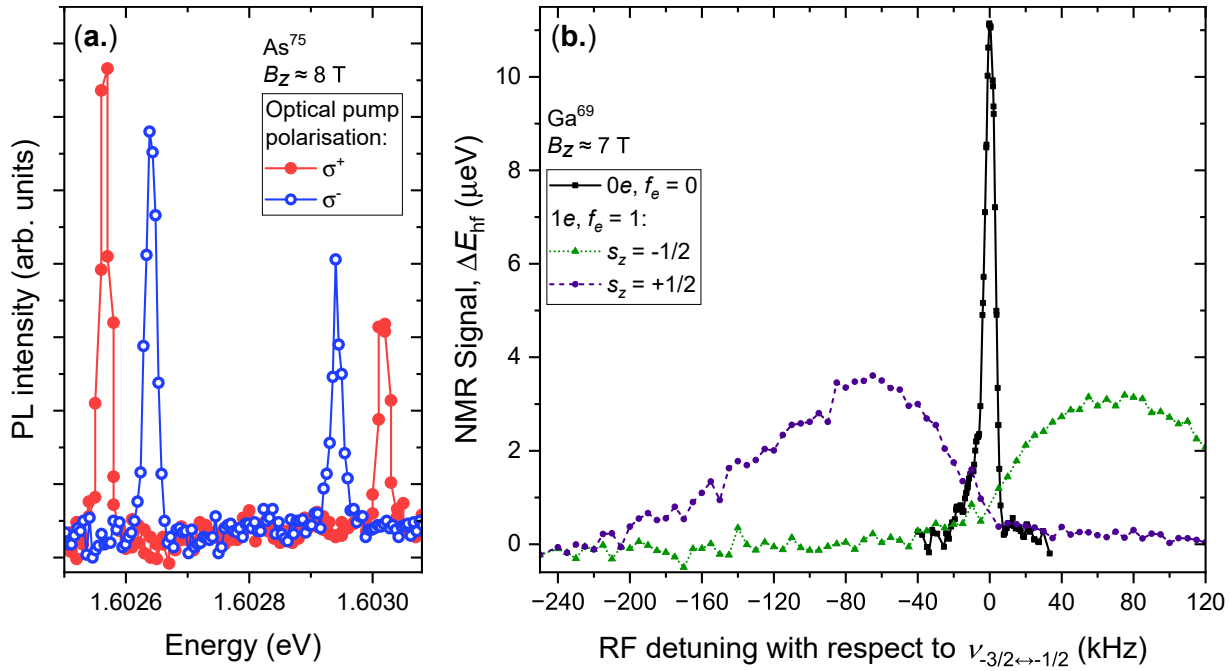


Figure 2.12: (a) Two PL spectra measured on the same QD after optical pumping with a few second-long laser pulse. The PL lines are split in energy due to the combined effects of the external field $B_z = 8$ T and the nuclear Overhauser field B_{OH}. Differences in the PL splitting is caused by differences in B_{OH} when the nuclei are polarised in different orientations along the z axis, achieved by optically pumping the sample with circularly polarised light. (b) Comparison of the $-3/2 \leftrightarrow -1/2$ NMR transition when the QD is unoccupied ($0e$, black solid squares) and occupied ($1e$) with an electron with its spin in the $s_z = +\frac{1}{2}$ state (purple circles, dotted) and $s_z = -\frac{1}{2}$ state (green triangles, dashed). Introduction of the electron Knight field B_{K} causes a shift in the NMR frequency as well as a broadening of the NMR transition. $0e$ data was collected using the inverse NMR technique (Section 3.5.2 [110]), $1e$ data obtained using off-resonant pulsed NMR (Chapter 5).

The magnetic field a given nucleus experiences due to the electron spin is given by [103, 123]:

$$B_{\mathrm{K,i}} = f_e \frac{v_0}{\mu_N g_N} A^i |\psi(\mathbf{r}_i)|^2 \langle \hat{\mathbf{s}}^e \rangle, \tag{2.47}$$

where $f_e \in [0,\ 1]$ is the filling factor which characterises the occupation of the QD by an electron. This is required as the Knight field vanishes when the dot is empty. Similar to the electron, the nuclei experience a total Zeeman splitting $H_{\mathrm{Zeeman}} = \mu_N g_N B_{\mathrm{Tot}}$ with $B_{\mathrm{Tot}} = B_z + B_{\mathrm{K,i}}$. The result is a frequency shift in the nuclear Larmor frequency, with the direction of the frequency shift dependent on the electron spin projection s_z. However, the strength of B_{K} varies significantly between each nuclear site and is particularly strong for nuclei in close proximity to the electron, meaning there is a large broadening of the nuclear NMR transitions which is shown in Fig 2.12b. The broadening is a significant challenge to achieving high fidelity control of the nuclear spins. In Chapters 5 and 6 we use detuned RF pulses to probe the Knight field, which is how the results in

Fig 2.12b were obtained.

The second term in Eq. 2.43 is, similar to the nuclear dipole-dipole interaction (Eq. 2.25), the flip-flop term. This enables the exchange of spin between the electron and nucleus, which increases relaxation of the electron spin and allows the electron to increase spin diffusion by mediating spin flip-flops between distant nuclei [116]. It is also the reason that DNP can be generated, by allowing spin polarised, optically excited electrons to transfer their spin to the nuclear spin bath [134].

The other two terms in Eq. 2.39 become relevant for hole spins where $H_{\text{hf}}^{\text{FC}} = 0$ due to the lack of overlap between the nuclei and the hole p-like wavefunction. The first term, $H_{\text{hf}}^{\text{Dip}}$, describes the interaction between the electron and nuclear dipoles [103, 123]:

$$H_{\text{hf}}^{\text{Dip}} = v_0 \sum_i \frac{A_i^h}{1+\beta_h^2} |\psi(\mathbf{r}_i)|^2 \left(\hat{I}_z^i \hat{s}_z^h + \frac{\alpha}{2} (\hat{I}_+^i \hat{s}_-^h + \hat{I}_-^i \hat{s}_+^h) \right), \tag{2.48}$$

where β_h, as introduced previously, is the *hh*-*lh* mixing term and $\alpha = 2|\beta_h|/\sqrt{3}$ is the anisotropy factor. As discussed in Section 2.1.2, the lowest lying hole state in the QD VB is the *hh* band, with total momentum $J = \frac{3}{2}$. For a spin flip-flop to occur between the hole and nuclear spins a momentum change $\Delta J = 1$ is required, meaning *hh*-nuclear spin flip-flops are forbidden. Flip-flops could arise by accessing the *lh* states yet, due to the strain in QDs, there is an energy splitting Δ_{hh-lh} between the *hh* and *lh* bands making such exchanges energetically forbidden. The only possible way for hole-nuclear spin flip-flops is that there exists a mixing, characterised by the term β_h in Eq. 2.48, between the *hh* and *lh* states [108, 109]. This state mixing can occur if there is anisotropic strain in the QD. This term is therefore also called the anisotropic hyperfine interaction. β_h is much smaller than unity due to the energy splitting Δ_{hh-lh} between the hole states [103].

The form of Eq. 2.48 is similar to Eq. 2.43 yet, while both Fermi-contact and dipolar interactions are sensitive to the isotopes and positions of the given nuclei, the dipolar interaction strength is also sensitive to the degree of *hh*-*lh* mixing β_h and is therefore weaker. Despite being weaker, the dipolar term still leads to an acceleration of hole relaxation times [103, 107, 111].

The final term in Eq. 2.39 is the nuclear orbital interaction $H_{\text{hf}}^{\text{Orb}}$ which gives the strength of the coupling between the nuclear dipoles and the carrier orbital angular momentum, which occurs due to the carriers orbital motion through the Overhauser field. This term vanishes for s-like wavefunctions as they possess $\mathbf{L} = 0$. Therefore, electrons are unaffected. By comparison, holes have p-like wavefunctions with angular momentum $\mathbf{L} = 1$, meaning that they experience an additional interaction given by [123]:

$$H_{\text{hf}}^{\text{Orb}} = -\frac{\mu_0}{4\pi} \sum_i \gamma_s \gamma_{N,i} \frac{\mathbf{I}_i \cdot \mathbf{L}_i}{\mathbf{r}_i^3}, \tag{2.49}$$

where $\mathbf{L}$ is the hole orbital angular momentum. The combined effects of $H_{\text{hf}}^{\text{Dip}}$ and $H_{\text{hf}}^{\text{Orb}}$ gives a full description of the hyperfine interaction for holes in the QD VB. It has been shown, both

theoretically and experimentally, that the magnitude of the hole hyperfine coupling constant A^h is approximately 10 times smaller than A [103]. Surprisingly, experiments have also demonstrated cases where A^h is negative, believed to be made possible due to further mixing with the d-shell hole states [110].

2.4 Spin Control in Quantum Dots

To realise a functioning qubit for quantum computing applications from the spin system of a GaAs QD we need to be able to achieve three things: First, we need to be able to reliably prepare the spins into a desired and arbitrary initial state. Then, the spins need to manipulated in such a way that the desired computation is carried out. After, the final state needs to be readout with high fidelity. In the following sections we discuss how this can be achieved for electrons and nuclear spin ensembles. We additionally discuss relaxation mechanisms which drive errors and limit the functionality of these types of spin qubits.

2.4.1 State Initialisation

Electron Spin

Polarisation of the electron spin can be achieved optically using the spin shelving technique [30]. Consider a system where an external field B_z is applied in Faraday geometry. The degeneracy of the two electron spin states is lifted and they become separated in energy, this has the added benefit of extending the electron coherence time due to the suppression of electron-nuclear spin flip-flops [106].

Using a bias voltage to trap an electron within the QD, an electron can become polarised by resonant optical pumping of the negative trion (X^-) transition. However, as the external field B_z breaks the degeneracy of the spin states, the system becomes a four level system given by the two electron and two trion spin states. Due to the optical selection rules, each electron spin state can only access one of the trion states: the other transition is forbidden. Tuning to one of the optical transitions allows the formation of trions with the same spin. There is a finite chance that instead of undergoing normal optical recombination to form the original electron state, the recombination will instead undergo a forbidden recombination transition to the other electron spin state. While forbidden, this alternative recombination can still occur, owing to strain induced hh-lh mixing, small variations in the orientation of B_z and fluctuations of the in-plane nuclear Overhauser field [30, 103, 109, 140, 141]. The rate γ of this forbidden transition is low but with a short ($T_{e,\mathrm{Pump}} \approx 100\ \mu s$ for the work in this thesis) optical pump polarisations of up to 99.8% can be obtained [30, 137, 142]. Once an

electron enters the non-optically coupled state it is effectively 'shelved' and the QD becomes transparent. Unfortunately, interactions with the surrounding nuclear spins can cause relaxation into the ground spin state via the spin flip-flop term of the electron-nuclear hyperfine interaction [105]. The rate of the nuclear mediated relaxation γ_{hf} influences the efficiency of the polarisation. If B_z is small then $\gamma_{\mathrm{hf}} > \gamma$ and the electron cannot be polarised. For larger B_z (≈ 200 mT), the flip-flops are suppressed and γ becomes the dominant process allowing electron spin polarisation [103].

Nuclear Spins

Initialisation of the nuclear spin ensemble can be conducted by exploiting the hyperfine interaction between the nuclei and optically excited carriers. As the nuclei are an ensemble of $N \approx 5 \times 10^4$ individual spins they cannot all be polarised into a given spin state at once. Instead, polarisation of the nuclei accumulates over the duration of a long optical excitation (pumping) of the QD. The optical pumping can either be resonant or non-resonant with the given exciton optical transition, the method of both approaches varies, but the general effect is the same.

The generation of DNP follows a three step cyclic process. First, using circularly polarised light (σ^+ or σ^-), spin polarised electrons can be repeatedly generated in the QD, owing to the optical selection rules. While the polarised electrons are only present for the short optical lifetime $\tau \approx 300$ ps, this is sufficient time for the electron to couple to the nuclear spins and undergo a spin flip-flop via the hyperfine interaction. The electron thus exchanges its spin with one of the nuclei before undergoing recombination, leaving the dot free for another exciton to be generated. This process then repeats, allowing the nuclei to become polarised as more and more spin flip-flops occur [124, 133, 138, 143–145].

The large number of nuclei in QDs makes it difficult to achieve large degrees of polarisation. Typically values of 50% can be reached reliably, though higher values of DNP have been demonstrated by pumping optically forbidden transitions [144]. There are several contributing factors to this limitation and the actual full dynamics are still not fully understood. One key process is spin diffusion [116]. Due to the nuclear dipole-dipole interaction, nuclei are able to undergo spin flip-flops with nearby nuclei, allowing the polarised nuclei within the QD to transfer their spin polarisation to the nuclei in the bulk material. This drives a relaxation process which competes with the electron-nuclear flip-flop rate. Therefore, the maximum DNP achievable occurs when the electron-nuclear flip-flop rate is equal to the rate of nuclear spin relaxation. Typically this is when the optical transition becomes saturated and the rate of exciton formation and recombination becomes the limiting factor. This is not the full picture, however; both quadrupolar effects and the electron induced Knight field can both alter the spin diffusion rate [116, 124]. Also the formation of dark states has been identified as key limiting factor to realising higher values of DNP [146].

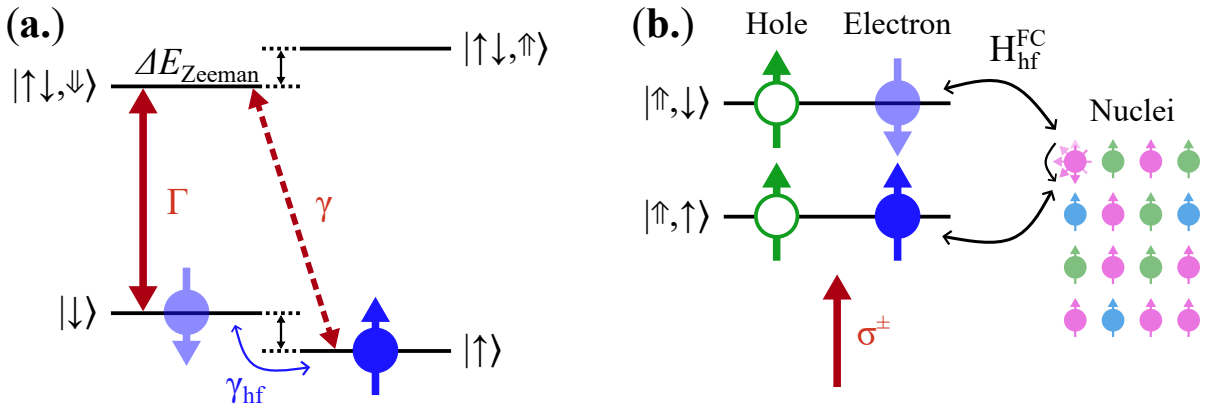


Figure 2.13: (a) Initialisation of the electron spin using resonant pumping of the X^- trion. The pump laser is tuned into resonance with one of the optical transitions ($|\downarrow\rangle \leftrightarrow |\uparrow\downarrow,\Downarrow\rangle$) which drives optical excitation at the rate Γ. Due to several processes, the forbidden relaxation pathway to the $|\uparrow\rangle$ state is actually able to occur weakly at rate γ, initialising the electron spin. The electron in the $|\uparrow\rangle$ state is said to be 'shelved' as it is trapped in this state. However, the hyperfine interaction with the nuclei provides a pathway for the spin to relax to the $|\downarrow\rangle$ state which occurs with rate γ_{hf}. Therefore spin initialisation is impossible if $\gamma_{hf} > \gamma$. (b) Initialisation of the nuclear spin ensemble by optically generated DNP, which follows a three-step cyclic process. Polarised light is used to generate optically excited polarised electrons in the QD. These electrons can then exchange their spin with a nuclei via the flip-flop term of the hyperfine interaction, transferring polarisation to the nuclei. Finally, the electron undergoes optical recombination freeing the dot for a new exciton. Over many repetitions of this process, DNP of at least 50% can be generated, sufficient to initialise the nuclei.

Additionally, due to the Zeeman splitting of the electron spin states, the hyperfine mediated flip-flops are not energy conserving, meaning energy needs to be supplied. This leads to the maximum DNP being dependent on the externally applied field. This also introduces a dependence on the circular polarisation of the optical pump. If the Overhauser field B_{OH} generated by the polarised nuclear state acts against the external magnetic field B_z, there will be an enhancement in the generation of DNP due to the reduction in the electron Zeeman splitting reducing the energy required to undergo a spin flip-flop. Comparatively, if the Overhauser field and external field are aligned there is a suppression of DNP [124, 147].

A consequence of not being able to reach 100% polarisation is that the nuclei are left populating all four spin states, with the relative state populations given by a Boltzmann distribution. The nuclear spin states are driven towards the highest or lowest spin state depending on the polarisation of the optically excited electrons. For example, if the electrons are spin $\uparrow$ ($\downarrow$) the nuclei are driven towards the $I_z = +\frac{3}{2}$ ($I_z = -\frac{3}{2}$) state which becomes the most populated, this leaves the $I_z = -\frac{3}{2}$ ($I_z = +\frac{3}{2}$) the least populated state.

Finally, we briefly discuss new work where polarisations of 95% have been achieved [148]. This was made possible by applying a large negative bias across the QD allowing for rapid removal of electrons from the dot faster than the optical recombination rate. This increases the rate of electron-nuclear spin flip-flops while minimising the chance of a parasitic second flip-flop occurring, enabling DNP values approaching unity to be achieved [148]. For the work in this thesis, we use optically generated DNP values of 50-70%, which is still sufficient to allow the nuclear spin bath to be exploited as the quantum resource.

2.4.2 Spin Control

From a generated initial spin state, a functioning quantum computer needs to be able to perform arbitrary manipulations of the qubit spin state in order to perform computations. As we have discussed in the previous sections, a particle's spin makes it sensitive to applied magnetic fields, which can be exploited to perform rotations of the particle's spin alignment using alternating magnetic fields. Such techniques were developed in the 1930s and for nuclei is referred to as NMR [149]. NMR has been widely used in chemistry for probing the structures of molecules through the spins of their constituent atoms, and has been extended to a form of medical imagining termed MRI. Similarly, this process can be applied to the spins of electrons, termed electron spin resonance (ESR). While they operate on the same basic principles, ESR has proven to be very difficult to experimentally implement in QDs. Therefore, while the discussion below describes both techniques, we are limited to only controlling the nuclear spins using NMR for the work in this thesis.

In the following, we consider a simplified single $S = \frac{1}{2}$ spin particle system. A static external field B_z (where the z axis lies along the sample growth direction) is applied and the two spin states become separated in energy due to Zeeman splitting $\Delta E_{\text{Zeeman}} = \mu_N g_N I_z B_z = \hbar\omega_L$. Here, the field causes the spins to precess about B_z with an angular frequency ω_L, which is termed the Larmor frequency. To manipulate the spins an alternating magnetic field is applied perpendicular to B_z with frequency ω. The field is given by [125]:

$$B_x(t) = B_{x,0}\cos(\omega t), \tag{2.50}$$

where $B_{x,0}$ denotes the field magnitude along the x axis, which for the work in this thesis will be aligned perpendicular to the sample growth direction. The simplest way to analyse the effect of this applied field is to split it into two rotating components, one clockwise B_L and one anticlockwise B_R, related to the total field by $B_x = \frac{1}{2}(B_L + B_R)$. These two components are defined as:

$$B_R = B_1(\boldsymbol{i}\cos(\omega t) + \boldsymbol{j}\sin(\omega t)) \tag{2.51}$$

$$B_L = B_1(\boldsymbol{i}\cos(\omega t) - \boldsymbol{j}\sin(\omega t)), \tag{2.52}$$

where B_1 is another scaling factor. We therefore can see that one of the above terms will rotate with the procession of the spin dipole moment, while the other rotates in the opposite direction. It can be shown that near the resonance condition $\omega = \omega_L$ that the component rotating opposite to the spin will vanish [125]. Therefore, the resulting alternating field is given by one of the above two equations, which for the rest of this section we will use B_R and redefine it as $B_1 = B_R$. B_L can still be recovered when ω is negative. We can now create an equation of motion for the spin under both the static field B_z and alternating magnetic field B_1:

$$\frac{d\boldsymbol{\mu}}{dt} = \boldsymbol{\mu} \times \gamma(\boldsymbol{B}_z + \boldsymbol{B}_1(t)). \tag{2.53}$$

To remove the time dependence of $\mathbf{B}_1$ we can rewrite the equation in a different coordinate system that is rotating about the z axis. As long as $\mathbf{B}_1$ precesses with frequency ω_L it is static in this new frame, which is termed the rotating frame, as opposed to the static 'laboratory' frame. As the rotating frame precesses about the z axis $\mathbf{B}_z$ remains stationary. In this new frame of reference Eq. 2.53 becomes:

$$\frac{d\boldsymbol{\mu}}{dt} = \boldsymbol{\mu} \times (\boldsymbol{k}(\omega + \gamma B_z) + \boldsymbol{i}\gamma B_1), \tag{2.54}$$

which we can finally rewrite in terms of the spin precessing around an effective magnetic field $\boldsymbol{B}_{\text{eff}}$:

$$\frac{d\boldsymbol{\mu}}{dt} = \boldsymbol{\mu} \times \boldsymbol{B}_{\text{eff}} \tag{2.55}$$

$$\boldsymbol{B}_{\text{eff}} = \left(B_z - \frac{\omega}{\gamma}\right)\boldsymbol{k} + B_1\boldsymbol{i}. \tag{2.56}$$

Here, the first term has been rewritten to highlight the resonance condition. Specifically as ω represents the magnitude of the alternating field frequency, its sign simply switches the field between B_R and B_L. Therefore, we can substitute $\omega = -\omega$ without changing Eq. 2.54. We can see from Eq. 2.56 that the effective magnetic field possesses both an x and z component. However, if ω is chosen such that $B_z - \frac{\omega}{\gamma} = 0$, then the first term vanishes and the effect of the applied field is to cause the spin dipoles to precess around the x axis in the rotating frame. The resonance condition is met when $\omega = \omega_L$. Typically for nuclear spins ω_L is on the the order of MHz, corresponding to RF alternating magnetic fields, meaning that ω is also commonly termed ω_{RF}. Using NMR to investigate and control the nuclear spin dynamics has been studied extensively in QDs [70, 87, 116, 131, 134, 145, 148, 150, 151]. For electrons, the corresponding driving frequency is instead GHz due to the Bohr magneton being significantly larger than the nuclear magneton ($\mu_B > \mu_N$); a consequence of the higher nuclear mass. This has made implementing microwave electron spin

control extremely challenging due to the additional electric fields generated by microwave sources disrupting the electron. As such microwave ESR has only been experimentally observed once to date [31], and instead optical control in Voigt geometry is used [152].

We now see that the application of alternating magnetic fields will drive a gradual precession of a spin about the axis of the applied field. Therefore applying a field of strength B_1 for a time T_{RF} will cause the spin to be rotated by angle $\theta = \gamma B_1 T_{\mathrm{RF}}$. Assuming T_{RF} is sufficiently long, and for a spin aligned parallel to the static field B_z, the spin will be rotated in the y-z plane. As it rotates it will become anti-parallel with B_z before returning again to become parallel. This can be exploited to achieve specific rotations of the spin by calibrating T_{RF} such that θ equals a specific angle. The most common types of rotations are 90° and 180°, more commonly referred to as $\frac{\pi}{2}$ and π pulses respectively.

In the above discussion, Eq. 2.55 implies that the spin rotates indefinitely as long as the alternating field B_1 is applied. However, a polarised spin lies far from its equilibrium state meaning we would expect there to be some timescale over which the spin returns to its equilibrium magnetisation M_0 due to interactions with the environment. The equations needed to describe this relaxation process were developed by Bloch [153]. Consider a system of a single spin in a static magnetic field B_z. The magnetisation produced by the spin is $\boldsymbol{M}(t)$. The spin is then polarised so that it is aligned parallel to B_z. First, we would expect the magnetisation of the spin M_z to decay to its equilibrium value over a time defined as T_1, which gives the equation of motion [125]:

$$\frac{dM_z}{dt} = \gamma(\boldsymbol{M} \times \boldsymbol{B})_z + \frac{M_0 - M_z}{T_1}. \tag{2.57}$$

Likewise, if the spins are polarised along an axis in the x-y plane we expect that they will relax to align parallel with the external field. Therefore, over a time-scale T_2 we expect the x and y components of the magnetisation to decay to zero. The equations of motion are therefore [125]:

$$\frac{dM_x}{dt} = \gamma(\boldsymbol{M} \times \boldsymbol{B})_x - \frac{M_x}{T_2}, \tag{2.58}$$

$$\frac{dM_y}{dt} = \gamma(\boldsymbol{M} \times \boldsymbol{B})_y - \frac{M_y}{T_2}. \tag{2.59}$$

We define the time-scale for transverse relaxation differently to the longitudinal relaxation. This is due to the fact that it is expected for $T_2 < T_1$ as the transverse relaxation does not always conserve energy [125].

For reasons that will be discussed in the next section, we are primarily interested in the relaxation times of a spin in the absence of an alternating external field. Therefore, working in the rotational frame and without any alternating magnetic field, $\boldsymbol{B} = 0$. We can then solve Eqs. 2.57-

2.59 to obtain the time dependence of the three components of the spin magnetisation [154]:

$$M_x(t) = M_x(0)e^{-\frac{t}{T_2}} \tag{2.60}$$

$$M_y(t) = M_y(0)e^{-\frac{t}{T_2}} \tag{2.61}$$

$$M_z(t) = M_0 - (M_0 - M_z(0))e^{-\frac{t}{T_1}}, \tag{2.62}$$

where we have defined M_0 as the equilibrium magnetisation of the spin along the z axis. From Eqs. 2.60-2.62 we see that for a polarised spin we expect to observe an exponential decay of magnetisation over time until it reaches its equilibrium magnetisation, which will be aligned with the externally applied static field. The above description was for a single spin $S = \frac{1}{2}$ particle. For the nuclei in a QD we now have a system of $N \approx 5 \times 10^4$ spin $I = \frac{3}{2}$ particles, with a magnetisation given by $\boldsymbol{M} = \sum_i \boldsymbol{\mu}_i$. Despite these differences the above description is still valid. In the next section we discuss the causes and differences of each type of spin relaxation.

2.4.3 Relaxation

In the previous section, we have demonstrated that by applying an alternating RF magnetic field perpendicular to a spin (or ensemble of spins in the case of nuclei) will cause the spin to rotate, which can be exploited to control the spin to perform computations. This means we have a qubit we can initialise and control. Unfortunately, once a spin is initialised there is a limit on how long it can be used for computations before it has relaxed back to its equilibrium magnetisation, given by Eqs. 2.60-2.62. Long spin relaxation times are therefore a key part of realising a working quantum computer. Fig. 2.14 shows schematic diagrams of three types of spin relaxation discussed here.

Again, consider a spin $S = \frac{1}{2}$ particle in an external static magnetic field B_z, once initialised the components of its magnetisation begin to decay, which occurs over two timescales given by T_1 and T_2. First, we consider the longitudinal relaxation time T_1. T_1 is the time on which the spin magnetisation component M_z aligned along the external static field axis decays to its equilibrium magnetisation M_0, which will lie parallel with the external field. This relaxation occurs due to the spin systems energy being transferred to the environment and is commonly called spin-lattice relaxation. Fundamentally, once the equilibrium magnetisation has been reached the system must be reinitialised in order to begin further computations. Therefore T_1 is referred to as the spin lifetime. The loss of longitudinal magnetisation is characterised by spin flips between the different spin states, though the mechanism that drives the relaxation varies for the electron and nuclei.

For electrons, spin lifetimes are typically $T_{1,e} \approx 0.1 - 10$ ms. For high magnetic fields $B_z > 2$ T, the relaxation is dominated by interactions with thermal phonons. The primary mechanism for this is caused by a spin-orbit interaction driven mixing of the ground electron spin states with excited

states possessing opposite spin, spin flips can then occur through spin independent electron-phonon coupling [87, 137, 155, 156]. However, phonon driven spin flips are strongly dependent on the external magnetic field. Therefore for $B_z < 2$ T spin relaxation via phonons becomes very slow. Instead, for lower fields, relaxation becomes primarily driven by electron cotunnelling, which is where the confined electron exchanges its spin with an electron in the Fermi reservoir [87]. In Chapter 6 we discuss the primary cause of electron spin flips in more detail, as well as investigate the electron $T_{1,e}$ time in GaAs QDs. Nuclear spin relaxation is dominated by spin diffusion, which can be accelerated further by the introduction of a confined electron, though in both cases nuclear spin lifetimes significantly exceed the electron spin lifetime owing to the weaker coupling of the nuclear spins to the environment. First, when there is no electron present, nuclear spin lifetimes are typically $T_{1,N} \approx 10-20$ s. The introduction of an electron reduces this to $T_{1,N} \approx 1-10$ s as the electron can mediated nuclear-nuclear spin flip-flops between distant nuclei, accelerating the spin diffusion [116, 157]. This is in contrast to strained SK grown QDs, where the larger strain leads to a freezing of the spin diffusion due to the quadrupolar interaction [158] and nuclear spin diffusion becomes dominated by electron mediated phonon coupling and cotunelling as described above [87], processes which are suppressed by the low strain environment of GaAs/AlGaAs QDs [116].

We also expect the components of the spin magnetisation perpendicular to the applied field to decay to zero. This transverse relaxation describes a loss of phase information and occurs over a time T_2 referred to as the coherence time. T_2 times are typically much shorter than T_1 as the relaxation does not require any transfer of energy. The loss of phase is driven by random spin-spin interactions, which are often called decoherence effects. However, there is a second contribution to the loss of a system's phase information: local inhomogeneities in the magnetic field will cause spins to precess at slightly different rates. Therefore, in the rotating frame the spins will begin to 'spread out' around the x-y plane of the Bloch sphere over a time termed the dephasing time T_2^*. As it includes these random fluctuations T_2^* is always shorter than T_2.

For electrons, decoherence is primarily driven by the surrounding nuclear spins in the QD, which can be well described by the Merkulov-Efros-Rosen (MER) model [105]. Nuclear spin induced decoherence creates three distinct processes that occur over different timescales. First, there is a rapid loss of coherence over $\approx$ 1 ns due to the electrons precession around the nuclear field fluctuations; next there is the slower decoherence effect over $\approx$ 1 μs driven by the nuclei precessing around the electron's Knight field. Finally, the longest timescale is decoherence driven by nuclear dipole-dipole spin flip-flops near the electron which gives an upper limit on the coherence time of $\approx$ 100 μs [48, 105]. The first process is heavily dependent on electron-nuclear spin flips being energy conserving. Therefore it is rapidly suppressed by the introduction of a magnetic field, which separates the spin states in energy due to Zeeman splitting [105, 106]. The fields used for this thesis

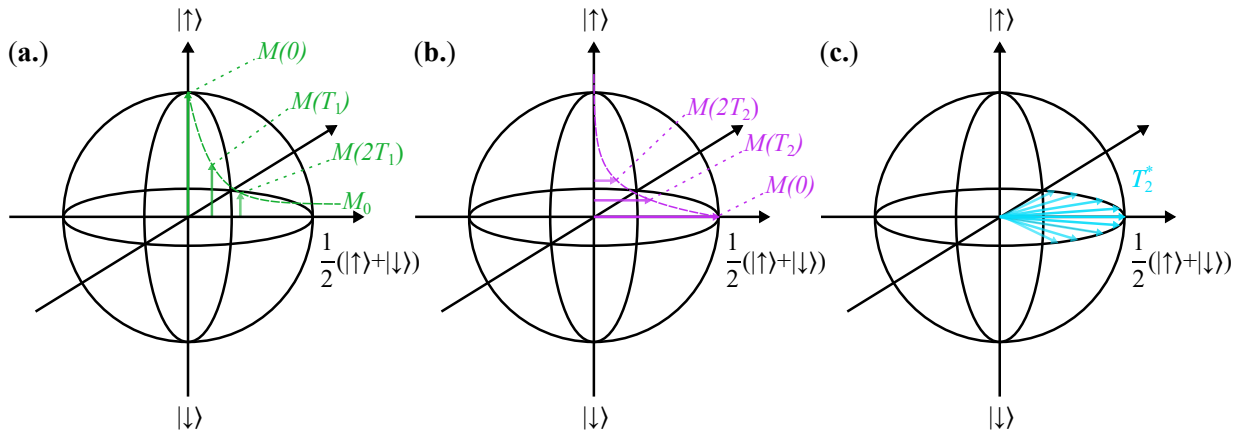


Figure 2.14: Diagram of the three relaxation pathways for spins. Diagrams show a single spin $S = \frac{1}{2}$ system in the rotating frame in a static field along the positive vertical axis ($+z$). The different spin projections are represented as different orientations on a sphere, which is commonly called the Bloch sphere. (a) Spin-lattice relaxation causes a loss in the longitudinal component of the magnetisation over the spin lifetime T_1. This will eventually return the system to its magnetisation at thermal equilibrium M_0. (b) Transverse relaxation caused by spin-spin interactions causes the magnetisation components perpendicular to the applied static field to decay to 0, characterised by the coherence time T_2. The decay represents a loss of phase information. T_2 can be prolonged if the system can be decoupled from its environment using so-called dynamical decoupling techniques, as we will discuss in Chapter 7. (c) Spins will precess at slightly different rates due to inhomogeneities in the local field strength caused by imperfection in the static field as well as the Overhauser field for electrons and quadrupolar interactions for nuclei. This drives dephasing as the spins will spread out over the Bloch sphere over a time T_2^*. Techniques such as the Hahn echo can refocus the spin dephasing to recover the spin state.

when investigating the electron spin are typically $1-8$ T, significantly higher than the $\approx$ 100 mT required to suppress the decoherence due to the frozen nuclear field. Therefore we expect $T_{2,e}$ approaching $\approx$ 1 μs. Unfortunately we are currently unable to measure the electron coherence time in our QDs as we have no way to control the electron spin. However, electron spins in GaAs QDs have been investigated optically using Voigt geometry where the dephasing time is found to be $T^*_{2,e} \approx 2.56-3.92$ ns [126, 159]. The dephasing time can be further improved by cooling the nuclear spin ensemble to reduce the random fluctuations of the nuclear field giving an improved $T^*_{2,e} \approx 608$ ns [159]. Nuclear spin decoherence is again dependent on the presence of an electron inside the QD, which accelerates nuclear spin decoherence due to spectral broadening [131]. For the nuclei in an unoccupied QD the dephasing is caused due to fluctuations in the localised magnetic field due to an imperfect static field and the quadrupolar interaction, which gives a dephasing time of $T^*_{2,N} \approx 250$ μs [70].

It is possible to preserve spin coherence through the use of specific rotations of the spins. This

can be done either optically in the case of electron spins in Voigt geometry or, as in our case, the use of RF pulses. For example it was found by Hahn [160] that after leaving nuclear spins to dephase for a time τ and then applying a single π pulse that an 'echo' in the NMR signal would appear after a further τ delay. This can be explained as follows. Over time T_2^* the nuclear spins will spread around the *x*-*y* plane of the Bloch sphere due to local fluctuations in the magnetic field, giving them slightly different Larmor precession frequencies. However, when the π pulse is applied the spins are flipped and their dephasing motion now causes them to refocus, which takes the same amount of time as taken for them to dephase. Therefore this technique, well known as the Hahn echo, effectively removes dephasing allowing the coherence time T_2 to be observed. This technique has been applied for GaAs QDs, giving $T_{2,e}^{\mathrm{HE}} \approx 2.93-3.82\ \mu$s [126, 159] and $T_{2,N} \approx 1.5$ ms respectively [70]. Such methodology can be further extended by adding more pulses such as the Carr-Purcell (CP) and Carr-Purcell-Meiboom-Gills (CPMG) sequences [161, 162], giving greater improvements in the coherence times leading to recently reported coherence times of $T_{2,e}^{\mathrm{CPMG}} \approx 113-228\ \mu$s (the variation is caused by the different number of applied rotations) [126, 159]. For nuclei the coherence time becomes limited by dipole-dipole interactions between the nuclei. This interaction can be effectively minimised by applying a series of $\frac{\pi}{2}$ pulses, a technique named the Solid echo [163]. The effect of the pulses on the nuclei is less intuitive than for the Hahn echo but it can effectively be seen as a form of motional averaging. The Hahn and Solid echo techniques can be combined to form CHASE sequences, which can effectively decouple the nuclear spins both from quadrupolar induced field inhomogeneities and dipolar couplings [150], enabling coherences times of $T_{2,N} \approx 10-20$ ms [70] to be demonstrated. In Chapter 7 we implement new CHASE sequences in a strain engineered sample to reach nuclear coherence times of up to 100 ms.

Another consideration for the nuclear coherence times in the presence of a confined electron spin is motional narrowing. This is where the electron spin relaxation rate becomes fast enough that electron-nuclear spin flips become suppressed, manifesting as a reduction in the spectral broadening of the NMR linewidth by the Knight field and in turn increasing coherence. The $T_{1,e}$ times needed for this to occur typically require high magnetic fields or a gate bias V_{Gate} that is close to certain electron occupation energies (i.e. $1e \leftrightarrow 2$e). Which then causes a reduction in $T_{1,e}$ due to the tunnelling of the electron [103, 131].

We have now described the sources of relaxation for both electrons and nuclei in QDs and the principal timescales over which they occur. T_1 and T_2 are related as the longitudinal relaxation drives a loss of energy to the environment, which in turn drives a loss of phase information. The three times can be related by the equation:

$$\frac{1}{T_2} = \frac{1}{2T_1} + \frac{1}{T_2^*} \tag{2.63}$$

As we have seen, T_2^* can be removed by applying refocusing π pulse sequences, leaving the final relation $T_2 = 2T_1$. Therefore, we see that T_1 is indeed the fundamental limit on the operational time of a qubit. Despite this, in current experiments we see $T_2^* < T_2 < T_1$ meaning that it is currently T_2 that is the limiting factor on qubit operation times. As such, a much better understanding of the processes driving decoherence are required to realise a QD based spin qubit.

2.4.4 State Readout

We have now discussed how we can initialise and control (for a time limited by relaxation) our spin qubits. The final step required is to be able to readout the spin state using a measurement. For the nuclei, this is a relatively simple procedure. As seen in Fig 2.12a, when the nuclei are polarised in different orientations there is a detectable shift in the splitting between the two exciton PL lines, caused by changes in B_{OH}. As B_{OH} is directly proportional to the strength of the hyperfine interaction, by measuring the change in the PL splitting we can measure the ensemble's polarisation [134]. For carriers the spin state can be obtained using resonance florescence [30]. Yet, as we discuss in Chapter 5, we instead measure the electron spin for the work in this thesis via the nuclear spin ensemble of the QD [137].

Chapter 3

Experimental Techniques

3.1 Sample

The work in this thesis was all carried out on the same charge-tunable GaAs/AlGaAs sample. As briefly discussed in Section 2.1.1, the samples were grown using MBE and nanohole infilling was used to form lattice-matched GaAs QDs. The sample was grown at Johannes Kepler University Linz by S. Manna, S. F. Covre da Silva and A. Rastelli. These types of samples have already been studied in several other works [116, 126, 148]. Fig. 3.1 shows a cross-section of the sample used in this work, where the layered structure is shown. The layer-by-layer growth process will now be described in more detail.

The growth process starts on a GaAs substrate and growth proceeds in the $z+$ (arbitrarily chosen) direction. First, a layer of $Al_{0.95}Ga_{0.05}As$ is grown on the substrate, followed by a layer of $Al_{0.20}Ga_{0.80}As$ and then another layer of $Al_{0.95}Ga_{0.05}As$. These three layers form a Bragg reflector to enhance the collected optical emission from the sample during experiments. The next step is to form the *n*-type layer that will form a part of the *p-i-n* diode. A 95 nm thick layer of $Al_{0.15}Ga_{0.85}As$ is grown, followed by another 95 nm thick layer of $Al_{0.15}Ga_{0.85}As$ doped with Si using a volume concentration of 1.0×10^{18} cm^{-3}. The doping of AlGaAs with Si can lead to the formation of DX centres, which can trap charge carriers and alter the electrical and optical properties of the semiconductor. To avoid this, a low Al concentration of 0.15 is used for the Si doped layer, which suppresses the formation of DX centres [164–167]. Once the *n*-doped layer is grown the next step is to form the electron tunnel barrier layers. A 5 nm thick layer of $Al_{0.15}Ga_{0.85}As$ is grown using a reduced temperature of 560 °C, which suppresses the segregation of Si from the doped layer. Next is another $Al_{0.15}Ga_{0.85}As$ layer grown at 600 °C to a thickness of 10 nm. The tunnel barrier is then completed by a final 15 nm thick layer of $Al_{0.33}Ga_{0.66}As$. This layer is then used to form the QDs. As discussed in Section 2.1.1, Al is deposited onto the surface of the $Al_{0.33}Ga_{0.66}As$ and forms

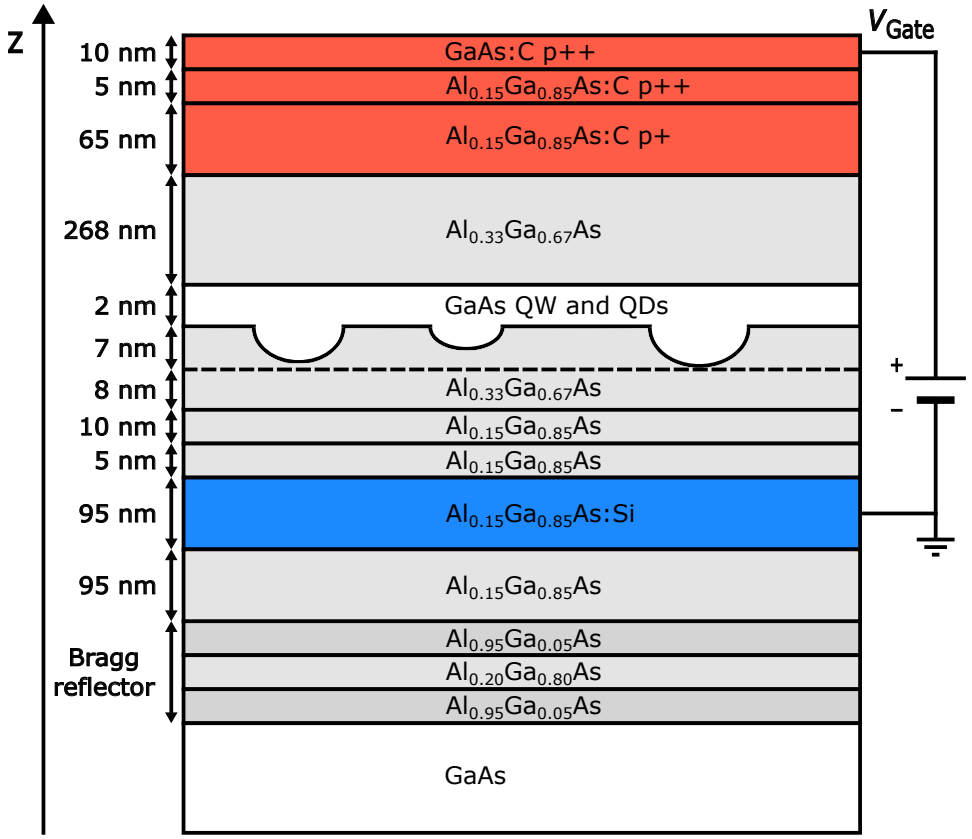


Figure 3.1: Schematic diagram of the GaAs/AlGaAs QD sample structure.

droplets. These droplets then etch away at the $Al_{0.33}Ga_{0.67}As$ to create nanoholes that can be used to form QDs. The size of the nanoholes formed by this process have been studied using AFM and typically have a diameter of ≈ 70 nm and a depth of ≈ 6.5 nm. Next the QDs are formed by infilling the nanoholes during the growth of a 2.1 nm thick layer of GaAs. This overfills the nanoholes and creates a QW layer above the QDs. Therefore the maximum possible QD height is ≈ 9 nm in the growth direction (along $z+$). Next, a 268 nm thick layer of $Al_{0.33}Ga_{0.67}As$ is grown above the QW, forming the hole tunnel barrier layer. The thickness of this layer ensures the suppression of hole tunnelling. Finally, a 65 nm thick layer of $Al_{0.15}Ga_{0.85}As$ is grown which is doped with carbon (C) at a concentration of 5.0×10^{18} cm^{-3}. This is followed by a 5 nm thick layer of $Al_{0.15}Ga_{0.85}As$ doped with C at a 9.0×10^{18} cm^{-3} concentration and then a 10 nm layer of GaAs doped with a 9.0×10^{18} cm^{-3} concentration. These three C doped layers form the *p*-type contact for the *p-i-n* diode.

After this the sample is processed into a *p-i-n* diode structure. This begins by etching away the *p*-doped layers and then depositing Ni(10 nm)/AuGe(150 nm)/Ni(40 nm)/Au(100 nm) on the etched areas, forming mesa structures with a height of 250 nm. Next the sample is annealed to

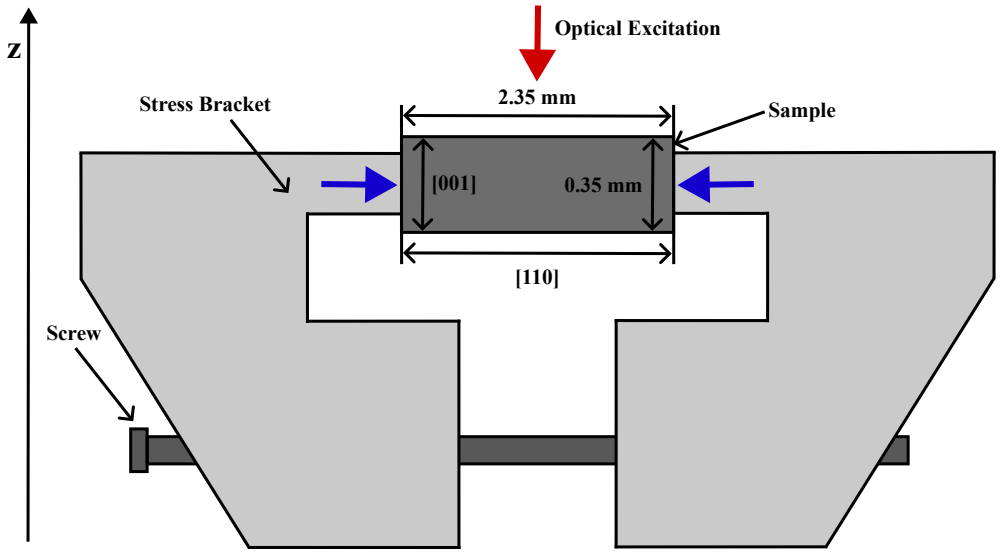


Figure 3.2: Schematic diagram of the sample placed in the stress bracket used for the experiments in this thesis. The sample is mounted so that the stress bracket is in contact with the two 0.7 mm $\times$ 0.35 mm sides of the sample. This means that the compressive stress (blue arrows) is applied along the [110] crystallographic axis. The magnitude of the applied stress is controlled by the stress mount screw. Additionally the sample is oriented so that the growth direction lies along the positive z axis, with optical excitation (red arrow) being directed onto the top surface of the sample.

enable diffusion down to the n-doped layer, forming the ohmic back contact. To form the top gate contact, Ti(15 nm)/Au(100 nm) is deposited onto the p-type surface of the mesa areas. The sample bias V_{Gate} is the bias of the p-type top contact with respect to the grounded n-type back contact. The large thickness of the top $Al_{0.33}Ga_{0.67}As$ layer suppresses the tunnelling of holes, while tunnel coupling with the n-type layer enables deterministic charging of the QD with electrons by changing V_{Gate}.

For the work in this thesis we exploit the strain sensitive (via EFGs) quadrupolar interaction of the nuclear spins and externally apply strain in order to resolve the NMR transitions (see Chapter 4). We therefore apply uniaxial compressive mechanical stress to the sample. To achieve this, the sample is cleaved into a small piece which has a rectangular surface area of 0.7 mm $\times$ 2.35 mm, with the edges aligned along the [110] and [1$\bar{1}$0] crystallographic directions. Thickness of the sample is 0.35 mm and is aligned along the [001] growth direction, meaning the sample has a parallelepiped shape. The sample is then inserted into a stress bracket. The orientation of the sample places the two 0.7 mm $\times$ 0.35 mm surfaces of the sample in contact with the flat titanium surfaces of the stress cell bracket. The compressive stress is applied using a titanium screw, with the stress applied along the 2.35 mm long edge of the sample. Fig 3.2 shows a schematic diagram of this setup. The applied stress used in this work is measured in Chapter 4 from inverse NMR

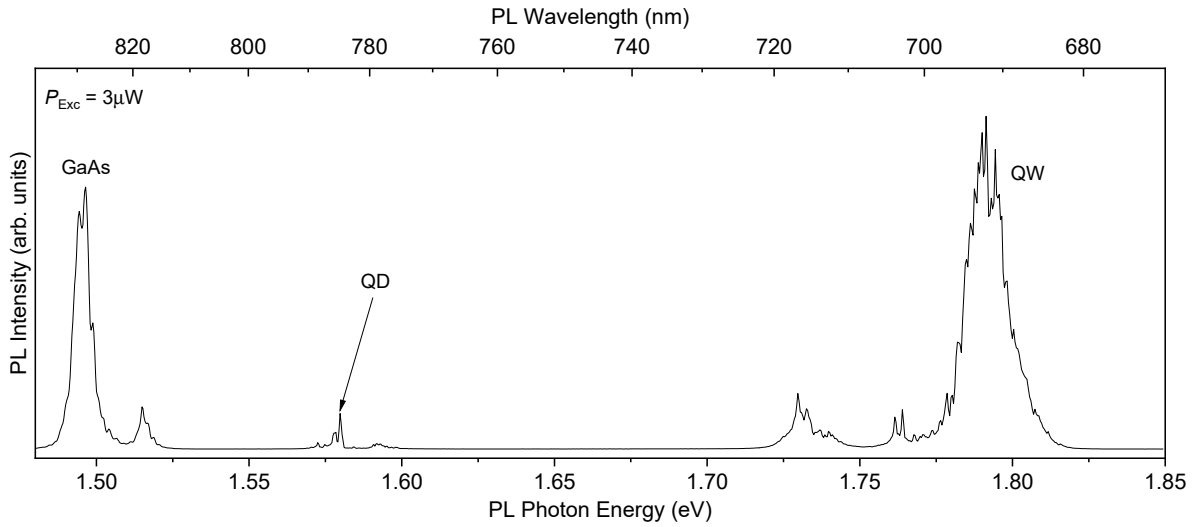


Figure 3.3: PL spectra of GaAs/AlGaAs sample measured at $T \approx 4.35$ K. A 755 nm diode laser, using an excitation power of $P_{\text{Exc}} = 3\ \mu$W, was used to optically excite the sample. Emission from a QD can be observed at $\approx$ 782 nm, while broad emission from both bulk GaAs and the QW layer can be seen at $\approx$ 830 nm and $\approx$ 690 nm respectively. The measurement was kindly performed by Peter Millington-Hotze using a different experimental setup on an unstrained piece of the same sample.

measurements and is found to be $P \approx -0.363$ GPa. For a small number of experiments in this thesis an identical sample without externally applied stress is used, this will be noted in the text where relevant.

During experiments, excitation and collection of the QD PL occurs through the top of the sample. A PL spectra measured on a GaAs/AlGaAs sample is shown in Fig. 3.3. The spectra was collected using a 755 nm diode laser at an excitation power of $P_{\text{Exc}} = 3\ \mu$W. There are three notable features in the spectra. First, we observe the emission of bulk GaAs at 830 nm, then we observe a narrow emission between 780 nm-790 nm which is the emission from a QD. Finally another broad feature can be found at 690 nm which is emission from the QW layer that forms above the QD layer, as seen in Fig. 3.1.

3.2 Bath Cryostat Setup

The work conducted in this thesis necessitates that the samples be cooled to cryogenic temperatures. We achieve this by placing the sample inside an Attocube bath cryostat where liquid helium is used as a coolant. The sample is contained in a long metal insert tube which is submerged into the bath of liquid helium. This allows stable cryogenic temperatures, typically $T \approx 4.2$ K, to be maintained consistently. Before being inserted into the cryostat, the insert tube is vacuum pumped to

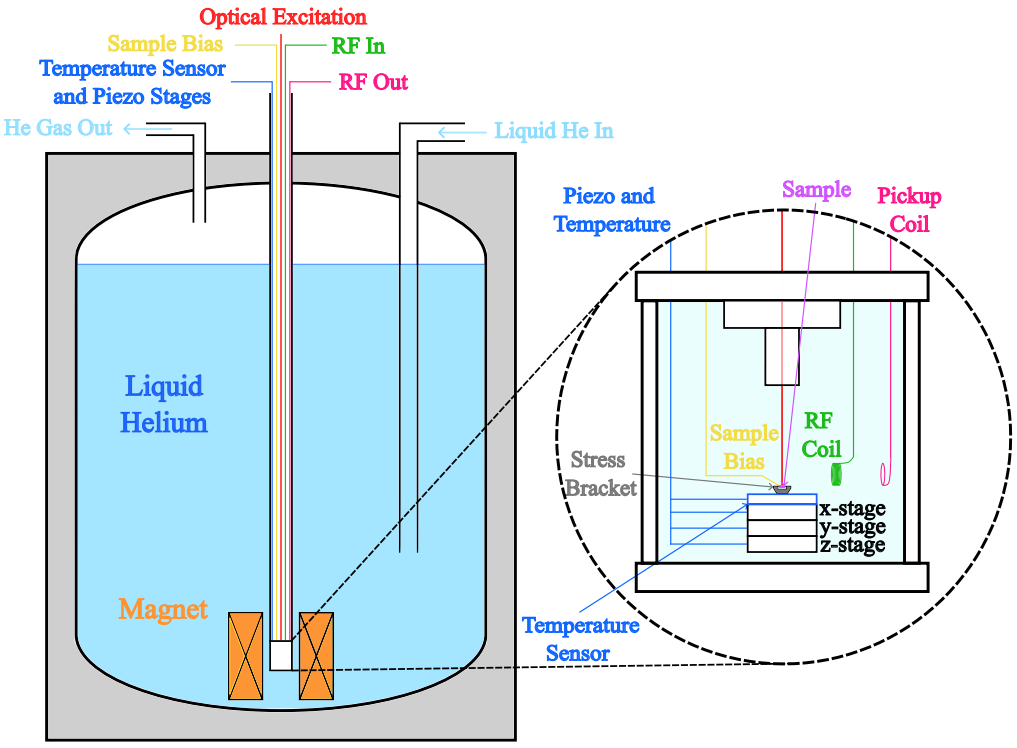


Figure 3.4: Schematic diagram of Attocube bath cryostat. The sample is placed into a metal tube insert which is submerged into liquid helium. The insert is vacuum pumped with only a small amount of helium gas added after to enable thermal exchange between the sample and helium bath, keeping the sample at $T \approx 4.2$ K. The sample is mounted on a resistive temperature sensor and three nanopositioner stages connected to external controllers by two 12-pin connectors at the top of the insert. A coil needed for NMR is positioned close to the sample, while a second coil used for detecting the generated RF signal is placed nearby. The two coils, as well as the sample bias are connected to external generators via three Bayonet Neill-Concelman radio frequency connector/cable (BNC) connectors. Finally laser light (emitted PL) can be directed to (collected from) the sample through a window slit at the top of insert, while a lens is used to focus (collimate) the light.

remove any atmospheric gases that would freeze at cryogenic temperatures, before a small amount of helium gas is added to allow thermal exchange between the sample and the liquid helium bath. A schematic diagram of the bath cryostat setup is shown in Fig. 3.4. When the insert is placed into the cryostat it is aligned so that the bottom of the tube lies within the bore of a superconducting ring magnet, which produces the external field aligned parallel to the sample growth direction B_z, enabling measurements to be conducted in Faraday geometry. Control of the magnet is achieved using a Mercury iPS control unit, allowing the generation of static magnetic fields up to $B_z = 8$ T.

Fig. 3.4 also shows a diagram of the setup constructed at the bottom of the insert. The stress bracket, with the sample being held by the two arms, is connected to three nanopositioner stages which are in turn held in place by a cage system. The three nanopositioners each allow translation

along one axis, giving full movement of the sample along the x, y and z directions. As the laser spot is a fixed point, the movement of the sample enables different dots to be measured as well as optimisation of the optical excitation. The three stages are connected to a 12-pin connector mounted at the top of the insert which is in turn linked to an Attocube ANC150 piezo control unit. The control unit allows tuning of the step size and frequency of the three stages, enabling precise control of the sample position. Additionally, a second 12-pin connector is used to connect a resistive temperature sensor positioned below the sample to a CryoCon 1200 cryogenic temperature monitor. The sensor is needed to monitor the heating caused by the optical excitation and high power RF pulses, which can cause damage to the sample and RF coil. Two wires are attached to the sample gate contacts. These cables are connected via a BNC connector at the top of the sample insert to a generator that can be used to apply a voltage bias across the sample, critical for measurements requiring the QDs to be occupied by electrons (see Chapters 5 and 6).

For NMR measurements, a coil is used to generate the necessary oscillating magnetic field $B_x \perp z$. The coil is made from 0.1 mm diameter enamelled copper wire, and consists of 10 turns wound on a $\approx$ 0.4 mm diameter spool in 5 layers, with 2 turns in each layer. Another BNC connector is used to connect the coil to the external RF generator. There is second RF coil placed into the insert tube that is used to detect the RF signal emitted by the primary coil. This coil is connected to a spectral analyser via a third BNC connector at the top of the insert. The primary NMR coil is positioned as close to the sample as possible to maximise the magnetic field that can be generated. However, this needs to be compromised with leaving enough room to move the sample, as hitting the sample with the coil could damage both components. Another consideration is the stress bracket, which has a greater extent than the short 0.7 mm sample edge. Therefore while it is possible to have the coil positioned between the arms of the stress bracket, this can only be done in a narrow range otherwise the coil will hit the stress bracket. For most of the sample, only a narrow region is accessible for experiments. The pickup coil is then positioned on the other side of the NMR coil from the sample.

To enable optical experiments, the excitation laser and emitted PL are able to pass through the top of the insert through a small window slit. A lens near the sample is used to focus the excitation light and collimate any sample emission. One of the nanopositioner stages can be used to change the z position of the sample in order to focus the laser onto the sample, which optimises optical emission.

3.3 Optical Spectroscopy

All investigations of the QD spin system in this work are conducted via optical spectroscopy. The use of microphotoluminesence (μ-PL) to probe QDs is a well documented and studied subject

[103], made possible as QDs are optically active. In this section, we describe the experimental set-up used for the pump-probe optical excitation and measurement of QDs, following the schematic diagram shown in Fig. 3.5. The optical setup is separated onto two breadboards, connected by optical fibres. An optical bench is used to mount one of the breadboards and contains the lasers needed to excite the QD, as well as ways to limit and control the laser power. The other breadboard is placed above the cryostat, mounted directly onto the sample insert and contains the necessary optics to generate the polarised light needed for experiments and to collect the emitted PL from the sample.

We begin by discussing the optical bench setup. As can be seen in Fig. 3.5, the setup is separated into two arms, one for the pump laser (red), which is used for initialisation of the electron and nuclear spins, and one for the probe (green), which is used for optical readout. For efficient pumping, the pump laser is high power ($P_{\text{Pump}} \approx$ 1-2 mW) while the probe laser is weaker ($P_{\text{Probe}} \approx 50\,\mu$W), as measured on the power meter included in the setup. The pump laser used is a wavelength tunable Toptica DLC DL pro, which has a wavelength range 760-800 nm, enabling resonant and quasi-resonant pumping of the QD. The laser was connected to a controller which was in turn connected to a PC, enabling automated control of the pump wavelength during experiments. Optical probing was conducted using a 760 nm Roithner RLT760-30G, allowing non-resonant excitation of the QD. The laser beams are coupled into two separate optical fibres which lead to the cryostat breadboard. On the pump arm, several optical components are placed between the laser and optical fibre. A 90:10 beam splitter (BS) is used to split off a fraction of the pump laser power where it is fed into a wavelength meter to allow measurement of the pump laser wavelength. Additionally, a filter attached to a stepper motor is used to attenuate the laser power, this is combined with a powermeter to allow automated control of the laser power during measurements. For some experiments a flipper mirror was added to allow further attenuation of the laser power. For the measurements in Chapters 5 and 6 it was required that the electron was pumped optically requiring fast modulation of the laser, to this end an electro-optic modulator (EOM) was placed into the optical path as well as an acousto-optic modulator (AOM) along the fibre path to allow for this in these experiments.

Both beams are then transferred by optical fibres to the breadboard above the cryostat. Both beams are passed through half-wave plates (HWPs) to enable maximisation of the laser power through rotation of the laser polarisation. After this the pump beam additionally passes through a linear polariser, ensuring the light is polarised followed by a motorised HWP to allow automatic control of the polarisation during measurements. The beam then passes through a 90:10 pellicle BS, which directs a small amount of the power into a power meter to use for automatic measurements of the laser power during experiments. The probe laser is also directed into the same pellicle BS, which directs most of the power to the power meter. However this is not a problem as only small powers are required for optical readout. From this point, the pump and probe arms have been

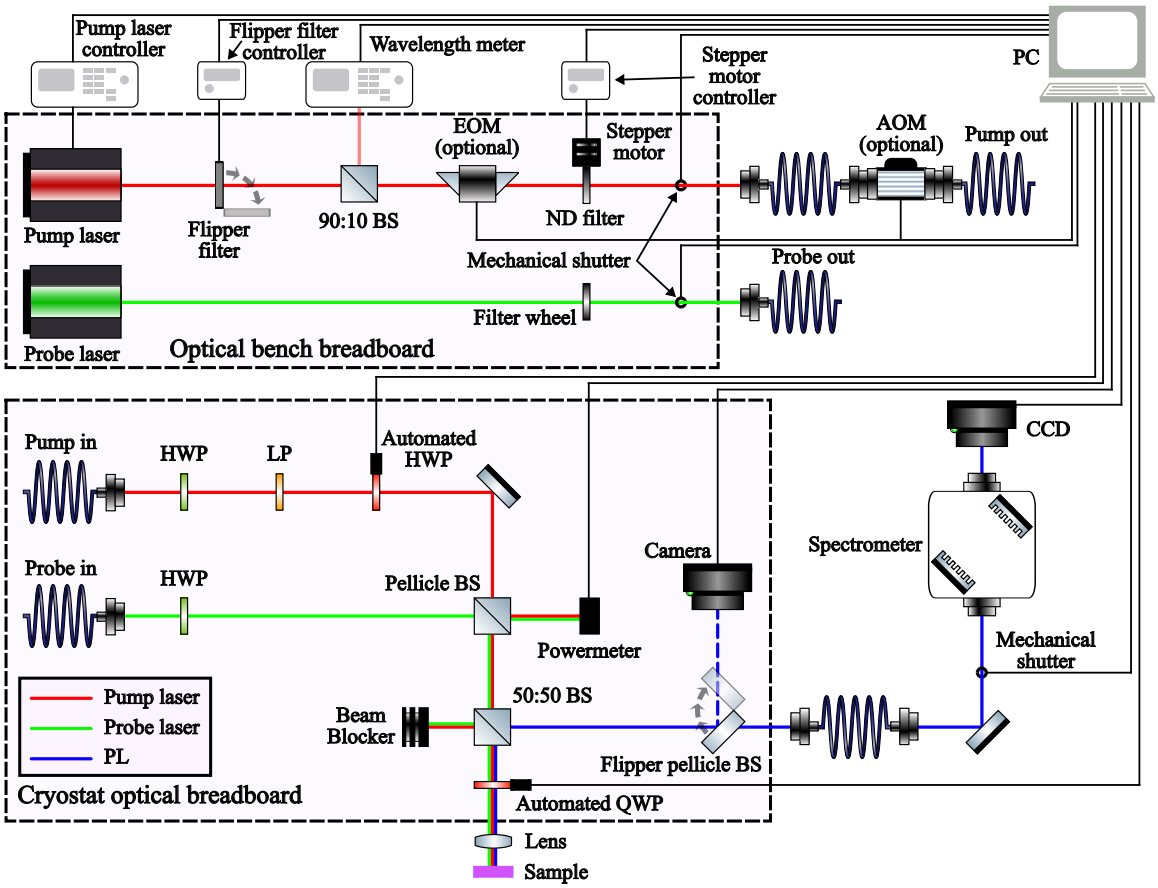


Figure 3.5: Schematic diagram of the optical setup used for pump-probe experiments. The setup is separated over two breadboards. The first, mounted on an optical bench contains the pump (red) and probe (green) lasers, which are coupled into two separate optical fibres. Additionally the pump arm contains a beam splitter, to direct light to a wavelength meter as well as filters to allow control of the pump laser power. Additionally, an EOM and AOM can be added to allow optical polarisation of a confined electron. The fibres are used to transfer the laser light to a second breadboard above the cryostat, where a 50:50 beam splitter is used to direct light down to sample and direct emitted PL (blue) to the spectrometer and CCD for measurements. A pellicle BS is used to direct a portion of the laser to a power meter to allow the laser power to be monitored during measurements. The circular polarisation of the pump beam is controlled by the combination of a PC controlled HWP and QWP. Three mechanical shutters are used to create the laser pulses needed for experiments. Figure made with aid from [168].

merged and the beams follow the same path. The beams then pass through another 50:50 BS which is mounted above the cryostat sample insert. The BS directs the laser down to the sample, first passing through an automated quarter-wave plate (QWP), which functions to circularly polarise light from the pump beam, while the HWP on the probe arm is used to ensure the QWP does not affect the probe polarisation, leaving it linearly polarised. As discussed in Section 3.2 the beam then passes through a small window slit before being focused onto the sample by an aspheric lens, where it is either absorbed or reflected. Emitted PL from the sample is collimated by the lens before passing through the window slit at the top of the insert. At the beam splitter the light is directed along a different path and is coupled into another optical fibre, where it is then directed to a double grating spectrometer (U1000 Jobin Yvon). A pair of achromatic lens doublets are then used to magnify the output of the spectrometer by a factor of 3.75 which is then finally projected onto an electrically cooled charge-coupled device (CCD). The resulting energy resolution of the measurement setup is $\approx$ 15 μeV which was measured from the full width half maximum (FWHM) of a laser with a true linewidth of $<$ 0.4 μeV. Before the optical fibre another pellicle BS on a flipper mount can be introduced to the beam path, directing the light to a CCTV camera allowing the laser spot on the sample to be visualised. This is greatly helpful when moving the sample, as well as when trying to focus the spot onto the sample surface and ensure the laser spot is approximately circular, with a typical diameter $\approx$ 1 μm. The CCD exposure time can be set to an arbitrary duration as required for different measurements and during QD alignment. Additionally shown in Fig. 3.5 are three mechanical shutters, two placed on the optical bench breadboard along the beam path of the pump and probe arm respectively, and a third one positioned before the spectrometer. These are used to generate the pump and probe optical pulses during experiments, as they can fully block the laser light while having a time resolution of $\approx$ 1 ms. This is preferred over switching the lasers on and off as this causes instability in the laser power. Additionally the third mechanical shutter is used to block the CCD from the pump laser which, due to the wavelength being nearly resonant, can significantly damage the CCD.

3.4 Dynamic Nuclear Polarisation

For the measurement of spin dynamics in QDs using the experimental setup described in Sections 3.2 and 3.3, we utilise the well known pump-probe measurement cycle. Generally, these experiments follow a similar structure. First, a long high power laser pulse is used to generate a polarised nuclear spin state, then RF oscillating magnetic fields are used to manipulate the spins, before a final shorter and lower powered optical pulse is used to probe the final spin state. More detailed timing diagrams are shown in each experimental chapter. The lasers used for the pump and probe pulses have already been discussed in Section 3.3. In this section we discuss the calibration

measurements used to optimise the optical pumping and probing of the nuclei, explaining how the experimental parameters used in the following chapters are obtained.

3.4.1 Optical Pumping

We begin by discussing the pump laser parameters. The pump process is made possible due to the optical selection rules in QDs. The ground state energy levels for a QD are shown in Fig. 3.6a. The conduction band states have *s* shell character, giving two states for the electron spin projections $s_z = \pm 1/2$, in contrast the valence band has *p* shell character which gives four valence band states (the split off band is ignored here due to the large energy separation.) for the $J_z = \pm 1/2, \pm 3/2$ states. These valence band states are a mixture of the orbital and spin angular momentum components, which are able to mix due to the spin-orbit coupling [48]. This mixing of orbital and spin angular momenta also means that orbital momentum carried by photons can be used to change the spin orientation of the charge carriers. Photons can carry angular momentum if they are circularly polarised, where their field components rotate either clockwise (σ^+, $L = +1$) or anticlockwise (σ^-, $L = -1$). Due to the conservation of momentum, there exists optical selection rules for this system where only certain transitions are allowed, which are shown by the arrows in Fig. 3.6a. Additionally, the $J_z = \pm 1/2$ and $J_z = \pm 3/2$ states are separated by the $hh - lh$ splitting. Therefore by selecting the photon energy and polarisation, specific transitions can be driven leading to the repeated generation of optically polarised electrons in the conduction band (a hole is also formed in the valence band). These electrons can transfer their spin polarisation to the nuclear spin ensemble through hyperfine interaction spin flip-flops leading to a gradual build up in the nuclear spin polarisation (see Section 2.4.1).

It is therefore important to calibrate the necessary experimental variables to ensure efficient and effective pumping of the nuclear spins to generate sufficient DNP for measurements. We begin by showing how efficient circularly polarised light is produced. As seen in Fig. 3.3 light from the pump laser is passed through a linear polariser followed by two automated waveplates, one HWP and one QWP. The HWP functions to rotate the orientation of the linearly polarised light, while the QWP converts the linear polarisation into circular polarisation. In experiments it is desired that the pumping produces the maximum nuclear spin polarisation, observed for maximum (minimum) PL spectral spitting for σ^+ (σ^-). We therefore measure the spectral splitting for different HWP and QWP orientations to find the optimal values for generating polarised light, an example is shown in Fig. 3.6b. We see that for a given HWP angle, rotating the QWP angle changes the measured spectral splitting as the changing helicity of the light alters the nuclear spin polarisation produced. We therefore use a HWP angle of 45° combined with QWP angles of -11° and +37° for σ^+ and σ^- pumping respectively.

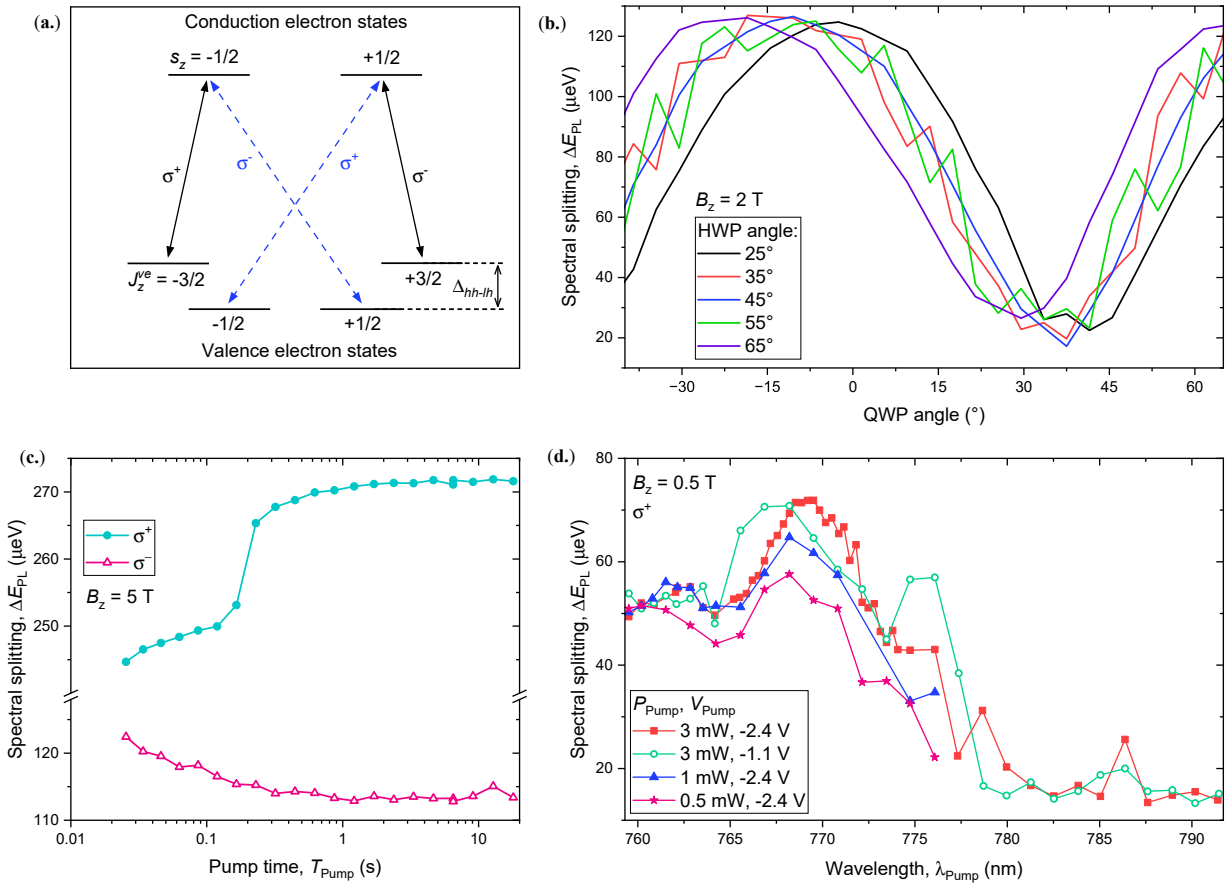


Figure 3.6: (a) Schematic diagram of the QD electron energy levels. By applying circularly polarised light with the right photon energy specific transitions can be driven, allowing repeated generation of spin polarised electrons that can then drive polarisation of the nuclear spin ensemble. This image has been adapted from [103] (b) Results from a HWP and QWP angle calibration measurement, we find optimal HWP angle 45° and QWP angles -11° and +37° for σ^+ and σ^- polarised light respectively. (c) Calibration of the pump time T_{Pump}. We see the shift in the spectral splitting increase as T_{Pump} increases due to the increasing nuclear spin polarisation. Typical values used for the work in this thesis are $T_{\text{Pump}} = 3.5 - 5.5$ s. (d) Wavelength dependence of optical pumping under different pump powers P_{Pump} and gate bias V_{Pump}, we see an increase in the spectral splitting for $\lambda_{\text{Pump}} < 780$ nm where the photons have sufficient energy to excite electrons into the CB, under reduced pump power we see a decrease in the maximum spectral splitting. Additionally altering the bias can be used to alter the electron energy levels which in turn changes the pump wavelength dependence.

As discussed in Section 2.4.1, nuclear spin pumping is a cyclic process. A spin polarised electron is excited into the CB, and then exchanges its spin with a nuclear spin, before optical recombination removes the electron from the CB freeing the dot for the process to repeat. Therefore the pumping must be sufficiently long enough that DNP can be built up. However excessive pumping can be wasteful, as eventually the generation rate of DNP reaches an equilibrium point due to the loss of DNP caused by processes like spin diffusion. Fig. 3.6c shows a measurement of the spectral splitting as the pumping time T_{Pump} is varied. As expected, increasing the duration of the optical pulse increases the change in spectral splitting. This plateaus for times $T_{\text{Pump}} > 1$ s where the rate of generation and decay of DNP equalises. We find that $T_{\text{Pump}} = 3.5 - 5.5$ s is good compromise between generating a high amount of DNP and the experiment time. Also we briefly point out a non-linearity seen in Fig. 3.6c for the σ^+ pumping. This is caused by bistability of the nuclear spin polarisation, which we will discuss in more detail later in this section.

Finally, the photons used in the optical pumping need to have sufficient energy to excite an electron from the VB to the CB meaning the wavelength of the laser needs to be below a certain value for resonant, quasi-resonant or non-resonant pumping of the nuclear spins. An example of measuring the spectral splitting from pumping at different wavelengths is shown in Fig. 3.6d. Focusing on the data measured with a pump power $P_{\text{Pump}} \approx 3$ mW and a bias $V_{\text{Pump}} = -2.4$ V (solid squares) we see for wavelengths $\lambda_{\text{Pump}} > 780$ nm that the spectral splitting is constant, due to the photon energy being below the ground state energy, preventing excitation of electrons and hence the generation of DNP. After a certain wavelength, the spectral splitting begins to increase as the photon energy is sufficient to excite the electron and DNP is generated, sweeping the wavelength allows the optimal wavelength to be found. Additionally shown in Fig. 3.6d are measurements conducted at different pump powers and biases. The results for pump powers $P_{\text{Pump}} \approx 1$ mW (solid triangles) and $P_{\text{Pump}} \approx 0.5$ mW (solid stars) show that lower pump powers generally reduce the maximum achievable DNP as the rate at which electrons can be excited into the CB decreases. Another measurement is shown in Fig. 3.6d which is measured at a different bias of $V_{\text{Pump}} = -1.1$ V, where we see that the trend of generated DNP is different for this case. The relation between the optical pumping and the applied bias is not seen directly, but the application of an electric field alters the electron energy levels, which can have knock on effects to the wavelength needed for excitation and how rapidly the electron can be excited or undergo recombination.

The exact value of the nuclear spin polarisation P_{N} achieved for the work in this thesis was not measured directly. Additionally it is likely to have varied for the various different experimental parameters used throughout this work. However from previous works it is likely that the value was in the range $P_{\text{N}} \approx 0.5 - 0.7$ [70]. As shown in Figs. 3.10 and 3.12 the nuclear spins follow a Boltzmann distribution after optical pumping. This leads to describing the nuclear spin polarisation as a temperature, called the spin temperature T_N [169]. In this description the optical pumping cools

the nuclear spin bath, reducing statistical fluctuations. The spin temperature can be related to P_{N} by the equation [148]:

$$P_{\mathrm{N}} = \frac{1}{2I}\left((2I+1)\coth\left[\left(\mathrm{I}+\frac{1}{2}\right)\beta\right] - \coth\left[\frac{\beta}{2}\right]\right), \tag{3.1}$$

where $I = 3/2$ is the nuclear spin and $\beta = h\nu_L/k_{\mathrm{B}}T_{\mathrm{N}}$ is the dimensionless inverse temperature [139]. We can therefore see from Eq. 3.1 that the temperature is dependent on the magnetic field B_z and the type of nuclei (via ν_L). Therefore across the range of parameters measured in this thesis we put an upper limit on the nuclear spin temperature of $P_{\mathrm{N}}^{^{75}\mathrm{As},\ \mathrm{B_z}\ =\ 8\ \mathrm{T}} \approx 4.16$ mK and $P_{\mathrm{N}}^{^{69}\mathrm{Ga},\ \mathrm{B_z}\ =\ 8\ \mathrm{T}} \approx 5.84$ mK for ^{75}As and ^{69}Ga respectively. The lower limit is hard to predict as the maximum P_{N} achievable decreases at low B_z as will be discussed in Chapter 4. Previously in a study on a similar sample found $P_{\mathrm{N}}^{^{75}\mathrm{As}} \approx 1.3$ mK to be the lowest achievable spin temperature [139]. We therefore conclude that the nuclear spin temperatures generated by optical pumping is on the order of a few mK for the scope of the work in this thesis. Recently large reverse biases combined with high optical power has been demonstrated to overcome the limitation on the optical recombination rate ($\tau \approx 300$ ps), enabling nuclear polarisation values approaching 100 % (corresponding to a spin temperature $T_{\mathrm{N}} = 0$ K) to be achieved [148]. However we do not use such techniques for the work in this thesis.

3.4.2 Optical Probing

As with optical pumping, the optical pulse used to probe the final nuclear spin state also needs to be optimised. First in order to measure the PL spectral splitting accurately (from which the NMR signal is obtained) there needs to be sufficient PL signal. This can be done by increasing the power of the probe pulse. However, it is important to keep the power below the level needed to saturate the dot, as beyond this point the relation between the PL and probe power becomes non-linear, and the resolution of the PL lines decreases. Generally probe powers $P_{\mathrm{Probe}} = 30 - 50\ \mu$W are used, which will have been selected at a level just below saturation. Another important consideration is the duration of the probe pulse T_{Probe}. Much like with pumping, the probe pulse excites electrons into the CB. However these electrons are not spin polarised as the optical excitation is not circularly polarised. Therefore, spin flips between the nuclei and the unpolarised electrons provide a route for the nuclear spin polarisation to decay which can distort or prevent measurement of the nuclear spin state. An example of this is shown in Fig 3.7 where, after pumping with σ^+ (σ^-) light, the spectral splitting is seen to decrease (increase) as T_{Probe} increases, resulting from the loss of DNP due to spin flip-flops with the optically excited electrons. For the work in this thesis typical $T_{\mathrm{Probe}} = 40 - 50$ ms are used which allows for sufficient PL to be collected while only causing a

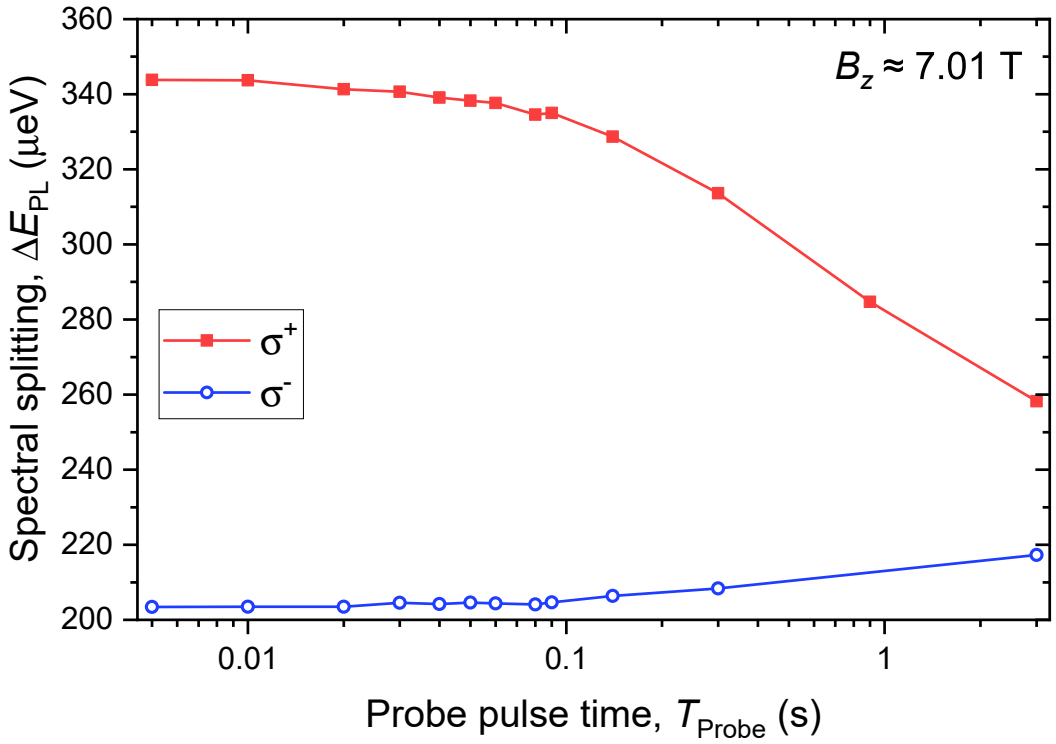


Figure 3.7: Measurement of PL splitting with varying T_{Probe} after pumping with σ^+ (solid squares) and σ^- (open circles) polarised light. As T_{Probe} increases the spectral splitting is observed to decay to its equilibrium value due to spin flip-flops between the nuclei and the optically excited electrons. Typical experimental values are $T_{\text{Probe}} = 40 - 50$ ms.

small loss in DNP.

3.4.3 Nuclear Polarisation Bistability

As discussed, accumulation of nuclear spin polarisation requires spin flip-flops between optically excited electrons and the nuclear spins. Yet the flip-flop rate itself is dependent on the magnetic field the spins experience. For most cases this field will be dominated by the externally applied field B_z. However, the nuclei themselves generate a net magnetic field (Overhauser) that is aligned parallel or antiparallel with B_z and in turn increases or decreases the total field exerted on the electron. The strength of this field increases with the DNP level and it exerts a back action on the electron spin flip-flop rate, and hence the rate of DNP generation. The consequence of this back action is that, for a certain range of magnetic fields and pumping parameters, there can be two stable nuclear spin states for the same experimental parameters which can induce non-linearities in the accumulation or loss of DNP [170–172]. Such an example can be seen in Fig. 3.6c where under σ^+ pumping there is an observed sharp increase in the spectral splitting at around $T_{\text{Pump}} = 200 - 300$ ms, compared to the purely exponential decrease in splitting under σ^- pumping. For the work in this

thesis we avoid these unstable bistability regimes through the selection of the external field as well as the optical and NMR parameters.

3.5 Nuclear Magnetic Resonance

While incident optical excitation allows for the initialisation of the nuclei, through the generation of DNP, and readout of the nuclear spin state through ODNMR, for control of the nuclear spins longer wavelength photons are required to match the smaller energy spacing between the nuclear spin levels. We therefore require RF oscillating magnetic fields to manipulate the nuclei which we achieve using a copper coil as discussed in Section 3.2. However, the coil needs to be fed the correct AC signal to generate the required magnetic fields, which is achieved through a series of waveform generators and other electrical components. In this section we discuss the experimental setup used to generate the oscillating magnetic fields needed for NMR before discussing the implementations of the two different types of NMR used for this work: pulsed NMR, used for precise rotations of nuclear spins, and inverse NMR used for probing the nuclear spin frequencies.

3.5.1 NMR Setup

The two different types of NMR used in this thesis both require different types of RF waveforms. The full setup used to generate these waveforms is shown in Fig. 3.8. Two different systems are used to generate the short, monofrequency RF pulses and broad combs needed for pulsed and inverse NMR respectively. For pulsed NMR an arbitrary waveform generator (Keysight M8190) is used to generate one or more amplitude modulated sine waves. The frequency, amplitude modulation, and duration can be set to allow any of the nuclear spin transitions to be manipulated into any desired orientation on the Bloch sphere. We will discuss the calibration of these pulses in Section 3.5.3. For inverse NMR the waveform instead contains a broad range of frequencies $\Delta f_{\text{Band}} \approx 1500\,\text{kHz}$. The broadband waveform is implemented using a two channel waveform generator (Keysight 33600a). One channel generates a carrier signal containing the broadband frequency components, while the other produces an envelope function used to modulate the amplitude of the waveform. The actual range of frequencies is not full due to the experimental complexities needed to achieve this. Instead many discrete RF modes are generated with small spacing between them $f_{\text{MS}} \approx 125\,\text{Hz}$. This technique, called frequency combs, can approximate a white noise continuum that is sufficient to drive depolarisation of the nuclei as long as f_{MS} is smaller than the homogeneous broadening of the NMR transitions [173]. The two signals are passed through a multiplier which combines them into one signal. The pulsed and broadband setups are then wired into a switching relay, which is separately connected to another control generator. By applying a 10 V modulation using the control

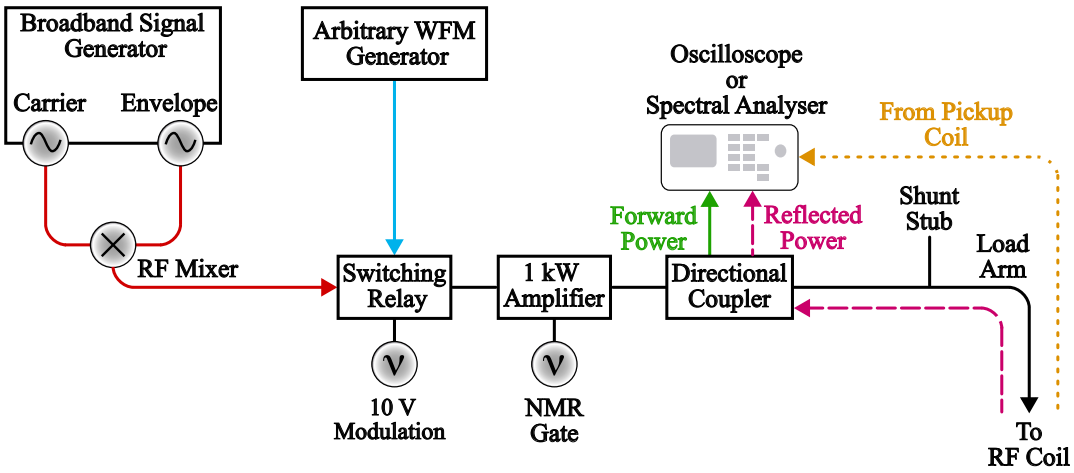


Figure 3.8: Schematic diagram of the experimental setup used to produce RF oscillating magnetic fields required for NMR. An arbitrary waveform generator is used to generate the waveforms needed for pulsed NMR, while a two channel generator is used to create the carrier and envelope signals used for inverse NMR. The carrier and envelope signals are combined by an RF mixer. The output of the two generators is then fed to a switching relay, allowing only one of the signals to be transmitted to the RF coil. A 1 kW amplifier is used to amplify the signal, while a directional coupler connected to an oscilloscope allows analysis of the forward and reflected signal. Finally a shunt stub is added to match the impedance of the coil to the 50 Ω amplifier, minimising reflection. Figure made with aid from [168].

generator the input signal can be switched from the broadband signal to the pulsed signal, ensuring that only one of the signals can be sent to the RF coil at a time.

After the switch a coaxial cable connects the switch output to a 1 kW Tomco pulsed class-AB amplifier, which applies a $\approx$ 60 dB gain to the RF signal. As this gain is constant, the amplitude of the waveforms is controlled through the generators, though for pulsed NMR the amplifier can serve as the ultimate limit on the waveform amplitude due to the amplifier's compression regime which causes non-linearities in the amplification, increasing the risk of damage. The amplified signal is then sent through a directional coupler, which can be connected to either an oscilloscope or spectral analyser to investigate both the waveforms being sent to the RF coil and the reflected signal being sent back to the amplifier output. Monitoring the reflected signal is important as it both measures the amount of input power that is not being converted by the coil into an oscillating magnetic field, and because sufficiently strong reflection signals can cause significant damage to the amplifier. Additionally the amplifier has a gate that allows the input signal to be blocked meaning that transmission is only possible during RF waveform application, preventing noise from being amplified and sent to the sample during dark times or optical stages of the experiments.

Due to the risk caused by reflection at the coil, we desire to match the impedance of the load

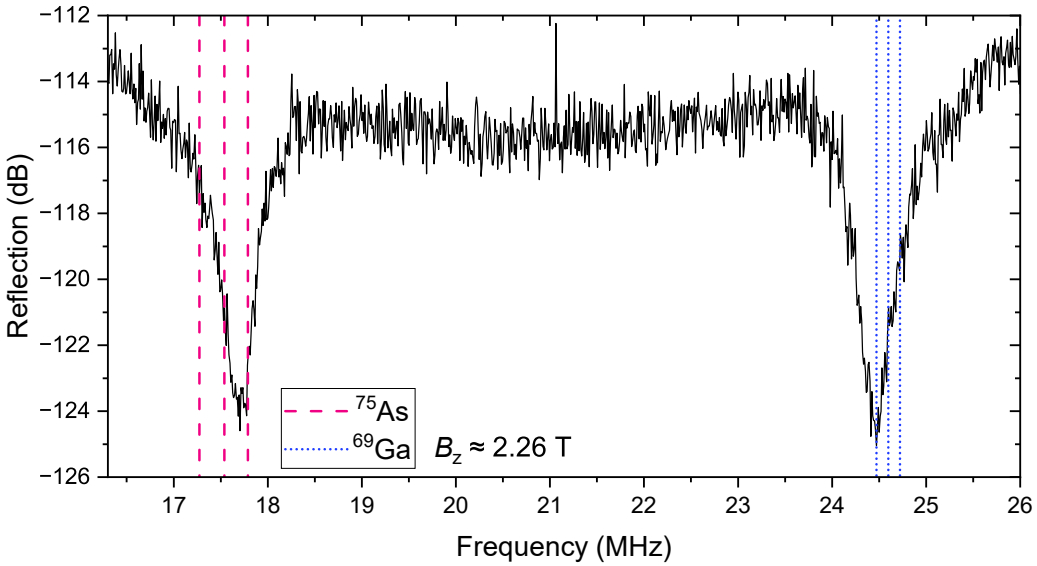


Figure 3.9: Spectra of the time averaged reflected white noise by the RF coil. We observe two dips in the reflection caused by the resonance condition of the connected shunt stub. The frequencies of the NMR transitions of ^{75}As and ^{69}Ga are shown by the dashed and dotted lines respectively. The shunt stub has been selected specifically so that the resonances and NMR frequencies coincide.

(i.e. the coil) to the $Z_0 = 50\ \Omega$ impedance of the amplifier and RF source. To achieve this we add a "shunt stub" cable of varying length along side the (1.5 m + l) BNC cable connecting the coil to the rest of the setup, referred to as the load cable. Here, l is the length of an additional BNC cable added between the shunt stub and the cryostat; while the 1.5 meters corresponds to the length of the cable inside the cryostat. By altering the length of the load (via l) and the stub arms, the impedance can be matched for a desired frequency [174]. The desired frequency is dependent on the external B_z, as the nuclear spin frequencies increase with external fields, with values of up to 80 MHz used for the work in this thesis. Additionally, for certain works we need to be able to address two isotopes simultaneously requiring a carefully selected stub where two specific resonance frequencies are required. Such an example is shown in Fig. 3.9. While the required length of the two arms can be calculated, we typically use an empirical approach. Broadband white noise is sent to the coil and the reflected signal from the directional coupler is sent to a spectral analyser, allowing the reflection of each frequency component to be observed. Looking at Fig. 3.9, we see two clear dips in the reflection signal at frequencies $\approx$ 17.6 MHz and $\approx$ 24.4 MHz, which are two of the resonance conditions for the load and stub configuration used. The dashed and dotted lines show the frequencies of the ^{75}As and ^{69}Ga NMR transitions respectively. We see that in this setup the cascade resonances are aligned with the NMR frequencies. Typically, we aim to align the CT of a given isotope with the cascade though it is beneficial in this case to align instead with the ^{75}As higher ST and the ^{69}Ga lower ST as they were used to perform detuned RF measurements

(see Chapter 5 and 6). Other considerations are the depths and FWHM of the cascade resonances. The resonance depth is important as it describes the reduction in reflection and the increase in absorption by the coil, allowing larger magnetic fields to be generated without risk of damaging any of the components. In Fig. 3.9 the cascades have depth of $\approx$ 10 dB which is typically the minimum values that can be used for pulsed NMR, normally values $\approx$ 20 dB are used. The cascade width needs to be sufficient so that RF pulses can be applied to any of the nuclear spin transitions, which are separated in frequency by the quadrupolar interaction. For inverse NMR the lower powers and long pulses means that a resonance cascade is not strictly necessary. Instead, a broadband cascade can be used which is implemented by changing the length of the wire between the directional coupler and coil. While the strength of reflection will vary over the frequency range, the variation is generally small enough that the applied power is evenly distributed over the frequency range.

With the coil impedance matched the waveform can be effectively transmitted to the RF coil where it is converted into magnetic field B_x. At distance x along the central axis the coil produces a field given by the equation:

$$B_x(x) = \frac{\mu_0}{4\pi} \frac{2\pi n R^2 I}{(x^2 + R^2)^{3/2}}, \tag{3.2}$$

where μ_0 is the permeability of free space, n is the number of turns and R is the coil radius. The values used in this work are given in Section 3.2 from which we estimate a maximum field value of $B_x \approx 50$ mT. As discussed in Section 2.4.2 this oscillating field then drives either specific rotations or depolarises the nuclei depending on the experimental parameters.

3.5.2 Inverse NMR

We have now seen how we can optically polarise and readout the nuclear spins, and we have seen the experimental setup required to perform NMR. We now move on to the first of the NMR measurement types used in this work, called inverse NMR. To understand how inverse NMR works, we first need to discuss standard saturation NMR. During optical pumping with σ^+ (σ^-) polarised light the nuclei are pumped towards the $I_z = -3/2$ ($I_z = +3/2$) state, which leaves the nuclear spin population distribute amongst the four nuclear spin states following the Boltzmann distribution, which is shown in Fig. 3.10a. If a continuous wave (CW) RF magnetic field is applied at a frequency that is in resonance with one of the nuclear spin transition frequencies then the nuclei with be rotated. This is shown in Fig. 3.10b, where the CW RF is in resonance with -3/2↔-1/2 transition. The application of RF couples the $I_z = -3/2, -1/2$ states and, over sufficiently long RF times, equalises the two nuclear spin populations, leading to a loss in nuclear spin polarisation P_N. By sweeping the frequency of the applied RF, the RF can be brought into resonance with the other nuclear spin transitions, measuring the change in P_N optically as the frequency is swept allows

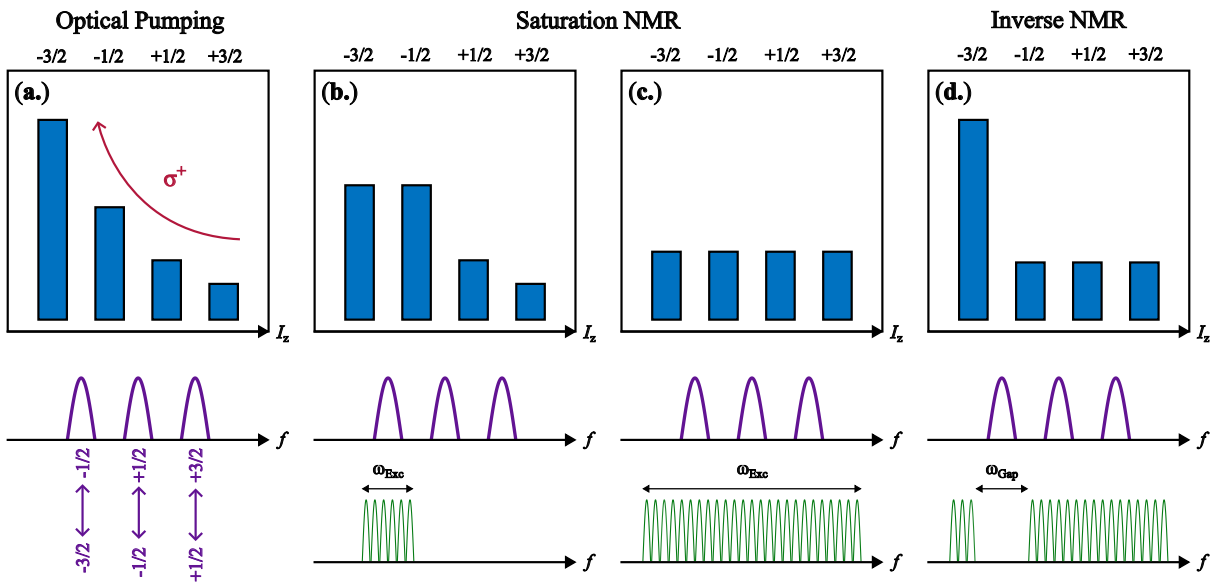


Figure 3.10: (a) Schematic of the populations for the four nuclear spin states after optical pumping with σ^+ polarised light, which pumps the nuclei toward the $I_z = -3/2$ state, leaving the polarised nuclear spin population as a Boltzmann distribution. (b) After optical spin pumping applying a range ω_{Exc} of frequencies to the nuclei can depolarise them as long as ω_{Exc} overlaps with the NMR frequencies. The overall effect causes the populations of states driven by the RF to equalise. (c) If ω_{Exc} is increased so that it overlaps all three nuclear spin transitions the nuclear spin bath becomes fully depolarised, with the populations of all four states returning to thermal equilibrium. (d) The inverse NMR technique involves applying two RF waveforms of width ω_{Exc} separated by a gap of width ω_{Gap}. If the gap is resonant with an NMR transition it will not be depolarised, while the other states do become depolarised, which increases the size of the spin state population change and hence the size of the NMR signal.

the NMR frequencies of the nuclei to be obtained. However, the narrow RF range ω_{Exc} used only alters the populations of two of the states at a time, limiting the signal. The signal can be increased by increasing the population change, which can be achieved if multiple transitions are driven at the same time. Such an example is shown in Fig 3.10c where ω_{Exc} is large enough to cover all three transitions, leading to all four nuclear spin populations being equalised i.e. a fully depolarised state. However in this case the NMR transitions cannot be resolved individually.

In order to improve the NMR signal without losing the ability to resolve the transitions we make use of the inverse NMR method [71]. Rather than a single frequency band of width ω_{Exc} being applied, two frequency bands both of width ω_{Exc} separated in frequency by ω_{Gap} are used instead. This creates a central frequency region where there is no RF while on either side a broad range of frequencies are applied. ω_{Exc} is selected to ensure that for all measured central frequencies the applied RF will overlap all nuclear spin transitions, meaning that in the case where the gap is out of resonance with any of the transitions the RF causes the nuclei to become fully depo-

larised, as in Fig. 3.10c. However, if the gap is moved into resonance with one of the transitions, as seen in Fig. 3.10d where the gap overlaps with the $-3/2 \leftrightarrow -1/2$ transition, the population of the $I_z = -3/2$ state is not coupled to the other three states, while the populations of the $I_z = -1/2,\ +1/2$, and $+3/2$ states become depolarised as their populations equalise. The name 'inverse' comes from the fact that the used waveforms are an inverse of the typical waveforms used in saturation NMR. As three of the state populations are altered by this process, compared to the two altered in saturation NMR, inverse NMR yields an increased signal making it easier to measure the nuclear spin frequencies. The signal is improved at least by a factor of $(I + 1/2)^3$ which, for the spin 3/2 nuclei studied in this work, yields an 8 times increase in the signal [71]. The $(I + 1/2)^3$ term is obtained from the ratio of the change in polarisation caused by inverse and saturation NMR when in resonance with a transition. The dependence on I is due to the fact that inverse NMR depolarises all non-resonant transitions, meaning the number of transitions, and hence I, alters the magnitude of the depolarisation [71]. The gap size ω_{Gap}, much like for saturation NMR, can be increased to improve the signal, as the number of nuclei decoupled from the depolarisation increases. However this again comes at the cost of resolution meaning the gap size must be selected carefully. Measurements are typically performed as differential measurements where the results of an inverse NMR measurement is compared against the result for a broad saturation NMR measurement such as the one in Fig. 3.10c, from which the NMR signal is obtained.

3.5.3 Pulsed NMR

The application of CW NMR drives the depolarisation of the nuclear spins, while this affect can be beneficial for allowing measurements of the nuclear spin transition frequencies, it does not allow for the spins to be controlled, which is critical for developing a working qubit. Control can be implemented using a different type of NMR called pulsed NMR. Applying short, mono-frequency RF bursts can cause the nuclei to be rotated, allowing the orientation of the nuclei on the Bloch sphere to be precisely controlled. For π pulses the rotation causes the populations of two states to be exchanged, as shown in Fig. 3.12d. The field required for this must be applied perpendicular to the static magnetic field B_z, and consists of a sine wave carrier frequency with a modulated amplitude to control the pulse shape. Fig. 3.11a shows an example RF pulse used in experiments. The pulse envelope has a raised cosine shape, with an amplitude rise and fall region of equal duration T_{RiseFall} giving a total pulse duration $T_{\text{RF}} = 2T_{\text{RiseFall}}$. The pulse duration can be set below $2T_{\text{RiseFall}}$ which will reduce the amplitude of the pulse. Due to hardware limitations the minimum pulse duration is $T_{\text{RF}} = 1\ \mu$s, while the pulse can also be increased beyond $2T_{\text{RiseFall}}$ introducing a region of constant amplitude between the rise and fall regions. The frequency of the carrier sine wave can be tuned to any of the three NMR transitions for any of the isotopes present in the QD allowing control

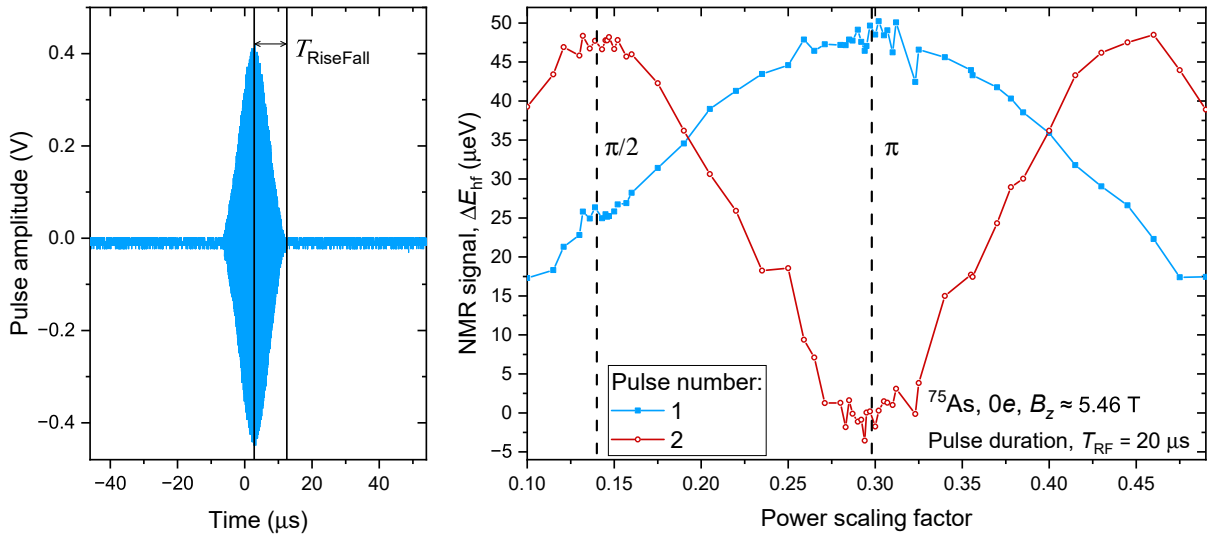


Figure 3.11: (a) Oscilloscope capture of a $T_{RF} = 20\ \mu$s RF pulse. The pulse is set so that the rise and fall regions have time $T_{RiseFall} = 10\ \mu$s, giving the pulse a raised cosine envelope. The zero time has been set arbitrarily on the oscilloscope. Changing the amplitude of the pulse can be used to produce different nuclear spin rotations. (b) Calibration of RF pulse amplitudes. Increasing the pulse amplitude drives Rabi oscillations for a pulse of fixed time $T_{RF} = 20\ \mu$s. From the single pulse measurements (solid squares) we obtain a π pulse amplitude of ≈ 0.295, while from the two pulse measurements (open circles) we find a $\pi/2$ pulse amplitude of ≈ 0.14.

of the full nuclear spin bath, which is made possible by the small inhomogeneous broadening of the NMR transitions due to the low internal sample strain.

The rotation of the nuclei can be controlled by varying different properties of the RF waveform. The axis of rotation in the x-y plane can be controlled by altering the phase ϕ of the carrier sine wave, while the angle of rotation of the nuclear spins can be controlled by two parameters, the pulse duration T_{RF} and the pulse amplitude. T_{RF} must be selected carefully as the rotation speed influences the accuracy of the rotation due to two effects. First, unwanted nuclear spin relaxation is minimised during fast rotations, meaning shorter T_{RF} improves the pulse fidelity. Second, as T_{RF} decreases the spectral range of the pulse increases. In the case of small T_{RF}, the spectral range becomes large enough to cause significant overlap with the other NMR transitions, leading them to be driven as well causing additional nuclear spin relaxation and decoherence. In some cases the increase in the spectral width is desired. As we will discuss in Chapters 5 and 6, the introduction of an electron can cause significant broadening of the NMR transitions meaning the pulses need to be spectrally broader to ensure the nuclei are rotated correctly. Due to the above considerations T_{RF} times are selected based on the needs of the current measurement, with times $T_{RF} \approx 10 - 60\ \mu$s used for the work in this thesis. Instead we control the angle of rotation for a set pulse duration by altering the amplitude of the RF pulse. Fig. 3.11b shows a Rabi oscillation measurement used to calibrate the amplitude of a $T_{RF} = 20\ \mu$s RF pulse. The amplitude is changed using a scaling

factor, which multiplies the maximum 700 mVpp amplitude that the arbitrary waveform generator is capable of. We see in Fig. 3.11b that as the pulse amplitude increases the NMR signal oscillates due to the nuclear spin alignment along the z axis changing. We find that a scaling factor of ≈ 0.295 produces a π rotation of the nuclei. To obtain the scaling factor needed for a $\pi/2$ rotation, we conduct another measurement where two pulses are applied (open circles). Here the nuclear π rotation point (≈ 0.14) now corresponds to the amplitude for a $\pi/2$ rotation, as each pulse rotates the nuclei by $\pi/2$ to produce an overall π rotation.

The waveform generator can generate sequences of pulses that can be sent to the coil as a pulse train. The amplitude, duration and phase can be altered between pulses to produce different rotations. These sequences can be used to implement well know measurements such as free induction decay or a Hahn echo measurement. In Chapter 7 we use RF pulse trains consisting of up to 2400 pulses to attempt to extend the nuclear coherence time $T_{2,N}$. It is also possible to control the time delay between the RF pulses to allow the nuclei to evolve freely between the control pulses. Due to hardware limitations these delays are limited to a minimum time of 0.3 μs, imposing a minimum time on the length of these pulse sequences beyond the minimum pulse duration.

3.5.4 Population Transfer

While we can conduct ODNMR measurements using just control pulses as discussed in Section 3.5.3, the change in the nuclear spin state populations is small which can limit the NMR signal making it difficult to measure. We therefore manipulate the nuclear spin populations before and after the measurement using RF pulses [137, 175]. To understand this consider the case where the nuclei are optically polarised using σ^+ polarised light. This pumps the nuclei towards the $I_z = -3/2$ state leaving the population distributed as a Boltzmann distribution, with $I_z = -3/2$ as the most populated state and the $I_z = +3/2$ state is left the least populated (Fig. 3.12a). Now consider we wish to conduct measurements on the $-3/2 \leftrightarrow -1/2$ transition. The signal can be maximised if we can transfer the $I_z = +3/2$ population to the $I_z = -1/2$ state. This can be achieved by applying RF pulses to produce π rotations of the nuclei which exchanges the populations of two states. Therefore for the given example we first apply a pulse to the $+1/2 \leftrightarrow +3/2$ transition (Fig. 3.12b), leaving $I_z = +1/2$ as the least populated state followed by a pulse on the $-1/2 \leftrightarrow +1/2$ transition (Fig. 3.12c), which finally leaves $I_z = -1/2$ as the least populated state. The measurement can now be conducted and once the control pulses have been applied (Fig. 3.12d) the result can be obtained optically. However, applying additional population transfers can increase the NMR signal. We perform a reverse of the population transfer conducted before the measurement (Fig. 3.12e). A pulse (shown in green in Fig. 3.12e) is first applied to the $-1/2 \leftrightarrow +1/2$ transition to transfer the $I_z = -1/2$ population to the $I_z = +1/2$ state before a second pulse (shown in red

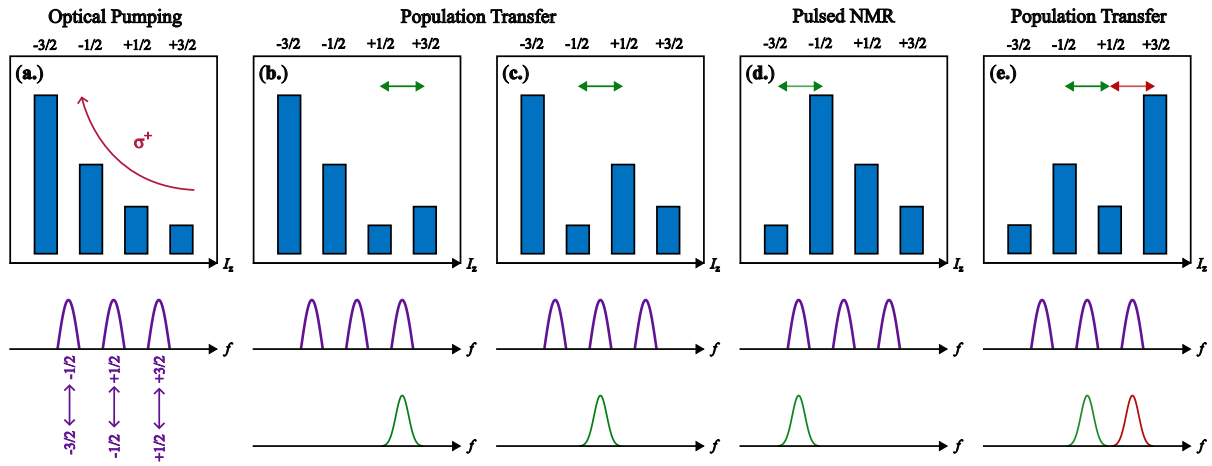


Figure 3.12: (a) Schematic of the populations for the four nuclear spin states after optical pumping with σ^+ polarised light. (b) After optical initialisation the nuclear spin populations are then transferred to maximise the NMR signal. In this example we wish to conduct a measurement on the $-3/2 \leftrightarrow -1/2$ transition. To this end we apply a π RF pulse (green) to the $+1/2 \leftrightarrow +3/2$ transition. This rotates the spins, causing the populations of the states to be exchanged. The $I_z = +1/2$ state is left the least populated. (c) To finish the population transfer a second pulse is applied to the $-1/2 \leftrightarrow +1/2$ transition to exchange their populations. This leaves the $I_z = -1/2$ state the least populated. We now see that by performing population transfer we have maximised the population difference between the $I_z = -3/2,\ -1/2$ states. This in turn maximises the measured ODNMR signal. (d) Next, the pulsed NMR measurement is conducted. For this example the measurement consists of a single π RF pulse to the $-3/2 \leftrightarrow -1/2$ transition, which is the same type of measurement as those conducted in Chapters 5 and 6. $I_z = -1/2$ is now the most populated state while $I_z = -3/2$ is the least populated. (e) Finally the population transfer conducted in (b) and (c) is performed in reverse. A pulse (green) to the $-1/2 \leftrightarrow +1/2$ transition exchanges the $I_z = -1/2,\ +1/2$ states. A second (red) pulse to the $+1/2 \leftrightarrow +3/2$ transition then exchanges the $I_z = +1/2,\ +3/2$ populations, finally leaving $I_z = +3/2$ as the most populated state. The combined effect of the measurement and population transfer is to exchange the $I_z = -3/2,\ +3/2$ states, as the populations of the $I_z = -1/2,\ +1/2$ states are approximately the same in (a) and (e). Therefore the measurement is performed over the $I_z = \pm 3/2$ subspace as opposed to the $I_z = -1/2,\ -3/2$ subspace, yielding an approximate 3 times increase in the observed ODNMR signal.

in Fig. 3.12e) to the $+1/2 \leftrightarrow +3/2$ transition transfers the population back to the $I_z = +3/2$ state. In comparison to the case where no population transfer occurs, where the NMR signal is encoded in the populations of the $I_z = -1/2,\ -3/2$ subspace, the NMR signal after population transfer is now encoded across the full spin 3/2 space which approximately triples the NMR signal. This method is flexible and the order and frequency of the pulses can be altered to optimise the nuclear spin populations for measurements on any of the nuclear spin transitions. This technique is used in all pulsed NMR work conducted in this thesis, which is used in Chapters 5, 6 and 7.

3.5.5 Optically Detected Nuclear Magnetic Resonance

Now that we have discussed the full experimental setup we briefly summarise how the various techniques discussed in this chapter are combined to perform measurements. One method to measure NMR is to use a coil to measure the changing magnetic field produced by the sample. The resulting transmitted current can then be used to measure the NMR signal. However, we instead exploit the optical properties of QDs and perform the NMR measurements optically, a technique termed ODNMR. First in any measurement, the nuclei will need to be initialised away from equilibrium. As discussed this is performed using circularly polarised light, where a few-second pulse is sufficient to build-up DNP for measurements. After this, for CW inverse NMR measurements, the RF comb is applied to depolarise the nuclei. The pulsed NMR case is more complicated. Typically population transfer (termed population transfer initialisation) is first applied to optimise the nuclear spin populations to improve the signal. Then the bias across the sample can be changed to load an arbitrary number of electrons into the QD, something that is important for the measurements in Chapters 5 and 6. After this the control sequence is applied. This is the sequence of RF pulses needed to manipulate the spins for the given measurement. Specific details on these control sequences will be provided in each experimental chapter. Then the bias is reverted back to unload any electrons and population transfer is performed again (population transfer finalisation) leaving the nuclear spins ready for optical readout.

Optical probing by a short optical pulse produces PL that is measured using a CCD camera to produce spectra like the two in Fig. 3.13. The QD PL lines are found to have Gaussian lineshape and the spectral splitting ΔE_{PL} is obtained from fitting the two PL lines with a Gaussian equation and measuring the energy separation between them. Additionally from fitting we obtain a typical linewidth of $\approx$ 14 μeV. The measurement resolution is however $\approx$ 15 μeV (Section 3.3) meaning the linewidths measured are likely to be resolution limited. The PL spectra in Fig. 3.13 were measured over three 40 ms exposures giving a typical count rate in our experiments of 1000-2000 counts/s. The spectral splitting ΔE_{PL} has contributions from the Zeeman splitting $\Delta E_{\mathrm{Zeeman}}$, the fine structure splitting ΔE_{FSS}, and the Overhauser field induced hyperfine splitting ΔE_{hf}. For some excitons $\Delta E_{\mathrm{FSS}} = 0$. This means for experiments such as Fig. 3.6c and Fig. 3.7, where no RF is applied only the spectral splitting can be obtained and direct measurements of the change in the hyperfine splitting cannot be measured. In NMR measurements we are able to directly measure ΔE_{hf} by conducting differential measurements. To do this a measurement is conducted using a waveform with a gap for inverse NMR or with a control sequence for pulsed NMR, before another measurement is performed with a no gap waveform or no control sequence. The resulting spectral splittings are subtracted from one another and as we expect $\Delta E_{\mathrm{Zeeman}}$ and ΔE_{FSS} to remain constant under the same experimental parameters, differences in ΔE_{PL} will be due to changes in the hyperfine shift

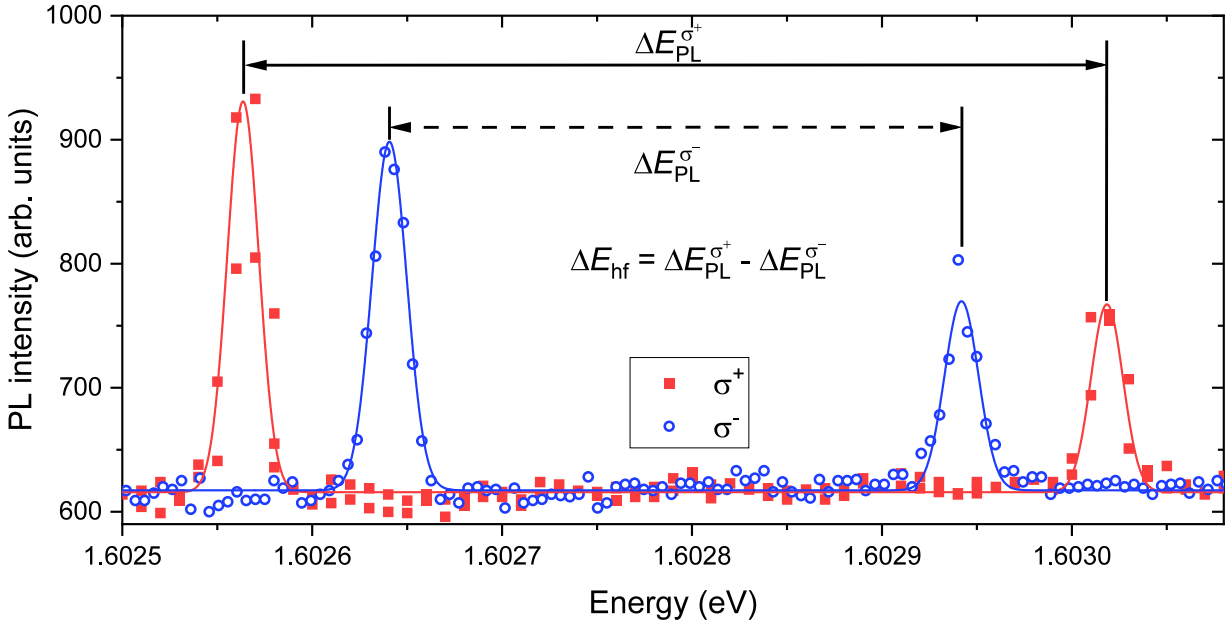


Figure 3.13: PL spectra measured after pumping with σ^+ (solid squares) and σ^- (open circles) polarised light. The solid red (blue) line is a double Gaussian fit of the two σ^+ (σ^-) PL lines, from which E_{PL} is obtained. The spectral splittings $\Delta E_{\mathrm{PL}}^{\sigma^+}$ and $\Delta E_{\mathrm{PL}}^{\sigma^-}$ are obtained from fitting before being subtracted from one another to extract the change in ΔE_{hf} caused by the different pumping parameters. The PL spectra are a combination of three 40 ms exposures with a typical number of counts $\approx$ 100-300 (Varying for different QDs and experimental parameters). The PL lines are Gaussian in shape. From fitting we also obtain typical linewidths of $\approx$ 14 μeV which are likely resolution limited.

ΔE_{hf}. As the only difference between the measurements is the applied RF the measured ΔE_{hf} must be a result of the NMR allowing direct measurements of the nuclear spin state. This is illustrated in Fig. 3.13 where the difference between the two spectral splittings obtained under different optical pumping polarisations can be used to obtain ΔE_{hf}. Commonly multiple measurements are conducted for each experimental parameter and averaged to minimise errors from noise and small fluctuations in the experimental parameters, though in Chapters 5 and 6 the measurements are not averaged.

Chapter 4

Low-field Quadrupolar Effects in Uniaxially Strained GaAs QDs

4.1 Introduction

As we have discussed, realisation of a usable qubit requires a quantum system that can be rapidly and precisely controlled. For a spin ensemble of nuclei in a QD, fast control can be achieved with short RF bursts that are calibrated to produce a desired rotation angle. However, the system is complicated by the quadrupolar interaction, which couples the spin $I = 3/2$ nuclei to the local strain-induced EFG, and the dipole-dipole interaction, which couples the nuclear spin dipoles to one another. The contribution of the dipole-dipole interactions is a broadening of the NMR transitions, caused by inhomogeneity in the nuclear spin induced magnetic field at each lattice site. The quadrupolar interaction is more complicated. First it causes a splitting between the three NMR transitions, and secondly, due to inhomogeneities within the QD volume in the strain environment and hence the EFG, there is a further broadening of the NMR transitions. Both of these effects are problematic for realising precise qubit control. Broadening of the NMR transitions means that pulses need to be spectrally broader to ensure all the nuclei are rotated correctly, so-called 'hard' pulses. Additionally it also means the coherence times of the nuclear spins are reduced. The quadrupolar induced splitting varies for different nuclei, but is typically not large enough that the transitions can be resolved separately from one another. This means that either the pulse spectral width must be increased further to ensure all transitions are driven, or that there will be errors introduced by partial rotations of the other transitions.

To improve the performance of nuclear spin qubits we therefore want to minimise the inhomogeneous broadening of the NMR transitions. In the historically used self-assembled QDs grown via the SK growth mode, such as InGaAs/GaAs, the inhomogeneous strain in the dot is large due to

the lattice mismatch between the two materials, resulting in NMR linewidths on the order of several MHz [71, 173, 176]. In comparison, dots grown by nanohole infilling are lattice-matched and therefore possess much narrower NMR linewidths, while the quadrupolar interaction is still sufficient to suppress nuclear spin flip-flops and achieve $T_{1,N}$ times on the order of self-assembled QDs [117, 124]. Despite GaAs QDs having low inhomogeneous strain they still possess quadrupolar split nuclear spin transitions, with the splitting on the order of 10s of kHz, meaning the transitions are resolvable but they are poorly spectrally isolated. Additionally, as we will see in Chapter 6, this is still significantly smaller than the Knight field broadened NMR transitions, meaning it is impossible to independently address the transitions in the presence of an electron.

To solve the issues of spectrally near NMR transitions we use strain engineering, which is the idea of manipulating a given quantum system to have the desired properties by applying strain to the sample. Such techniques have been demonstrated previously to enable the tuning of ^{75}As donors in Si [177], or of excitons in GaAs/AlGaAs QDs [178, 179]. Here we apply uniaxial compressive stress along the [110] crystallographic axis to increase the separation of the nuclear spin transitions to be on the order of 100s kHz. We then use NMR measurements to probe the strain environment of the QDs, which is a well established method that has been used on these types of samples previously [139, 180, 181]. However, in the previous studies [180, 181] the experiments have been limited to studying only the first-order quadrupolar shift [180] , which limits the strain information obtainable unless the sample is tilted and studied in numerous orientations [181]. Here, due to the large applied uniaxial stress, we are able to extend this technique in this work to enable the measurement of the second-order quadrupolar shift at low external magnetic fields without needing to tilt the sample, enabling the measurement of the S_{44} parameter for GaAs. We are also able to obtain additional measurements of the magnitude and alignment of the applied stress.

4.2 Methods

The main principles of the experimental techniques used in this chapter are laid out in Chapter 3. Here, we instead focus on the specific parameters used in the measurements as well as their structure. Probing of the nuclear spin energy levels is conducted using inverse NMR [71], with the nuclear spin polarisation being measured using ODNMR. Fig. 4.1 shows the timing diagram for the inverse NMR measurements. Each measurement cycle is composed of effectively three steps: generation of DNP using a long optical pump, depolarisation of nuclei by applied RF magnetic field and finally probing of the remaining DNP by a short optical probe.

The first step, optical generation of DNP, is achieved following the mechanism laid out in Section 2.4.1, which we will briefly summarise here. Optical pumping is a three step process, first a spin polarised electron is generated using circularly polarised light. The electron then exchanges

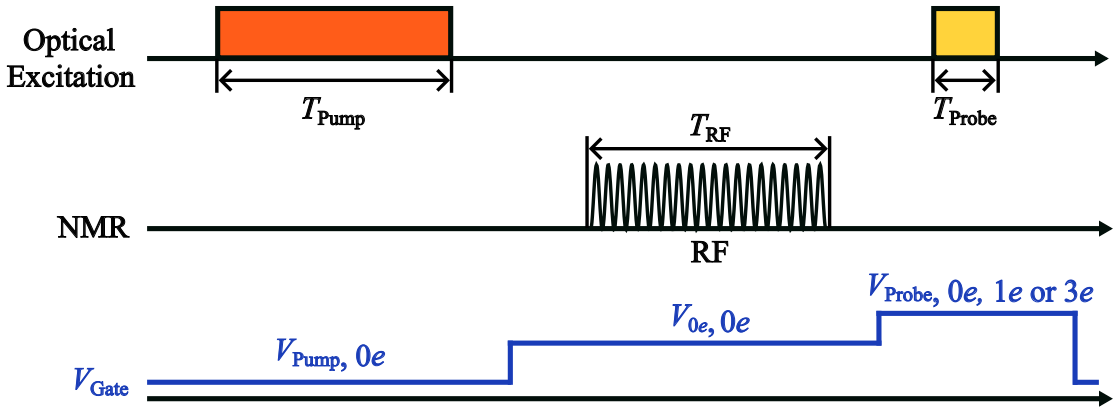


Figure 4.1: Timing diagram for the inverse NMR measurements. First the nuclear spins are optically pumped using circularly polarised photons, generating nuclear spin polarisation of $\approx$ 60 %. The optical pump has a duration T_{Pump} = 5.5 s. After, a RF magnetic field comb is applied to drive depolarisation of the nuclear spins, with duration T_{RF}. Finally the remaining nuclear spin polarisation is probed by a short T_{Probe} = 40 ms optical probe. During the measurement cycle the sample bias is varied to ensure the dot is empty during pumping and NMR, and to generate the desired exciton for optical probing. This can mean the QD is empty or occupied with one or three electrons.

its spin with a nuclear spin via the hyperfine interaction. Finally the electron undergoes optical recombination, freeing the QD for another polarised electron to be generated. This process then repeats allowing nuclear spin polarisations of $\approx$ 60% to be generated. The time duration of the optical pumping is set to be T_{Pump} = 5.5 s, while a bias of V_{Pump} = -2.4 V is applied to the sample to ensure the QD is unoccupied.

Next a broad RF comb magnetic field is applied to depolarise the nuclei, which occurs when the comb overlaps with a given nuclear spin transition. We perform differential measurements between measurements using RF combs with and without a gap. There are four main parameters. First is the RF amplitude which is chosen to be the maximum possible without causing any significant heating or sparking with the resulting spectral density being constant. The amplitude is therefore dependent on the RF cascade (see Section 3.5.3), which can either be narrow or broadband. Next is the RF time, T_{RF}. The duration of the RF comb is calibrated to maximise the NMR signal in the shortest time possible. The calibration is determined by measuring the change in the NMR signal as T_{RF} is increased, as shown in Fig. 4.2a. Here, we see that as T_{RF} increases there is a decrease in the NMR signal, caused by a reduction in the Overhauser shift as the nuclei are depolarised. The decrease is greater in the no gap case as the full spin $I = \frac{3}{2}$ space is depolarised. We are mainly interested in maximising the difference between gap and no gap measurements, as this is the limit on the inverse NMR signal. Fig. 4.2b shows the difference between the two measurements from which we obtain T_{RF} = 231 ms as the optimal value for use in experiments. Finally, both the RF

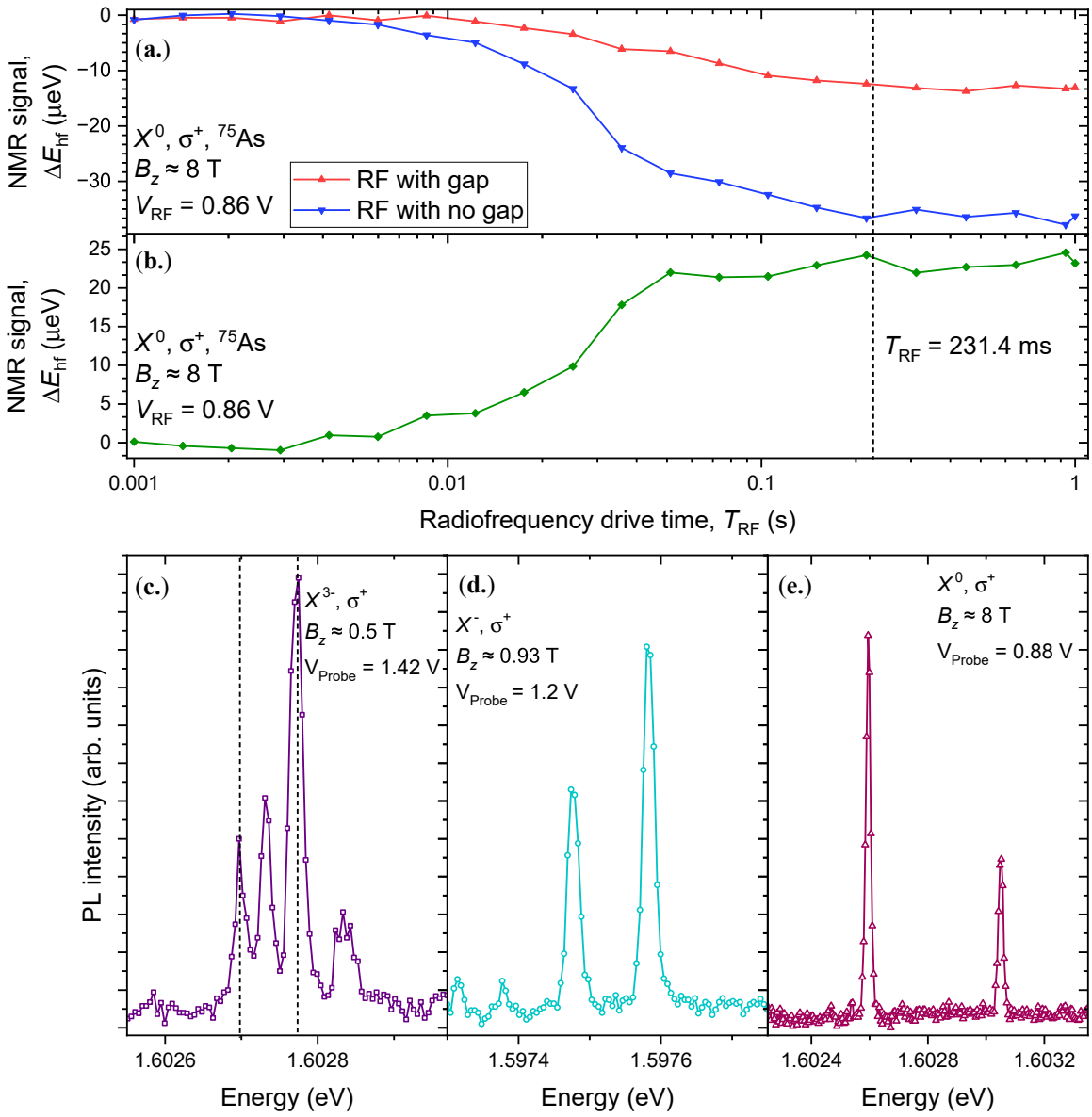


Figure 4.2: (a) Example T_{RF} calibration conducted at B_z = 8 T on ^{75}As, using σ^+ optical pumping. Measurements are conducted using RF combs both with a gap (red, triangles) and no gap (blue, inverted triangles). As T_{RF} increases the NMR signal decreases as the nuclei are depolarised. As the central transition lies within the gap, the depolarisation is faster for the no gap case. (b) Same as (a) but this time the difference between the gap and no gap measurements is plotted against T_{RF}. Here, we see that maximum signal can be obtained using T_{RF} = 231.4 ms. (c) Example PL spectra for the X^{3-} exciton measured at B_z = 0.5 T under σ^+ optical pumping, which maximises the spectral splitting. The dashed lines are used to identify the two PL lines used for ODNMR (d) Same as (c) but instead measured on the X^- exciton at B_z = 0.93 T. (e) Same as (c) but instead measured on the X^0 exciton at B_z = 8 T.

gap width and RF comb width must be considered. The comb width is generally chosen to be wide enough to cover all three NMR transitions at all comb central frequencies, giving a minimum full width of at least 1100 kHz, though typically widths of 1300-1500 kHz are used. At low fields the separation between the transitions of different isotopes becomes small meaning the comb can overlap with multiple isotopes, which can cause issues with the measurement if a new transition starts being depolarised at the same time as the gap is overlapping another. At low fields this is managed by setting the comb width so that this does not occur, ensuring the signal is accurate. Therefore we reach RF comb widths of down to 600 kHz for some measurements. The gap size is chosen to be as small as possible to maximise the resolution of the measurement. This is often a compromise however with the need to collect sufficient signal. Typical gap widths are 2 kHz on the CT and 5 kHz on the broader STs. Though, at low external fields, broader gaps of up to 15 kHz were needed due to a loss of achievable maximum nuclear polarisation. During RF excitation the bias is set to V_{0e} = -1.3 V to ensure the dot remains empty.

Once the depolarising RF has been applied a final short optical pulse is used to probe the remaining nuclear polarisation. The emitted PL is used to measure the change in the Overhauser shift via changes in the spectral splitting, from which the NMR signal is obtained. The exciton used for readout is varied for different external fields B_z to maximise the sensitivity of the readout to the Overhauser shift. The neutral exciton X^0 is used for fields above 1 T. Between 1 T and 0.5 T the negative exciton X^- is used. Finally, for fields of 0.5 T and below, the X^- PL spectral splitting becomes unresolvable and the X^{3-} exciton is used instead. Example PL from the three excitons is shown in Fig. 4.2c, d and e. During optical probing V_{Gate} is selected to ensure generation of the correct exciton, and to maximise the PL signal. The probe duration is set to be T_{Probe} = 40 ms, maximising signal without causing a significant loss of DNP.

4.3 NMR on GaAs

First, we introduce the nuclear spin system of GaAs QDs. GaAs/AlGaAs QDs are comprised of four different nuclei. The two most abundant are ^{75}As and ^{69}Ga which are the primary focus of this study. Also present is ^{71}Ga, making up around 40% of all Ga nuclei in the QD. Despite being relatively abundant we only discuss it here for completeness as it has similar quadrupolar properties to ^{69}Ga. The final isotope is ^{27}Al, which can be incorporated into the dot during growth due to substitution. The substitution of Ga for Al is an important affect as it can increase the magnitude of the inhomogeneous strain. Unfortunately, due to the very small amounts present, it is currently not possible to measure the spins of ^{27}Al nuclei in the studied QDs and we therefore do not discuss them further.

Fig. 4.3a, b and c show NMR spectra conducted on ^{75}As, ^{69}Ga and ^{71}Ga respectively. There

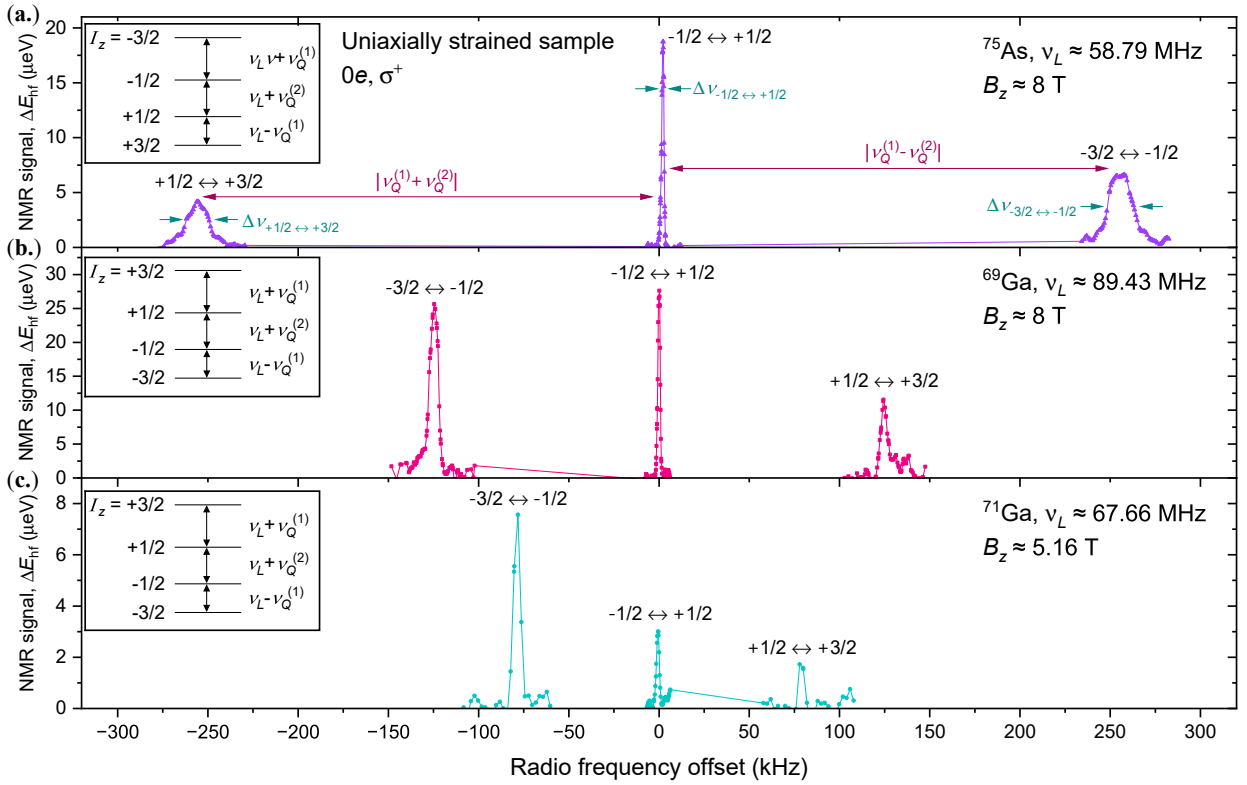


Figure 4.3: (a) NMR spectrum of the ^{75}As nuclei in an uncharged ($0e$) QD measured at external field $B_z \approx 8$ T. The inset shows the energy level diagram for the spin $I = 3/2$ nuclei. We observe the CT between the -1/2↔+1/2 spin states with a frequency $\nu_{-1/2\leftrightarrow+1/2} \approx 58.79$ MHz, which is a combination of the Larmor frequency ν_L and a small shift caused by the second order quadrupolar interaction $\nu_Q^{(2)} \approx 2.13$ kHz. The other two transitions experience a first order quadrupolar effect, splitting them by $\pm\nu_Q^{(1)} \approx \pm 255.6$ kHz, which is dominated by the applied uniaxial stress. The data has been centred on $\nu_{-1/2\leftrightarrow+1/2}$. All three transitions are broadened by inhomogeneous strain, we find FWHMs $\Delta\nu_{-1/2\leftrightarrow+1/2} < 2$ kHz (resolution limited) and $\Delta\nu_{-3/2\leftrightarrow-1/2} \approx \Delta\nu_{+1/2\leftrightarrow+3/2} \approx 13.8$ kHz. The STs experience greater broadening as they are sensitive to first order quadrupolar effects. (b) Same as (a) but measured on ^{69}Ga. We find $\nu_{-1/2\leftrightarrow+1/2} \approx 89.43$ MHz with second order shift $\nu_Q^{(2)} \approx 0$ kHz. The first order quadrupolar splitting is found to be $\pm\nu_Q^{(1)} \approx \pm 124.8$ kHz. The measured FWHMs are $\Delta\nu_{-1/2\leftrightarrow+1/2} < 2$ kHz (resolution limited) and $\Delta\nu_{-3/2\leftrightarrow-1/2} \approx \Delta\nu_{+1/2\leftrightarrow+3/2} \approx 5.30$ kHz. (c) Same as (a) but measured on ^{71}Ga at $B_z \approx 5.16$ T . We find $\nu_{-1/2\leftrightarrow+1/2} \approx 67.66$ MHz with second order shift $\nu_Q^{(2)} \approx 0.6$ kHz. The first order quadrupolar splitting is found to be $\pm\nu_Q^{(1)} \approx \pm 78.8$ kHz.

are some general features shared between all three nuclei. First, all three nuclear isotopes are spin $I = 3/2$ particles and therefore in the presence of an external magnetic field B_z the four nuclear spin states are separated in energy by $\Delta E_{\text{Zeeman}} = h\nu_L$, where h is the Plank constant and and ν_L is the Larmor frequency. Then, as discussed in Section 2.3.2, the quadrupolar interaction acts as a perturbation on the Zeeman interaction, separating the transition frequencies via two effects. The first is the STs (-3/2↔-1/2 and +1/2↔+3/2) become split by the first order quadrupolar interaction $\nu_Q^{(1)}$, leaving the three transitions equally spaced in frequency. Second, the CT (-1/2↔+1/2) is shifted by the second order term $\nu_Q^{(2)}$, which increases in magnitude as the external field B_z decreases (for the external fields used in Fig. 4.3 the second order shift is on the order of 1 kHz). Therefore in all three spectra we observe three transitions separated in frequency by $\nu_Q^{(1)}$ with some small contribution from $\nu_Q^{(2)}$. At low fields the value of $\nu_Q^{(2)}$ will increase to the point where the transitions are visibly not equidistantly separated in frequency, as we will see in Section 4.5.

There are several noticeable differences between the three spectra in Fig. 4.3. We see that the magnitude for $\nu_Q^{(1)}$ differs for the three nuclei. From fitting the data we measure $\nu_Q^{(1),^{75}\text{As}} \approx 255.6$ kHz, $\nu_Q^{(1),^{69}\text{Ga}} \approx 124.8$ kHz and $\nu_Q^{(1),^{71}\text{Ga}} \approx 78.8$ kHz. We attribute these differences in the measured $\nu_Q^{(1)}$ values to the different quadrupolar moments Q of the three nuclei, which have been measured previously and are found to be $Q^{^{75}\text{As}}S_{11}^{^{75}\text{As}} \approx 0.758 \times 10^{-6}$ V and $Q^{^{69}\text{Ga}}S_{11}^{^{69}\text{Ga}} \approx -0.377 \times 10^{-6}$ V [180]. Here, as we will prove in Section 4.4 [117, 180], we observe that $\nu_Q^{(1)}$ is proportional to $S_{11}Q$ where S_{11} is a component of the tensor describing the coupling between the EFG and the strain. The value of $Q^{^{69}\text{Ga}}S_{11}^{^{69}\text{Ga}}$ is approximately half the value of $Q^{^{75}\text{As}}S_{11}^{^{75}\text{As}}$ and we see a similar decrease in the respective $\nu_Q^{(1)}$ values. We therefore also expect $Q^{^{71}\text{Ga}}S_{11}^{^{71}\text{Ga}} < Q^{^{69}\text{Ga}}S_{11}^{^{69}\text{Ga}}$ as $\nu_Q^{(1),^{71}\text{Ga}}$ is smaller than $\nu_Q^{(1),^{69}\text{Ga}}$. Next we consider the inhomogeneous strain which can be inferred from the FWHM of the NMR transitions. All of the CTs measured here have FWHM $\Delta\nu_{-1/2\leftrightarrow+1/2} < 2$ kHz [175]. We are currently unable to measure the actual values using inverse NMR due to limitations in the measurement resolution (2 kHz). For ^{75}As the STs are found to have a linewidth $\Delta\nu_{-3/2\leftrightarrow-1/2}^{^{75}\text{As}} \approx \Delta\nu_{+1/2\leftrightarrow+3/2}^{^{75}\text{As}} \approx 13.8$ kHz. The reason for the increased broadening on the STs is due to the first-order quadrupolar shift, which does not effect the CT. Comparatively, for ^{69}Ga the STs are found to have linewidth $\Delta\nu_{-3/2\leftrightarrow-1/2}^{^{69}\text{Ga}} \approx \Delta\nu_{+1/2\leftrightarrow+3/2}^{^{69}\text{Ga}} \approx 5.3$ kHz. The smaller broadening of the ^{69}Ga transitions is again due to $Q^{^{69}\text{Ga}}S_{11}^{^{69}\text{Ga}} < Q^{^{75}\text{As}}S_{11}^{^{75}\text{As}}$, meaning the ^{69}Ga nuclei are less sensitive to the inhomogeneous strain. In either case the measured linewidths are smaller than the values measured for self-assembled QDs ($\approx$ 1 MHz) [71, 173, 176], highlighting the reduced internal strain of the sample grown from lattice-matched materials.

Finally we note an asymmetry in the relative amplitudes of the transitions between ^{75}As and the Ga nuclei. Considering that the nuclear spin pumping is spin conserving and that all of the measurements in Fig. 4.3 are conducted using σ^+ polarised optical pumping, we know that the spins

must be pumped towards the $I_z = -3/2$ spin state. We therefore expect the -3/2↔-1/2 transition to have the largest amplitude of the STs. Knowing this, and looking at the amplitudes of the STs in Fig. 4.3, we conclude that the sign of $\nu_Q^{(1)}$ is different for ^{75}As and Ga, also seen in the above quoted $S_{11}Q$ values. As the value of Q is positive for all three nuclei, the reason for the sign change must be caused by the coupling term S_{11} which has a different sign for the two nuclear species, specifically $S_{11}^{^{75}\mathrm{As}} > 0$, while $S_{11}^{^{71}\mathrm{Ga}} < 0$ and $S_{11}^{^{71}\mathrm{Ga}} < 0$, as has been reported before [180].

4.4 Derivation of Strain

In Section 2.3.2 we discussed the Hamiltonian describing the interaction between a given nuclear spin and the strain induced EFG. There, we assumed that the strain was axially symmetric and only consider the influence of the angle θ, describing the angle between the growth direction z and the principal axis of the EFG z', on the strength of the quadrupolar interaction. While this is sufficient to obtain an energy level diagram showing the four nuclear spin states shifted in energy by the first and second order quadrupolar terms, we require a different definition in order to analyse the individual EFG components acting on the spins. For completeness we rewrite the Hamiltonian for the quadrupolar interaction independent of the Cartesian coordinate frame [182]:

$$H_Q = \frac{eQ}{6\hbar I(2I-1)} \sum_{\alpha,\beta=x,y,z} V_{\alpha\beta} \left[\frac{3}{2}(\hat{I}_\alpha \hat{I}_\beta + \hat{I}_\beta \hat{I}_\alpha) - \delta_{\alpha\beta} I(I+1) \right], \tag{4.1}$$

where $V_{\alpha\beta} = \frac{\delta^2 U}{\delta\alpha\delta\beta}\Big|_{r=0}$ are the Cartesian components of the EFG at the nucleus with U being the electrostatic potential at the nucleus and $\delta_{\alpha\beta}$ is the Kronecker delta symbol. $V_{\alpha\beta}$ is a second-rank symmetrical tensor. Again we consider H_Q to be a perturbation on the Zeeman splitting caused by the externally applied magnetic field B_z. The Zeeman splitting is described by the Hamiltonian $H_Z = -\omega_L \hat{I}_z$ where ω_L is the Larmor frequency expressed as an angular frequency $\omega_L = 2\pi\nu_L$. The most convenient way to obtain the first and second order perturbation terms for the quadrupolar interaction is to consider the system in the rotating frame, meaning the frame is rotating compared to the static laboratory frame with a frequency ω_L [182]. The quadrupolar interaction then becomes:

$$H_Q(t) = e^{iH_Z t} H_Q e^{-iH_Z t}. \tag{4.2}$$

This causes the quadrupolar interaction to become time dependent, though the terms that commute with $\hat{I}_z$ remain static. To remove the time dependence we then average $H_Q(t)$ over one Larmor

period $\frac{2\pi}{\omega_L}$ up to first order using the Magnus expansion, which is given by:

$$\langle H_Q(t)\rangle = \frac{\omega_L}{2\pi}\int_0^{\frac{2\pi}{\omega_L}} H_Q(t)dt - \frac{i\omega_L}{4\pi}\int_0^{\frac{2\pi}{\omega_L}}\int_0^t [H_Q(t), H_Q(t')]dt'dt = H_Q^{(0)} + H_Q^{(1)} \tag{4.3}$$

where $H_Q^{(1)}$ and $H_Q^{(2)}$ are the first and second order terms of the quadrupolar interaction respectively (with the Zeeman Hamiltonian being the zeroth order term). Substituting Eq. 4.1 into Eq. 4.3 and solving for a spin $I = \frac{3}{2}$ particle we obtain the 4×4 matrix:

$$H_Q^{(0)} + H_Q^{(1)} =$$

$$\begin{pmatrix} -\frac{eQ(V_{xx}+V_{yy}-2V_{zz})}{12\hbar} & 0 & 0 & 0 \\ 0 & +\frac{eQ(V_{xx}+V_{yy}-2V_{zz})}{12\hbar} & 0 & 0 \\ 0 & 0 & +\frac{eQ(V_{xx}+V_{yy}-2V_{zz})}{12\hbar} & 0 \\ 0 & 0 & 0 & -\frac{eQ(V_{xx}+V_{yy}-2V_{zz})}{12\hbar} \end{pmatrix} +$$

$$\begin{pmatrix} -\frac{(eQ)^2(4V_{xy}^2+(V_{xx}-V_{yy})^2+8(V_{xz}^2+V_{yz}^2))}{96\omega_L\hbar^2} & -\frac{i(eQ)^2(iV_{xz}+V_{yz})(V_{xx}+V_{yy}-2V_{zz})}{12\sqrt{3}\omega_L\hbar^2} \\ +\frac{(eQ)^2(V_{xz}+iV_{yz})(V_{xx}+V_{yy}-2V_{zz})}{12\sqrt{3}\omega_L\hbar^2} & -\frac{(eQ)^2(4V_{xy}^2+(V_{xx}-V_{yy})^2-8(V_{xz}^2+V_{yz}^2))}{96\omega_L\hbar^2} \\ +\frac{(eQ)^2(V_{xx}+2iV_{xy}-V_{yy})(V_{xx}+V_{yy}-2V_{zz})}{48\sqrt{3}\omega_L\hbar^2} & 0 \\ 0 & -\frac{(eQ)^2(V_{xx}+2iV_{xy}-V_{yy})(V_{xx}+V_{yy}-2V_{zz})}{48\sqrt{3}\omega_L\hbar^2} \\ +\frac{(eQ)^2(V_{xx}-2iV_{xy}-V_{yy})(V_{xx}+V_{yy}-2V_{zz})}{48\sqrt{3}\omega_L\hbar^2} & 0 \\ 0 & -\frac{(eQ)^2(V_{xx}-2iV_{xy}-V_{yy})(V_{xx}+V_{yy}-2V_{zz})}{48\sqrt{3}\omega_L\hbar^2} \\ +\frac{(eQ)^2(4V_{xy}^2+(V_{xx}-V_{yy})^2-8(V_{xz}^2+V_{yz}^2))}{96\omega_L\hbar^2} & -\frac{i(eQ)^2(iV_{xz}+V_{yz})(V_{xx}+V_{yy}-2V_{zz})}{12\sqrt{3}\omega_L\hbar^2} \\ +\frac{(eQ)^2(V_{xz}+iV_{yz})(V_{xx}+V_{yy}-2V_{zz})}{12\sqrt{3}\omega_L\hbar^2} & +\frac{(eQ)^2(4V_{xy}^2+(V_{xx}-V_{yy})^2+8(V_{xz}^2+V_{yz}^2))}{96\omega_L\hbar^2} \end{pmatrix} \tag{4.4}$$

As H_Q is being treated as a perturbation of H_Z, we can ignore the non-diagonal terms that do not commute with $\hat{I}_z$ [182, 183], which then diagonalises the second matrix. This additionally means the equations are unaffected when we convert back from the rotating frame to the laboratory frame. The Hamiltonian for the full system is given by:

$$H = H_Z + H_Q = H_Z + H_Q^{(1)} + H_Q^{(2)} \tag{4.5}$$

Where $H_Q^{(1)}$ and $H_Q^{(2)}$ are the first and second order perturbation terms on H_Z. We can then obtain the frequencies for the four nuclear spin states:

$$\begin{aligned}
\omega_{I_z=+3/2} &= \frac{3}{2}\omega_L - \frac{eQ}{12\hbar}(V_{xx}+V_{yy}-2V_{zz}) - \frac{(eQ)^2}{96\omega_L\hbar^2}(4V_{xy}^2+(V_{xx}-V_{yy})^2+8(V_{xz}^2+V_{yz}^2)) \\
\omega_{I_z=+1/2} &= \frac{1}{2}\omega_L + \frac{eQ}{12\hbar}(V_{xx}+V_{yy}-2V_{zz}) - \frac{(eQ)^2}{96\omega_L\hbar^2}(4V_{xy}^2+(V_{xx}-V_{yy})^2-8(V_{xz}^2+V_{yz}^2)) \\
\omega_{I_z=-1/2} &= -\frac{1}{2}\omega_L + \frac{eQ}{12\hbar}(V_{xx}+V_{yy}-2V_{zz}) + \frac{(eQ)^2}{96\omega_L\hbar^2}(4V_{xy}^2+(V_{xx}-V_{yy})^2-8(V_{xz}^2+V_{yz}^2)) \\
\omega_{I_z=-3/2} &= -\frac{3}{2}\omega_L - \frac{eQ}{12\hbar}(V_{xx}+V_{yy}-2V_{zz}) + \frac{(eQ)^2}{96\omega_L\hbar^2}(4V_{xy}^2+(V_{xx}-V_{yy})^2+8(V_{xz}^2+V_{yz}^2)).
\end{aligned} \tag{4.6}$$

Finally, taking the differences between the four states we obtain terms describing the frequency of the three NMR transitions as seen in Fig. 4.3:

$$\begin{aligned}
\nu_{+1/2\leftrightarrow+3/2} &= \nu_L - \frac{eQ}{6h}(V_{xx}+V_{yy}-2V_{zz}) - \frac{(eQ)^2}{6\nu_L h^2}(V_{xz}^2+V_{yz}^2) \\
\nu_{-1/2\leftrightarrow+1/2} &= \nu_L - \frac{(eQ)^2}{48\nu_L h^2}(4V_{xy}^2+(V_{xx}-V_{yy})^2-8(V_{xz}^2+V_{yz}^2)) \\
\nu_{-3/2\leftrightarrow-1/2} &= \nu_L + \frac{eQ}{6h}(V_{xx}+V_{yy}-2V_{zz}) - \frac{(eQ)^2}{6\nu_L h^2}(V_{xz}^2+V_{yz}^2),
\end{aligned} \tag{4.7}$$

where we have converted all angular frequencies ω to non-angular frequencies ν, which remains consistent if we also replace $\hbar$ with h. Eqs. 4.7 is written in the form $H_z + H_Q^{(1)} + H_Q^{(2)}$. We confirm that only the STs are sensitive to $H_Q^{(1)}$ and that all three transitions experience a second order shift. All three transitions experience a second order shift term that is dependent on V_{xz} and V_{yz}, with the sign for this term being different for the CT and the two STs. The CT second order shift also has a second term, dependent on V_{xy}, V_{xx} and V_{yy}. We also confirm that the first order shift is independent of the external magnetic field, while the second order terms are inversely dependent on B_z through ν_L.

We now have a mathematical description for the results seen in experiments, but they are currently expressed in terms of the EFG components. It is more practical to express Eqs. 4.7 in terms of strain ε_{kl}. We have shown the relation between the EFG and the applied strain already in Section 2.3.2 where it is given by Eq. 2.26. The strength of the coupling between the EFG and the strain is described by a rank four tensor S_{ijkl}, which possesses 81 individual components. However, due to the high symmetry of the crystal lattice structure many of these components are not independent. For a zincblende structure, combined with additional symmetry arising from V_{ij} and ε_{kl} both being symmetric, S_{ijkl} actually only has 21 non-zero components defined by three terms S_{xxxx}, S_{xxyy} and S_{yzyz}, allowing V_{ij} to be written in terms of the components of S_{ijkl} and ε_{kl} [180].

Substituting these terms into Eqs. 4.7 we obtain:

$$\begin{aligned}
\nu_{+1/2\leftrightarrow+3/2} &= \nu_L - \frac{eQ}{2h}S_{11}\varepsilon_b + \frac{2}{3\nu_L}\left(\frac{eQ}{h}\right)^2 S_{44}^2(\varepsilon_{xz}^2+\varepsilon_{yz}^2) \\
\nu_{-1/2\leftrightarrow+1/2} &= \nu_L + \frac{1}{192\nu_L}\left(\frac{eQ}{h}\right)^2 (9S_{11}^2(\varepsilon_{xx}-\varepsilon_{yy})^2 + 64S_{44}^2(\varepsilon_{xy}^2 - 2(\varepsilon_{xz}^2+\varepsilon_{yz}^2)) \\
\nu_{-3/2\leftrightarrow-1/2} &= \nu_L + \frac{eQ}{2h}S_{11}\varepsilon_b + \frac{2}{3\nu_L}\left(\frac{eQ}{h}\right)^2 S_{44}^2(\varepsilon_{xz}^2+\varepsilon_{yz}^2),
\end{aligned} \tag{4.8}$$

where we have used the common convention $S_{xxyy} = -S_{xxxx}/2$ [184] and the definitions $S_{11} = S_{xxxx}$ and $S_{44} = S_{yzyz}$ from Voigt notation. Finally, we have substituted $\varepsilon_b = \varepsilon_{zz} - (\varepsilon_{xx}+\varepsilon_{yy})/2$, where ε_b is the biaxial component of the strain.

From Eqs. 4.8 we can see how different components of strain affects the measured NMR spectra. First, we note that the NMR is insensitive to hydrostatic strain $\varepsilon_h = \varepsilon_{xx}+\varepsilon_{yy}+\varepsilon_{zz} = 0$ [180]. The first order splitting is seen to be dependent only on S_{11} and the biaxial strain ε_b. The second order shifts are however more complicated. We observe that all transitions are dependent on S_{44} and the sum of the shear strain components out of the x-y plane. The CT then has additional terms. First, there is a term dependent on S_{11} and the two strain components in the x-y plane along the two crystallographic axes, which we will refer to as the deviatoric strain $\varepsilon_\eta = \varepsilon_{xx}-\varepsilon_{yy}$. Second there is a term dependent on S_{44} and the shear strain in the x-y-plane. As we are limited to measuring only the values of $\nu_{+1/2\leftrightarrow+3/2}$, $\nu_{-1/2\leftrightarrow+1/2}$ and $\nu_{-1/2\leftrightarrow-3/2}$ we are unable to obtain a measured value of ν_L. We are therefore limited in what information we can extract from the NMR spectra. However there is information that we can obtain by measuring the separation between the three transitions. First, we can measure the separation between the two STs:

$$\nu_Q^{(1)} = \frac{\nu_{+1/2\leftrightarrow+3/2} - \nu_{-3/2\leftrightarrow-1/2}}{2} = -\frac{eQ}{2h}S_{11}\varepsilon_b. \tag{4.9}$$

This eliminates both the dependency on the Zeeman splitting and the ST second order term $\nu_Q^{(2),\mathrm{ST}}$, leaving just the first order splitting $\nu_Q^{(1)}$, matching the relation found in previous studies [180]. As S_{11} is a known value for GaAs, we can obtain an estimate for the magnitude of the biaxial strain ε_b from the measured value of $\nu_Q^{(1)}$.

The second term is the difference between $\nu_{-1/2\leftrightarrow+1/2}$ and the mean of the two ST frequencies:

$$\begin{aligned}
&\nu_{-1/2\leftrightarrow+1/2} - \left(\frac{\nu_{+1/2\leftrightarrow+3/2}+\nu_{-3/2\leftrightarrow-1/2}}{2}\right) = \\
&\frac{1}{192\nu_L}\left(\frac{eQ}{h}\right)^2 (9S_{11}^2(\varepsilon_{xx}-\varepsilon_{yy})^2 + 64S_{44}^2(\varepsilon_{xy}^2 - 4(\varepsilon_{xz}^2+\varepsilon_{yz}^2)),
\end{aligned} \tag{4.10}$$

which is effectively the difference between the CT second order shift $\nu_Q^{(2),\mathrm{CT}}$ and $\nu_Q^{(2),\mathrm{ST}}$. As we will discuss in the next section, Eq. 4.10 can be used to probe the value of S_{44} or alternatively, how well the externally applied uniaxial stress is aligned along the [110] crystallographic axis. We ideally need to remove the dependence of the first term on S_{11} to obtain a term dependent on the ratio of S_{44}/S_{11}. To achieve this we divide Eq. 4.10 by $(\nu_Q^{(1)})^2$ to finally obtain:

$$\Delta\nu_Q^{(2)} = \frac{\nu_Q^{(2),\mathrm{CT}} - \nu_Q^{(2),\mathrm{ST}}}{(\nu_Q^{(1)})^2} = \frac{\nu_{-1/2\leftrightarrow+1/2} - \left(\frac{\nu_{+1/2\leftrightarrow+3/2}+\nu_{-3/2\leftrightarrow-1/2}}{2}\right)}{(\nu_Q^{(1)})^2}$$

$$\Delta\nu_Q^{(2)} = \frac{1}{\varepsilon_b^2\nu_L}\left(\frac{3}{16}(\varepsilon_{xx}-\varepsilon_{yy})^2 + \frac{4}{3}\left(\frac{S_{44}}{S_{11}}\right)^2(\varepsilon_{xy}^2 - 4(\varepsilon_{xz}^2+\varepsilon_{yz}^2)\right) \tag{4.11}$$

As we will discuss in the next section Eq. 4.11, along with assumptions about how the sample is strained, can be used to assess the alignment of the externally applied uniaxial strain from the dependence of $\Delta\nu_Q^{(2)}$ on B_z.

4.5 Sample Strain Analysis

We performed NMR measurements on ^{75}As and ^{69}Ga at different magnetic fields to determine the affects of the applied uniaxial stress. NMR spectra for ^{75}As and ^{69}Ga at different B_z is shown in the waterfall plots Fig. 4.4a and b respectively. The data has been centred on the CT for each field. Looking at Fig. 4.4a we see at high fields ($B_z \geq 3.5$ T), the first order quadrupolar splitting between the three NMR transitions of $\nu_Q^{(1),^{75}\mathrm{As}} \approx 255$ kHz as already shown in Fig 4.3a. As B_z decreases we see that the separation between the CT and STL (STH) increases (decreases), meaning the three transitions are no longer equidistant. This is due to $\nu_Q^{(2)}$ increasing, following the $1/\nu_L$ dependence as given by Eq. 4.11. Again, in Fig. 4.4b $\nu_Q^{(1)}$ is found to be smaller for ^{69}Ga $\nu_Q^{(1),^{69}\mathrm{Ga}} \approx 125$ kHz. Interestingly, we do not observe any change in the separation between the three transitions as B_z is decreased, again this is likely due to $Q^{^{69}\mathrm{Ga}}S_{11}^{^{69}\mathrm{Ga}} < Q^{^{75}\mathrm{As}}S_{11}^{^{75}\mathrm{As}}$, meaning the value of $\nu_Q^{(2),^{69}\mathrm{Ga}}$ is too small to be observed at the accessible magnetic fields. Also the lowest value of B_z that spectra could be obtained for differs between the two nuclei. The reason for this limitation is an observed loss in the maximum DNP that could be generated optically at low B_z, which in turn limits the NMR signal. This will be discussed in more detail in Section 4.6.

To obtain values for the components of the applied strain we need to calculate the values for $\nu_Q^{(1)}$ and $\Delta\nu_Q^{(2)}$. The NMR spectra are fitted using a triple Gaussian equation, from which the three transition frequencies $\nu_{-3/2\leftrightarrow-1/2}$, $\nu_{-1/2\leftrightarrow+1/2}$ and $\nu_{+1/2\leftrightarrow+3/2}$ are obtained. We can then derive the values of $\nu_Q^{(1)}$ which are plotted against the external field strength in Fig. 4.5a, b for ^{75}As and

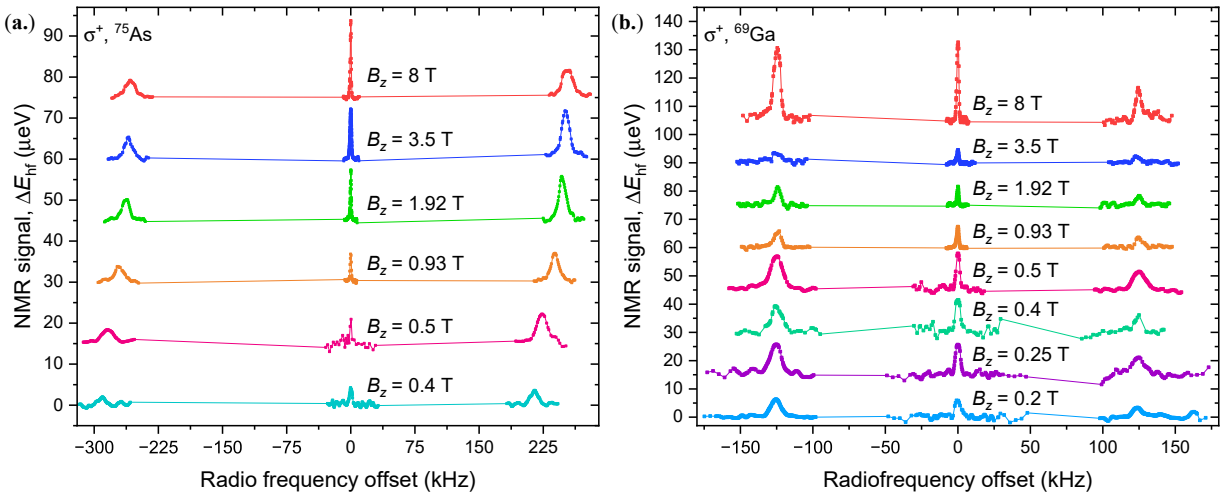


Figure 4.4: (a) Waterfall plot of ^{75}As NMR spectra at various external fields B_z. The CT frequency obtained from fitting as been subtracted from each dataset. We see at high fields the three transitions are evenly separated by the first-order quadrupolar interaction $\nu_Q^{(1),^{75}\mathrm{As}} \approx 255.6$ kHz. As B_z decreases we see the splitting becomes asymmetric, a consequence of the increasing second-order shift on primarily the CT. (b) Same as (a) but measuring ^{69}Ga. The first-order splitting is observed to be smaller $\nu_Q^{(1),^{69}\mathrm{Ga}} \approx 124.8$ kHz. The asymmetry between the transition splitting that developed at low B$_z$ for ^{75}As is absent here, due to the fact that ^{69}Ga has a smaller quadrupolar moment and so the second-order shift is too small to measure. Also we are able to measure at fields down to $B_z = 0.2$ T for ^{69}Ga as opposed to $B_z = 0.4$ T for ^{75}As. This is due to a reduction in the generation of DNP at low B_z.

^{69}Ga respectively. Interestingly, we see a weak dependence on B_z for ^{75}As in Fig. 4.5a despite that from Eq. 4.9 it should be independent. The cause for this is unknown. It could be due to uncertainty in the measured values arising from the lower resolution of the measurements conducted at small B_z. Alternatively, it could be a consequence of a higher-order term in the Hamiltonian. To avoid distorting the value of $\nu_Q^{(1),^{75}\mathrm{As}}$, we use the values obtained at high fields $B_z \geq 3.5$ T where the measurement accuracy is highest and any term inversely dependent on ν_L would be minimised. We obtain the value $\nu_Q^{(1),^{75}\mathrm{As}} \approx 255.6$ kHz. Comparatively, for ^{69}Ga we observe no dependence on B_z, likely due to the smaller quadrupolar moment of ^{69}Ga. Taking the average of the measured values we obtain $\nu_Q^{(1),^{69}\mathrm{Ga}} \approx 124.8$ kHz. In order to obtain ε_b we substitute the measured $\nu_Q^{(1)}$ values into Eq. 4.9 and solve for ε_b. Using the values $Q^{^{75}\mathrm{As}} S_{11}^{^{75}\mathrm{As}} = +0.758 \times 10^{-6}$ V and $Q^{^{69}\mathrm{Ga}} S_{11}^{^{69}\mathrm{Ga}} = -0.377 \times 10^{-6}$ V [180] we calculate $\varepsilon_b^{^{75}\mathrm{As}} = 0.2789\%$ and $\varepsilon_b^{^{69}\mathrm{Ga}} = 0.2738\%$. As expected, the measured values confirm that the ^{75}As and ^{69}Ga nuclei experience the same strain.

We now move on to analysis of $\Delta\nu_Q^{(2)}$. Fig. 4.6a and b show plots of $\Delta\nu_Q^{(2)}$ against B_z for ^{75}As and ^{69}Ga respectively. We see a clear dependence of $\Delta\nu_Q^{(2)}$ on $1/B_z$ for ^{75}As in Fig. 4.6a, while for ^{69}Ga there is again no observable dependence on the externally applied magnetic field due to its

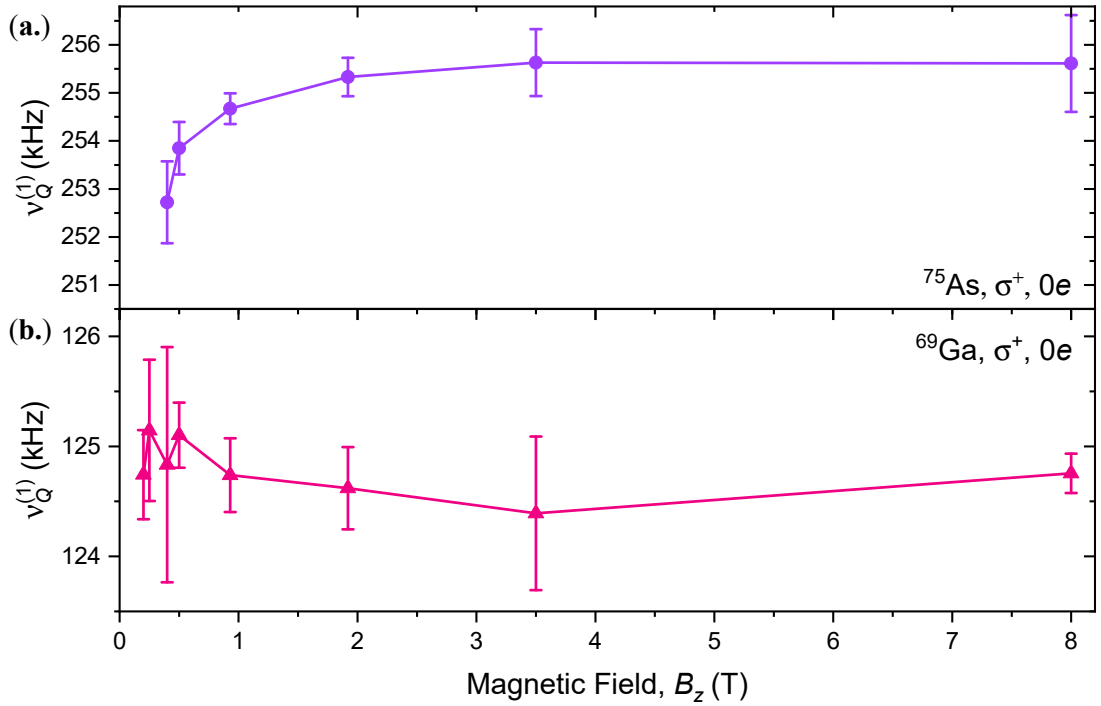


Figure 4.5: (a) Dependence of $\nu_Q^{(1)}$ on B_z for ^{75}As. There is an unexpected small drop in $\nu_Q^{(1)}$ at small B_z, which could be due to uncertainty in the measured values. Alternatively, the dependence appears to be inversely proportional on ν_L suggesting some contribution from either a higher order term or a breakdown in the validity of treating H_Q as a perturbation. Using the $\nu_Q^{(1)}$ values obtained at higher fields ($B_z \geq 3.5$ T) to avoid the unaccounted for dependence, we obtain $\nu_Q^{(1),^{75}\mathrm{As}} = 255.6$ kHz. (b) Same as (a) but for ^{69}Ga with $\nu_Q^{(1),^{69}\mathrm{Ga}} = 124.8$ kHz. The smaller quadrupolar moment of ^{69}Ga means we do not observe any dependence on ν_L.

smaller quadrupolar moment. We therefore are only able to probe the sample strain through the ^{75}As nuclei in the following discussion.

In order to extract information about the strain from the data in Fig. 4.6a we need to understand the stress being applied to the QD. We again note that these NMR measurements are insensitive to hydrostatic strain $\varepsilon_h = 0$, and that the diagonal components can be defined by the already discussed biaxial strain ε_b and the deviatoric strain ε_η. The stress bracket applies uniaxial stress along the [110] crystallographic direction though it is likely to deviate by a few degrees due to errors in how the sample was sheared and its alignment in the stress bracket; we adopt the same notation as used in [181] and denote this as stress P. As the stress corresponds to compression, $P < 0$. A full 3D model for the strain produced by the resulting stress has been considered in [181]. However, this only accounts for observations of the first order quadrupolar shift. Here we can simplify the following as we assume that the uniaxial strain lies perfectly in the x-y plane perpendicular to the growth direction and B_z. We therefore only need to consider the angle ξ between P and the x axis,

additionally due to the boundary conditions $\varepsilon_{xz} = \varepsilon_{yz} = 0$ [181]. Ultimately, there are two values we can investigate using different assumptions. The first is to assume that P is perfectly aligned along the [110] direction meaning $\xi = \pi/4$, therefore $\varepsilon_{xx} = \varepsilon_{yy}$ and the deviatoric strain becomes 0. The removal of ε_η cancels the first term in Eq. 4.11 leaving:

$$\Delta\nu_Q^{(2)} = \left(\frac{S_{44}}{S_{11}}\right)^2 \frac{4\varepsilon_{xy}^2}{3\varepsilon_b^2 \nu_L}. \tag{4.12}$$

It can be shown, in combination with using Hooke's law that ε_{xy} and ε_b are related by $\varepsilon_{xy}/\varepsilon_b = -(c_{11} - c_{12})\sin 2\xi / 2c_{44}$ where $c_{11} = 118.8$ GPa, $c_{12} = 53.8$ GPa, and $c_{44} = 59.4$ GPa are the stiffness constants of GaAs [185], giving the final equation:

$$\Delta\nu_Q^{(2)} = \frac{4}{3\nu_L}\left(\frac{S_{44}}{S_{11}}\right)^2 \left(\frac{-(c_{11} - c_{12})\sin 2\xi}{2c_{44}}\right)^2 = \frac{1}{3\nu_L}\left(\frac{S_{44}}{S_{11}}\right)^2 \left(\frac{-(c_{11} - c_{12})}{c_{44}}\right)^2, \tag{4.13}$$

where we have used the fact that $\sin(2\pi/4) = 1$. Fitting the data in Fig. 4.6a with Eq. 4.13 using $\gamma^{^{75}\mathrm{As}} = 7.315 \times 10^6$ HzT^{-1} we obtain $S_{44}/S_{11} = 2.053 \pm 0.014$ which is similar value to $S_{44}/S_{11} = 1.98$ that was measured in previous NMR measurements and nuclear acoustic resonance measurements [181, 186]. The fit is shown by the solid line in Fig. 4.6a. As $S_{11}^{^{75}\mathrm{As}}$ has already been measured with good accuracy the value of S_{44} is then found to be $S_{44} \approx 4.96 \times 10^{22}$ Vm^{-2}. We mention that the last works required measuring the NMR with the sample tilted at different angles. Here, we measure the sample at different external fields making the two measurements independent.

An alternative study of the $\Delta\nu_Q^{(2)}$ is to use the already measured value of S_{44}/S_{11} and instead measure the deviatoric strain, which is in turn linked to the value of ξ. We can use this to probe how effectively the stress bracket is able to apply stress along the [110] direction and how well the sample was cleaved. We return to Eq. 4.11, now only applying the boundary conditions $\varepsilon_{xz} = \varepsilon_{yz} = 0$, giving us a new equation:

$$\Delta\nu_Q^{(2)} = \frac{4}{3\nu_L}\left(\frac{S_{44}}{S_{11}}\right)^2 \left(\frac{\varepsilon_{xy}}{\varepsilon_b}\right)^2 + \frac{3}{16\nu_L}\left(\frac{\varepsilon_\eta}{\varepsilon_b}\right)^2. \tag{4.14}$$

It can again be shown that ε_η and ε_b are also related by $\varepsilon_\eta/\varepsilon_b = -2\cos 2\xi$ [181]. Substituting this into Eq. 4.11 along with $\varepsilon_{xy}/\varepsilon_b = -(c_{11} - c_{12})\sin 2\xi / 2c_{44}$ gives the new equation:

$$\Delta\nu_Q^{(2)} = \frac{1}{3\nu_L}\left(\frac{S_{44}}{S_{11}}\right)^2 \left(\frac{-(c_{11} - c_{12})\sin 2\xi}{2c_{44}}\right)^2 + \frac{3}{4\nu_L}(\cos 2\xi)^2, \tag{4.15}$$

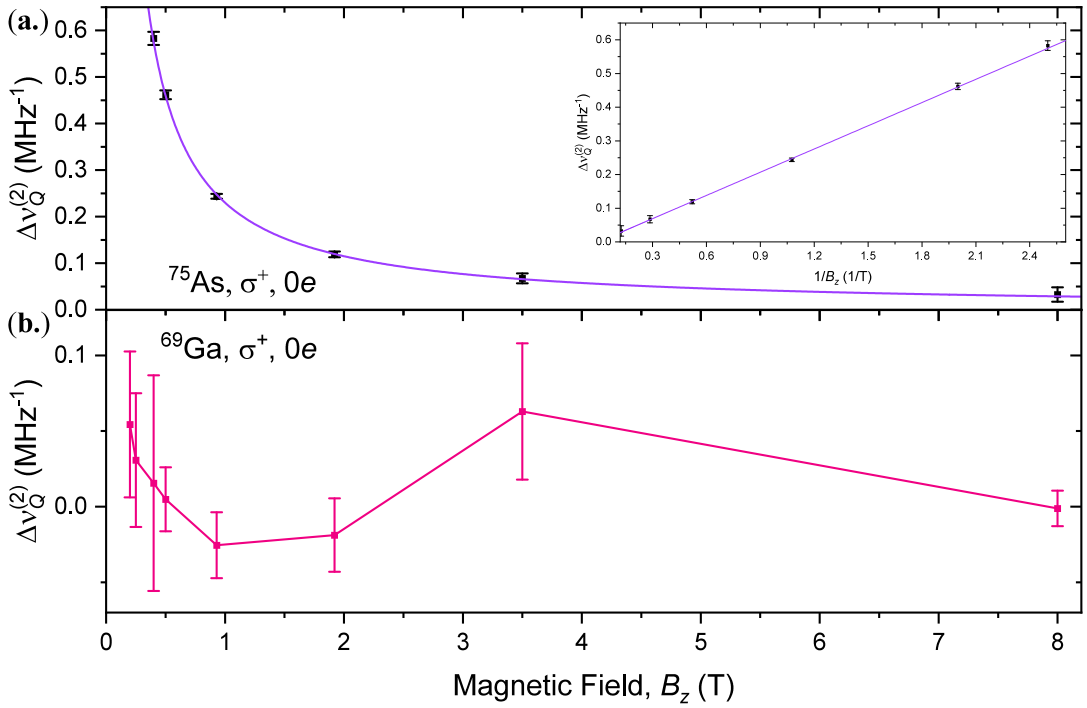


Figure 4.6: (a) Dependence of $\Delta\nu_Q^{(2)}$ on B_z for ^{75}As, the $1/B_z$ dependence is clearly observed. The solid line shows the fit using Eq. 4.13 from which an estimate of the ratio S_{44}/S_{11} is obtained. The inset shows the same data but plotted against $1/B_z$ where the linear relation is clearly seen. (b) Same as (a) but for ^{69}Ga. The smaller quadrupolar moment of ^{69}Ga means that no second order shift is observed.

which gives an equation dependent on the angle ξ. Fitting Fig. 4.6a with Eq. 4.15 we are unable to obtain an accurate estimate for ξ. This is a consequence of Eq. 4.15 being periodically dependent on ξ, with a maxima at $\xi = \pi/4$. Therefore, as the previously measured S_{44}/S_{11} value is smaller than the value obtained here it is impossible to accurately fit the data. This does however mean we can infer that our measured value of S_{44}/S_{11} is an underestimate of the true value, as the introduction of a misalignment of the applied stress from the [110] axis, which is likely to be a few degrees in the measured sample, will cause a decrease in the measured $\Delta\nu_Q^{(2)}$ values which is passed on as an error in the fitted value of S_{44}/S_{11}.

Finally, the actual magnitude of P is currently unknown. Fortunately P is related to the biaxial strain through the equation [181]:

$$\varepsilon_b = -\frac{P}{(2c_{11} - 2c_{12})} \tag{4.16}$$

from which we obtain $P \approx -0.363$ GPa.

The inverse dependence on B_z observed in this work is expected to eventually breakdown for smaller magnetic fields. This is due to the fact that we have treated the quadrupolar interaction

as a small perturbation on the Zeeman interaction. This is already close to not being the case in the regime studied for ^{75}As; where we estimate an equivalent magnetic field from the quadrupolar interaction as $B_Q = h\nu_Q^{(1)}/g_N\mu_N \approx 200$ mT (half of the smallest $B_z = 400$ mT measured in this work for ^{75}As) [103]. At $B_z = 0$ T the quadrupolar interaction acting alone splits the $I_z = \pm\frac{1}{2}$ and $I_z = \pm\frac{3}{2}$ states in energy. This gives two doubly degenerate states with a single transition between them [121]. The introduction of a weak magnetic field adds a perturbation to this inducing a Zeeman splitting between the $I_z = \pm\frac{3}{2}$ states, while the $I_z = \pm\frac{1}{2}$ states are split in energy and mixed. The result of this is that the single NMR transition observed at $B_z = 0$ T is replaced by four [121] transitions. We are unable to observe both of these regimes in this work due to being unable to generate sufficient DNP at low B_z to conduct ODNMR (see Section 4.6 for an more detailed discussion of why this occurs). This would be a interesting study for future work, particularly the values of B_z at which the transitions between the three regimes occur.

4.6 Comparison Between Unstrained and Strained Samples

We now include a brief discussion about the advantages and disadvantages of using a uniaxially strained sample. First we compare the NMR spectra of an unstrained sample and the strained sample used throughout this thesis, which are shown in Fig. 4.7a and b respectively. Both measurements were performed using the same inverse NMR resolutions. For the unstrained sample we obtain a $\nu_Q^{(1)} \approx 24.47$ kHz which gives an estimated value for the peak biaxial strain $\varepsilon_b \approx 0.0267\%$. Therefore the applied uniaxial stress dominates the biaxial strain acting on the QD leading to the 10-fold increase in the first order splitting between the STs. As seen in Fig. 4.7b, the benefit of this is that the three NMR transitions are separated enough that they become individually resolvable, enabling a higher degree of control over the nuclear spin system. As we will discuss in Chapter 5, the first order quadrupolar shift is also large enough that some of the Knight shifted NMR transitions can be resolved, specifically those of the STs shifted away from the CT in frequency. Comparing the linewidths of the NMR transitions for the QDs in both samples, we find that for the CT the measured FWHMs are smaller than the gap size used in the measurements of 2 kHz, meaning they are resolution limited [175]. The typical values for the STs FWHMs are $\Delta\nu_{-3/2\leftrightarrow-1/2} \approx \Delta\nu_{+1/2\leftrightarrow+3/2} \approx 8.05$ kHz and $\Delta\nu_{-3/2\leftrightarrow-1/2} \approx \Delta\nu_{+1/2\leftrightarrow+3/2} \approx 11.6$ kHz for the unstrained and strained sample respectively, meaning the ST linewidths are similar. Future measurements where the same QD is studied under varying external strain would allow for the effects of the external strain on the NMR linewidths to be measured. In either case the inhomogeneous strain remains small, and the linewidths obtainable are still smaller than those in self assembled QDs, again enabling a higher degree of control over the nuclear spins [150].

However, there are consequences to using uniaxial stress to perform strain engineering. The

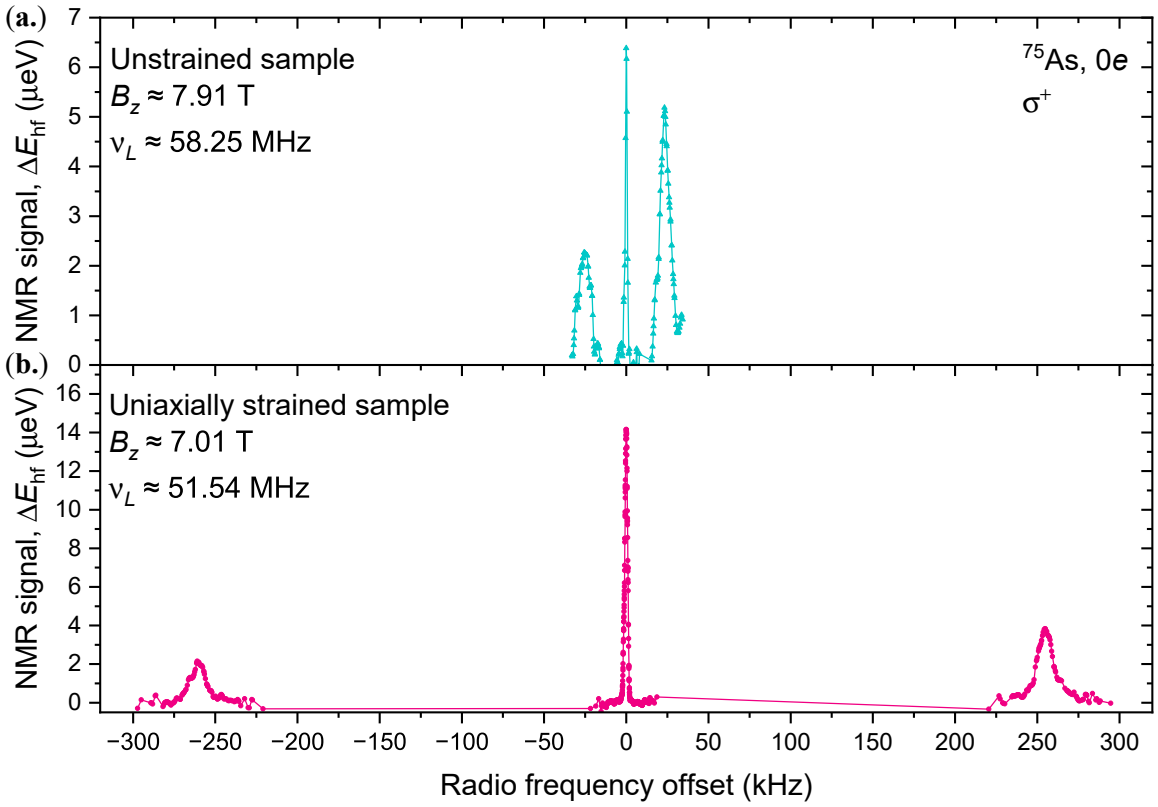


Figure 4.7: (a) NMR spectra of ^{75}As nuclei from a QD in an unstrained sample. The data has been centred on the CT. The first order splitting is found to be $\nu_Q^{(1)} \approx 30$ kHz corresponding to peak biaxial strain $\varepsilon_b = 0.0267\%$. (b) The same as (a) but measured on a uniaxially strained sample.

magnitude of the second order quadrupolar shift on the ^{75}As nuclei, as seen in Fig. 4.6a, is sensitive to any applied uniaxial stress along the [110] crystallographic axis. This is undesirable as it causes the separation between the CT and one of the STs to decrease at low-fields (Fig. 4.4a), limiting the field range where the three transitions are resolvable. The other major issue caused by the application of uniaxial stress is the significant reduction in achievable DNP at small B_z. Fig. 4.8a shows the maximum (minimum) achievable PL spectral splitting ΔE_{PL} using σ^+ (σ^-) polarised light at various B_z, shown by light blue open circles (burgundy open triangles). The total spectral splitting ΔE_{PL} will have contributions from the Zeeman splitting ΔE_{Zeeman}, the fine structure splitting ΔE_{FSS}, and the nuclear spin Overhauser field ΔE_{OH}. The contribution from ΔE_{OH} will be positive under σ^+ pumping and negative under σ^- pumping. Comparatively, the data represented by orange squares are results collected with no optical pumping showing exciton PL separation in the absence of the Overhauser field, which will be some combination of the fine structure splitting of the respective exciton and the magnetic field induced Zeeman splitting. For X^- $\Delta E_{\text{FSS}} = 0$ while for the other two excitons measured ΔE_{FSS} will have some finite value. Fig. 4.8a shows that as B_z decreases the PL spectral splitting decreases, as expected due to the reduction in Zeeman split-

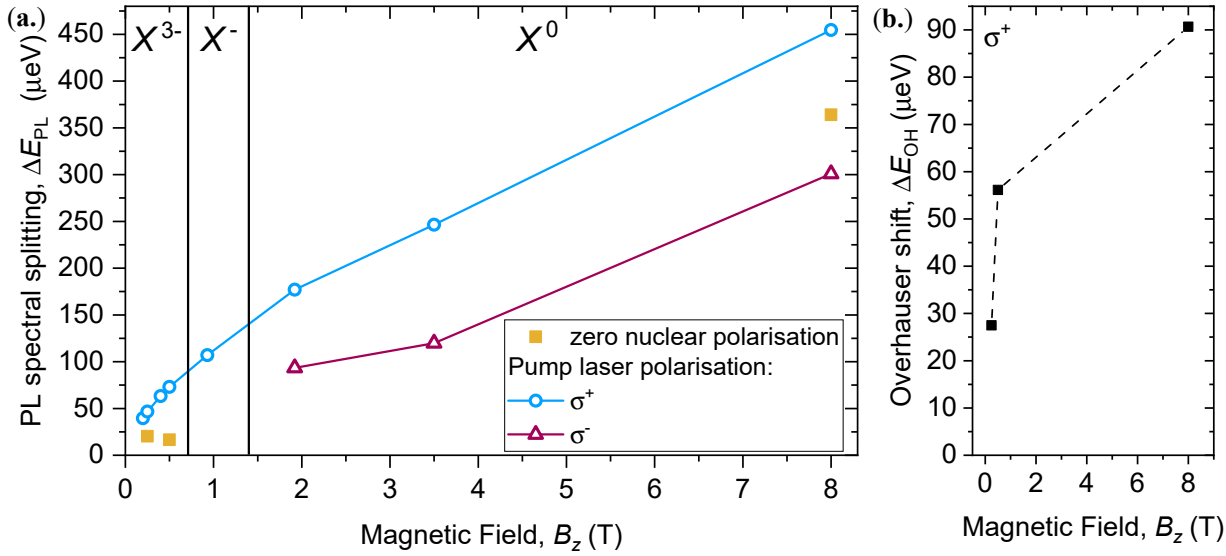


Figure 4.8: Measurement of the spectral splitting ΔE_{PL} at different magnetic fields. In the absence of optical pumping the PL splitting has contributions from the Zeeman and fine structure splitting and is shown by the orange solid squares. In the presence of optical pumping with σ^+ (σ^-) polarised light ΔE_{PL} is increased (decreased) due to the generation of DNP creating an additional Overhauser shift ΔE_{OH} which is shown by the light blue open circles (burgundy open triangles). The vertical black lines are used to show which excitons were used to measure each data point. For the negative exciton X^- $\Delta E_{\mathrm{FSS}} = 0$ while for the other excitons ΔE_{FSS} will have a finite value. We observe a decrease in the PL splitting as B_z decreases due to a reduction in the Zeeman splitting. There is an additional loss in the total ΔE_{OH}. (b) Plot of the Overhauser shift ΔE_{OH} against B_z. We see at high fields $\Delta E_{\mathrm{OH}} \approx 90.6\ \mu$eV while at low fields $\Delta E_{\mathrm{OH}} \approx 25\ \mu$eV. This ≈ 3 times decrease in ΔE_{OH} is a consequence of the uniaxial strain causing a rotation of the nuclear spin quantisation axis away from the z axis.

ting. However, we also observe a decrease in the achievable ΔE_{OH}, obtained from the difference between the data with and without optical pumping. At $B_z = 8$ T, under σ^+ pumping, we measure $\Delta E_{\mathrm{OH}} = 90.6\ \mu$eV, while for $B_z = 0.25$ T $\Delta E_{\mathrm{OH}} = 26.3\ \mu$eV, this is shown in Fig. 4.8b. This is a reduction in the maximum Overhauser shift by a factor of ≈ 3. We attribute this reduction to the applied uniaxial strain, primarily because in experiments a much faster loss in NMR signal is found for ^{75}As than for ^{69}Ga, as seen in Fig. 4.4, where we are unable to measure the NMR for ^{75}As at fields $B_z < 0.4$ T, while we are able to measure ^{69}Ga at fields down to $B_z < 0.2$ T. This finding aligns with ^{75}As being more sensitive to strain as $Q^{^{75}\mathrm{As}} S_{11}^{^{75}\mathrm{As}} > Q^{^{69}\mathrm{Ga}} S_{11}^{^{69}\mathrm{Ga}}$. Due to the applied uniaxial strain being aligned along the [110] direction, the EFG principal axis is closely aligned to the x-y plane. As such, when B_z is small the approximation that the quadrupolar interaction acts as a perturbation of the Zeeman splitting begins to breakdown, which can be seen if we approximate the quadrupolar affect as an additional field given by $B_Q = h\nu_Q^{(1)}/g_N\mu_N \approx 200$ mT for the strained sample. Therefore, as B_z decreases, the nuclear spin quantisation axis begins to rotate from

the growth axis towards the EFG principle axis, as has been shown from excitons in QDs. As the quantisation axis rotates further away from the z axis there will be a loss in the effectiveness of the optical pumping and hence a loss in the maximum achievable DNP [103, 181]. This further limits the usability of these uniaxially stressed QDs at low magnetic fields where it becomes increasingly difficult to generate DNP, preventing nuclear spin initialisation.

4.7 Summary

We have used NMR to probe the strain in uniaxially stressed GaAs/AlGaAs QDs. Taking into account quadrupolar effects up to second order we obtain an estimate of the applied biaxial strain $\varepsilon_b \approx 0.2789\%$, significantly higher than the $\varepsilon_b \approx 0.0267\%$ observed in an unstrained sample. This increases the observed first order splitting to by a factor of ≈ 10, enough to enable the three nuclear spin transitions to be resolved independently by RF pulses. The measured dependence on the second-order quadrupolar shift of the CT is sufficient to measure the S_{44} value for GaAs without needing to tilt the sample in the cryostat. The obtained value $S_{44}/S_{11} = 2.054 \pm 0.014$ is a close match to those obtained in previous measurements [181, 186]. We also demonstrate that the second-order shift can be used to measure the alignment of the applied uniaxial stress, but this approach is limited by the accuracy of the measured S_{44}/S_{11} value and all we can conclude from this analysis is that the value obtained from fitting will be an underestimate. We also identify drawbacks to performing strain engineering with uniaxial stress. Primarily the uniaxial stress causes a large second order quadrupolar shift for ^{75}As, reducing the separation of the CT and higher ST and hence their resolvability. Additionally we see a strain induced reduction in the generated DNP at low B_z. We assess that this is due to a shift in the quantisation axis for the nuclear spins towards the EFG principal axis, limiting the range of magnetic fields that ODNMR could be performed at.

Chapter 5

Is Wavefunction Collapse Necessary? Explaining Quantum Nondemolition Measurement of a Spin Qubit Within Linear Evolution

In the previous chapter we characterised the nuclear spin system of a GaAs QD exposed to uniaxial external strain. In this chapter we now investigate the nuclei in the presence of a confined electron spin. As discussed in Chapter 1, a key requirement for a usable qubit is efficient and high fidelity readout of the qubit state [11, 12]. For QDs, readout of a confined electrons spin state can be performed optically using resonance florescence, but the high power optical excitation of the electron has sufficient energy that it can drive a spin-flip leading to incorrect readouts [187–189]. This imposes a limit on the maximum achievable readout fidelity. An alternative would be to implement QND measurements, where the system being probed is only weakly coupled to the measurement apparatus, resulting in only a small perturbation and meaning multiple measurements can be conducted [12, 190, 191].

The nuclear spins in a QD are sensitive to the electron spin state through the hyperfine interaction. The electron spin introduces an additional magnetic field called the Knight field [129] that shifts the NMR frequencies; the direction of this shift is dependent on the electron spin state. In this chapter we implement readout of the electron spin z projection. The measurement is conducted by applying detuned RF pulses to the nuclei which, due to the Knight-field-induced shift in the NMR frequencies, causes nuclear spin flips (no flips) only in the case that the Knight field shifts the NMR frequencies into (out of) resonance with the applied RF pulse. The measurements are performed single shot and the resulting readout statistics demonstrate a bimodal distribution, with each mode

corresponding to one of the two electron spin states. We demonstrate that this approach allows single shot, QND measurements with high readout fidelity $F \approx 99.85$ %, comparable to other state of the art techniques [192–196]. The QND property of the experiment is demonstrated through a two pulse double readout measurement [191], while simulations confirm the weak perturbative nature of the measurement. Observed electron spin flips are attributed to phonon processes [87], with simulations confirming that the nuclei and the RF pulse are unable to drive electron spin flips due to the low energy non-resonant nature of the measurement.

During the measurement the nuclei can be viewed as an 'observer' of the electron spin state at all times through the hyperfine interaction. During readout we use the detuned RF pulses to map 'snapshots' of the electron spin z projection to the spin state of the $N \approx 10^4 - 10^5$ nuclei, where it is stored and later retrieved during optical probing. Due to the size of the nuclear spin bath, depolarisation during optical readout does not invoke any wavefunction collapse and the whole measurement can be described without such phenomenon. This introduces questions about the nature of quantum measurements and potentially provides evidence for other interpretations of quantum mechanics, such as Quantum Darwinism [197, 198].

This work is presented as a paper, which was published in a peer-review journal on 19th of April 2024 where I am first author:

H. E. Dyte, G. Gillard, S. Manna, S. F. Covre da Silva, A. Rastelli, E. A. Chekhovich. "Is wavefunction collapse necessary? Explaining quantum nondemolition measurement of a spin qubit within linear evolution". *Phys. Rev. Lett.* **132**, 160804 (2024). DOI: https://doi.org/10.1103/PhysRevLett.132.160804

Is Wave Function Collapse Necessary? Explaining Quantum Nondemolition Measurement of a Spin Qubit within Linear Evolution

Harry E. Dyte,[1] George Gillard,[1] Santanu Manna,[2] Saimon F. Covre da Silva,[2] Armando Rastelli,[2] and Evgeny A. Chekhovich[1,3,*]

[1]Department of Physics and Astronomy, University of Sheffield, Sheffield S3 7RH, United Kingdom
[2]Institute of Semiconductor and Solid State Physics, Johannes Kepler University Linz, Altenberger Strasse 69, 4040 Linz, Austria
[3]Department of Physics and Astronomy, University of Sussex, Brighton BN1 9QH, United Kingdom

(Received 4 July 2023; revised 28 January 2024; accepted 14 March 2024; published 19 April 2024)

The measurement problem dates back to the dawn of quantum mechanics. Here, we measure a quantum dot electron spin qubit through off-resonant coupling with a highly redundant ancilla, consisting of thousands of nuclear spins. Large redundancy allows for single-shot measurement with high fidelity ≈99.85%. Repeated measurements enable heralded initialization of the qubit and backaction-free detection of electron spin quantum jumps, attributed to burstlike fluctuations in a thermally populated phonon bath. Based on these results we argue that the measurement, linking quantum states to classical observables, can be made without any "wave function collapse" in agreement with the Quantum Darwinism concept.

DOI: 10.1103/PhysRevLett.132.160804

High fidelity qubit readout is essential in quantum information processing. Usually, such readout starts with conversion of a fragile quantum state into a more robust form, detectable by a classical apparatus. Some readout techniques rely on high-energy excitations, making this conversion dissipative (irreversible). Examples include spin-to-charge conversion [1–4], single photon detection [5], optical readout of spin in defects [6–11], and quantum dots (QDs) [12–14]. An alternative is unitary (reversible) conversion. One example is the off-resonant (Ising) coupling between the main and ancilla electron spin qubits, which enables quantum nondemolition (QND) measurement [15]. Other QND demonstrations include superconducting qubits under off-resonant (dispersive-regime) coupling [16] and mechanical resonators [17].

Here, we implement unitary conversion of a QD electron spin, but the off-resonant ancilla consists of $\approx 10^4$–10^5 low-energy nuclear spin qubits. The large redundancy of the ancilla results in a very high measurement fidelity. Moreover, the method is particularly robust and simple to implement, since the nuclei are essentially the same in all QDs, eliminating the need for QD-specific calibrations. Addressing the controversial measurement problem, we argue that high fidelity is what an observer perceives as a deterministic classical outcome of a measurement. Crucially, in our system, the transition from the microscopic quantum-mechanical evolution to this perceived determinism is achieved without requiring any nonunitary wave function reduction ("collapse").

We study epitaxial GaAs/AlGaAs QDs [18–22] in a *p-i-n* diode structure, where bias tuning can inject individual electrons from the *n*-type Fermi reservoir [Fig. 1(b)]. A static magnetic field B_z is applied along the growth axis z. A typical QD consists of $N \approx 10^5$ atoms, whose nuclei are spin-3/2 particles. The sample is subject to uniaxial stress, which induces nuclear quadrupolar shifts [23]. This isolates the two-level subspace with spin projections $I_z = -3/2, -1/2$, allowing the nuclei to be treated as effective spin-1/2 particles. Individual QDs are addressed optically using focused laser excitation and photoluminescence (PL) spectroscopy. A copper coil is used to generate a radiofrequency (rf) magnetic field orthogonal to B_z. (See further details in Supplemental Material, Secs. 1 and 3 [24].)

The quantum system of a QD charged with a single electron ($1e$) is described with reference to the level diagram in Fig. 1(a). The hyperfine interaction Hamiltonian is $\mathcal{H}_{\rm hf} = \Sigma_k a_k \hat{\mathbf{s}} \cdot \hat{\mathbf{I}}_k$, where a_k describes the coupling between the spin vector $\mathbf{s}$ of the resident electron and the kth nuclear spin vector $\mathbf{I}_k$. This interaction has a twofold effect. First, in addition to the bare Larmor frequency $\nu_{\rm N}$, each nucleus acquires a Knight [53] frequency shift $s_z a_k/(2h)$. Second, the electron states with $s_z = \pm 1/2$ acquire the (Overhauser) hyperfine shifts $\pm E_{\rm hf}/2$, arising from the net polarization of the nuclear spin ensemble [Fig. 1(d)]. The average hyperfine shift is defined as $E_{\rm hf} = \Sigma_k a_k \langle \hat{I}_{z,k} \rangle$, where $\langle \ldots \rangle$ is the expectation

Published by the American Physical Society under the terms of the Creative Commons Attribution 4.0 International license. Further distribution of this work must maintain attribution to the author(s) and the published article's title, journal citation, and DOI.

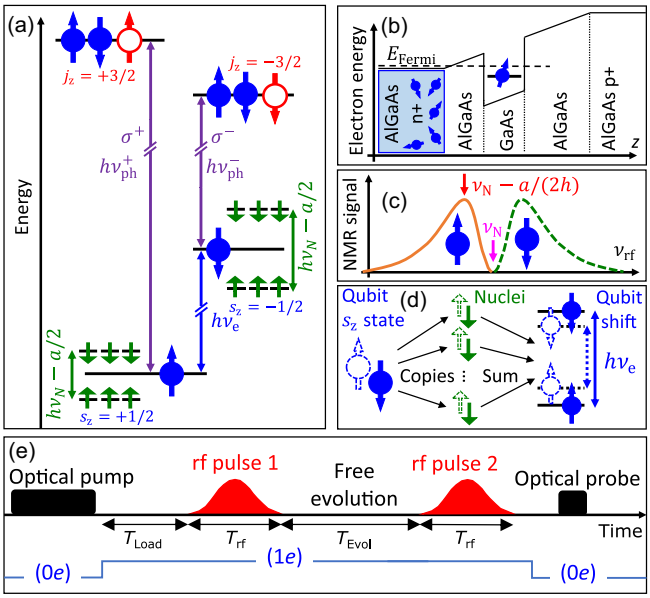


FIG. 1. (a) Energy level diagram of the nuclear spins (short green arrows), the electron (solid blue circle and arrow), and the optically excited trion, containing one hole (open red circle and arrow) and two electrons. (b) Conduction band energy diagram of the semiconductor structure, showing the GaAs quantum dot, AlGaAs barriers, and the doped AlGaAs layers. (c) The solid (dashed) curve shows schematically the nuclear magnetic resonance spectrum in the presence of a spin-up (spin-down) electron. Vertical arrows show the bare nuclear frequency ν_N and the frequency $\nu_N - a/(2h)$ of the detuned radiofrequency (rf) pulse. (d) The electron spin qubit projection is first copied into multiple nuclear spin ancillae by the rf pulse. The total nuclear polarization is then measured from the hyperfine shifts E_{hf} in the time-averaged PL spectra. (e) Timing diagram showing optical pump and probe, rf pulses, and the switching of the QD between the neutral ($0e$) and electron-charged ($1e$) states.

value. The electron spin energy splitting $h\nu_e$, is the sum of E_{hf} and the bare Zeeman splitting $h\nu_{e,0} = \mu_B g_e B_z$, where $g_e \approx -0.1$ is the electron g-factor and μ_B is the Bohr magneton. The optically excited trion contains a spin-singlet pair of electrons and an unpaired valence band hole with momentum projection $j_z = \pm 3/2$. Because of the selection rules, there are two dipole-allowed circularly polarized ($\sigma^\pm$) optical transitions with photon energies $h\nu_{ph}^\pm$. The optically detected spectral splitting $\Delta E_{PL} = h(\nu_{ph}^+ - \nu_{ph}^-)$ yields E_{hf} [54].

Traditional readout uses resonant driving of a cyclic optical transition [e.g., σ^+ in Fig. 1(a)] to convert the electron spin state into the presence or absence of scattered photons [12–14]. However, there is a finite probability for the measurement process to destroy the spin qubit if the recombination goes via one of the "forbidden" channels [e.g., from $j_z = +3/2$ to $s_z = -1/2$ in Fig. 1(a)]. Here, we take a different approach, using the long coherence of the nuclear spins [55] and the large energy detunings $\nu_{ph}^\pm \gg \nu_e \gg \nu_N$ to turn the nuclei into a QND measurement apparatus.

Figure 1(e) shows the timing diagram of the measurement cycle. It starts with a long (few seconds) circularly polarized optical pumping of an empty ($0e$) QD, which polarizes the nuclear spins up to ≈80% [56,57]. Next, an electron is loaded from the Fermi reservoir ($1e$) and is allowed to equilibrate for a time T_{Load}. Nuclear magnetic resonance (NMR) is performed by applying a rf pulse with a total duration T_{rf}, calibrated to induce a π rotation of the nuclear spins. In some experiments, a second rf pulse is applied, following a free evolution time T_{Evol}. The final step is the illumination of the QD with a short (tens of milliseconds) continuous wave optical probe in order to collect the PL spectrum and derive E_{hf}. Importantly, all measurements are done in one cycle, i.e., for the electron spin projection s_z the measurement is single-shot.

The readout of the electron spin qubit is explained in Fig. 1(c). An electron in state $s_z = +1/2$ ($-1/2$) Knight-shifts the QD NMR spectrum to the lower (higher) frequency side of ν_N. A single rf pulse is applied at a radiofrequency $\nu_N - a/(2h)$, where a is a weighted average of a_k in a QD. For the electron in the $s_z = +1/2$ ($-1/2$) state, the rf pulse is in (out of) resonance, so the QD nuclei are flipped (remain in the initial state) [6]. Statistics of the measured single-cycle PL probe spectra [Fig. 2(a)] show a clear bimodality in the spectral splitting (red and black traces), arising from the bimodal distribution of the rf-induced variation of the hyperfine shift ΔE_{hf}. A systematic dependence of ΔE_{hf} on the rf detuning from ν_N is shown in Fig. 2(b), where the two branches corresponding to $s_z = +1/2$ and $-1/2$ are traced by the solid and dashed

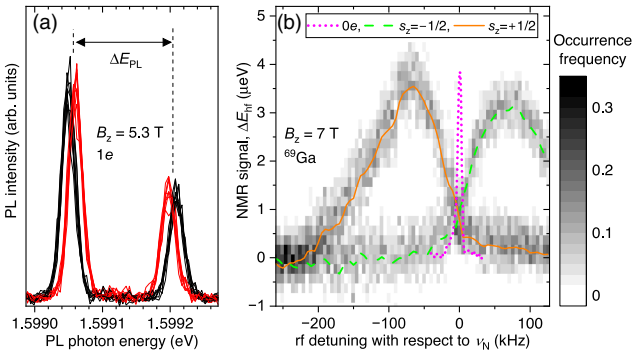


FIG. 2. (a) A random set of 16 probe PL spectra following the detuned rf π pulse applied to a charged ($1e$) QD. The changes in the doublet splitting ΔE_{PL} are due to the changes ΔE_{hf} in the hyperfine shift E_{hf}. The bimodality in ΔE_{PL} (and ΔE_{hf}) corresponds to the two s_z states of the electron. (b) Histogram of the single-cycle NMR signals ΔE_{hf} measured at variable detunings from the ^{69}Ga bare NMR frequency ν_N ($\nu_N \approx 72.15$ MHz at $B_z \approx 7$ T). The solid (dashed) line traces the branch of the NMR resonance corresponding to the $s_z = +1/2$ ($-1/2$) electron spin state. The dotted line shows the same single-QD resonance but measured in a neutral charge state ($0e$) via "inverse" NMR [58].

lines, respectively. The broadening of these traces arises from the inhomogeneous distribution of a_k, while in an empty QD ($0e$, dotted line) the broadening of the NMR spectrum is due to the much smaller quadrupolar inhomogeneity. The optimal resolution of the two electron spin states (the maximum difference in ΔE_{hf}) is observed when the rf detuning matches the typical Knight shift $a/(2h) \approx 70$ kHz.

Using the optimal detuning, we collect detailed statistics of the single-cycle NMR signals ΔE_{hf}. In an empty QD [$0e$, Fig. 3(a)] the distribution of ΔE_{hf} is a single mode, broadened by the noise in probe PL spectra. The mode is centered at a small $\Delta E_{\mathrm{hf}} \approx 1.7$ μeV, indicating partial rotation of the nuclei by the detuned rf pulse. The same measurement in a charged QD [$1e$, Fig. 3(b)] shows a bimodal distribution around two discrete values of ΔE_{hf}.

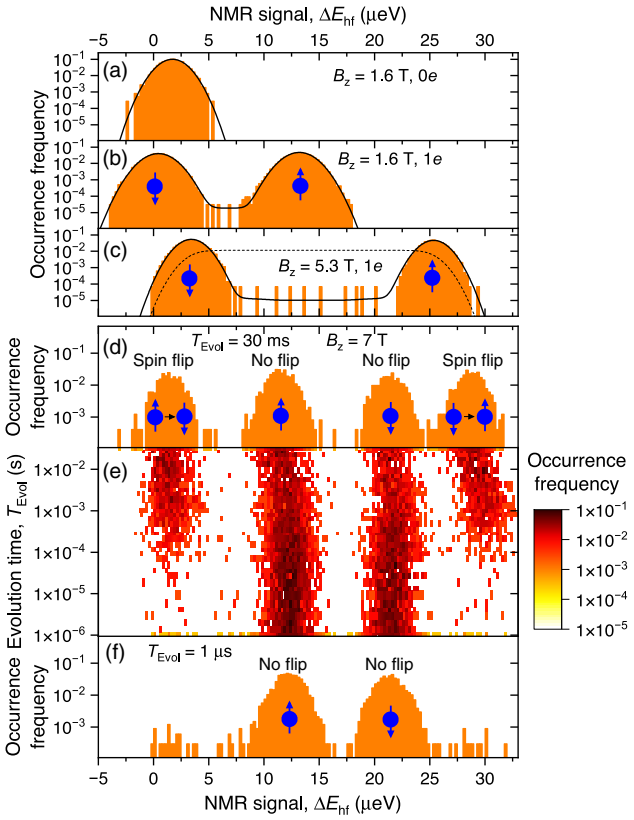


FIG. 3. (a),(b) Histograms of the single-cycle NMR signals ΔE_{hf} measured at $B_z = 1.6$ T on the same individual QD in a neutral charge state ($0e$, a), and in a single-electron charged state ($1e$, b). The NMR signals are produced by a single detuned rf π pulse. Solid lines show the best model fitting. (c) Same as (b) but on a different QD and at $B_z = 5.3$ T, where more efficient nuclear spin polarization results in a larger separation of the histogram modes. The dashed line shows a model distribution for a randomly oriented electron spin. (d),(e) Histograms of the single-cycle NMR signals ΔE_{hf} measured at $B_z = 7$ T with two rf π pulses applied to ^{75}As and ^{69}Ga and delayed by T_{Evol}. A full 2D histogram at variable T_{Evol} is shown in (e), while (d) and (f) show the cross sections at long and short T_{Evol}, respectively.

The mode centered at $\Delta E_{\mathrm{hf}} \approx 0.4$ μeV (≈13.2 μeV) corresponds to the $s_z = -1/2$ ($+1/2$) state, where the electron Knight-shifts the nuclei out of (into) resonance with the rf pulse. Thus, the electron's quantum variable $\hat{s}_z$ is measured via single-shot optically detected NMR.

We note a small number of events where the NMR signal deviates from either of the modes [8 μeV $\lesssim \Delta E_{\mathrm{hf}} \lesssim$ 21 μeV in Fig. 3(c)]. We ascribe such intermediate readouts to electron spin flips during the rf pulse, resulting in partial rotation of the nuclear spins. We model this process by assuming a probability p_{Flip} for the electron spin to flip during T_{rf}. The optical readout noise is also included in the model (see Supplemental Material, Sec. 4 [24]). The best-fit results are shown by the solid lines in Figs. 3(b) and 3(c). Using the fitted mode positions $\Delta E^{-}_{\mathrm{hf}}$ and $\Delta E^{+}_{\mathrm{hf}}$, we set the threshold at $(\Delta E^{-}_{\mathrm{hf}} + \Delta E^{+}_{\mathrm{hf}})/2$ and calculate the probability that the detected ΔE_{hf} is below (above) the threshold when the electron state is $s_z = -1/2$ ($+1/2$). This probability is the qubit readout fidelity, found to be $F \approx 0.9985$, matching or exceeding the state of the art in a range of qubit systems [2,8,10,11,59]. Since the two histogram modes are well resolved, the loss of fidelity is dominated by the random electron spin flips, leading to $F \approx 1 - p_{\mathrm{Flip}}/2 \approx 1 - T_{\mathrm{rf}}/(4T_{1,\mathrm{e}})$, where $T_{1,\mathrm{e}}$ is the electron spin lifetime. Nuclear spin relaxation ($T_{1,\mathrm{N}} \approx 1$–$10$ s [21]) and decoherence ($T_{2,\mathrm{N}} \approx 1$ ms [55]) are slow, and therefore do not limit the choice of T_{rf}. The lower limit $T_{\mathrm{rf}} \gtrsim h/a$ comes from the need to resolve the $s_z = \pm 1/2$ Knight-shifted NMR spectra with a short (spectrally broad) rf pulse. Our experiments with $T_{\mathrm{rf}} \approx 10$–$20$ μs are already close to this limit, constrained by the QD size through $a \propto N^{-1}$. The other limitation comes from $T_{1,\mathrm{e}}$, which ranges from milliseconds to tens of milliseconds for temperature $T \approx 4.2$ K and our typical electron spin splitting $h\nu_{\mathrm{e}} \approx 50$ μeV. Further increase in $T_{1,\mathrm{e}}$ (and hence increase in F) can be achieved by lowering the temperature toward $k_{\mathrm{B}}T \approx h\nu_{\mathrm{e}}$, and by lowering $h\nu_{\mathrm{e}}$ through reduced magnetic field and nuclear spin polarization.

Immediate repeatability is a key requirement for any measurement [60,61], which we verify in an experiment with two rf pulses [Fig. 1(e)]. The first pulse applied to ^{75}As nuclei records the initial state, while the second pulse on ^{69}Ga stores the s_z state after the interpulse delay T_{Evol}. The optically measured ΔE_{hf} is the total NMR signal produced by the two pulses. Figure 3(e) shows a two-dimensional histogram of ΔE_{hf} measured at different T_{Evol}. A cross section at short $T_{\mathrm{Evol}} \approx 1$ μs [Fig. 3(f)] reveals the same bimodal distribution as in Figs. 3(b) and 3(c), with only two "no-flip" modes corresponding to $s_z = \pm 1/2$. This shows that the measured observable $\hat{s}_z$ is not altered by the rf pulses, confirming the QND character of the measurement [60]. The two additional "spin-flip" modes, corresponding to s_z inversion during T_{Evol}, emerge only at long T_{Evol} [≈30 ms in Fig. 3(d)]. Analysis of the entire T_{Evol} dependence reveals the spin lifetime $T_{1,\mathrm{e}} \approx 0.58$ ms at

$B_z = 7$ T, measured in equilibrium without any active initialization of the electron spin. Instead, a heralded initialization is performed by the first rf pulse, which stores the initial s_z in the ^{75}As polarization, to be retrieved by the optical probe afterward.

The readout time $T_{rf} = 20$ μs is short enough to follow the electron spin evolution on the timescale of $T_{1,e}$. However, Fig. 3(e) shows that the electron spin is nearly always detected in either of the eigenstates $s_z = \pm 1/2$, with very rare intermediate NMR readouts ΔE_{hf}. This suggests a random telegraph process, where the electron is in one of the eigenstates $s_z = \pm 1/2$ most of the time, occasionally experiencing quantum jumps that are much faster than T_{rf}.

We gain further insight with the aid of the first-principle numerical modeling, where the Schrödinger equation is propagated from the initial wave function state ψ_{Init} into the final state ψ_{Fin} (see details in Supplemental Material, Sec. 6 [24]). Initially the nuclei are in a polarized state and the electron spin is in a general superposition $\psi_{Init} = \alpha|+1/2\rangle + \beta|-1/2\rangle$ with the z-projection expectation value $s_{z,Init} = (|\alpha|^2 - |\beta|^2)/2$. Following the detuned rf pulse, we find that (i) the final polarization of each nucleus equals the initial electron polarization $I_{z,k,Fin} \approx s_{z,Init}$ and (ii) the electron polarization is nearly unchanged $s_{z,Fin} \approx s_{z,Init}$. Such nondemolition copying of the quantum variable $\hat{s}_z$ comes at the expense of completely erasing the conjugate variable [60], which manifests in $s_{x,Fin} \approx s_{y,Fin} \approx 0$ regardless of the initial electron state. This is in agreement with the no-cloning theorem, since only s_z is copied, but not the entire spin state of the electron. These results can be understood qualitatively through the large detuning $\nu_N \ll \nu_e$, meaning that the nuclei sense only the slowly varying average electron polarization s_z. Conversely, since $\nu_e > N\nu_N$ the nuclei do not have enough energy to flip the electron spin, which therefore follows adiabatically any rf-induced evolution of the nuclear spin polarization [62].

If all electron spin superpositions had equal probabilities, the linear response of the measurement apparatus $I_{z,k,Fin} \approx s_{z,Init}$ would have resulted in a nearly uniform distribution of the single-shot NMR signals, calculated and shown by the dashed line in Fig. 3(c). And yet the measurements yield a sharp bimodal distribution, revealing the energy eigenstates $s_z = \pm 1/2$ as a preferential basis. Quantum mechanics does not prescribe any preferential eigenbasis toward which the superpositions should decohere. Such a preferential basis can arise from the interaction of the qubit with the environment, known as einselection [61,63]. The nuclear spin environment has been ruled out above—its energy is too small to "project" the high-energy electron spin qubit into the $s_z = \pm 1/2$ eigenstates. We also argue that "projection" of nuclear spin polarization itself, e.g., by the optical probe, is unlikely (Supplemental Material, Sec. 3C [24]). By contrast, the lattice vibrations (phonons) are known to be the high-energy environment that drives electron spin relaxation, enabled by spin-orbit mixing [64–70]. We therefore conjecture that the phonons are responsible for einselection and quantum jumps.

The inverse dependence of $T_{1,e}$ on B_z (see Supplemental Material, Sec. 5 [24]) confirms the dominant role of the phonons [64–70]. The effective spin-phonon coupling is $\propto (\hat{s}_x\mathcal{E}_x - \hat{s}_y\mathcal{E}_y)$, where $\mathcal{E}_{x,y}$ are the Cartesian components of the phonon-induced piezo-strain electric field [64]. This form of interaction suggests that electron spin quantum jumps are driven by quasiresonant electric fields, occurring in the form of short ($\ll 10$ μs) random bursts, separated by long (milliseconds) random intervals. The QND nature of the measurement assures that the observed jumps are a spontaneous equilibrium process [71], as opposed to previous QD studies [8,13], where the observation process (continuous optical excitation) could itself induce the qubit jumps. Spontaneous collapses and burstlike revivals have been investigated in bosonic systems, such as photons [72] and phonons [73,74], and are typically associated with high mode population numbers $\bar{n} \gtrsim 100$. The appearance of spontaneous revivals at much lower average phonon numbers $\bar{n} \approx 6.8$ (for $T = 4.2$ K and $h\nu_e \approx 50$ μeV used here) is somewhat unexpected, calling for further investigation.

The measurement time $T_{rf} \approx 10$–20 μs is short compared both to $T_{1,e}$ and the electron spin coherence time $T_{2,e} \approx 100$ μs [22]. Thus, our QND readout method should allow for single-shot probing of the electron spin coherence without the burden of dynamical decoupling, required in time-averaged measurements. Conversely, a detuned rf pulse can be used to generate and study the Greenberger-Horne-Zeilinger (Schrödinger cat) nuclear states.

Finally, we discuss the broader implications of our experiments. The interpretation of quantum mechanics is a long-standing and controversial topic. The measurement problem is one of its manifestations, seeking to understand how linear quantum-mechanical evolution of the wave function turns into classical discrete measurement outcomes. Radically different hypotheses range from dynamical reduction models, which argue for nonlinear evolution and real wave function collapse, e.g., due to gravity [75], to models such as Quantum Darwinism [61,76], which seek an explanation within the standard linear evolution (see Supplemental Material, Sec. 7 [24]). At present, no experiment can resolve this dilemma. Hence, our analysis, presented below, should be treated as an open invitation for further academic debate. We argue that our results support the Quantum Darwinism perspective. While we cannot rule out wave function collapses, if only because we cannot verify effects such as gravity, we argue that such "collapses" are not necessary to describe our experiments. Our quantum system benefits from an accurate microscopic picture of the couplings between the electron, the nuclei, and the rf fields, as well as the excellent isolation of the

nuclear spins from the solid state environments [21,55]. This permits a purely linear-evolution description of the first stage of the measurement, where the fast ($T_{\mathrm{rf}} < T_{2,\mathrm{e}}, T_{2,\mathrm{N}}, T_{1,\mathrm{e}}, T_{1,\mathrm{N}}$) coherent rf pulse copies the electron state s_z into nuclear states $I_{z,k}$ [see Fig. 1(d)]. Thanks to the large number $\approx 10^4$–10^5 of nuclear copies, their arithmetic sum (nuclear magnetization) is essentially a classical variable, in a sense that it is not "collapsed" by the subsequent (second stage) optical measurement. Indeed, illumination by the probe laser degrades the nuclear magnetization, but only gradually, and slowly enough to generate $\approx 10^8$ PL photons (Supplemental Material, Sec. 3C [24]), whose hyperfine spectral shifts $\pm E_{\mathrm{hf}}/2$ return the measurement outcome for the $\hat{s}_z$ quantum variable. Since a nonunitary "wave function collapse" is not needed to describe the measurement in our system, we argue that it may be a mere simplification in other settings too, invoked because the microscopic picture is missing, for example if the measurement involves coupling of the qubit to a high-energy apparatus, such as optical fields.

H. E. D. was supported by an EPSRC doctoral training grant. E. A. C. was supported by a University Research Fellowship from the Royal Society. G. G. and E. A. C. were supported by EPSRC Grant No. EP/V048333/1. A. R. acknowledges support of the Austrian Science Fund (FWF) via the Research Group FG5, I 4320, I 4380, I 3762, the Linz Institute of Technology (LIT), and the LIT Secure and Correct Systems Lab, supported by the State of Upper Austria, the European Union's Horizon 2020 research and innovation program under Grant Agreements No. 899814 (Qurope), No. 871130 (Ascent+), the QuantERA II project QD-E-QKD, and the FFG (Grant No. 891366).

S. M., S. F. C. S., and A. R. developed, grew, and processed the quantum dot samples. H. E. D. and G. G. conducted the experiments. H. E. D., G. G., and E. A. C. analyzed the data. H. E. D., E. A. C., and G. G. drafted the manuscript with input from all authors. H. E. D. and G. G. contributed equally to this letter. E. A. C. performed numerical modeling and coordinated the project.

*Corresponding author: e.chekhovich@sussex.ac.uk

[1] J. M. Elzerman, R. Hanson, L. H. Willems van Beveren, B. Witkamp, L. M. K. Vandersypen, and L. P. Kouwenhoven, Single-shot read-out of an individual electron spin in a quantum dot, Nature (London) **430**, 431 (2004).

[2] B. Hensen, W. Wei Huang, C.-H. Yang, K. Wai Chan, J. Yoneda, T. Tanttu, F. E. Hudson, A. Laucht, K. M. Itoh, T. D. Ladd, A. Morello, and A. S. Dzurak, A silicon quantum-dot-coupled nuclear spin qubit, Nat. Nanotechnol. **15**, 13 (2020).

[3] T. Meunier, I. T. Vink, L. H. Willems van Beveren, F. H. L. Koppens, H. P. Tranitz, W. Wegscheider, L. P. Kouwenhoven, and L. M. K. Vandersypen, Nondestructive measurement of electron spins in a quantum dot, Phys. Rev. B **74**, 195303 (2006).

[4] M. Veldhorst, J. C. C. Hwang, C. H. Yang, A. W. Leenstra, B. de Ronde, J. P. Dehollain, J. T. Muhonen, F. E. Hudson, K. M. Itoh, A. Morello, and A. S. Dzurak, An addressable quantum dot qubit with fault-tolerant control-fidelity, Nat. Nanotechnol. **9**, 981 (2014).

[5] R. H. Hadfield, Single-photon detectors for optical quantum information applications, Nat. Photonics **3**, 696 (2009).

[6] L. Jiang, J. S. Hodges, J. R. Maze, P. Maurer, J. M. Taylor, D. G. Cory, P. R. Hemmer, R. L. Walsworth, A. Yacoby, A. S. Zibrov, and M. D. Lukin, Repetitive readout of a single electronic spin via quantum logic with nuclear spin ancillae, Science **326**, 267 (2009).

[7] L. Robledo, H. Bernien, T. v. d. Sar, and R. Hanson, Spin dynamics in the optical cycle of single nitrogen-vacancy centres in diamond, New J. Phys. **13**, 025013 (2011).

[8] M. Raha, S. Chen, C. M. Phenicie, S. Ourari, A. M. Dibos, and J. D. Thompson, Optical quantum nondemolition measurement of a single rare earth ion qubit, Nat. Commun. **11**, 1605 (2020).

[9] J. M. Kindem, A. Ruskuc, J. G. Bartholomew, J. Rochman, Y. Q. Huan, and A. Faraon, Control and single-shot readout of an ion embedded in a nanophotonic cavity, Nature (London) **580**, 201 (2020).

[10] R. E. Evans, M. K. Bhaskar, D. D. Sukachev, C. T. Nguyen, A. Sipahigil, M. J. Burek, B. Machielse, G. H. Zhang, A. S. Zibrov, E. Bielejec, H. Park, M. Lončar, and M. D. Lukin, Photon-mediated interactions between quantum emitters in a diamond nanocavity, Science **362**, 662 (2018).

[11] M. K. Bhaskar, R. Riedinger, B. Machielse, D. S. Levonian, C. T. Nguyen, E. N. Knall, H. Park, D. Englund, M. Lončar, D. D. Sukachev, and M. D. Lukin, Experimental demonstration of memory-enhanced quantum communication, Nature (London) **580**, 60 (2020).

[12] A. N. Vamivakas, C. Y. Lu, C. Matthiesen, Y. Zhao, S. Fält, A. Badolato, and M. Atatüre, Observation of spin-dependent quantum jumps via quantum dot resonance fluorescence, Nature (London) **467**, 297 (2010).

[13] A. Delteil, Wei-bo Gao, P. Fallahi, J. Miguel-Sanchez, and A. Imamoğlu, Observation of quantum jumps of a single quantum dot spin using submicrosecond single-shot optical readout, Phys. Rev. Lett. **112**, 116802 (2014).

[14] N. O. Antoniadis, M. R. Hogg, W. F. Stehl, A. Javadi, N. Tomm, R. Schott, S. R. Valentin, A. D. Wieck, A. Ludwig, and R. J. Warburton, Cavity-enhanced single-shot readout of a quantum dot spin within 3 nanoseconds, Nat. Commun. **14**, 3977 (2023).

[15] J. Yoneda, K. Takeda, A. Noiri, T. Nakajima, S. Li, J. Kamioka, T. Kodera, and S. Tarucha, Quantum non-demolition readout of an electron spin in silicon, Nat. Commun. **11**, 1144 (2020).

[16] A. Blais, R.-S. Huang, A. Wallraff, S. M. Girvin, and R. J. Schoelkopf, Cavity quantum electrodynamics for superconducting electrical circuits: An architecture for quantum computation, Phys. Rev. A **69**, 062320 (2004).

[17] M. Rossi, D. Mason, J. Chen, Y. Tsaturyan, and A. Schliesser, Measurement-based quantum control of mechanical motion, Nature (London) **563**, 53 (2018).

[18] C. Heyn, A. Stemmann, T. Koppen, C. Strelow, T. Kipp, M. Grave, S. Mendach, and W. Hansen, Highly uniform and strain-free GaAs quantum dots fabricated by filling of self-assembled nanoholes, Appl. Phys. Lett. **94**, 183113 (2009).

[19] P. Atkinson, E. Zallo, and O. G. Schmidt, Independent wavelength and density control of uniform GaAs/AlGaAs quantum dots grown by infilling self-assembled nanoholes, J. Appl. Phys. **112**, 054303 (2012).

[20] M. Gurioli, Z. Wang, A. Rastelli, T. Kuroda, and S. Sanguinetti, Droplet epitaxy of semiconductor nanostructures for quantum photonic devices, Nat. Mater. **18**, 799 (2019).

[21] P. Millington-Hotze, S. Manna, S. F. Covre da Silva, A. Rastelli, and E. A. Chekhovich, Nuclear spin diffusion in the central spin system of a GaAs/AlGaAs quantum dot, Nat. Commun. **14**, 2677 (2023).

[22] L. Zaporski, N. Shofer, J. H. Bodey, S. Manna, G. Gillard, M. H. Appel, C. Schimpf, S. F. Covre da Silva, J. Jarman, G. Delamare, G. Park, U. Haeusler, E. A. Chekhovich, A. Rastelli, D. A. Gangloff, M. Atatüre, and C. Le Gall, Ideal refocusing of an optically active spin qubit under strong hyperfine interactions, Nat. Nanotechnol. **18**, 257 (2023).

[23] E. A. Chekhovich, I. M. Griffiths, M. S. Skolnick, H. Huang, S. F. Covre da Silva, X. Yuan, and A. Rastelli, Cross calibration of deformation potentials and gradient-elastic tensors of GaAs using photoluminescence and nuclear magnetic resonance spectroscopy in GaAs/AlGaAs quantum dot structures, Phys. Rev. B **97**, 235311 (2018).

[24] See Supplemental Material at http://link.aps.org/supplemental/10.1103/PhysRevLett.132.160804 for additional information and discussion, which includes Refs. [25–52].

[25] A. Oshiyama and S. Ohnishi, DX center: Crossover of deep and shallow states in Si-doped $Al_xGa_{1-x}As$, Phys. Rev. B **33**, 4320 (1986).

[26] P. M. Mooney, Deep donor levels (DX centers) in III-V semiconductors, J. Appl. Phys. **67**, R1 (1990).

[27] L. Zhai, M. C. Löbl, G. N. Nguyen, J. Ritzmann, A. Javadi, C. Spinnler, A. D. Wieck, A. Ludwig, and R. J. Warburton, Low-noise GaAs quantum dots for quantum photonics, Nat. Commun. **11**, 4745 (2020).

[28] G. L. Bir and G. E. Pikus, *Symmetry and Strain-induced Effects in Semiconductors* (Wiley, New York, 1974).

[29] W. A. Coish and J. Baugh, Nuclear spins in nanostructures, Phys. Status Solidi (b) **246**, 2203 (2009).

[30] E. A. Chekhovich, S. F. C. da Silva, and A. Rastelli, Nuclear spin quantum register in an optically active semiconductor quantum dot, Nat. Nanotechnol. **15**, 999 (2020).

[31] C. P. Slichter, *Principles of Magnetic Resonance* (Springer, New York, 1990).

[32] A. Ulhaq, Q. Duan, E. Zallo, F. Ding, O. G. Schmidt, A. I. Tartakovskii, M. S. Skolnick, and E. A. Chekhovich, Vanishing electron g factor and long-lived nuclear spin polarization in weakly strained nanohole-filled GaAs/AlGaAs quantum dots, Phys. Rev. B **93**, 165306 (2016).

[33] E. A. Chekhovich, M. M. Glazov, A. B. Krysa, M. Hopkinson, P. Senellart, A. Lemaître, M. S. Skolnick, and A. I. Tartakovskii, Element-sensitive measurement of the hole-nuclear spin interaction in quantum dots, Nat. Phys. **9**, 74 (2013).

[34] D. Gammon, A. L. Efros, T. A. Kennedy, M. Rosen, D. S. Katzer, D. Park, S. W. Brown, V. L. Korenev, and I. A. Merkulov, Electron and nuclear spin interactions in the optical spectra of single GaAs quantum dots, Phys. Rev. Lett. **86**, 5176 (2001).

[35] B. Eble, O. Krebs, A. Lemaître, K. Kowalik, A. Kudelski, P. Voisin, B. Urbaszek, X. Marie, and T. Amand, Dynamic nuclear polarization of a single charge-tunable InAs/GaAs quantum dot, Phys. Rev. B **74**, 081306(R) (2006).

[36] J. Skiba-Szymanska, E. A. Chekhovich, A. V. Nikolaenko, A. I. Tartakovskii, M. N. Makhonin, I. Drouzas, M. S. Skolnick, and A. B. Krysa, Overhauser effect in individual $InP/Ga_xIn_{1-x}P$ dots, Phys. Rev. B **77**, 165338 (2008).

[37] G. Ragunathan, J. Kobak, G. Gillard, W. Pacuski, K. Sobczak, J. Borysiuk, M. S. Skolnick, and E. A. Chekhovich, Direct measurement of hyperfine shifts and radio frequency manipulation of nuclear spins in individual CdTe/ZnTe quantum dots, Phys. Rev. Lett. **122**, 096801 (2019).

[38] E. A. Chekhovich, M. Hopkinson, M. S. Skolnick, and A. I. Tartakovskii, Suppression of nuclear spin bath fluctuations in self-assembled quantum dots induced by inhomogeneous strain, Nat. Commun. **6**, 6348 (2015).

[39] M. Atature, J. Dreiser, A. Badolato, A. Hogele, K. Karrai, and A. Imamoğlu, Quantum-dot spin-state preparation with near-unity fidelity, Science **312**, 551 (2006).

[40] W. T. Wenckebach, The solid effect, Appl. Magn. Reson. **34**, 227 (2008).

[41] E. A. Chekhovich, M. N. Makhonin, K. V. Kavokin, A. B. Krysa, M. S. Skolnick, and A. I. Tartakovskii, Pumping of nuclear spins by optical excitation of spin-forbidden transitions in a quantum dot, Phys. Rev. Lett. **104**, 066804 (2010).

[42] C. Schimpf, M. Reindl, P. Klenovský, T. Fromherz, S. F. Covre Da Silva, J. Hofer, C. Schneider, S. Höfling, R. Trotta, and A. Rastelli, Resolving the temporal evolution of line broadening in single quantum emitters, Opt. Express **27**, 35290 (2019).

[43] C.-P. Yang, Y.-x. Liu, and F. Nori, Phase gate of one qubit simultaneously controlling n qubits in a cavity, Phys. Rev. A **81**, 062323 (2010).

[44] K. A. Serrels, E. Ramsay, P. A. Dalgarno, B. Gerardot, J. A. O'Connor, R. H. Hadfield, R. J. Warburton, and D. T. Reid, Solid immersion lens applications for nanophotonic devices, J. Nanophoton. **2**, 021854 (2008).

[45] M. Munsch, G. Wust, A. V. Kuhlmann, F. Xue, A. Ludwig, D. Reuter, A. D. Wieck, M. Poggio, and R. J. Warburton, Manipulation of the nuclear spin ensemble in a quantum dot with chirped magnetic resonance pulses, Nat. Nanotechnol. **9**, 671 (2014).

[46] J. Dubois, U. Saalmann, and J. M. Rost, Symmetry-induced decoherence-free subspaces, Phys. Rev. Res. **5**, L012003 (2023).

[47] K. S. Cujia, J. M. Boss, K. Herb, J. Zopes, and C. L. Degen, Tracking the precession of single nuclear spins by weak measurements, Nature (London) **571**, 230 (2019).

[48] M. Pfender, P. Wang, H. Sumiya, S. Onoda, W. Yang, D. B. R. Dasari, P. Neumann, X.-Y. Pan, J. Isoya, R.-B. Liu, and J. Wrachtrup, High-resolution spectroscopy of single

nuclear spins via sequential weak measurements, Nat. Commun. **10**, 594 (2019).
[49] B. Young, B. Cabrera, A. Lee, and B. Dougherty, Detection of elementary particles using silicon crystal acoustic detectors with titanium transition edge phonon sensors, Nucl. Instrum. Methods Phys. Res., Sect. A **311**, 195 (1992).
[50] I. Alkhatib *et al.* (SuperCDMS Collaboration), Light dark matter search with a high-resolution athermal phonon detector operated above ground, Phys. Rev. Lett. **127**, 061801 (2021).
[51] W. H. Zurek, Decoherence, einselection, and the quantum origins of the classical, Rev. Mod. Phys. **75**, 715 (2003).
[52] A. S. Oja and O. V. Lounasmaa, Nuclear magnetic ordering in simple metals at positive and negative nanokelvin temperatures, Rev. Mod. Phys. **69**, 1 (1997).
[53] W. D. Knight, Nuclear magnetic resonance shift in metals, Phys. Rev. **76**, 1259 (1949).
[54] B. Urbaszek, X. Marie, T. Amand, O. Krebs, P. Voisin, P. Malentinsky, A. Högele, and A. Imamoğlu, Nuclear spin physics in quantum dots: An optical investigation, Rev. Mod. Phys. **85**, 79 (2013).
[55] G. Gillard, E. Clarke, and E. A. Chekhovich, Harnessing many-body spin environment for long coherence storage and high-fidelity single-shot qubit readout, Nat. Commun. **13**, 4048 (2022).
[56] E. A. Chekhovich, A. Ulhaq, E. Zallo, F. Ding, O. G. Schmidt, and M. S. Skolnick, Measurement of the spin temperature of optically cooled nuclei and GaAs hyperfine constants in GaAs/AlGaAs quantum dots, Nat. Mater. **16**, 982 (2017).
[57] P. Millington-Hotze, H. E. Dyte, S. Manna, S. F. C. da Silva, A. Rastelli, and E. A. Chekhovich, Approaching a fully-polarized state of nuclear spins in a semiconductor quantum dot, Nat. Commun. **15**, 985 (2024).
[58] E. A. Chekhovich, K. V. Kavokin, J. Puebla, A. B. Krysa, M. Hopkinson, A. D. Andreev, A. M. Sanchez, R. Beanland, M. S. Skolnick, and A. I. Tartakovskii, Structural analysis of strained quantum dots using nuclear magnetic resonance, Nat. Nanotechnol. **7**, 646 (2012).
[59] Q. Zhang, Y. Guo, W. Ji, M. Wang, J. Yin, F. Kong, Y. Lin, C. Yin, F. Shi, Y. Wang, and J. Du, High-fidelity single-shot readout of single electron spin in diamond with spin-to-charge conversion, Nat. Commun. **12**, 1529 (2021).
[60] T. C. Ralph, S. D. Bartlett, J. L. O'Brien, G. J. Pryde, and H. M. Wiseman, Quantum nondemolition measurements for quantum information, Phys. Rev. A **73**, 012113 (2006).
[61] W. H. Zurek, Quantum theory of the classical: Quantum jumps, Born's Rule and objective classical reality via quantum Darwinism, Phil. Trans. R. Soc. A **376**, 20180107 (2018).
[62] I. A. Merkulov, A. L. Efros, and M. Rosen, Electron spin relaxation by nuclei in semiconductor quantum dots, Phys. Rev. B **65**, 205309 (2002).
[63] M. Schlosshauer, Decoherence, the measurement problem, and interpretations of quantum mechanics, Rev. Mod. Phys. **76**, 1267 (2005).
[64] A. V. Khaetskii and Y. V. Nazarov, Spin-flip transitions between Zeeman sublevels in semiconductor quantum dots, Phys. Rev. B **64**, 125316 (2001).
[65] S. I. Erlingsson and Y. V. Nazarov, Hyperfine-mediated transitions between a Zeeman split doublet in GaAs quantum dots: The role of the internal field, Phys. Rev. B **66**, 155327 (2002).
[66] L. M. Woods, T. L. Reinecke, and Y. Lyanda-Geller, Spin relaxation in quantum dots, Phys. Rev. B **66**, 161318(R) (2002).
[67] M. Kroutvar, Y. Ducommun, D. Heiss, M. Bichler, D. Schuh, G. Abstreiter, and J. J. Finley, Optically programmable electron spin memory using semiconductor quantum dots, Nature (London) **432**, 81 (2004).
[68] C.-Y. Lu, Y. Zhao, A. N. Vamivakas, C. Matthiesen, S. Fält, A. Badolato, and M. Atatüre, Direct measurement of spin dynamics in InAs/GaAs quantum dots using time-resolved resonance fluorescence, Phys. Rev. B **81**, 035332 (2010).
[69] L. C. Camenzind, L. Yu, P. Stano, J. D. Zimmerman, A. C. Gossard, D. Loss, and D. M. Zumbühl, Hyperfine-phonon spin relaxation in a single-electron GaAs quantum dot, Nat. Commun. **9**, 3454 (2018).
[70] G. Gillard, I. M. Griffiths, G. Ragunathan, A. Ulhaq, C. McEwan, E. Clarke, and E. A. Chekhovich, Fundamental limits of electron and nuclear spin qubit lifetimes in an isolated self-assembled quantum dot, npj Quantum Inf. **7**, 43 (2021).
[71] M. Hatridge, S. Shankar, M. Mirrahimi, F. Schackert, K. Geerlings, T. Brecht, K. M. Sliwa, B. Abdo, L. Frunzio, S. M. Girvin, R. J. Schoelkopf, and M. H. Devoret, Quantum back-action of an individual variable-strength measurement, Science **339**, 178 (2013).
[72] J. H. Eberly, N. B. Narozhny, and J. J. Sanchez-Mondragon, Periodic spontaneous collapse and revival in a simple quantum model, Phys. Rev. Lett. **44**, 1323 (1980).
[73] V. Hizhnyakov, Relaxation jumps of strong vibration, Phys. Rev. B **53**, 13981 (1996).
[74] O. V. Misochko, M. Hase, K. Ishioka, and M. Kitajima, Observation of an amplitude collapse and revival of chirped coherent phonons in bismuth, Phys. Rev. Lett. **92**, 197401 (2004).
[75] A. Bassi and G. Ghirardi, Dynamical reduction models, Phys. Rep. **379**, 257 (2003).
[76] W. H. Zurek, Quantum Darwinism, Nat. Phys. **5**, 181 (2009).

Supplemental Material: Is Wave Function Collapse Necessary? Explaining Quantum Nondemolition Measurement of a Spin Qubit within Linear Evolution

Harry E. Dyte and George Gillard
Department of Physics and Astronomy, University of Sheffield, Sheffield S3 7RH, United Kingdom

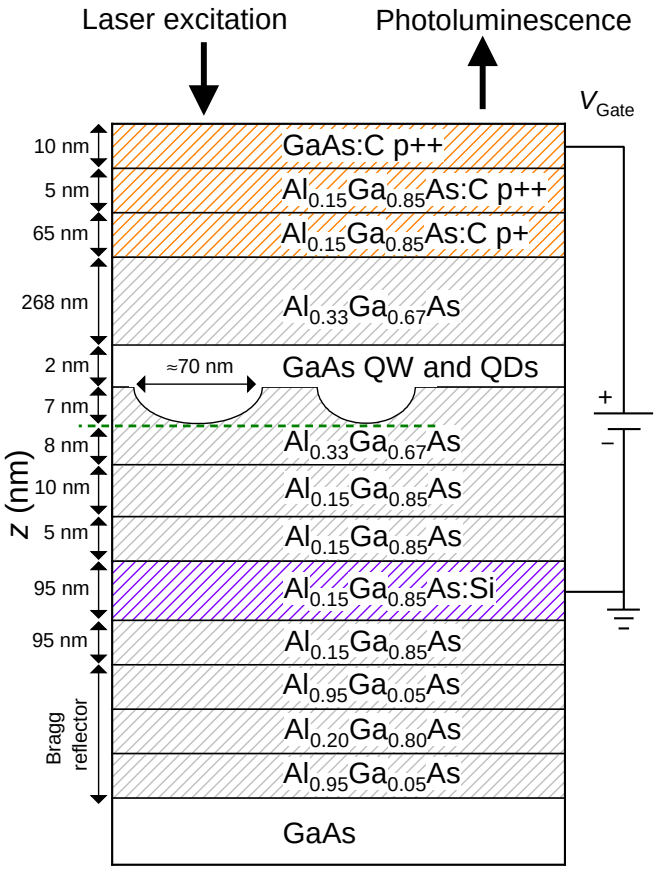
Santanu Manna, Saimon F. Covre da Silva, and Armando Rastelli
Institute of Semiconductor and Solid State Physics,
Johannes Kepler University Linz, Altenberger Strasse 69, 4040 Linz, Austria

Evgeny A. Chekhovich*
Department of Physics and Astronomy, University of Sheffield, Sheffield S3 7RH, United Kingdom and
Department of Physics and Astronomy, University of Sussex, Brighton BN1 9QH, United Kingdom

Supplementary Section 1. SAMPLE STRUCTURE

The sample structure used in this work is the same semiconductor wafer that was used previously in Refs. [1–3]. The sample is grown using molecular beam epitaxy (MBE) on a semi-insulating GaAs (001) substrate. The layer sequence of the semiconductor structure is shown in Supplementary Fig. 1. The growth starts with a layer of $Al_{0.95}Ga_{0.05}As$ followed by a single pair of $Al_{0.2}Ga_{0.8}As$ and $Al_{0.95}Ga_{0.05}As$ layers acting as a Bragg reflector in optical experiments. Then, a 95 nm thick layer of $Al_{0.15}Ga_{0.85}As$ is grown, followed by a 95 nm thick layer of $Al_{0.15}Ga_{0.85}As$ doped with Si at a volume concentration of 1.0×10^{18} cm^{-3}. The low Al concentration of 0.15 in the Si doped layer mitigates the issues caused by the deep DX centers [4–6]. The n-type doped layer is followed by the electron tunnel barrier layers: first a 5 nm thick $Al_{0.15}Ga_{0.85}As$ layer is grown at a reduced temperature of 560 °C to suppress Si segregation, followed by a 10 nm thick $Al_{0.15}Ga_{0.85}As$ and then a 15 nm thick $Al_{0.33}Ga_{0.67}As$ layer grown at 600 °C. Aluminium droplets are grown on the surface of the $Al_{0.33}Ga_{0.67}As$ layer and are used to etch the nanoholes [7, 8]. Atomic force microscopy shows that typical nanoholes have a depth of ≈ 6.5 nm and are ≈ 70 nm in diameter [1]. Next, a 2.1 nm thick layer of GaAs is grown to form QDs by infilling the nanoholes as well as to form the quantum well (QW) layer. Thus, the maximum height of the QDs in the growth z direction is ≈ 9 nm. The GaAs layer is followed by a 268 nm thick $Al_{0.33}Ga_{0.67}As$ barrier layer.

* e.chekhovich@sussex.ac.uk



Supplementary Figure 1. Schematic of the quantum dot sample structure.

Finally, the p-type contact layers doped with C are grown: a 65 nm thick layer of $Al_{0.15}Ga_{0.85}As$ with a 5×10^{18} cm^{-3} doping concentration, followed by a 5 nm thick layer of $Al_{0.15}Ga_{0.85}As$ with a 9×10^{18} cm^{-3} concentration, and a 10 nm thick layer of GaAs with a 9×10^{18} cm^{-3} concentration.

The sample is processed into a p-i-n diode structure. Mesa structures with a height of 250 nm are formed by etching away the p-doped layers and depositing Ni(10 nm)/AuGe(150 nm)/Ni(40 nm)/Au(100 nm) on the etched areas. The sample is then annealed to enable diffusion down to the n-doped layer to form the ohmic back contact. The top gate contact is formed by depositing Ti(15 nm)/Au(100 nm) on to the p-type surface of the mesa areas. Quantum dot photoluminescence (PL) is excited and collected through the top of the sample. The sample gate bias V_{Gate} is the bias of the p-type top contact with respect to the grounded n-type back contact. Due to the large thickness of the top $Al_{0.33}Ga_{0.67}As$ layer, the tunneling of holes is suppressed, whereas tunnel coupling to the n-type layer enables deterministic charging of the quantum dots with electrons by changing V_{Gate}.

In order to resolve the quadrupolar components of the nuclear magnetic resonance (NMR) spectra, the semiconductor sample used in most experiments of this work is subject to a uniaxial mechanical stress. To this end, the semiconductor wafer is first cleaved into a small piece with a rectangular surface area of 0.7 mm × 2.35 mm. The edges of the rectangular profile are aligned along the [110] and [1$\bar{1}$0] crystallographic directions. The thickness of the sample along the [001] growth direction is 0.35 mm. Thus, the sample is shaped as a parallelepiped. The sample is then inserted into a home-made stress cell. This is done in such a way that the two 0.7 mm × 0.35 mm surfaces of the sample are contacted to the flat titanium surfaces of the stress cell bracket. A titanium screw is then used to apply compressive stress, directed along the 2.35 mm long edge of the sample. For some of the supporting experiments we use an unstrained piece of the same sample, which is noted in the text.

Supplementary Section 2. ELECTRON-NUCLEAR SPIN SYSTEM

The crystal lattice of a semiconductor is a many-body system, where the interactions between the electrons of the individual atoms results in a complicated spectrum of electronic states. Finding the exact spectrum of the many-body electronic states is a difficult problem. However, in many cases a simplified description is sufficiently accurate. In semiconductors, electronic states form well-defined bands. In pure GaAs at zero temperature, the uppermost valence band is completely filled, while the lowest conduction band is separated by a large energy gap (≈ 1.519 eV) and thus remains empty. As a result, neither band contributes to transport or spin effects. By doping the semiconductor (e.g. Si doping in GaAs) it is possible to introduce additional electrons, which occupy the lowest-energy available states in the conduction band. While the crystal is still a many-body system, at low doping concentration each additional electron behaves in many ways as a free electron in vacuum, but with a different effective mass ($m^* \approx 0.067 m_\mathrm{e}$ in GaAs, where m_e is the free electron mass).

The state of a conduction band electron can be described by a two-component spinor $\psi = \{\psi_\uparrow(\mathbf{r}), \psi_\downarrow(\mathbf{r})\}$, which satisfies the Schrödinger-Pauli equation (§17 in [9]). The spin-up $\psi_\uparrow(\mathbf{r})$ and spin-down $\psi_\downarrow(\mathbf{r})$ components, with spin projections $s_\mathrm{z} = +1/2$ and $s_\mathrm{z} = -1/2$ respectively, are both functions of the electron coordinate vector $\mathbf{r}$. The spatial profile of $\psi_\uparrow(\mathbf{r})$ is in general distinct from that of $\psi_\downarrow(\mathbf{r})$. However, for an electron trapped in a quantum dot, we can assume with good accuracy that the components of the spinor have the same spatial profile. The wave function $\psi = \{\alpha_\uparrow, \alpha_\downarrow\}\phi(\mathbf{r})$ can then be factored into the orbital part $\phi(\mathbf{r})$ and a spin part, represented by a

spin vector $\{\alpha_\uparrow, \alpha_\downarrow\}$, which does not depend on the spatial coordinates. In essence, this corresponds to projecting the quantum state onto the spin subspace [10]. The resulting "spin wave function" $\{\alpha_\uparrow, \alpha_\downarrow\}$ is an approximation, which is commonly implied when considering solid-state electron spin qubits.

The "spin wave function" approximation has its limitations. In the case of electrons in semiconductor quantum dots this is due to the spin-orbit interaction. The ground orbital state with spin projection $s_\mathrm{z} = \pm 1/2$ has some finite admixture of the higher orbitals with the opposite spin projection $s_\mathrm{z} = \mp 1/2$. Such admixture is what enables electron spin relaxation through interaction with acoustic phonons [11–13]. The electron spin relaxation time $T_{1,\mathrm{e}}$ is found in this work to be in a millisecond range. Moreover, electron spin coherence times measured recently on QDs from the same sample reach $T_{2,\mathrm{e}} \approx 100$ μs. These intrinsic timescales can be used to characterize the deviation from the "spin wave function" approximation. Crucially, $T_{1,\mathrm{e}}$ and $T_{2,\mathrm{e}}$ are significantly longer than the typical duration $T_\mathrm{rf} \approx 10 - 20$ μs of the rf pulse used to copy the electron spin projection s_z into the nuclear spins. The same argument applies to the nuclear spins, whose lifetimes $T_{1,\mathrm{N}} \approx 1 - 10$s [1] and coherence times $T_{2,\mathrm{N}} \approx 1 - 10$ ms [14, 15] are significantly longer than $T_\mathrm{rf} \approx 10 - 20$ μs. Thus, during the intervals between the low-probability phonon-induced jumps of the electron spin the measurement of the electron spin can be described as a coherent (unitary) evolution of the electron-nuclear "spin wave function".

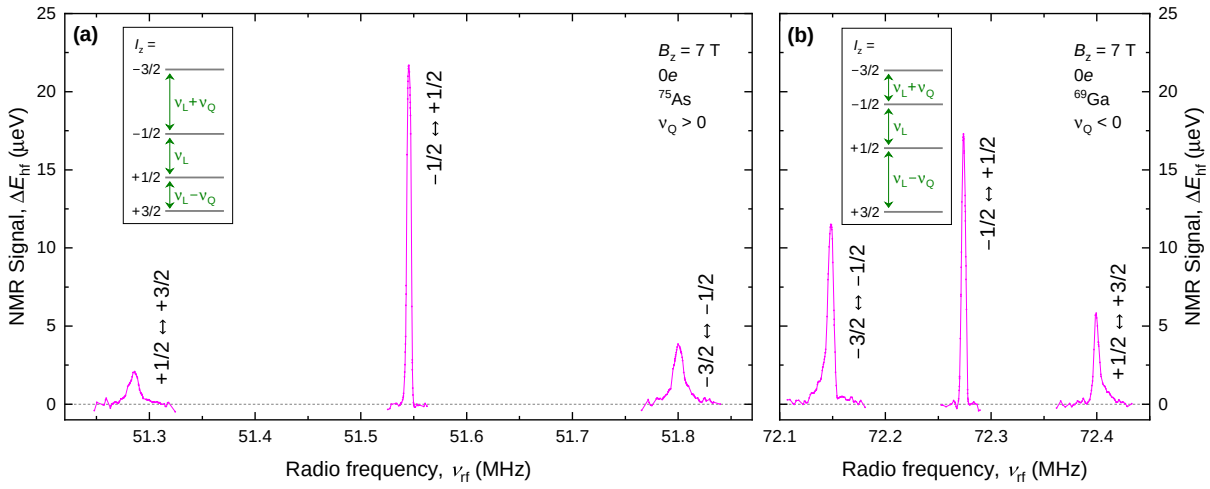
The Hamiltonian describing the nuclear spin system includes the magnetic dipole (Zeeman) and the electric quadrupolar terms. We also consider the magnetic dipole-dipole interactions between the nuclei. The Zeeman term accounts for the coupling of the QD nuclear spins $\mathbf{I}_k$ to the static magnetic field B_z directed along the z axis:

$$\mathcal{H}_\mathrm{Z,N} = -\sum_{k=1}^{N} \hbar \gamma_k B_\mathrm{z} \hat{I}_{\mathrm{z},k}, \tag{S1}$$

where the summation goes over all individual nuclei $1 \leq k \leq N$, $\hbar = h/(2\pi)$ is the reduced Planck's constant, γ_k is the gyromagnetic ratio of the k-th nuclear spin and $\hat{\mathbf{I}}_k$ is a vector of spin operators with Cartesian components $(\hat{I}_{\mathrm{x},k}, \hat{I}_{\mathrm{y},k}, \hat{I}_{\mathrm{z},k})$. The result of the Zeeman term alone is a spectrum of equidistant single-spin eigenenergies $-I_\mathrm{z} \hbar \gamma_k B_\mathrm{z}$. These $2I + 1$ states are also the eigenstates of the $\hat{I}_\mathrm{z}$ spin projection operator with eigenvalues I_z satisfying $-I \leq I_\mathrm{z} \leq +I$.

The interaction of the nuclear electric quadrupolar moment with the electric field gradients is described by the term (Ch. 10 in Ref. [17]):

$$\mathcal{H}_\mathrm{Q,N} = \sum_{k=1}^{N} \frac{q_k}{6} [3\hat{I}^2_{\mathrm{z}',k} - I^2_k + \eta_k (\hat{I}^2_{\mathrm{x}',k} - \hat{I}^2_{\mathrm{y}',k})], \tag{S2}$$



Supplementary Figure 2. Nuclear magnetic resonance spectra of a single GaAs/AlGaAs quantum dot. (a) ^{75}As spectrum. (b) ^{69}Ga spectrum. All spectra are measured with the inverse NMR technique [16] at $B_z \approx 7$ T in a neutral QD state ($0e$). Insets show the energy level diagrams of the spin-3/2 nuclei in strong external magnetic field B_z.

where q_k and η_k describe the magnitude and asymmetry of the electric field gradient tensor, whose principal axes are $x'y'z'$. The strain is inhomogeneous within the QD volume, so that q_k and η_k vary between the individual nuclei. The axes $x'y'z'$ are different for each nucleus and generally do not coincide with crystallographic axes or magnetic field direction. For the as-grown (unstrained) GaAs/AlGaAs QDs the most likely quadrupolar shift is around $|q_k|/h \approx 24$ kHz [1, 18]. The full width at half maximum of the $|q_k|/h$ distribution is ≈ 14 kHz. For a small fraction of arsenic nuclei, adjacent to aluminium atoms, the shifts are as large as $|q_k|/h \approx 200$ kHz [2]. In the strained sample structure, q_k are dominated by the extrinsic uniaxial stress. All experiments are conducted under sufficiently strong magnetic fields, where $|\hbar\gamma_k B_z| \gg |q_k|$ and quadrupolar effects can be treated perturbatively. In this perturbative regime, the main effect of the quadrupolar shifts is the anharmonicity of the nuclear spin eigenenergies and the resulting quadrupolar NMR multiplet of $2I$ magnetic-dipole transitions, split by $\nu_Q \approx q_k/h$. The $I_z = \pm 1/2$ projection states of a half-integer nuclear spin are influenced by quadrupolar effects only in the second order. These second order shifts scale as $\propto \nu_Q^2/\nu_N$, where $\nu_N = \gamma B_z/(2\pi)$ is the nuclear spin Larmor frequency. Under typical experimental conditions the second order shifts do not exceed ≈ 1 kHz.

The nuclear spin energy spectrum is probed using optically-detected NMR spectroscopy of individual QDs. Supplementary Fig. 2 shows the NMR spectra of ^{75}As (a) and ^{69}Ga (b) spin-3/2 nuclei measured on an empty ($0e$) QD in a strained sample. The insets show the corresponding

diagrams of the nuclear spin energy levels and the allowed magnetic dipole NMR transitions. As expected for $I = 3/2$, each NMR spectrum is a triplet. The first order quadrupolar shifts are $\nu_{\mathrm{Q}} \approx +260$ kHz and $\nu_{\mathrm{Q}} \approx -125$ kHz for ^{75}As and ^{69}Ga, respectively. The signs of ν_{Q} are opposite due to the opposite signs of the gradient elastic tensors of the group-III and group-V elements [19]. The quadrupolar shifts are the witnesses of the strain induced by the external stress. The strain is estimated to be $\epsilon_{\mathrm{b}} \approx 0.0025$.

Direct interaction between the nuclei is described by the dipole-dipole Hamiltonian:

$$\mathcal{H}_{\mathrm{DD}} = \sum_{1 \leq j < k \leq N} b_{j,k} \left(3 \hat{I}_{\mathrm{z},j} \hat{I}_{\mathrm{z},k} - \hat{\mathbf{I}}_j \cdot \hat{\mathbf{I}}_k \right), \qquad b_{j,k} = \frac{\mu_0 \hbar^2}{4\pi} \frac{\gamma_j \gamma_k}{2} \frac{1 - 3\cos^2 \theta_{j,k}}{r_{j,k}^3} \tag{S3}$$

Here, $\mu_0 = 4\pi \times 10^{-7}$ NA^{-2} is the magnetic constant and $r_{j,k}$ denotes the length of the vector, which forms an angle θ with the z axis and connects the two spins j and k. The Hamiltonian of Supplementary Eq. (S3) has been truncated to eliminate all spin non-conserving terms – this is justified for static magnetic field exceeding $\gtrsim 1$ mT. The typical magnitude of the interaction constants for the nearby nuclei in GaAs is $\max(|b_{j,k}|)/h \approx 100$ Hz. Consequently, the typical timescales of the processes driven by the many-body dipole-dipole interactions are on the order of 1 ms. This is much slower than the duration of the QND measurement $T_{\mathrm{rf}} \approx 10$ μs. As a result, nuclear-nuclear interactions play only a minor role in the context of the current work.

The interaction of the conduction band electron spin $\mathbf{s}$ with the ensemble of the QD nuclear spins is dominated by the contact (Fermi) hyperfine interaction, with the following Hamiltonian:

$$\mathcal{H}_{\mathrm{hf}} = \sum_{k=1}^{N} a_k (\hat{s}_{\mathrm{x}} \hat{I}_{\mathrm{x},k} + \hat{s}_{\mathrm{y}} \hat{I}_{\mathrm{y},k} + \hat{s}_{\mathrm{z}} \hat{I}_{\mathrm{z},k}), \tag{S4}$$

where the hyperfine constant of an individual nucleus k is $a_k = A^{(k)} |\psi(\mathbf{r}_k)|^2 v$. Unlike a_k, the hyperfine constant $A^{(k)}$ is a parameter describing only the material and the isotope type to which nucleus k belongs, $|\psi(\mathbf{r}_k)|^2$ is the density of the electron envelope wave function at the nuclear site $\mathbf{r}_k$ of the crystal lattice, and v is the crystal volume per one cation or one anion.

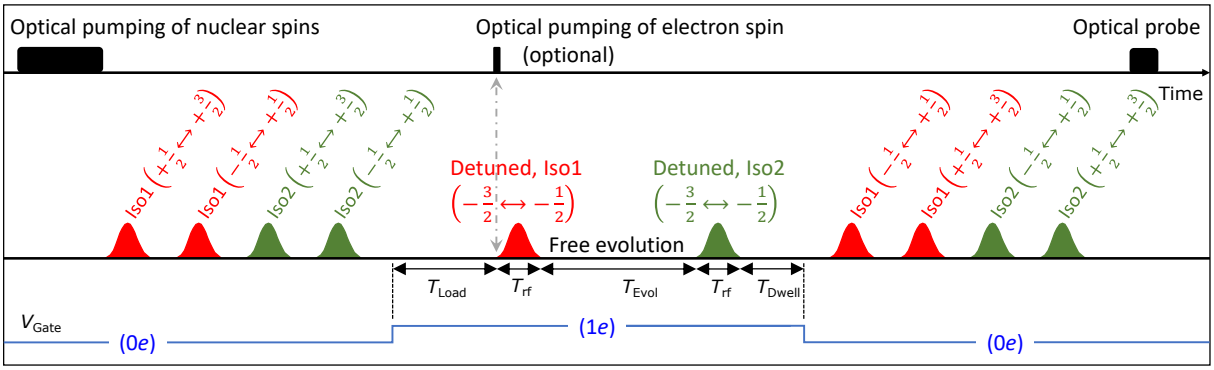
The definitions of the hyperfine constants differ between different sources. With the definition adopted here, a fully polarized isotope with spin I, hyperfine constant A and a 100% abundance (e.g. ^{75}As), would shift the energies of the electron spin states $s_{\mathrm{z}} = \pm 1/2$ by $\pm AI/2$, irrespective of the shape of $|\psi(\mathbf{r})|^2$. With such a definition, the typical values in GaAs are $A \approx 50$ μeV (Ref. [20]). The frequency Knight shift of an individual nucleus coupled to a polarized electron with spin projection $s_{\mathrm{z}} = \pm 1/2$ is $\pm a_k/(2h)$. The typical Knight shift can be estimated from the

histograms of the frequency-detuned single-cycle (single-shot) NMR spectra shown in Fig. 2(b) of the main text. The peak (i.e. most likely) value is found to be $a_k/(h) \approx 140$ kHz or $a_k \approx 0.58$ neV for the ^{69}Ga isotope. Taking the ratio A/a_k we roughly estimate the effective number of nuclei $N \approx 10^5$ coupled to the QD electron spin. This is in agreement with $N \approx 6.5 \times 10^4$ estimated recently from electron spin dephasing times in the same QDs [2]. The largest $a_k/(h) \approx 400$ kHz are found for the nuclei at the center of the QD, decreasing to zero with an increasing distance from the QD center. This is evidenced through an inhomogeneous broadening of the $1e$ NMR spectra (Fig. 2(b) of the main text). For most nuclei the hyperfine constant a_k is larger than the deviation of the quadrupolar shift $|q_k|$ from its peak value. Thus, when the QD is charged with a single electron, the Knight field inhomogeneous broadening dominates over the quadrupolar inhomogeneous broadening.

The hyperfine interaction of the valence band holes is an order of magnitude smaller than the hyperfine interaction of the conduction band electrons [21] and can therefore be ignored in the context of this work.

Supplementary Section 3. EXPERIMENTAL DETAILS AND CALIBRATION RESULTS

The sample is placed in a liquid helium bath cryostat with a base temperature of ≈ 4.2 K. A superconducting coil is used to apply magnetic fields up to $B_z = 8$ T. The field is parallel to the sample growth direction [001] and the optical axis z (Faraday geometry). The field and the optical axis are orthogonal to the direction of the applied mechanical stress. We use a confocal microscopy configuration. An aspheric lens with a focal distance of 1.45 mm and NA = 0.58 is used as an objective for optical excitation of the QD and for photoluminescence (PL) collection. The excitation laser is focused into a spot with a diameter of ≈ 1 μm. The collected PL is analysed in a two-stage Czerny-Turner spectrometer. In each stage the light is first collimated and directed to a plane diffraction grating. Upon dispersion, the light is focused by a mirror with a 1 m focal length. The spectrometer is followed by a pair of achromatic lens doublets, which transfers the spectral image onto a charge-coupled device (CCD) photo-detector with a magnification of 3.75. The changes in the spectral splitting ΔE_{PL} of either a neutral exciton X^0 or a negatively charged trion X^-, derived from the PL spectra, are used to measure the hyperfine shifts E_{hf}, which are proportional to the nuclear spin polarization degree. Mechanical shutters are used to form pump and probe laser pulses, as well as to block the input of the optical spectrometer during the optical pump pulse.



Supplementary Figure 3. Timing diagram of the pulsed nuclear magnetic resonance experiment.

Supplementary Fig. 3 is a detailed version of Fig. 1(e) of the main text and shows the timing of a pulsed single-cycle NMR measurement. In what follows we describe the individual steps of the timing sequence.

A. Optical pumping of the quantum dot nuclear spins

Optical pumping of the QD nuclear spin polarization (labelled Pump in Supplementary Fig. 3) is achieved using the emission of a tunable single-mode circularly polarized diode laser. Optical dynamical nuclear spin polarization is a well known process, that has been observed in many types of QDs [18, 22–25], see Ref. [26] for a review. In the context of the present study, we simply use the fact that optical pumping is a reliable tool for achieving nuclear spin polarizations exceeding 50% on a timescale of a few seconds. The physics of nuclear spin pumping in the semiconductor wafer studied here are discussed in Ref. [3]. In brief, dynamic nuclear polarization is a three-stage cyclic process. At the first stage a spin polarized electron is created optically. This is made possible by the selection rules, which allow conversion of the circularly polarized photons into spin-polarized electron-hole pairs in group III-V semiconductors. At the second stage, the electron exchanges its spin with one of the nuclei through the flip-flop term of the electron-nuclear hyperfine Hamiltonian (Supplementary Eq. S4). The third stage is the electron-hole optical recombination or tunnel escape, which removes the flipped electron. This final step is required in order to let the QD accept new spin-polarized electrons and continue polarizing the ensemble of $N \approx 10^5$ nuclear spins of the QD. During the optical pumping the sample gate is set to a large reverse bias, typically $V_{\mathrm{Gate}} = -2$ V. The pump power is ≈ 1 mW, which is three orders of magnitude higher than the ground-state PL saturation power. The photon energy of the pump laser is typically $\approx 5 - 10$ meV

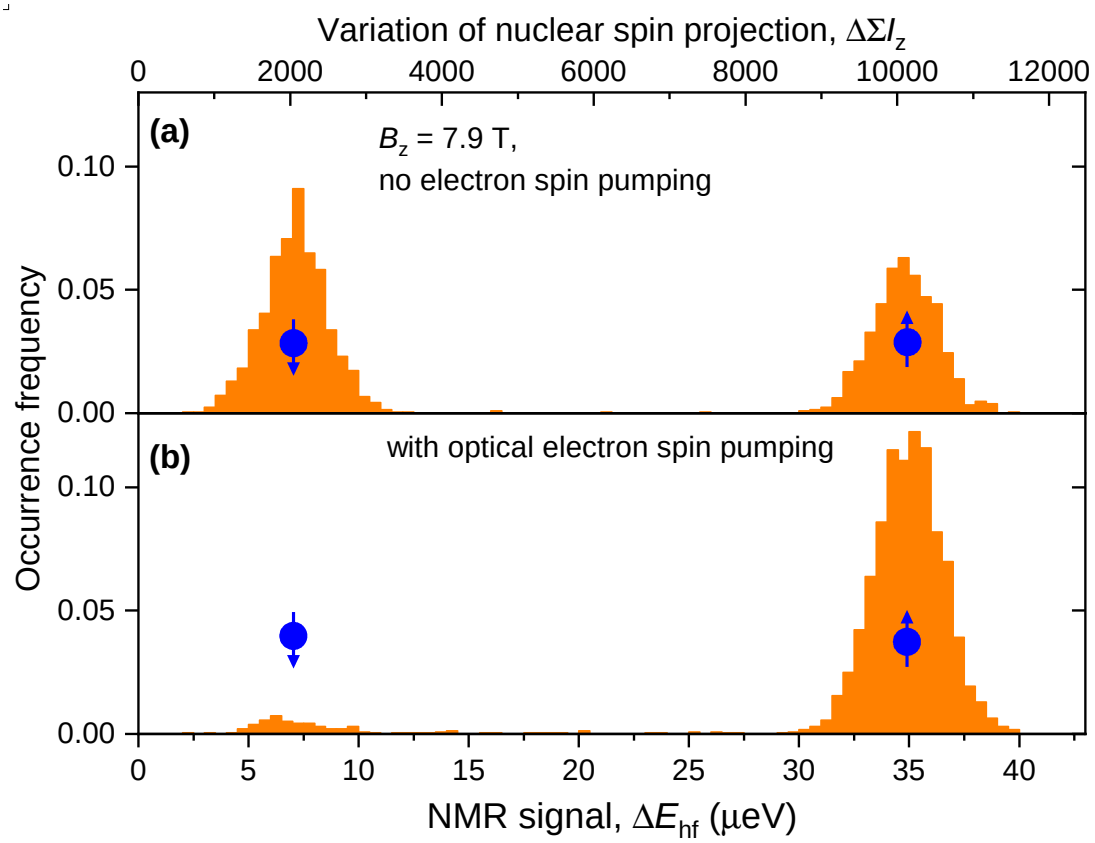
above the X^0 PL energy. The pump duration is $T_{\mathrm{Pump}} = 3.5$ s. A 10 ms delay is introduced after the pump pulse to ensure the mechanical shutter, which forms the laser pulse, is fully closed.

B. Nuclear magnetic resonance

The oscillating magnetic field $B_{\mathrm{x}} \perp z$, required to perform NMR, is produced by a copper wire coil placed at a distance of ≈ 0.5 mm from the QD sample. The coil is made of 10 turns of a 0.1 mm diameter enamelled copper wire wound on a ≈ 0.4 mm diameter spool in 5 layers, with 2 turns in each layer. The coil is driven by a class-AB radiofrequency (rf) amplifier (Tomco BT01000-AlphaSA rated up to 1000 W) which is fed by the output of an arbitrary waveform generator Keysight M8190.

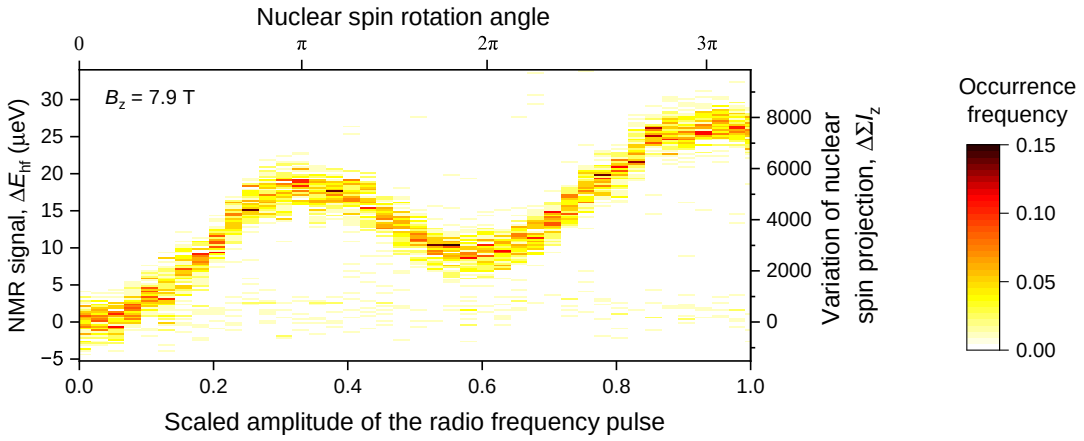
Supplementary Fig. 3 shows the timing diagram of a two-pulse experiment, which we now discuss in more detail. We consider the case of σ^+ polarized optical pump, which produces a Boltzmann distribution of the nuclear spin z projections [3], populating predominantly the $I_z = -3/2$ nuclear spin state, while leaving the $I_z = +3/2$ state the least populated. The electron to nuclear spin state transfer is performed using the $-3/2 \leftrightarrow -1/2$ NMR transition. In order to increase the NMR signal, we maximize the initial population difference of the $I_z = -3/2, -1/2$ nuclear states. This is achieved through state population transfer [27]. A pair of rf pulses performing π rotations (i.e. inversions) is applied to each of the two isotopes used in the experiment. First, the $+1/2 \leftrightarrow +3/2$ transition is driven to exchange the populations of the $I_z = +1/2, +3/2$ states of the first isotope (labelled "Iso1" in Supplementary Fig. 3), making $I_z = +1/2$ the least populated state. The second π pulse applied to the $-1/2 \leftrightarrow +1/2$ transition transfers the smallest population to $I_z = -1/2$. The same population-transfer sequence is applied to the second isotope (labelled "Iso2" in Supplementary Fig. 3). The state transfer is performed under reverse bias, which keeps the QD empty of all charges ($0e$). The absence of charges eliminates the Knight shifts, thus maximizing the fidelity of the state transfer performed by the NMR pulses. The individual pulses of the population transfer sequences are separated by 1 ms delays, sufficiently long to dephase any unwanted coherence of the nuclear spin ensemble, which may arise from the imperfect pulse rotations.

Following the NMR state transfer, the sample gate bias is increased in order to load a single electron from the Fermi reservoir into the QD ($1e$ charge state). The actual electron tunneling takes place on a submicrosecond timescale. However, the electron is then left to equilibrate for a time interval T_{Load}. We typically use $T_{\mathrm{Load}} \in [30, 90]$ ms. This is much longer than the measured



Supplementary Figure 4. (a) Histograms of the single-cycle NMR signals $\Delta E_{\rm hf}$ measured at $B_{\rm z} = 7$ T with a rf π pulse detuned by -30 kHz (i.e. to lower frequencies) from the $-1/2 \leftrightarrow +1/2$ transition. Without loss of generality, in this particular experiment we use an unstrained piece of the same QD sample, where the quadrupolar splitting of ^{75}As is $\nu_{\rm Q} \approx +24$ kHz. The rf pulse performs approximately a non-selective π rotation of the entire spin-3/2 state. (b) Same as (a) but with an optical electron spin pumping pulse. The top horizontal axis shows the NMR signal in terms of the variation $\Delta\Sigma I_z$ of the total spin projection ΣI_z of the QD nuclei. The variation is estimated as $\Delta\Sigma I_z \approx N\Delta E_{\rm hf}/(3F_{\rm tot})$, where the factor of 3 accounts for the amplification of the reverse population transfer, $N \approx 65000$ is the estimated number of nuclear spins in a QD [2], and $IF_{\rm tot} \approx 112$ μeV is the hyperfine shift of the fully polarized $I = 3/2$ nuclei measured in the studied type of QDs [3].

electron spin lifetimes $T_{1,\rm e}$, ensuring that any transient effects decay before the electron spin state is measured. Due to the small electron g-factor in the studied QDs ($g_{\rm e,z} \approx -0.1$), the equilibrium electron spin polarization is small. Supplementary Fig. 4(a) shows a histogram of electron spin readouts collected at $B_{\rm z} = 7$ T. Fitting reveals a small electron spin polarization $\rho_{\rm e} \approx -0.11$. In Supplementary Fig. 4(b) we show for reference a histogram collected in a similar experiment but with a 100 μs long quasiresonant optical pulse applied at the end of the $T_{\rm Load}$ interval and before the first detuned rf pulse. A non-equilibrium electron spin polarization of $\rho_{\rm e} \approx 0.91$ is observed,



Supplementary Figure 5. Calibration measurement of the nuclear spin Rabi oscillations in presence of a spin polarized electron. Histograms of the single-cycle ^{75}As NMR signals $\Delta E_{\rm hf}$ measured at $B_{\rm z} = 7.9$ T with a detuned rf π pulse of a variable amplitude. The rf pulse amplitude is shown on the bottom horizontal axis normalized by the maximum available rf amplitude. The right vertical axis shows the NMR signal in terms of the variation of the total spin projection $\Delta\Sigma I_z$ of the QD nuclei. The rf pulse duration is fixed at $T_{\rm rf} = 50$ μs (pulse FWHM $T_{\rm rf}/2 = 25$ μs). An optical pulse is used to polarise the electron spin during $T_{\rm Load}$. The rf frequency is detuned by -30 kHz from the $-1/2 \leftrightarrow +1/2$ transition in order to match the Knight-shifted NMR resonance corresponding to the preferential electron spin orientation. In this particular experiment we use an unstrained piece of the same QD sample, where the rf pulse performs approximately a non-selective rotation of the entire spin-3/2 state. Rabi oscillations up to 3π are observed and are superimposed with a monotonic growth in $\Delta E_{\rm hf}$, arising from the nuclear spin ensemble dephasing. The dephasing is a result of the limited rf pulse bandwidth (≈ 40 kHz for $T_{\rm rf}/2 = 25$ μs), which is comparable to the quadrupolar splitting and the Knight shift spectral broadening. The pulse bandwidth is in turn limited by the maximum available rf amplitude. When the required nuclear spin rotation is limited to π, which is the case in our electron spin QND measurements, the rf pulse can be shortened to $T_{\rm rf} = 10$ μs, resulting in a larger pulse bandwidth and higher fidelity of nuclear spin rotations.

demonstrating that electron spin readout via nuclear spins is compatible with optical electron spin initialization. The initialization fidelity is limited to $\rho_{\rm e} \approx 0.91$, since we implement optical electron spin pumping via QD p-shell exciton transitions. Optical initialization of the electron spin with near-unity fidelity is possible in principle using the well known spin shelving process, which takes place under resonant optical pumping of the ground state trion [28]. However, this is not the primary aim of this study, hence throughout this work the electron spin is initialized close to equilibrium using long $T_{\rm Load}$, unless stated otherwise. Equilibrium initialization results in nearly equal probabilities to detect an electron spin with $s_{\rm z} = +1/2$ and with $s_{\rm z} = -1/2$.

Following the electron equilibration, a sequence of one or more rf pulses is applied in order

to control the nuclear spins. The rf pulses are sufficiently short for the nuclear spin rotations to be coherent. This is verified in Supplementary Fig. 5, where nuclear spin Rabi oscillations are observed when the amplitude of the rf pulse is varied. In the electron spin readout experiments the sequence of rf pulses starts with a frequency-detuned π pulse applied to the $-3/2 \leftrightarrow -1/2$ transition of the first isotope ("Iso1"). The detuning is chosen to be close to the weighted average nuclear hyperfine (Knight) shift and is typically ≈ 70 kHz for ^{69}Ga in the studied QDs. This pulse performs a QND measurement of the electron spin z projection, storing the outcome in the long-lived longitudinal nuclear spin polarization of "Iso1". The electron is then left for a time T_{Evol} to evolve freely without any optical or rf excitation. This is followed by the second frequency-detuned rf π pulse applied to "Iso2" in order to perform the second QND measurement of the electron spin projection. The pulses have cosine (near-Gaussian) envelopes and a total duration T_{rf}, counted between the zero-amplitude points at the start and the end of the pulse (the corresponding full width at half maximum is $T_{\mathrm{rf}}/2$). Depending on the measurement, T_{rf} is chosen to be between 10 and 40 μs. After the detuned rf pulses, the electron and the nuclei are left to evolve freely over a time interval T_{Dwell}. We typically use $T_{\mathrm{Dwell}} \in [20, 100]$ ms, which is much longer than the nuclear spin dephasing time $T^*_{2,\mathrm{N}} \approx 50 - 250$ μs and the nuclear spin coherence time $T_{2,\mathrm{N}} \lesssim 20$ ms [14], ensuring dissipation of any remaining coherence generated by the rf pulse sequence.

The results of the QND measurements are encoded in the $I_z = -3/2, -1/2$ nuclear spin subspaces where either the $I_z = -3/2$ or the $I_z = -1/2$ states are more populated, depending on the electron spin projection state s_z. At this stage, the nuclear spin polarization can already be retrieved optically. However, it is beneficial to multiply the NMR signal, by exploiting the entire $I = 3/2$ Hilbert space. To this end, the sample is biased back into an empty-QD state ($0e$) and the reverse population transfer is performed on both isotopes. Each reverse population transfer consists of a π pulse on the $-1/2 \leftrightarrow +1/2$ NMR transition, followed by a π pulse on the $+1/2 \leftrightarrow +3/2$ NMR transition. This provides a factor of ≈ 3 amplification in the NMR signal, which can be understood as follows. If the QND frequency-detuned pulse leaves the $I_z = -3/2$ state as the most populated, then the reverse population transfer has only a small effect on the nuclear spin polarization. In the opposite case, if QND leaves the $I_z = -1/2$ state as the most populated, the reverse population transfer makes the $I_z = +3/2$ state the most populated. Thus, instead of the $I_z = -3/2, -1/2$ subspace, the reverse population transfer encodes the NMR signal in the $I_z = -3/2, +3/2$ subspace, which approximately triples the optically-detected hyperfine shift ΔE_{hf}. Just as with the population transfer, the individual pulses of the reverse population transfer sequences are separated by 1 ms delays.

In some cases it is more convenient to perform QND using the $I_z = +1/2, +3/2$ nuclear spin subspaces, or a combination, where the $I_z = +1/2, +3/2$ states are used on one of the isotopes, while the $I_z = -3/2, -1/2$ states are used for the other isotope. In such cases the initial and reverse population transfer sequences are altered to match the chosen transitions, however, the principle described above remains the same. For the two-pulse experiments shown in Fig. 3(e) of the main text, the first rf pulse is detuned to the higher frequencies from the $-3/2 \leftrightarrow -1/2$ high-frequency NMR satellite transition of ^{75}As, while the second pulse is detuned to the lower frequencies from the $-3/2 \leftrightarrow -1/2$ low-frequency satellite of ^{69}Ga. In those experiments where only one rf pulse is used on a single isotope, the timing diagram is the same as in Supplementary Fig. 3, but omitting the pulses for the second isotope.

The number of the nuclei used in the QND measurement can be estimated as follows. The root mean square number of nuclei $N \approx 6.5 \times 10^4$ has been estimated previously from the electron spin dephasing dynamics in the same QD sample [2]. Half of these nuclei are arsenic. Moreover, due to the incomplete polarization of the nuclei, only $\approx 80\%$ are in the two-level subspace (such as $I_z = -3/2, -1/2$) used for the electron spin readout. Therefore, when ^{75}As is used for the readout, the number of active nuclei is $\approx \frac{1}{2} \times 0.8 \times (6.5 \times 10^4) \approx 2.6 \times 10^4$. When the readout is carried out via ^{69}Ga, we need to take into account the $\approx 60\%$ natural abundance of the isotope, which leads to $\approx 1.6 \times 10^4$ nuclei actively used in the electron spin QND measurement.

All NMR measurements are differential. In addition to the actual single-cycle measurements with the timing shown in Supplementary Fig. 3, we periodically collect the reference PL probe spectra. These reference probe spectra are measured with exactly the same timing sequence, including rf population transfers, but without the detuned rf pulses. The spectral splitting in the reference spectra is nominally a constant parameter, but may slowly change over time due to the drifts in the experimental settings, such as optical pump power. The difference of the spectral splittings from the main and the reference measurements yields the differential NMR signal ΔE_{hf} free from the unwanted drifts.

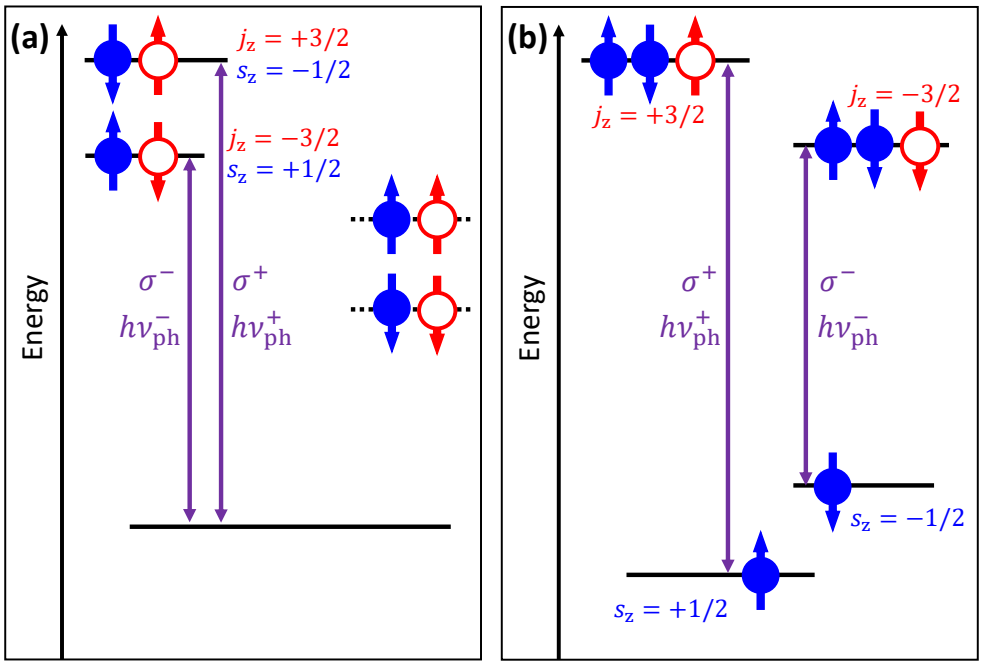
It is worth pointing out the importance of using the NMR pulses alone in order to achieve a high-fidelity electron spin readout. The energies of the nuclei and the rf quanta used to control these nuclei ($10 - 100$ MHz range in frequency units) are both strongly detuned from the electron spin resonance transition (10 GHz range). This ensures minimal backaction on the electron spin. The situation is far more complicated if the same electron-nuclear spin system is controlled via the higher-energy electronic transition. Apart from the direct electron spin resonance, microwave driving can induce the so-called Solid Effect [29, 30], where both the electron and nuclear spins get

flipped. Although the forbidden (Solid Effect) transitions are detuned in frequency, in real solid state systems they are often poorly resolved from the main (dipole-allowed) electron spin resonance transition. It is therefore difficult to control the electron spin without causing strong action on the nuclear spins. Thus, the sign of the energy asymmetry between the electron and the nuclei plays an important role in our QND readout scheme.

C. Optical probing of the quantum dot nuclear spins

During optical probing of the nuclear spin polarization the gate bias, typically $V_{\mathrm{Gate}} = +0.9$ V, and the probe power are chosen to maximize (saturate) PL intensity of the ground state exciton. A 10 ms delay is introduced after switching the bias and before activating the mechanical shutter, which forms the probe laser pulse. Fig. 2(a) of the main text shows neutral exciton (X^0) PL probe spectra measured at $B_{\mathrm{z}} = 5.31$ T following optical pumping with a σ^- circularly polarized laser. The PL arises from recombination of the electron-hole pairs in a QD. Probe PL is excited with a diode laser emitting at 760 nm, which corresponds to one of the excited states of the QD. Under such a nonresonant excitation, the spin polarization of the optically generated electron-hole pairs is randomized during relaxation to the ground exciton state. As a result, the time-integrated probe spectrum includes PL from all possible electron and hole spin orientations. For a neutral QD, the PL spectrum of the ground state exciton (X^0) is a doublet, where each component corresponds to the optically excited electron in a spin-up ($s_{\mathrm{z}} = +1/2$) or spin-down ($s_{\mathrm{z}} = -1/2$) projection state, as shown in Supplementary Fig. 6(a). Consequently, the splitting ΔE_{PL} of the PL spectral doublet is sensitive to polarization of the nuclei along the z axis. The variation of this spectral splitting reveals the variation of the electron hyperfine shift ΔE_{hf}. (Here, we neglect the valence band hole hyperfine shifts since they are an order of magnitude smaller [21].) These shifts are used to monitor the average QD nuclear spin polarization in NMR experiments.

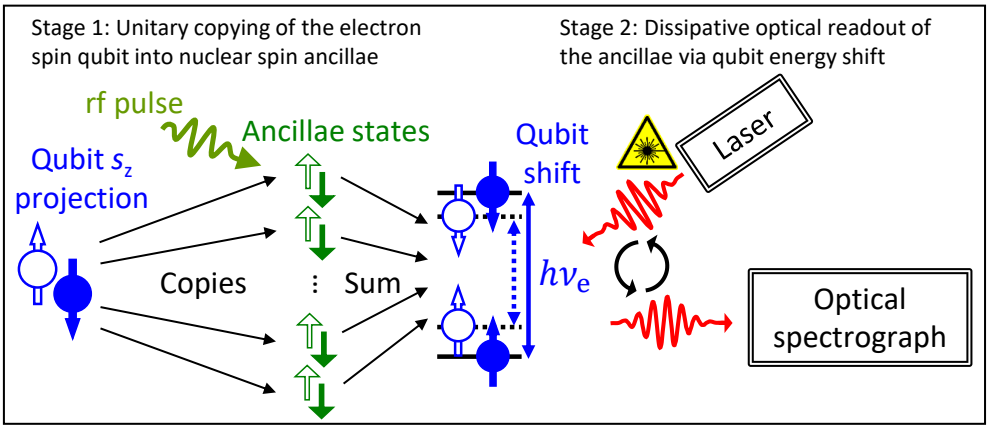
It is also possible to probe the nuclear spin polarization using PL of a negatively charged trion X^- [Supplementary Fig. 6(b)]. The charge state for optical probing is selected for each individual QD and magnetic field strength. This choice is governed by the linewidths and the brightness of PL. We note that in case of optical probing via X^0 the electron is ejected from the QD, directly destroying the spin qubit. In case of probing via X^- the resident electron is retained in the QD. However, the electron of the very first optically-generated electron-hole pair forms, together with the resident electron, a ground-orbital spin singlet. Such a singlet contains no information about the previous spin state of the resident electron. Consequently, in either case (X^0 or X^- probing),



Supplementary Figure 6. Energy levels of electrons (solid blue circle and arrow) and holes (open red circle and arrow) in a QD. (a) In a neutral QD the ground state contains no electrons or holes. The first optically excited manifold consists of four neutral exciton (X^0) states. The two bright states are formed by an electron and a hole with opposite momentum projections. The state with hole momentum projection $j_z = +3/2$ and electron spin projection $s_z = -1/2$ gives rise to a σ^+ polarized optical transition, while the state with $j_z = -3/2$ and $s_z = +1/2$ results in a σ^- polarized transition. The two states where j_z and s_z have the same sign are "dark" and are therefore not observed in PL. (b) In a negatively-charged QD the ground state contains a single electron with spin up ($s_z = +1/2$) or spin down ($s_z = -1/2$). The two optically excited trion states consist of an electron spin singlet and a hole with momentum projection $j_z = -3/2$ or $j_z = +3/2$. The two optically allowed transitions are circularly polarized ($\sigma^\pm$) and are shown by the vertical arrows.

the spin qubit is destroyed during the optical probing. However, such destruction of the original qubit has no effect on the measurement outcome which has already been stored in the nuclear spins.

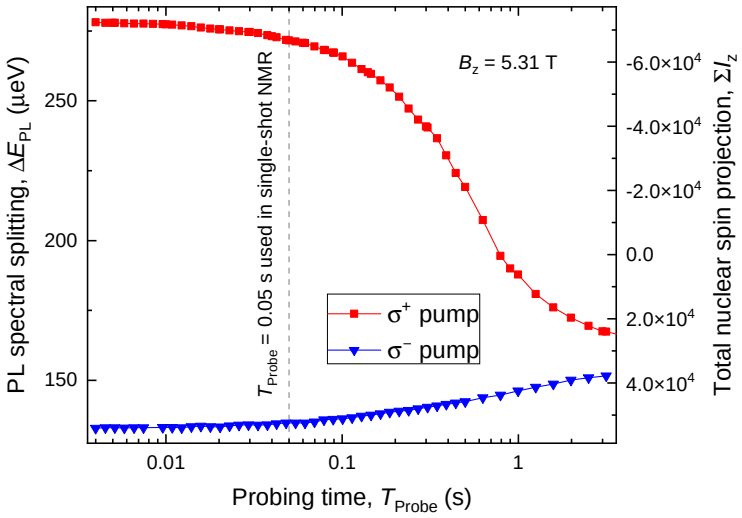
Illumination with a probe laser inevitably acts back on the nuclear spin polarization. Each optically excited electron has a finite probability to flip one of $N \approx 10^5$ nuclear spins. Eventually, the nuclear spin polarization reaches its steady-state, governed only by the power, wavelength and polarization of the probe laser. Therefore, the duration of the probe T_{Probe} must be short enough to retain sufficient information about the nuclear polarization at the start of the probe. On the other hand, at the optical probing stage we are only interested in the average nuclear spin



Supplementary Figure 7. Schematic of the qubit readout concept. First, a detuned radiofrequency pulse, applied to the nuclei, copies the electron spin qubit projection into a large number of nuclear spin ancillae. Next, the arithmetic sum of the ancilla spin projections is read out by measuring the hyperfine shifts of the electron spin energy gap $h\nu_e$. These energy shifts are probed through repeated optical injection of electrons and holes into the QD, in order to measure the optical spectrum of their recombination.

polarization, i.e. the arithmetic sum of all the copies transferred by the detuned rf pulse from the electron spin qubit into the nuclear spin z projections (see Supplementary Fig. 7). In other words, optical probing measures the z projection of a large total spin $\approx NI$ formed by thousands of nuclei. Due to the large N, this total spin is essentially a classical variable. Consequently, the QD can be excited optically many times, and a large number of photons can be collected before the decay of the average nuclear spin polarization causes any significant distortion in the measurement outcome. In order to determine the optimal T_{Probe} we perform calibration measurements, with a typical result shown in Supplementary Fig. 8. In this experiment the QD is first pumped with a σ^+ or σ^- polarized laser in order to create large initial nuclear polarization. A probe laser pulse is then applied. The PL spectral splitting ΔE_{PL} is measured at the end of this probe. It can be seen that the probe induces a decay of the nuclear spin polarization on a timescale of a few hundred milliseconds. The probe time T_{Probe} used in the single-cycle NMR experiments is chosen to ensure that any distortion of the measured ΔE_{hf} is small enough to resolve the ΔE_{hf} values corresponding to the opposite electron spin states. For example, for the data shown in Supplementary Fig. 8 we choose $T_{\mathrm{Probe}} = 0.05$ s.

We can estimate the number of optically-excited electron-hole pairs cycled through the QD during the probe pulse. The typical radiative lifetimes for the studied type of GaAs/AlGaAs QDs are $\approx$ 300 ps [31]. Since the probe excitation power is close to PL saturation, we can assume that the QD re-excitation time is also on the order of $\approx$ 300 ps. Therefore, during the typical



Supplementary Figure 8. Calibration of the optical probing of the QD nuclear spin polarization. PL spectral splitting (left scale) measured as a function of the probing time $T_{\rm Probe}$ following a σ^+ or σ^- pumping of the nuclear spin polarization in a QD. The right scale shows an estimated total nuclear spin projection $\Sigma I_{\rm z}$ corresponding to PL spectral splitting shown on the left axis. Vertical dashed line shows the $T_{\rm Probe}$ value chosen for the NMR measurements on this individual QD at this particular magnetic field of $B_{\rm z} = 5.31$ T.

probe time $T_{\rm Probe} = 0.05$ s, the QD is re-excited $\approx 10^8$ times. This is much larger than the number of nuclei $N \approx 10^5$, indicating that the backaction of the optical probe on the nuclear spin polarization is weak. Only a small fraction of the optical excitations (less than one in a thousand) results in unwanted nuclear spin flips, while the majority of the optically-generated excitons provide information about the nuclear spin polarization state without perturbing it.

Overall, the electron spin readout can be viewed as a two-stage process (Supplementary Fig. 7). The first stage is the copying of the electron spin qubit z projection into the nuclear spin ensemble, implemented with a detuned rf pulse, which is essentially an electron-controlled CNOT gate acting simultaneously on multiple nuclear qubits [32]. Since the evolution is unitary, this first stage can be seen as a quantum amplifier, with a gain given by the number of nuclear spins $N \approx 10^4 - 10^5$ driven by the detuned rf pulse. The second stage is the probing of the nuclear spin ensemble state, achieved through repeated optical injection of electrons to measure the hyperfine energy shift of the electron spin qubit. Since optical excitation involves energy relaxation of the charge carriers, this stage can be viewed as a classical (dissipative) amplifier, whose gain of $\approx 10^3$ is given by the number of useful photons collected for each unwanted flip of a single nuclear spin. Combined together, these two stages allow the quantum variable $\hat{s}_{\rm z}$ to be copied into $\approx 10^8$ photons, a fraction of which is then recorded by a classical instrument (optical spectrometer with a photo-detector).

According to the Quantum Darwinism concept, the large number of redundant copies of the same information is exactly what gives a human observer the classical (deterministic) notion of objective reality [33]. While the boundary is inevitably subjective, the $\approx 10^8$ redundancy, and even the $\approx 10^5$ redundancy produced by the first "quantum" stage, is sufficiently high to be interpreted as a deterministic measurement outcome.

Apart from calibrating the probe pulse duration, the results of Supplementary Fig. 8 help us to examine a hypothetical scenario where the equilibrium electron spin states take all the possible superpositions with equal probabilities. If the electron was in a superposition of the $s_z = \pm 1/2$ energy eigenstates, the detuned rf pulse would create an entangled electron-nuclear state. One may then ask whether the subsequent optical pulse could "collapse" the nuclear ensemble into either of the two polarization states observed in the bimodal histograms of Figs. 3(b) and 3(c) of the main text. Firstly, we note that the optical pulse is delayed by tens of milliseconds with respect to the detuned rf pulse, which is sufficient for any nuclear spin superpositions to decay through natural decoherence. Even if some coherence remains in the nuclear spin ensemble, we find that the nuclear spin states left by the QND measurement of the electron spin qubit are very distinct, in a sense that their total spin projections ΣI_z differ by $\approx 10^3 - 10^4$, as exemplified in Supplementary Figs. 5,10. However, in Supplementary Fig. 8 the backaction of the probe laser on the total nuclear polarization is seen to be gradual: the total z spin projection ΣI_z of the QD nuclei decays from the initial level (produced by optical spin pumping) without any signs of random "collapses", that would account for ΣI_z changing by $\approx 10^3 - 10^4$. These observations support out interpretation that the optical readout is not responsible for the observed discrete nature of the measured electron spin states. Furthermore, experimental evidence contradicts a possibility that the ejection of the electron by the gate bias (prior to the optical probe pulse) can "collapse" the nuclei. Probing via X^0 (with electron ejection) and via X^- (without electron ejection) give very similar results. In other words, pulsing of the sample gate bias to move the electrons in and out of the QD has no significant effect on the nuclear polarization. This is rather expected based on momentum conservation, since the electron has spin 1/2, while the output states of the nuclei observed in the electron spin readout experiments differ in total spin projection by a large magnitude $\mathcal{O}(N)$.

Finally, for future work we note that due to the weak backaction it is possible in principle to apply multiple optical probe pulses. This could be useful for isotope-selective retrieval of the NMR signals. For example, one can use a (Probe – rf π pulse – Probe) sequence to measure selectively the NMR transition chosen by the rf pulse. This could be beneficial in situations such as those shown in Supplementary Figs. 10(d)–10(f), where the "no-flip" NMR signals arising from the $s_z = \pm 1/2$

projections are not resolved. However, in the present work we rely on a simple implementation with one probe pulse, which is sufficient to demonstrate the concept.

Supplementary Section 4. READOUT FIDELITY MODELING

Here we discuss how the fidelity of the spin readout is derived from the histograms, such as shown in Figs. 3(b) and 3(c) of the main text. We need to construct the model probability distribution of the single-shot NMR signal amplitudes $\Delta E_{\rm hf}$. When constructing the probability density, we take into account the finite probability for the electron spin to flip within the rf pulse duration $T_{\rm rf}$. The flips are modelled as a random telegraph process, where the flips are instantaneous (infinitely fast) and are not correlated. In principle, the electron spin can flip m times during $T_{\rm rf}$, with the probability of such an event scaling as $\propto (T_{\rm rf}/T_{1,\rm e})^m$, where $T_{1,\rm e}$ is the electron spin lifetime. In all our experiments $T_{\rm rf} \ll T_{1,\rm e}$, so we only account for the terms up to the first order $m \leq 1$ (in other words, we ignore the possibility for the electron to flip more than once during $T_{\rm rf}$).

For a telegraph process, the probability of zero flips occurring during any given time interval $T_{\rm rf}$ is:

$$p_{m=0} = \exp\left[-\frac{\left(1-\rho_{\rm e}^2\right)T_{\rm rf}}{2T_{1,\rm e}}\right], \tag{S5}$$

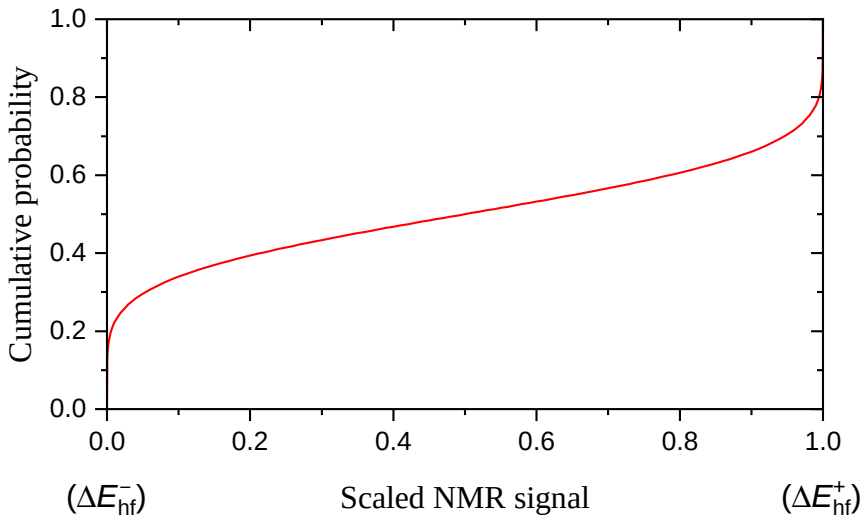
where $-1 \leq \rho_{\rm e} \leq 1$ is the equilibrium electron spin polarization degree. For the probability to have exactly one electron spin flip we write:

$$p_{m=1} = 1 - p_{m=0}, \tag{S6}$$

where we have used the simplifying assumption that two or more flips ($m \geq 2$) are not possible.

In the case of zero flips ($m = 0$), the electron is either in a spin up ($s_{\rm z} = +1/2$) or spin down ($s_{\rm z} = -1/2$) state throughout the entire rf measurement pulse. In the absence of noise, these two spin states would result in two discrete NMR readout values: $\Delta E_{\rm hf}^{+}$ and $\Delta E_{\rm hf}^{-}$, respectively. The relevant probability distributions are described by the delta functions centered at $\Delta E_{\rm hf}^{+}$ and $\Delta E_{\rm hf}^{-}$ for $s_{\rm z} = +1/2$ and $-1/2$. The total probabilities of detecting $s_{\rm z} = +1/2$ and $-1/2$ in equilibrium are $(1+\rho_{\rm e})p_{m=0}/2$ and $(1-\rho_{\rm e})p_{m=0}/2$, respectively.

Next, we consider the $m = 1$ case, where the electron flips at a timepoint $t_{\rm Flip}$. The distribution of $t_{\rm Flip}$ is uniform in the interval $[0, T_{\rm rf}]$. In order to evaluate the effect of the electron spin flip on the measured NMR signal we use simple geometrical calculations. We assume that all nuclear spins are exactly on resonance (completely out of resonance) with the rf pulse when the electron is



Supplementary Figure 9. Cumulative distribution function of the NMR signals detected in case where the electron spin flips once during the measurement rf pulse. The amplitude of the rf pulse is assumed to have a cosine envelope. The horizontal axis is scaled in the range $[\Delta E_{\rm hf}^{-}, \Delta E_{\rm hf}^{+}]$.

in the $s_{\rm z} = +1/2$ ($s_{\rm z} = -1/2$) spin state. Consider the case where the electron is in the $s_{\rm z} = +1/2$ state at the start of the rf pulse. Then the nuclei will be rotated from their initial $I_{\rm z} = +1/2$ states towards the inverted $I_{\rm z} = -1/2$ states. However, this rotation is interrupted at $t_{\rm Flip}$. We then calculate the change in $I_{\rm z}$ arising from such an interrupted rotation in the case of an rf pulse with a cosine shaped envelope. Linear rescaling of this change in $I_{\rm z}$ yields the NMR signal as a function of $t_{\rm Flip}$:

$$\Delta E_{\rm hf}(t_{\rm Flip}) = \Delta E_{\rm hf}^{-} + (\Delta E_{\rm hf}^{+} - \Delta E_{\rm hf}^{-})\frac{1}{2}\left(1 - \cos\left[\frac{1}{2}\sin\left(\frac{2\pi t_{\rm Flip}}{T_{\rm rf}}\right) - \frac{\pi t_{\rm Flip}}{T_{\rm rf}}\right]\right) \tag{S7}$$

This function is a scaled sigmoid, and, given that $t_{\rm Flip}$ is distributed uniformly, its appropriately scaled inverse is a cumulative distribution function (CDF) of the single-shot NMR signals $\Delta E_{\rm hf}$ detected in the case of exactly one electron flip ($m = 1$). There is no analytical inverse. The numerically evaluated CDF is shown in Supplementary Fig. 9. Its derivative is the probability density function (PDF) and also has to be evaluated numerically. Some properties of this PDF can be noted from Supplementary Fig. 9. Namely, it is approximately a sum of two sharp modes at $\Delta E_{\rm hf}^{-}$ and $\Delta E_{\rm hf}^{+}$, and a relatively uniform background in between these modes. This shape can be understood qualitatively as originating from the cosine envelope of the rf pulse. If the electron flips near the start or the end of the pulse, where the rf amplitude is ≈ 0, the nuclei either have not rotated much, or have already been flipped, respectively. Thus, the flips at the start and the end of the rf pulse give rise to NMR signals very close to $\Delta E_{\rm hf}^{-}$ and $\Delta E_{\rm hf}^{+}$, respectively. The case

where the electron is in the $s_z = -1/2$ state at the start of the rf pulse gives exactly the same distribution of the NMR signals ΔE_{hf}.

Summarising, we have the following three contributions to the distribution of the NMR signals ΔE_{hf}:

- (i) The delta-peak mode at ΔE_{hf}^{+} with a probability $\frac{1+\rho_e}{2} \exp\left[-\frac{(1-\rho_e^2)T_{rf}}{2T_{1,e}}\right]$, corresponding to the $s_z = +1/2$ electron state with no flips.

- (ii) The delta-peak mode at ΔE_{hf}^{-} with a probability $\frac{1-\rho_e}{2} \exp\left[-\frac{(1-\rho_e^2)T_{rf}}{2T_{1,e}}\right]$, corresponding to the $s_z = -1/2$ electron state with no flips.

- (iii) The bimodal distribution given by Supplementary Eq. S7 with a probability $1 - \exp\left[-\frac{(1-\rho_e^2)T_{rf}}{2T_{1,e}}\right]$, corresponding to the case where the electron spin flips once during the rf pulse.

These three contributions, weighted by their relevant probabilities, are added together to obtain the complete ideal PDF. The final step is to take into account the non-ideal nature of the optical readout of the single-shot NMR signals. The readout noise is modelled by assuming that the detected ΔE_{hf} values have a Gaussian distribution with a full width at half maximum w and centered on the true ΔE_{hf}. Thus, we convolve the complete ideal PDF with a Gaussian PDF. This convolved PDF is then fitted to the experimental single-shot NMR data, such as shown in the histograms of Figs. 3(b) and 3(c) of the main text. The best fit is found by maximizing the likelihood estimator, with ΔE_{hf}^{-}, ΔE_{hf}^{+}, ρ_e, $T_{1,e}$ and w used as fitting parameters.

The best fits are shown by the solid lines in Figs. 3(b) and 3(c) of the main text. The best fit Gaussian FWHM is $w \approx 2.4 - 2.7$ μeV, which is a good match to $w \approx 2.4$ μeV found in the reference measurement on a neutral QD [$0e$, Fig. 3(a) of the main text] where the data is fitted with a single Gaussian. This agreement confirms that optical readout noise is the main source of the histogram mode broadening and validates the model used for the $1e$ single-shot NMR. The fitted equilibrium electron spin polarization is small $|\rho_e| \leq 0.1$, owing to the small electron g-factor in the studied QDs [2, 18]. The best fit values for the electron spin lifetimes are $T_{1,e} \approx 1.7$ ms and $T_{1,e} \approx 0.58$ ms at $B_z = 1.6$ T and 5.3 T, respectively. These values are somewhat smaller than the more accurate measurements $T_{1,e} \approx 8.7$ ms and $T_{1,e} \approx 0.71$ ms obtained at the same magnetic fields via direct measurement of the electron spin relaxation. The $T_{1,e}$ parameter used in the model probability distribution essentially encodes the qubit readout infidelity $1 - F$. The

underestimated fitted values of $T_{1,e}$ suggest that the true qubit readout fidelities are even closer to unity than derived from fitting.

Once the fitting parameters are obtained, the qubit readout criterion is defined by setting the threshold value in the middle of the two modes at $(\Delta E_{\rm hf}^{-} + \Delta E_{\rm hf}^{+})/2$. Any single-cycle NMR signal $\Delta E_{\rm hf}$ below (above) this threshold is interpreted as $s_{\rm z} = -1/2$ ($s_{\rm z} = +1/2$). The readout fidelity F is defined as the average probability to detect the true $s_{\rm z}$ correctly. We have $F = p_{m=0}p_{\rm Opt} + p_{m=1}/2$, where $p_{\rm Opt}$ denotes the probability that the optical readout noise does not cause the measured $\Delta E_{\rm hf}$ to cross the detection threshold. The two modes in the measured histograms are well resolved, especially at high magnetic field [Fig. 3(c) of the main text], so that $p_{\rm Opt} \approx 1$. Therefore, the fidelity is $F = p_{m=0}p_{\rm Opt} + p_{m=1}/2 \approx p_{m=0} + p_{m=1}/2 = 1 - p_{m=1}/2$, dominated by the probability that the electron flips during the readout rf pulse. The $1/2$ factor in $p_{m=1}/2$ accounts for the fact that even when the electron spin is flipped randomly, there is still a 50% probability that the measured $\Delta E_{\rm hf}$ stays on the correct side of the detection threshold and the electron spin projection $s_{\rm z}$ is measured correctly. We find $F \approx 0.9985$ at both $B_{\rm z} = 1.6$ T and 5.3 T. We note that the same value of F is found despite the longer electron spin lifetime at $B_{\rm z} = 1.6$ T. This is likely explained by the longer measurement pulse $T_{\rm rf} \approx 20$ μs, as opposed to $T_{\rm rf} \approx 10$ μs used at $B_{\rm z} = 5.3$ T, and the smaller separation of the histogram modes, which means that at low magnetic fields $p_{\rm Opt}$ is not as close to unity as it is at high fields.

Supplementary Section 5. ADDITIONAL DATA FROM TWO-PULSE READOUT EXPERIMENTS

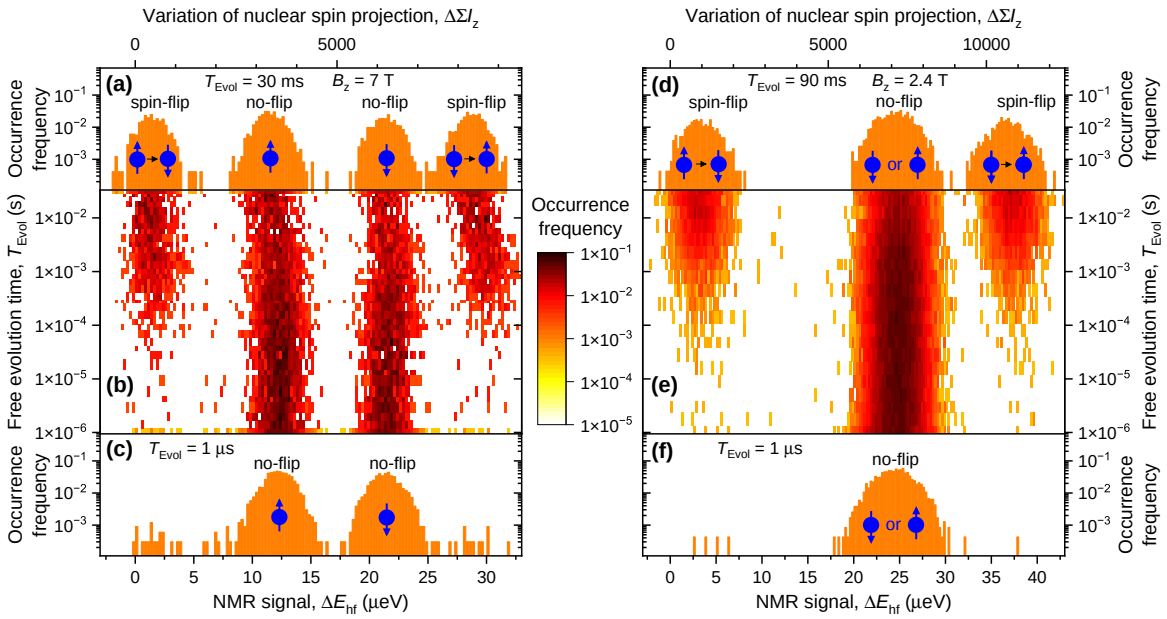
Supplementary Figs. 10(a)–10(c) replicate Figs. 3(d)–3(e) of the main text, where the results are shown for an experiment with two rf pulses. The first pulse applied to ^{75}As nuclei records the initial state of the electron spin, while the second pulse on ^{69}Ga stores the state after the interpulse free-evolution delay $T_{\rm Evol}$. The optically-measured $\Delta E_{\rm hf}$ is the total NMR signal produced by the two pulses. Supplementary Fig. 10(b) shows a two-dimensional histogram of the single-cycle NMR signals $\Delta E_{\rm hf}$ measured at different $T_{\rm Evol}$. A cross-section at short $T_{\rm Evol} \approx 1$ μs is shown in Supplementary Fig. 10(c), while the result for a long $T_{\rm Evol} \approx 30$ ms is shown in Supplementary Fig. 10(a). The relative weights of the "no-flip" and "spin-flip" modes reveal the probability for the electron spin to relax during $T_{\rm Evol}$. We model this relaxation probability by an exponential function of $T_{\rm Evol}$, to derive the spin lifetime $T_{1,e} \approx 0.58$ ms for this experiment conducted at $B_{\rm z} = 7$ T.

Supplementary Figs. 10(d)–10(f) show the additional results from the same two-pulse experi-

ment, but conducted at a reduced magnetic field of $B_z = 2.4$ T. In this dataset, the two "no-flip" outcomes merge into one mode at $\Delta E_{hf} \approx 25$ μeV. This overlap is due to a slight nonlinearity in the dependence of the optically-probed hyperfine shift ΔE_{hf} on the QD nuclear spin polarization. Such nonlinearity is a result of the well-known feedback effect occurring in the electron-nuclear spin system under optical pumping [26]. Apart from that, the results in Supplementary Figs. 10(d)–10(f) match qualitatively the results in Supplementary Figs. 10(a)–10(c), with the gradual emergence of the "spin-flip" modes at an increasing T_{Evol}. However, at $B_z = 2.4$ T the electron spin lifetime is significantly longer, found to be $T_{1,e} \approx 5.2$ ms from the exponential model fitting. The inverse dependence of $T_{1,e}$ on the applied magnetic field is a clear indication that the electron spin relaxation is dominated by acoustic phonons [11, 34].

The readout of the electron spin via nuclear spin environment is possible in a wide range of magnetic fields, as demonstrated in Figs. 3(b) and 3(c) of the main text, where similarly high fidelities are achieved at $B_z = 1.6$ T and $B_z = 5.3$ T. At high magnetic fields the readout fidelity is fundamentally limited by the shortening of the electron spin lifetime $T_{1,e}$. In the experiments, we have verified our readout techniques for magnetic fields up to $B_z = 8$ T.

At low magnetic fields, the readout is fundamentally limited by the backaction, as discussed in more detail in the next section. Backaction becomes particularly strong if the hyperfine shift $\approx Na$ of the nuclei used for the measurement (here N is the number of the polarized nuclei rotated by the rf pulse, rather than the total number of nuclei in a QD) is comparable to or larger than the electron Zeeman splitting $h\nu_{e,0}$. Under these conditions, the electron spin energy splitting $h\nu_e$, which is the sum of $h\nu_{e,0}$ and the hyperfine shift, can become very small or even zero at some point during the rf pulse. Then, the electron-nuclear spin flip-flops become energetically allowed, disrupting the electron spin qubit state. Such backaction can be remedied by using a smaller number of nuclei in the measurement, though the drawback is the reduced NMR signal ΔE_{hf}. In our experiments, electron spin readout has been verified down to $B_z = 0.41$ T. At this magnetic field the backaction is not yet the limiting factor. Instead, the limitation comes from the reduction of the optically-pumped nuclear polarization at small magnetic fields. This reduction leads to a smaller NMR signal ΔE_{hf}, and less resolved spin-up and spin-down modes in histograms, such as shown in Figs. 3(b) and 3(c) of the main text. However, such limitation is technical rather than fundamental, since PL collection efficiency in our setup can still be improved by one or two orders of magnitude, e.g. by using a solid-immersion lens (SIL) [35]. With better PL photon collection, the statistical noise in ΔE_{hf} can be reduced. Alternatively, a more accurate measurement of ΔE_{hf} can be achieved through resonance fluorescence [36], rather than PL. We therefore expect that our



Supplementary Figure 10. (a-c) Histograms of the single-cycle NMR signals $\Delta E_{\rm hf}$ measured at $B_{\rm z} = 7$ T with two rf π pulses applied to ^{75}As and ^{69}Ga and delayed by $T_{\rm Evol}$. A full 2D histogram at variable $T_{\rm Evol}$ is shown in (b), while (a) and (c) show the cross sections at long and short $T_{\rm Evol}$, respectively. (d-f) Same as (a-c) but on a different QD and at a lower magnetic field $B_{\rm z} = 2.4$ T. The two "no-flip" modes are not resolved in this measurement. The top horizontal axes show the NMR signals in terms of the variation of the total spin projection $\Delta\Sigma I_z$ of the QD nuclei. The variation is estimated as $\Delta\Sigma I_z \approx N\Delta E_{\rm hf}/(3F_{\rm tot})$, where the factor of 3 accounts for the amplification by the reverse population transfer, $N \approx 65000$ is the estimated number of nuclear spins in a QD [2], and $IF_{\rm tot} \approx 112$ μeV is the hyperfine shift $E_{\rm hf}$ of the fully polarized $I = 3/2$ nuclei measured in the studied type of QDs [3].

readout method should be applicable in GaAs QDs at least down to a few hundreds of mT.

Supplementary Section 6. NUMERICAL SIMULATION OF THE ELECTRON-NUCLEAR SPIN EVOLUTION

We perform exact numerical simulations on a system where the central electron spin **s** is coupled to an ensemble of N spin-1/2 nuclei via the contact hyperfine interaction (Supplementary Eq. S4):

$$\mathcal{H}_{\rm hf} = \sum_{k=1}^{N} a_k(\hat{s}_{\rm x}\hat{I}_{{\rm x},k} + \hat{s}_{\rm y}\hat{I}_{{\rm y},k} + \hat{s}_{\rm z}\hat{I}_{{\rm z},k}), \tag{S8}$$

The Zeeman terms are:

$$\mathcal{H}_{\mathrm{Z,e}} = h\nu_{\mathrm{e},0}\hat{s}_{\mathrm{z}}, \tag{S9}$$

$$\mathcal{H}_{\mathrm{Z,N}} = -h\sum_{k=1}^{N}\nu_{\mathrm{N},k}\hat{I}_{\mathrm{z},k}, \tag{S10}$$

where the nuclear Zeeman term of Supplementary Eq. S1 is rewritten in terms of the nuclear Larmor frequencies $\nu_{\mathrm{N},k}$. The bare electron Larmor frequency is $\nu_{\mathrm{e},0} = \mu_{\mathrm{B}} g_{\mathrm{e}} B_{\mathrm{z}}/h$, where μ_{B} is the Bohr magneton and g_{e} is the electron g-factor. For completeness, we include the nuclear-nuclear dipolar interaction (Supplementary Eq. S3). The term that describes the time-dependent radiofrequency (rf) excitation acting on the nuclei is given by the rotating magnetic field:

$$\mathcal{H}_{\mathrm{rf,N}} = -h\sum_{k}\nu_1(t)\left(\cos(2\pi\nu_{\mathrm{rf}}t)\hat{I}_{\mathrm{x},k} - \sin(2\pi\nu_{\mathrm{rf}}t)\hat{I}_{\mathrm{y},k}\right), \tag{S11}$$

where ν_{rf} is the rf carrier frequency, $\nu_1(t)$ is the slowly-varying rf pulse envelope, and the summation goes over only those nuclei that belong to the isotope that is resonant with the rf.

Direct numerical modeling is carried out for up to $N \leq 12$ nuclei with spin $I = 1/2$. We simplify the problem by assuming uniform nuclear Zeeman frequencies $\nu_{\mathrm{N},k} = \nu_{\mathrm{N}}$ and hyperfine constants $a_k = a$. In all computations we assume the case of a strong magnetic field, by choosing large electron ($\nu_{\mathrm{e},0} \in [4, 600]$ MHz) and nuclear ($\nu_{\mathrm{N}} \in [1, 5]$ MHz) Zeeman frequencies, significantly exceeding the magnitude of the nuclear-nuclear dipolar interactions ($\lesssim 100$ Hz). Nevertheless, the model is set up in an exact form in the laboratory frame, without truncating the dipolar couplings. The electron-nuclear coupling is varied between $a \in [0, 200]$ kHz. The unitary evolution of the system is simulated through numerical propagation of the Schrödinger equation from an initial wave function state ψ_{Init}. The computation is carried out using the software package Wolfram Mathematica 13.2. We chose ψ_{Init} as a product state of the electron and the nuclear spins, which means that the spins are not entangled initially. Moreover, the nuclear spin ensemble is initialized into a product of identical single-nucleus states. Next, we describe numerical simulations under different settings.

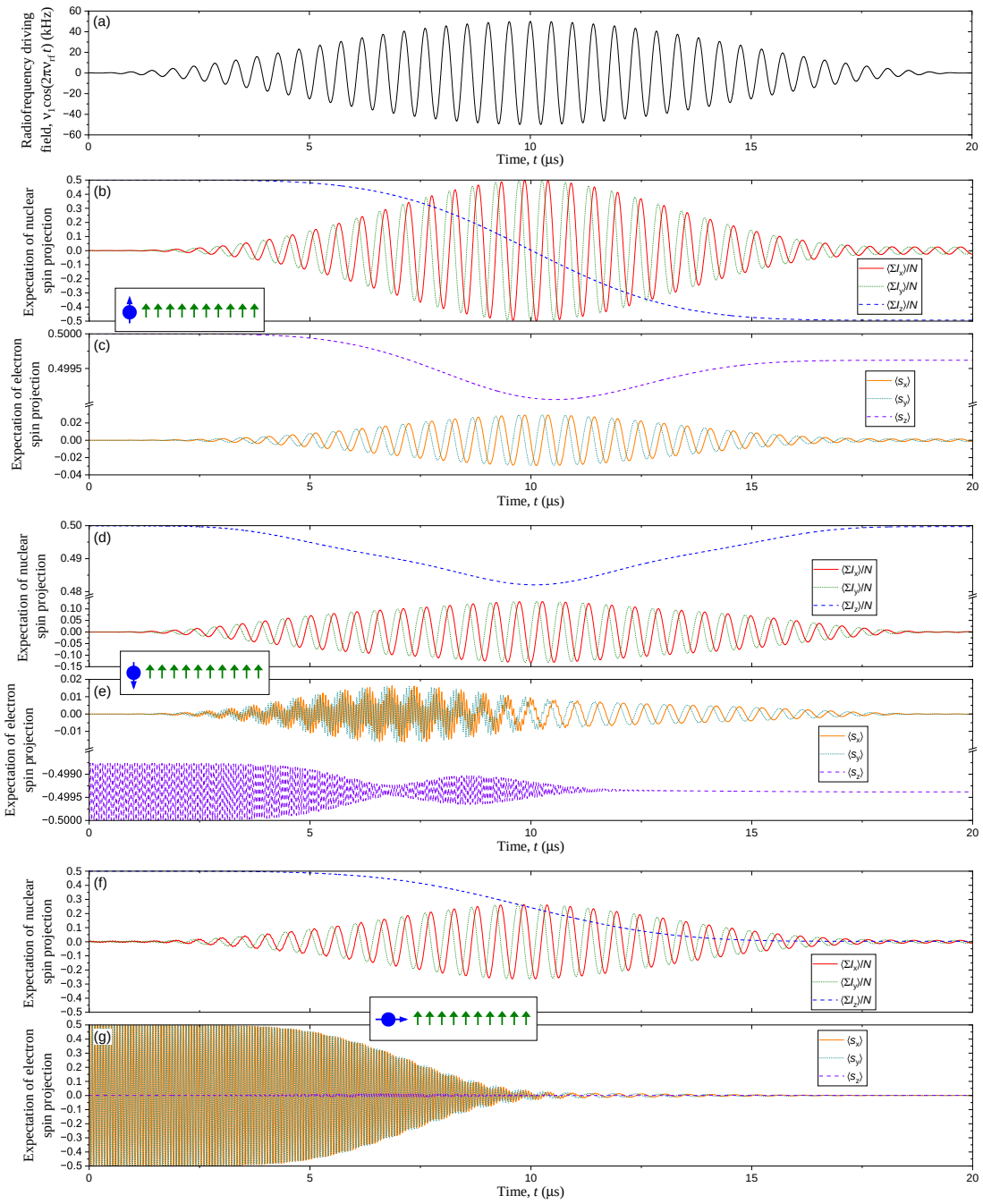
A. Electron-nuclear spin dynamics

We start by examining the full time evolution of the electron-nuclear spin system. As an example, we model the QND measurement process. The nuclei are initially in a fully-polarized state with $I_{\mathrm{z},k} = +1/2$ for all k. An rf pulse with a total duration of T_{rf} is applied. In order to match the experiments, we use a cosine amplitude envelope $\nu_1(t) \propto 1 - \cos(2\pi t/T_{\mathrm{rf}})$, where

the proportionality factor is chosen to produce a π rotation (inversion) of the nuclei when the rf frequency is in resonance with the nuclei. The rf frequency is $\nu_{\rm rf} = \nu_{\rm N} - a/(2h)$, detuned from the bare NMR frequency $\nu_{\rm N}$. For an electron in the $s_{\rm z} = +1/2$ ($s_{\rm z} = -1/2$) state the rf pulse is resonant (detuned), resulting in a full (negligible) inversion of the nuclear spins. We note certain similarities of this spin-to-spin conversion via off-resonant NMR with the dispersive (frequency-detuned) readout of a superconducting qubit coupled to a microwave cavity [37] – the role of the bosonic cavity mode is similar to that of the fermionic nuclear spin ensemble in our simulations and experiments on QDs. The results shown in Supplementary Fig. 11 are for a specific case of $\nu_{\rm e,0} = 15$ MHz, $\nu_{\rm N} = 2$ MHz, $a = 200$ kHz, and $T_{\rm rf} = 20$ μs. Supplementary Fig. 11(a) plots the x component of the rf magnetic field pulse.

Three cases of the initial electron spin state are considered: $s_{\rm z} = +1/2$ (results shown in Supplementary Figs. 11(b) and 11(c)), $s_{\rm z} = -1/2$ (Supplementary Figs. 11(d) and 11(e)), and $s_{\rm x} = +1/2$, which is a superposition of the $s_{\rm z} = \pm 1/2$ energy eigenstates (Supplementary Figs. 11(f) and 11(g)). The time-dependent polarization of each nucleus (with index k) is calculated from the expectation value $I_{j,k}(t) = \langle\psi(t)|\hat{I}_{j,k}|\psi(t)\rangle$, where the axis index runs through $j = x, y, z$. Supplementary Figs. 11(b), 11(d), and 11(f) show the total nuclear polarization $\sum_{k=1}^{N} I_{j,k}(t)/N$ normalized by the number of nuclear spins N. The time-dependent polarization of the electron is calculated from the expectation value $s_j(t) = \langle\psi(t)|\hat{s}_j|\psi(t)\rangle$, where $j = x, y, z$. Supplementary Figs. 11(c), 11(e), and 11(g) show the electron polarization dynamics.

For the $s_{\rm z} = +1/2$ initial electron state, the z projections of the nuclear spins are inverted by the detuned rf pulse (Supplementary Fig. 11(b)), which corresponds to the π rotation point in the experimental result of Supplementary Fig. 5. For the $s_{\rm z} = -1/2$ state (Supplementary Fig. 11(d)), the nuclear z polarization evolves nearly adiabatically during the pulse, returning very close to the initial value. These numerical results reproduce the main experimental result that the detuned rf pulse copies the electron spin z projection into the z projections of N individual nuclear spins. The transverse (x and y) components of the nuclear polarization are seen to oscillate at approximately the Larmor frequency $\nu_{\rm N} = 2$ MHz. These oscillations reach their peak approximately at the peak of the rf pulse amplitude. Unlike for the nuclear polarization, the evolution of the electron polarization is nearly adiabatic both for the $s_{\rm z} = +1/2$ and $-1/2$ initial states, as it should be for a QND measurement. In both cases the rf-induced tipping of the electron spin is small (Supplementary Fig. 11(c) and 11(e)), but is more pronounced for the $s_{\rm z} = +1/2$ initial state, for which the rf pulse is in resonance with the nuclei. The variation $\Delta s_{\rm z}$ of the electron spin polarization at the end of the rf pulse can be interpreted as a measurement backaction, which



Supplementary Figure 11. Numerically calculated time evolution of the electron-nuclear spin state induced by a detuned radiofrequency pulse. (a) Time dependence of the x component the rf magnetic field pulse. (b) Calculated expectations of the total nuclear spin projections normalized by the number of nuclei $N = 10$. The Cartesian components x, y, z are shown by the solid, dotted, and dashed lines, respectively. Initially, all nuclei are in the $I_{z,k} = +1/2$ energy eigenstate. The electron spin is initialized in the $s_z = +1/2$ energy eigenstate. (c) Expectation of the electron spin projections for the same time-dependent evolution as in (a). The Cartesian components x, y, z are shown by the solid, dotted, and dashed lines, respectively. (d,e) Same as (b,c) but with electron spin initialized in the $s_z = -1/2$ energy eigenstate. (f,g) Same as (b,c) but with electron spin initialized in the $s_x = +1/2$ state, which is a superposition of the $s_z = \pm 1/2$ states. Note the differences in the scales of the individual plots and the axes breaks.

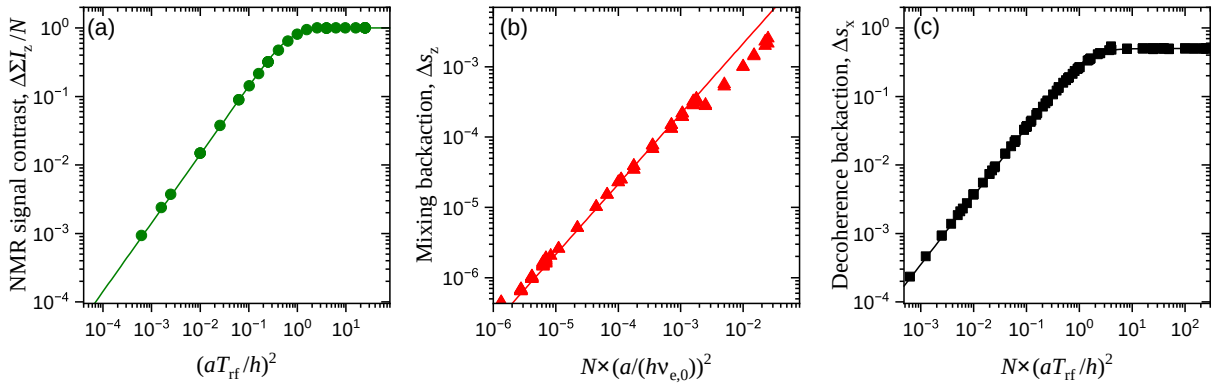
is discussed in more detail below. The transverse (x and y) components of the electron spins exhibit evolution, which contains oscillations both at the electron ($\nu_{e,0} = 15$ MHz) and nuclear ($\nu_N = 2$ MHz) Larmor frequencies, revealing intricate interplay of the many-body electron-nuclear spin dynamics. In the $s_z = -1/2$ case electron spin oscillations are observed even before the rf pulse, because the entire electron-nuclear state is not an eigenstate.

In case of the electron initialized in a transverse state $s_x = +1/2$, the rf pulse causes depolarization of the nuclear spins, accompanied by transient Larmor precession (Supplementary Fig. 11(f)). It is worth noting that the near-zero final z polarization of the nuclear spin ensemble is midway between the $\mp N/2$ final nuclear spin z polarizations observed for the $s_z = \pm 1/2$ initial electron spin states. In other words, our QND measurement scheme is "analogue", and the final z nuclear spin polarization can be used to uniquely distinguish any initial quantum-mechanical average (expectation) of the z polarization of the electron spin. This result supports our interpretation that the pronounced bimodality in the histograms of the measured single-cycle NMR readouts, such as shown in Fig. 3(b) and 3(c) of the main text, is due to the extrinsic einselection (e.g. caused by phonons), rather than due to the measurement-induced backaction or wave function collapse. As expected, prior to the rf pulse the electron spin undergoes precession at its Larmor frequency $\nu_{e,0}$ (Supplementary Fig. 11(g)). The rf pulse is seen to cause electron spin decoherence. At the end of the rf pulse all projections (x, y, z) of the electron spin and the total nuclear spin are close to zero. This is indicative of an entangled electron-nuclear spin state.

Next, we consider in more detail the different features of the electron-nuclear spin evolution. To this end, we omit the details of the electron-nuclear spin evolution, and focus on the net change in the electron and nuclear spin polarizations, by considering their values at the start and the end of the rf pulse.

B. Measurement contrast and backaction on the qubit

We continue analyzing electron-nuclear spin evolution induced by a detuned rf pulse. Using the wave function ψ_{Fin} in the final state, the final polarization of each nucleus is calculated from the expectation value $I_{z,k,Fin} = \langle \psi_{Fin} | \hat{I}_{z,k} | \psi_{Fin} \rangle$, with a total nuclear z polarization defined as $\Sigma I_{z,Fin} = \sum_{k=1}^{N} I_{z,k,Fin}$. The difference $\Delta\Sigma I_z$ in $\Sigma I_{z,Fin}$ obtained under $s_z = -1/2$ and $s_z = +1/2$ electron states can be interpreted as the measurement contrast. We conduct simulations for a wide range of parameters T_{rf}, a, N, ν_N and $\nu_{e,0}$, under the condition $\nu_N < \nu_{e,0}$. Despite these variations, we find that the normalized contrast $\Delta\Sigma I_z/N$ depends on a single combination $(aT_{rf}/h)^2$, as plotted



Supplementary Figure 12. Results of numerical simulations of the electron-nuclear spin dynamics. Each point in the plots is a result of a numerical modeling for a certain set of parameters $T_{\rm rf}$, a, N, $\nu_{\rm N}$ and $\nu_{\rm e,0}$. These parameters are varied in a wide range. The results are plotted as a function of the parameter combination that yields a universal functional dependence. (a) QND measurement contrast defined as a difference in the final nuclear spin polarizations $\Delta\Sigma I_{\rm z}$ produced by the spin up and spin down electrons. The normalized measurement contrast is plotted as a function of $(aT_{\rm rf}/h)^2$. (b) Backaction in the form of mixing, defined as the rf-induced variation in the electron spin z projection. The horizontal axis is $N\left(\frac{a}{h\nu_{\rm e,0}}\right)^2$. (c) Backaction in the form of decoherence, defined as the rf-induced variation in the electron spin x projection. The horizontal axis is $N(aT_{\rm rf}/h)^2$.

by the symbols in Supplementary Fig. 12(a). For short measurement times and/or weak hyperfine interaction $(aT_{\rm rf}/h)^2 \ll 1$, the NMR resonances under $s_{\rm z} = \pm 1/2$ electron states are resolved only partially, leading to a partial measurement contrast $\Delta\Sigma I_{\rm z}/N \ll 1$. In the opposite limit of slow measurement $(aT_{\rm rf}/h)^2 \geq 1$ the contrast saturates at $\Delta\Sigma I_{\rm z}/N \approx 1$, which is the regime used in our experiments. The transition from partial to full contrast is well described by the following empirical expression (plotted by the solid line):

$$\Delta\Sigma I_{\rm z}/N \approx \left(1 + (1.418 \times (aT_{\rm rf}/h)^2)^{-2}\right)^{-1/2} \tag{S12}$$

The contrast $\Delta\Sigma I_{\rm z}/N$ is the desired effect produced by the rf measurement pulse. We now evaluate the undesired effect of the same rf pulse, namely the disturbance of the electron spin qubit state. Following the rf pulse, the final electron spin polarization is calculated as $s_{\rm z,Fin} = \langle\psi_{\rm Fin}|\hat{s}_{\rm z}|\psi_{\rm Fin}\rangle$. Its deviation $\Delta s_{\rm z}$ from the initial $s_{\rm z}$ is a measure of backaction in the form of mixing between the measurement basis states. If the electron is in the $s_{\rm z} = -1/2$ state, $\Delta s_{\rm z}$ is found to be small. This is because the NMR is shifted out of resonance by the electron Knight field and the nuclei are not flipped. In other words, the rf pulse causes minimal evolution of the electron-nuclear spin system. For the $s_{\rm z} = +1/2$ electron spin state the backaction $\Delta s_{\rm z}$ is found to be larger.

In this case the nuclei are flipped by the rf pulse, and the transient hyperfine (Overhauser) field produced by the nuclei is what causes the backaction on the electron spin. Consequently, we focus on the worst-case scenario of $s_z = +1/2$. Once again, for a wide range of model parameters we find a universal functional dependence:

$$\Delta s_z \approx 0.214 \times N \left(\frac{a}{h\nu_{e,0}} \right)^2 , \tag{S13}$$

as can be seen in Supplementary Fig. 12(b). The mixing backaction is seen to be a perturbative effect, which vanishes when the electron-nuclear coupling $\propto a$ is small compared to the electron spin energy gap $h\nu_{e,0}$. Extrapolating the exact results obtained at $N \leq 12$ we estimate Δs_z for our experiments on GaAs QDs. The typical electron spin splitting is $h\nu_e \approx 50$ μeV, arising both from the Zeeman splitting $h\nu_{e,0}$ and the polarized nuclei that are not used in the electron spin readout. We note that the numerator in Supplementary Eq. S13 can be rearranged as $Na^2 = a \times (Na)$. The typical Knight shift is $a/(2h) \approx 70$ kHz. The product Na is the electron hyperfine (Overhauser) splitting due to the nuclei that are used in the electron spin readout (i.e. rotated by the rf pulse), and is typically $\lesssim 15$ μeV. Substituting these numbers we find $\Delta s_z \approx 6 \times 10^{-7}$. The smallness of the backaction on the measured variable s_z is a key defining property of the quantum non-demolition (QND) measurement [37, 38]. The backaction Δs_z can be interpreted as QND infidelity $1 - F_{QND}$. The estimated Δs_z is also small compared to the overall measurement infidelity $1 - F \approx 1 - 0.9985$, confirming that backaction is not the limiting factor, and that the sub-unity fidelity is caused by the electron spin qubit relaxation.

Conjugate to the observable s_z is the electron spin coherence, which can be written in terms of the azimuthal angle [39] of the electron spin in the xy plane. In order to evaluate the measurement backaction in the form of electron spin qubit decoherence we perform the same numerical simulations of the QND process. The only difference is that the electron is now initialized in a superposition of the spin up and down states $\psi_{Init} = 2^{-1/2}(|+1/2\rangle + |-1/2\rangle)$, which is the $s_x = +1/2$ eigenstate. Following the rf pulse, the $s_{x,Fin} = \langle \psi_{Fin} | \hat{s}_x | \psi_{Fin} \rangle$ expectation value is calculated to find the deviation Δs_x, which characterizes the degree of the measurement-induced electron spin qubit decoherence. The universal functional dependence is found to be of the form:

$$\Delta s_x \approx \left((1/2)^{-2} + (0.353 \times N(aT_{rf}/h)^2)^{-2} \right)^{-1/2} , \tag{S14}$$

as shown in Supplementary Fig. 12(c). There are two distinct cases. In the limit of short measurement $N(aT_{rf}/h)^2 \ll 1$ the decoherence Δs_x scales quadratically with aT_{rf}/h. In case of one nuclear spin ($N = 1$), the decoherence Δs_x can be interpreted as the phase acquired by the electron spin

through its interaction with the nucleus over the measurement time $T_{\rm rf}$. Note that $N(aT_{\rm rf}/h)^2 \ll 1$ implies $(aT_{\rm rf}/h)^2 \ll 1$. Taking into account Supplementary Eq. S12, this means that a small decoherence $\Delta s_{\rm x}$ can be achieved only at the expense of a reduced measurement readout contrast $\Delta\Sigma I_{\rm z}$ (i.e. reduced measurement fidelity). This is the case of a weak measurement, where the amount of information obtained is small and the backaction is also small for both the measured variable and the conjugate variable [38, 40–42]. In the opposite case $N(aT_{\rm rf}/h)^2 \geq 1$, the decoherence is nearly complete $s_{\rm x,Fin} \approx 0$, $\Delta s_{\rm x} \approx 1/2$. For $N = 1$ this is the same as the condition for a slow measurement, required to obtain good measurement contrast. For $N \gg 1$ electron spin qubit decoherence occurs before it is possible to achieve good measurement contrast. Moreover, we find that the expectation values of the other electron spin projections also vanish: $s_{\rm y,Fin} \approx s_{\rm z,Fin} \approx 0$. This indicates that electron spin coherence is lost through the measurement-induced entanglement of the electron spin with the nuclear spins, rather than through coherent electron spin precession. Substituting the experimental parameters, we find $N(aT_{\rm rf}/h)^2 \approx 8 \times 10^5 \gg 1$, indicating that our quantum-dot measurement of $s_{\rm z}$ is associated with a complete loss of the conjugate variable (i.e. complete qubit decoherence). In other words, our experiments can be described as a strong QND measurement.

C. Ruling out the measurement-induced "wave function collapse"

Experiments, such as those shown in Figs. 3(b) and 3(c) of the main text, indicate that in the vast majority of the single-cycle measurements the electron is detected in either of its two energy eigenstates $s_{\rm z} = \pm 1/2$. This observation brings up the following questions: Why is it that coherent superpositions are not observed? Does the measurement itself cause the "collapse" of the wave function, projecting the electron spin onto the $s_{\rm z}$ energy basis? At present, it is not possible to create coherent electron spin states in our experiments. Therefore, we use numerical modeling to study these regimes. Once again, we model the QND measurement process with nuclei initialized in a fully-polarized state with $I_{{\rm z},k} = +1/2$ for all $k \in [1, N]$. The electron spin is initialized in a general superposition $\psi_{\rm Init} = \alpha|+1/2\rangle + \beta|-1/2\rangle$ with real α and β, which corresponds to an electron spin eigenstate in the xz plane. The z-projection expectation value is initially $s_{\rm z,Init} = (|\alpha|^2 - |\beta|^2)/2$, while the initial x-projection expectation is $s_{\rm x,Init} = \alpha\beta$. In this calculation we use $N = 10$, $a/(2h) = 100$ kHz, $\nu_{\rm N} = 2$ MHz, $T_{\rm rf} = 25$ μs and $\nu_{\rm e,0} = 20$ or 200 MHz. These parameter sets correspond to the case of the well-resolved Knight-shifted NMR resonances ($aT_{\rm rf}/h > 1$) where the measurement contrast $\Delta\Sigma I_{\rm z}$ is close to its maximum value.

Following the detuned rf pulse we evaluate the expectation value of the spin z projection of the k-th nucleus: $I_{\mathrm{z},k,\mathrm{Fin}} = \langle\psi_{\mathrm{Fin}}|\hat{I}_{\mathrm{z},k}|\psi_{\mathrm{Fin}}\rangle$. With good accuracy we find that spin polarization of each nucleus replicates the initial electron spin polarization $I_{\mathrm{z},k,\mathrm{Fin}} \approx s_{\mathrm{z,Init}}$. This result can be understood qualitatively by noting the large difference in the nuclear and electron spin precession frequencies $\nu_{\mathrm{N}} \ll \nu_{\mathrm{e},0}$, meaning that the fast electron spin precession is averaged out and the nuclei effectively sense only the average polarization $s_{\mathrm{z,Init}}$ of the electron spin. An example of this averaging is found in Supplementary Fig. 11, where the evolution of the nuclear spin polarization components is seen to be slower than the electron spin precession.

Moreover, the electron spin z polarization is essentially unchanged by the measurement rf pulse $s_{\mathrm{z,Fin}} \approx s_{\mathrm{z,Init}}$, as expected for a QND measurement. This observation allows us to rule out the possibility that the measurement rf pulse can itself "collapse" the electron wave function onto the s_{z} eigenbasis. On the other hand, regardless of the initial $s_{\mathrm{x,Init}}$, the final transverse electron spin components are found to be small $s_{\mathrm{x,Fin}} \approx s_{\mathrm{y,Init}} \approx 0$, signifying electron spin decoherence through entanglement with the nuclear spins.

D. Ruling out the nuclei as a source of einselection

Histograms of the experimentally measured single-shot NMR signals (Figs. 3(b) and 3(c) of the main text) reveal sharp bimodal distributions of $\Sigma I_{\mathrm{z,Fin}}$, indicating that the electron is found preferentially in the $s_{\mathrm{z}} = \pm 1/2$ energy eigenstates. In order to verify this interpretation, we use the same model parameters as in Fig. 3(c), but assume a uniform distribution of the electron spin vector on a Bloch sphere (i.e. assume that the electron is in a random superposition of the $s_{\mathrm{z}} = \pm 1/2$ states). Given the linear response of the measurement $I_{\mathrm{z},k,\mathrm{Fin}} \approx s_{\mathrm{z,Init}}$ established above (Supplementary Section 6 C), the single-shot NMR signals ΔE_{hf} should have the same distribution as s_{z}. In other words, the NMR measurement is in principle capable of detecting the electron spin superposition states. The distribution calculated under the assumption of uniformly distributed electron spin superpositions is plotted by the dashed line in Fig. 3(c) of the main text. It is nearly uniform and is incompatible with the experimental histogram, confirming that electron spin superpositions are not realized under equilibrium conditions in our experiments. Quantum mechanics gives no a priori preference to the energy eigenbasis or any other basis. Such a preferential basis, to which the system decoheres from a superposition, can arise from the interaction of the qubit with the environments. This phenomenon is known as einselection [43, 44]. The bimodality of the NMR readouts confirms that such einselection takes place in the experiments. However, the results

of the numerical modeling presented in Supplementary Section 6 C rule out rf manipulation of the nuclear spins as a mechanism of einselection.

In order to complete this analysis, we consider the possibility of einselection induced by the slow equilibrium electron-nuclear spin dynamics, as opposed to the case of fast spin dynamics during the short (tens of μs) rf measurement pulse, as considered above. Here, we construct the initial wave function $\psi_{\rm Init}$ as a product state, where the nuclei and the electron are initially polarized in the xy plane (which is orthogonal to the static magnetic field direction z). The nuclei are aligned along the x axis, so that each nucleus is initially in a superposition $2^{-1/2}(|+1/2\rangle + |-1/2\rangle)$ of its single-particle eigenstates $I_{{\rm z},k} = \pm 1/2$. We consider different initial orientations of the electron spin, by taking the initial superposition of the $s_{\rm z} = \pm 1/2$ states as $2^{-1/2}(|+1/2\rangle \pm |-1/2\rangle)$ (corresponding to the $s_{\rm x} = \pm 1/2$ eigenstate) or $2^{-1/2}(|+1/2\rangle \pm i|-1/2\rangle)$ (corresponding to the $s_{\rm y} = \pm 1/2$ eigenstate). For all these states the z projection expectation value is $s_{\rm z,Init} = 0$. There is no rf pulse in this simulation – the electron-nuclear system is allowed to evolve freely for a few tens of milliseconds, which is much longer than all the relevant interaction timescales, and is therefore sufficient to achieve the steady state. We then calculate the final electron spin polarization $s_{\rm z,Fin} = \langle \psi_{\rm Fin}|\hat{s}_{\rm z}|\psi_{\rm Fin}\rangle$ that emerges from the electron-nuclear interaction. The value of $s_{\rm z,Fin}$ depends on the initial mutual orientation of the electron and nuclear spins. In case of the orthogonal orientation ($s_{\rm y} = \pm 1/2$) we find $s_{\rm z,Fin} \approx 0$. In the case where the electron spin $s_{\rm x} = -1/2$ ($s_{\rm x} = +1/2$) is initially aligned (antiparallel) parallel to the nuclei, we find negative (positive) $s_{\rm z,Fin}$. For a wide range of parameters we find that the magnitude follows an empirical relation:

$$|s_{\rm z,Emerg}| \approx 0.231 \times N \frac{a}{h\nu_{\rm e,0}}. \tag{S15}$$

Up to a factor on the order of unity, this result has a simple interpretation as a ratio of two energies. The initial mutual electron-nuclear hyperfine energy is $\pm Na/4$ according to Supplementary Eq. S8, while the electron spin energy splitting is $h\nu_{\rm e,0}$. We now extrapolate these results to the case of a real GaAs QD. In a thermal equilibrium any non-zero nuclear spin polarization is due to the statistical fluctuations, which scale as $\approx \sqrt{N}$. Thus we substitute N with $\sqrt{N}$ and $\nu_{\rm e,0}$ with $\nu_{\rm e}$ in Supplementary Eq. S15, and use the realistic values $h\nu_{\rm e} \approx 50$ μeV, $a/(2h) \approx 70$ kHz, $N \approx 10^5$ to find a small final nuclear spin polarization $|s_{\rm z,Emerg}| \approx 10^{-3}$. The emergence of a small electron spin polarization $|s_{\rm z,Emerg}| \ll 1/2$ has a simple interpretation in that the hyperfine energy of an equilibrium nuclear spin fluctuation is much smaller than the electron Zeeman energy, making it energetically impossible for the nuclei to "collapse" the electron spin superposition into its energy

eigenbasis. Thus we rule out the low-energy nuclear spin environment as a source of einselection for the electron spin.

Unlike the low-energy nuclear spins, the crystalline environment of the QD electron can act as a high-energy environment responsible for einselection. Coupling between the QD electron spin and the phonons manifests in electron spin relaxation. At low temperatures ($T = 4.2$ K), the electron spin relaxation is dominated by single-phonon processes [11, 34]. Reduction of the electron spin lifetime $T_{1,\mathrm{e}}$ with increasing magnetic field B_z indicates that the phonon coupling is the dominant electron spin relaxation channel. By contrast, relaxation of the QD electron spin due to its cotunneling coupling with the Fermi reservoir would have resulted in B_z-independent spin lifetimes [34]. Following Eq. 4 of Ref. [11] the effective spin-phonon coupling can be written as $\propto (\hat{s}_\mathrm{x}\mathcal{E}_\mathrm{x} - \hat{s}_\mathrm{y}\mathcal{E}_\mathrm{y})$, where $\mathcal{E}_\mathrm{x,y}$ are the Cartesian components of the phonon-induced piezo-strain electric field. Such form is akin to the magnetic spin resonance Hamiltonian $\propto (\hat{s}_\mathrm{x}B_\mathrm{x} + \hat{s}_\mathrm{y}B_\mathrm{y})$. Therefore, we expect that only the resonant or nearly-resonant spectral components of $\mathcal{E}_\mathrm{x,y}$ can cause the electron spin flips. The two-pulse QND measurement experiments, shown in Supplementary Fig. 10 and in the main text, indicate that electron spin relaxation is well described by a telegraph random process. The phonon-induced microwave electric fields, which drive this telegraph process, must therefore occur in the form of short bursts (much shorter than the rf pulse $\lesssim 10$ μs), separated by long (milliseconds) random intervals. Such electric field bursts can rotate the electron spin at random times and with random phases, which would explain both the spin relaxation and the einselection. Spontaneous collapses and burst-like revivals have long been investigated in Bosonic systems, such as photons [45] and phonons [46, 47], and are typically associated with high mode population numbers $\bar{n} \gtrsim 100$. For our experiments at $T = 4.2$ K and $h\nu_\mathrm{e} \approx 50$ μeV, the average phonon number is $\bar{n} \approx 6.8$. The appearance of spontaneous revivals at such low excitations is somewhat unexpected and calls for further investigation of quantum jumps at variable T and $h\nu_\mathrm{e}$, as well as development of the microscopic theory behind the electron spin einselection. Higher-order correlations of the electron spin quantum jumps can be studied using three or more readout pulses. Sensitive detection of the low-energy phonons is itself an interesting application in the context of particle detection [48] and dark matter research [49].

Supplementary Section 7. MEASUREMENT PROBLEM AND INTERPRETATION OF QUANTUM MECHANICS

The major success of the quantum theory is the accurate description of microscopic systems in terms of superposition states, evolving according to the linear Schrödinger equation. However, in order to gain information about a microsystem it must be brought into contact with another, typically much larger (macroscopic), system referred to as the measurement apparatus. The bulk of experimental evidence suggests that the macroscopic measurement apparatus takes only a limited set of eigenstates, but not the superpositions. The prevailing view, often referred to as "Copenhagen interpretation", asserts that quantum mechanics is intrinsically indeterministic, and that the probabilities of the macroscopic eigenstate outcomes should be calculated through a non-linear reduction ("collapse") of the wave function according to the "Born rule". Despite its successes in describing experimental phenomena, this approach struggles to reconcile the two incompatible principles of a linear state evolution and a discontinuous nonlinear state "collapse". The measurement problem is thus a problem of explaining how such a "collapse" occurs and whether it is even real. At present, there is no universally accepted solution to this problem. Various theories propose radically different interpretations. On the one hand, there are dynamical reduction models which assume non-linear state evolution and real wave function collapse, e.g. due to gravity [50]. On the other hand, models such as Quantum Darwinism [33, 44] seek to describe the measurement process within the standard linear evolution paradigm. Extensive reviews on the topic can be found in Refs. [43, 44, 50, 51]. Here, we present a brief discussion, specific to the context of our experimental results.

Firstly, one may ask if our experiments distinguish definitively between the "real wave function collapse" and "Quantum Darwinism" interpretations? The answer is negative. However, the same negative answer applies to any experimental verification. This is because (i) there is no commonly-accepted physical mechanism which would account for a real "collapse" of the wave function in any chosen quantum system, and (ii) one can always put forward an argument that a real wave function collapse can be induced by some weak mechanism, such as gravity, or some yet-undescribed force of nature. Thus, with the present state of knowledge in the field, there is no way to resolve the quantum measurement problem in a decisive and definitive manner.

While the strong question about the reality of the wave function collapse cannot be answered, we can pose a weaker question: Is it possible find at least one example where the measurement can be described in terms of linear evolution without relying on any "collapse". We argue that

our experimental results constitute such an example. We highlight the following two properties of the quantum dot electron-nuclear spin system, which allow for a linear-evolution description. (i) Despite its many-body nature, this quantum system is very "clean", in a sense that every microscopic interaction between the electron, the nuclei and the controlling rf fields is well known. On the timescale of the measurement process ($T_{\rm rf} \approx 10 - 20$ μs), it is essentially a closed system, coupled only to the rf magnetic field. The rf manipulation of the nuclei offers coherent control with very high fidelities. (ii) A key aspect of the measurement problem is the vagueness of the boundary between the quantum (microscopic) and the classical (macroscopic). To use the Schrödinger's cat paradox as an example, the overwhelming experimental evidence is that a cat is too big to be in a superposition, while the behaviour of a single atomic particle can be described accurately only with the use of superpositions. Yet it is generally impossible to say where the boundary lies between these two extremes. Our system is special in that the single particle (electron) is connected to a rather large ensemble consisting of $N \approx 10^5$ nuclei. This way we can conveniently cross the fuzzy quantum-classical boundary with a single high-fidelity rf pulse, which copies the electron spin projection into $\approx 10^4 - 10^5$ identical nuclei through a linear (unitary) evolution. The arithmetic sum of $\approx 10^4 - 10^5$ copies behaves as a good "classical" variable, which is verified in a simple calibration experiment of Supplementary Fig. 8: when the light is shone onto the nuclei, their polarization does not collapse but decays slowly and gradually. One can draw analogy with connecting a (classical) voltmeter to a (classical) capacitor: the measurement will inevitably discharge the capacitor, but would produce enough data to conclude whether the capacitor was charged or not in the first place. Measuring an electric charge of $\approx 10^4 - 10^5$ quanta is a straightforward task. Detecting such, or even smaller, charges is the basic operating principle of the digital (i.e. classical and deterministic) logic gates built from silicon field effect transistors and found in their billions in modern semiconductor microprocessors. In the same way, optical probing in our experiments reveals in a nearly deterministic manner whether the $\approx 10^4 - 10^5$ nuclei of a quantum dot are polarized or not, yielding the spin projection state of a single electron with very high fidelity. It is worth noting, that in the discussion above we rely on the absence of a long-range order and correlations between the $\approx 10^4 - 10^5$ nuclei that hold the individual copies of the electron spin $s_{\rm z}$ state. The distinction between quantum and classical systems based on the number of particles would not apply to correlated systems, such as Bose-Einstein condensates, superconductors and superfluids below their critical temperatures, where quantum effects dominate both the microscopic and macroscopic properties. Long-range ordering in nuclear spin lattices is possible at very low (nanokelvin range) temperatures [52]. In the context of the present work it is safe to treat the

$\approx 10^4 - 10^5$ nuclei as uncorrelated.

The experimental setting provided by the electron-nuclear spin system allows us to perform a quantum measurement in a way that does not require us to refer to any "wave function collapse", or consider any departure from the Schrödinger equation until we get to a reasonably "classical" level of $\approx 10^4 - 10^5$ quanta. Of course, as explained above, it does not mean that the real wave function collapse is ruled out by our experiments. There is always a possibility that such collapses happen with the QD electron spin qubit but are just too rare for us to distinguish from the more frequent phonon-induced quantum jumps. Currently, there is no way to eliminate such a possibility through experiment. But we can conduct our reasoning in a reverse direction by asking the following questions: if our quantum system does not require "collapses" to describe a measurement, then why would such collapses be needed in other systems? Is it not more plausible to accept that the reference to "collapse" appears when there is simply not enough information at hand to get a complete microscopic description of the system, or because the fanout factor in the copying of the quantum variable is too small (i.e. much smaller than $\approx 10^4 - 10^5$) to convince a human observer that the measurement outcome is sufficiently deterministic and "classical". The quantum measurement problem has been a puzzle for more than a century and is likely to remain unresolved for some time to come. However, we argue that our experimental results point in a certain direction, suggesting that the theories aiming to solve the measurement problem through linear evolution at least deserve serious attention.

Supplementary Section 8. RAW DATA

Raw data is provided in a tab-separated format for the single-cycle (single-shot) NMR histograms. The data for one-dimensional histograms shown in Figs. 3(a)–3(c) of the main text is given in a single-column format, where each line is a differential single-cycle NMR signal in μeV. The file names are Fig3a.txt, Fig3b.txt, Fig3c.txt. The corresponding sizes of the datasets are 3597, 31429 and 14037 single shots, respectively.

The data for the two-dimensional histogram shown in Fig. 2(b) of the main text is given in a two-column format, where each line corresponds to a differential single-cycle NMR measurement. The first column is the radiofrequency offset from the bare NMR frequency in kHz. The second column is the NMR signal in μeV. The size of the dataset in file Fig2b.txt is 6870 single shots. The rf pulse duration in this measurement is extended to $T_{\mathrm{rf}} = 40$ μs (compared to $T_{\mathrm{rf}} = 10 - 20$ μs in most single-shot readout experiments) in order to reduce spectral broadening of the measured

NMR spectra.

The data for the two-dimensional histogram shown in Supplementary Figs. 10(b) and 10(e) is also given in a two-column format. The first column is the free evolution time T_{Evol} in μs. The second column is the NMR signal in μeV. The sizes of the datasets in files FigS8b.txt and FigS8e.txt are 13380 and 60100 single shots, respectively.

The time-dependent data shown in Supplementary Fig. 11(a) is given in a two-column format, where each line corresponds to a timepoint. The first column is the time in s. The second column is the rf field given in terms of Rabi frequency in Hz. The file name is FigS11a.txt. The time-dependent data shown in Supplementary Figs. 11(b-g) is given in three files FigS11b,c.txt, FigS11d,e.txt, and FigS11f,g.txt. Each file consists of 7 columns. The first column is the time in s. The second column is the expectation of the total x spin projection of the nuclei, not normalized by the number of nuclei $N = 10$. The third and the fourth columns are the y and z total nuclear spin projections, respectively. The fifth, sixth, and seventh columns are the expectations of the x, y, and z spin projections of the electron.

---

[1] P. Millington-Hotze, S. Manna, S. F. Covre da Silva, A. Rastelli, and E. A. Chekhovich, Nuclear spin diffusion in the central spin system of a GaAs/AlGaAs quantum dot, Nat. Commun. **14**, 2677 (2023).

[2] L. Zaporski, N. Shofer, J. H. Bodey, S. Manna, G. Gillard, M. H. Appel, C. Schimpf, S. F. Covre da Silva, J. Jarman, G. Delamare, G. Park, U. Haeusler, E. A. Chekhovich, A. Rastelli, D. A. Gangloff, M. Atatüre, and C. Le Gall, Ideal refocusing of an optically active spin qubit under strong hyperfine interactions, Nat. Nanotechnol. **18**, 257–263 (2023).

[3] P. Millington-Hotze, H. E. Dyte, S. Manna, S. F. C. da Silva, A. Rastelli, and E. A. Chekhovich, Approaching a fully-polarized state of nuclear spins in a semiconductor quantum dot, arXiv:2302.05489 (2023).

[4] A. Oshiyama and S. Ohnishi, DX center: Crossover of deep and shallow states in Si-doped $Al_xGa_{1-x}As$, Phys. Rev. B **33**, 4320 (1986).

[5] P. M. Mooney, Deep donor levels (DX centers) in III-V semiconductors, Journal of Applied Physics **67**, R1 (1990).

[6] L. Zhai, M. C. Löbl, G. N. Nguyen, J. Ritzmann, A. Javadi, C. Spinnler, A. D. Wieck, A. Ludwig, and R. J. Warburton, Low-noise GaAs quantum dots for quantum photonics, Nat. Commun. **11**, 4745 (2020).

[7] C. Heyn, A. Stemmann, T. Koppen, C. Strelow, T. Kipp, M. Grave, S. Mendach, and W. Hansen, Highly uniform and strain-free GaAs quantum dots fabricated by filling of self-assembled nanoholes, Appl. Phys. Lett. **94**, 183113 (2009).

[8] P. Atkinson, E. Zallo, and O. G. Schmidt, Independent wavelength and density control of uniform GaAs/AlGaAs quantum dots grown by infilling self-assembled nanoholes, J. Appl. Phys. **112**, 054303 (2012).

[9] G. L. Bir and G. E. Pikus, *Symmetry and Strain-induced Effects in Semiconductors* (Wiley, 1974).

[10] W. A. Coish and J. Baugh, Nuclear spins in nanostructures, Physica Status Solidi (b) **246**, 2203 (2009).

[11] A. V. Khaetskii and Y. V. Nazarov, Spin-flip transitions between zeeman sublevels in semiconductor quantum dots, Phys. Rev. B **64**, 125316 (2001).

[12] S. I. Erlingsson and Y. V. Nazarov, Hyperfine-mediated transitions between a Zeeman split doublet in GaAs quantum dots: The role of the internal field, Phys. Rev. B **66**, 155327 (2002).

[13] L. M. Woods, T. L. Reinecke, and Y. Lyanda-Geller, Spin relaxation in quantum dots, Phys. Rev. B **66**, 161318(R) (2002).

[14] E. A. Chekhovich, S. F. C. da Silva, and A. Rastelli, Nuclear spin quantum register in an optically active semiconductor quantum dot, Nat. Nanotechnol. **15**, 999 (2020).

[15] G. Gillard, E. Clarke, and E. A. Chekhovich, Harnessing many-body spin environment for long coherence storage and high-fidelity single-shot qubit readout, Nature Commun. **13**, 4048 (2022).

[16] E. A. Chekhovich, K. V. Kavokin, J. Puebla, A. B. Krysa, M. Hopkinson, A. D. Andreev, A. M. Sanchez, R. Beanland, M. S. Skolnick, and A. I. Tartakovskii, Structural analysis of strained quantum dots using nuclear magnetic resonance, Nat. Nanotechnol. **7**, 646 (2012).

[17] C. P. Slichter, *Principles of Magnetic Resonance* (Springer, 1990).

[18] A. Ulhaq, Q. Duan, E. Zallo, F. Ding, O. G. Schmidt, A. I. Tartakovskii, M. S. Skolnick, and E. A. Chekhovich, Vanishing electron g factor and long-lived nuclear spin polarization in weakly strained nanohole-filled GaAs/AlGaAs quantum dots, Phys. Rev. B **93**, 165306 (2016).

[19] E. A. Chekhovich, I. M. Griffiths, M. S. Skolnick, H. Huang, S. F. Covre da Silva, X. Yuan, and A. Rastelli, Cross calibration of deformation potentials and gradient-elastic tensors of GaAs using photoluminescence and nuclear magnetic resonance spectroscopy in GaAs/AlGaAs quantum dot structures, Phys. Rev. B **97**, 235311 (2018).

[20] E. A. Chekhovich, A. Ulhaq, E. Zallo, F. Ding, O. G. Schmidt, and M. S. Skolnick, Measurement of the spin temperature of optically cooled nuclei and GaAs hyperfine constants in GaAs/AlGaAs quantum dots, Nat. Mater. **16**, 982 (2017).

[21] E. A. Chekhovich, M. M. Glazov, A. B. Krysa, M. Hopkinson, P. Senellart, A. Lemaître, M. S. Skolnick, and A. I. Tartakovskii, Element-sensitive measurement of the hole-nuclear spin interaction in quantum dots, Nat. Phys. **9**, 74 (2013).

[22] D. Gammon, A. L. Efros, T. A. Kennedy, M. Rosen, D. S. Katzer, D. Park, S. W. Brown, V. L. Korenev, and I. A. Merkulov, Electron and nuclear spin interactions in the optical spectra of single GaAs quantum dots, Phys. Rev. Lett. **86**, 5176 (2001).

[23] B. Eble, O. Krebs, A. Lemaître, K. Kowalik, A. Kudelski, P. Voisin, B. Urbaszek, X. Marie, and T. Amand, Dynamic nuclear polarization of a single charge-tunable InAs/GaAs quantum dot, Phys.

Rev. B **74**, 081306 (2006).

[24] J. Skiba-Szymanska, E. A. Chekhovich, A. E. Nikolaenko, A. I. Tartakovskii, M. N. Makhonin, I. Drouzas, M. S. Skolnick, and A. B. Krysa, Overhauser effect in individual InP/$Ga_xIn_{1-x}P$ dots, Phys. Rev. B **77**, 165338 (2008).

[25] G. Ragunathan, J. Kobak, G. Gillard, W. Pacuski, K. Sobczak, J. Borysiuk, M. S. Skolnick, and E. A. Chekhovich, Direct measurement of hyperfine shifts and radio frequency manipulation of nuclear spins in individual CdTe/ZnTe quantum dots, Phys. Rev. Lett. **122**, 096801 (2019).

[26] B. Urbaszek, X. Marie, T. Amand, O. Krebs, P. Voisin, P. Maletinsky, A. Högele, and A. Imamoğlu, Nuclear spin physics in quantum dots: An optical investigation, Rev. Mod. Phys. **85**, 79 (2013).

[27] E. A. Chekhovich, M. Hopkinson, M. S. Skolnick, and A. I. Tartakovskii, Suppression of nuclear spin bath fluctuations in self-assembled quantum dots induced by inhomogeneous strain, Nature Commun. **6**, 6348 (2015).

[28] M. Atature, J. Dreiser, A. Badolato, A. Hogele, K. Karrai, and A. Imamoğlu, Quantum-Dot Spin-State Preparation with Near-Unity Fidelity, Science **312**, 551 (2006).

[29] W. T. Wenckebach, The solid effect, Applied Magnetic Resonance **34**, 227 (2008).

[30] E. A. Chekhovich, M. N. Makhonin, K. V. Kavokin, A. B. Krysa, M. S. Skolnick, and A. I. Tartakovskii, Pumping of nuclear spins by optical excitation of spin-forbidden transitions in a quantum dot, Phys. Rev. Lett. **104**, 066804 (2010).

[31] C. Schimpf, M. Reindl, P. Klenovský, T. Fromherz, S. F. Covre Da Silva, J. Hofer, C. Schneider, S. Höfling, R. Trotta, and A. Rastelli, Resolving the temporal evolution of line broadening in single quantum emitters, Opt. Express **27**, 35290 (2019).

[32] C.-P. Yang, Y.-x. Liu, and F. Nori, Phase gate of one qubit simultaneously controlling n qubits in a cavity, Phys. Rev. A **81**, 062323 (2010).

[33] W. H. Zurek, Quantum Darwinism, Nat. Phys. **5**, 181 (2009).

[34] G. Gillard, I. M. Griffiths, G. Ragunathan, A. Ulhaq, C. McEwan, E. Clarke, and E. A. Chekhovich, Fundamental limits of electron and nuclear spin qubit lifetimes in an isolated self-assembled quantum dot, npj Quantum Inf. **7**, 43 (2021).

[35] K. A. Serrels, E. Ramsay, P. A. Dalgarno, B. Gerardot, J. A. O'Connor, R. H. Hadfield, R. J. Warburton, and D. T. Reid, Solid immersion lens applications for nanophotonic devices, Journal of Nanophotonics **2**, 021854 (2008).

[36] M. Munsch, G. Wust, A. V. Kuhlmann, F. Xue, A. Ludwig, D. Reuter, A. D. Wieck, M. Poggio, and R. J. Warburton, Manipulation of the nuclear spin ensemble in a quantum dot with chirped magnetic resonance pulses, Nature Nanotechnol. **9**, 671 (2014).

[37] A. Blais, R.-S. Huang, A. Wallraff, S. M. Girvin, and R. J. Schoelkopf, Cavity quantum electrodynamics for superconducting electrical circuits: An architecture for quantum computation, Phys. Rev. A **69**, 062320 (2004).

[38] T. C. Ralph, S. D. Bartlett, J. L. O'Brien, G. J. Pryde, and H. M. Wiseman, Quantum nondemolition

measurements for quantum information, Phys. Rev. A **73**, 012113 (2006).

[39] J. Dubois, U. Saalmann, and J. M. Rost, Symmetry-induced decoherence-free subspaces, Phys. Rev. Res. **5**, L012003 (2023).

[40] M. Hatridge, S. Shankar, M. Mirrahimi, F. Schackert, K. Geerlings, T. Brecht, K. M. Sliwa, B. Abdo, L. Frunzio, S. M. Girvin, R. J. Schoelkopf, and M. H. Devoret, Quantum back-action of an individual variable-strength measurement, Science **339**, 178 (2013).

[41] K. S. Cujia, J. M. Boss, K. Herb, J. Zopes, and C. L. Degen, Tracking the precession of single nuclear spins by weak measurements, Nature **571**, 230 (2019).

[42] M. Pfender, P. Wang, H. Sumiya, S. Onoda, W. Yang, D. B. R. Dasari, P. Neumann, X.-Y. Pan, J. Isoya, R.-B. Liu, and J. Wrachtrup, High-resolution spectroscopy of single nuclear spins via sequential weak measurements, Nature Communications **10**, 594 (2019).

[43] M. Schlosshauer, Decoherence, the measurement problem, and interpretations of quantum mechanics, Rev. Mod. Phys. **76**, 1267 (2005).

[44] W. H. Zurek, Quantum theory of the classical: quantum jumps, Born's Rule and objective classical reality via quantum Darwinism, Philosophical Transactions of the Royal Society A: Mathematical, Physical and Engineering Sciences **376**, 20180107 (2018).

[45] J. H. Eberly, N. B. Narozhny, and J. J. Sanchez-Mondragon, Periodic spontaneous collapse and revival in a simple quantum model, Phys. Rev. Lett. **44**, 1323 (1980).

[46] V. Hizhnyakov, Relaxation jumps of strong vibration, Phys. Rev. B **53**, 13981 (1996).

[47] O. V. Misochko, M. Hase, K. Ishioka, and M. Kitajima, Observation of an amplitude collapse and revival of chirped coherent phonons in bismuth, Phys. Rev. Lett. **92**, 197401 (2004).

[48] B. Young, B. Cabrera, A. Lee, and B. Dougherty, Detection of elementary particles using silicon crystal acoustic detectors with titanium transition edge phonon sensors, Nuclear Instruments and Methods in Physics Research Section A: Accelerators, Spectrometers, Detectors and Associated Equipment **311**, 195 (1992).

[49] I. Alkhatib, D. W. P. Amaral, T. Aralis, T. Aramaki, I. J. Arnquist, I. Ataee Langroudy, E. Azadbakht, S. Banik, D. Barker, C. Bathurst, D. A. Bauer, L. V. S. Bezerra, R. Bhattacharyya, T. Binder, M. A. Bowles, P. L. Brink, R. Bunker, B. Cabrera, R. Calkins, R. A. Cameron, C. Cartaro, D. G. Cerdeño, Y.-Y. Chang, M. Chaudhuri, R. Chen, N. Chott, J. Cooley, H. Coombes, J. Corbett, P. Cushman, F. De Brienne, M. L. di Vacri, M. D. Diamond, E. Fascione, E. Figueroa-Feliciano, C. W. Fink, K. Fouts, M. Fritts, G. Gerbier, R. Germond, M. Ghaith, S. R. Golwala, H. R. Harris, N. Herbert, B. A. Hines, M. I. Hollister, Z. Hong, E. W. Hoppe, L. Hsu, M. E. Huber, V. Iyer, D. Jardin, A. Jastram, V. K. S. Kashyap, M. H. Kelsey, A. Kubik, N. A. Kurinsky, R. E. Lawrence, A. Li, B. Loer, E. Lopez Asamar, P. Lukens, D. MacDonell, D. B. MacFarlane, R. Mahapatra, V. Mandic, N. Mast, A. J. Mayer, H. Meyer zu Theenhausen, E. M. Michaud, E. Michielin, N. Mirabolfathi, B. Mohanty, J. D. Morales Mendoza, S. Nagorny, J. Nelson, H. Neog, V. Novati, J. L. Orrell, S. M. Oser, W. A. Page, P. Pakarha, R. Partridge, R. Podviianiuk, F. Ponce, S. Poudel, M. Pyle, W. Rau, E. Reid, R. Ren,

T. Reynolds, A. Roberts, A. E. Robinson, T. Saab, B. Sadoulet, J. Sander, A. Sattari, R. W. Schnee, S. Scorza, B. Serfass, D. J. Sincavage, C. Stanford, J. Street, D. Toback, R. Underwood, S. Verma, A. N. Villano, B. von Krosigk, S. L. Watkins, L. Wills, J. S. Wilson, M. J. Wilson, J. Winchell, D. H. Wright, S. Yellin, B. A. Young, T. C. Yu, E. Zhang, H. G. Zhang, X. Zhao, L. Zheng, J. Camilleri, Y. G. Kolomensky, and S. Zuber (SuperCDMS Collaboration), Light dark matter search with a high-resolution athermal phonon detector operated above ground, Phys. Rev. Lett. **127**, 061801 (2021).

[50] A. Bassi and G. Ghirardi, Dynamical reduction models, Physics Reports **379**, 257 (2003).

[51] W. H. Zurek, Decoherence, einselection, and the quantum origins of the classical, Rev. Mod. Phys. **75**, 715 (2003).

[52] A. S. Oja and O. V. Lounasmaa, Nuclear magnetic ordering in simple metals at positive and negative nanokelvin temperatures, Rev. Mod. Phys. **69**, 1 (1997).

Chapter 6

Electron Spin Lifetimes in GaAs QDs

6.1 Introduction

In the previous chapter, we have demonstrated that detuned RF pulses can be used to turn the nuclear spins of GaAs QDs into a probe which, due to the energy scale mismatch, can perform high fidelity, QND, single shot measurements of the spin z projection of a confined electron [137]. In this chapter we now begin to investigate the properties of the electrons in these types of QDs. Confined electrons in QDs provide an excellent qubit for coupling to optical flying qubits (photons) [199–201], possessing high generation rates of both on-demand single [32, 202–204] and entangled photons [33, 205], while also having high entanglement rates with other electron qubits [34]. This makes them excellent candidates for roles in quantum communication.

Fundamental to realising usable QD electron spin qubits is understanding the time scales on which the qubit relaxes to its equilibrium state, as this defines the time that qubit operations can be conducted over. As discussed in Section 2.4.3, the three principal relaxation time scales are the spin lifetime T_1, coherence time T_2, and the dephasing time T_2^*. Recent measurements have demonstrated dephasing times of up to $T_{2,e}^* = 608$ ns and coherence times $T_{2,e} = 3.82$ μs [126, 159], yet the ultimate limitation on qubit operation times is the lifetime, which has been estimated for these QDs to be $T_{1,e} > 400$ μs [126]. However direct measurements have not been conducted previously. Additionally, while previous works have only focused on the case where a single electron is confined to the QD, it is possible to confine additional electrons giving access to p shell states which, due to the different wavefunctions, could potentially have improved properties compared to a single electron (s shell) state. An additional consideration is the interaction between the nuclear spins and the electron's Knight field, which can significantly limit both the control and lifetimes of the nuclear spins [87, 131].

In this chapter we present part of the work conducted on investigating the spin dynamics and

properties of various electron states in GaAs QDs. The full work is presented in [206]. Here, we present initial experiments where nuclear spin relaxation times are used to probe the charge state of the QD and to provide some insight into the electron spin interactions, while the full analysis requiring additional measurements and theoretical modelling are out of the scope of this work and not discussed. We then investigate the one and three electron states as potential spin qubits, first by mapping the effect of the electron Knight field on the nuclear spins, followed by measuring the $T_{1,e}$ times for both states using the method demonstrated in Chapter 5. This technique has already been used to measure $T_{1,e}$ in QDs, however this previous work was conducted on SK grown InGaAs/GaAs QDs and only the $1e$ state was studied [131]. We identify the primary relaxation mechanisms for both electron states. We also find that the current maximum lifetime is $T_{1,e} \approx 50$ ms, though we do also identify routes to improve the lifetime of both electron states.

6.2 Methods

Probing of electron spin lifetimes in this chapter were conducted using the detuned RF protocol demonstrated and studied in Chapter 5, allowing for single-shot QND measurements of the electron spin z projection [137]. The measurements follow the same general outline, though we do use two different variations of the experiment to achieve initialisation of the electron spin either through optical pumping or through measurement, as shown in Fig. 6.1a and b respectively. In both cases the experiment cycle begins with a long optical pump ($T_{\text{Pump}} = 3.5-5.5$ s) to initialise the nuclear spins into a polarised state; then we conduct nuclear spin population transfer to maximise the NMR signal (see Section 3.5.4). During the initial preparation of the nuclear spins the bias across the sample is set to $V_{\text{Gate}} = -2.4$ V to ensure the QD is empty. After this the bias is changed to load the QD with a set number of electrons with typical values $\text{V}_{1e} \approx 1$ V and $\text{V}_{3e} \approx 1.4$ V for the one electron ($1e$) and three electron ($3e$) states respectively. The electron is then left to equilibrate for a short time $T_{\text{Load}} = 30-90$ ms.

Next the electron is initialised. In Fig. 6.1a this is achieved through a short optical pump, which we implement using the same laser as used for the nuclear spin pumping. To ensure rapid control of the pump duration, the laser power is modulated using an AOM in addition to the usual mechanical shutter. The wavelength of the laser therefore needs to be carefully selected to ensure that there is sufficient polarisation of both the nuclei and electron. Fig. 6.2a shows a calibration of the electron spin pumping wavelength, we see over the measured wavelength region that the electron spin polarisation, measured through the same detuned RF pulse protocol, varies significantly with the changing laser wavelength. We select $\lambda_{\text{Pump}} \approx 772.6$ nm for the pump wavelength as polarisations of $P_e \approx 97$ % can be achieved and the polarisation remains stable in the surrounding wavelength region. The effect of the optical pumping on the electron spin z projection is shown in the his-

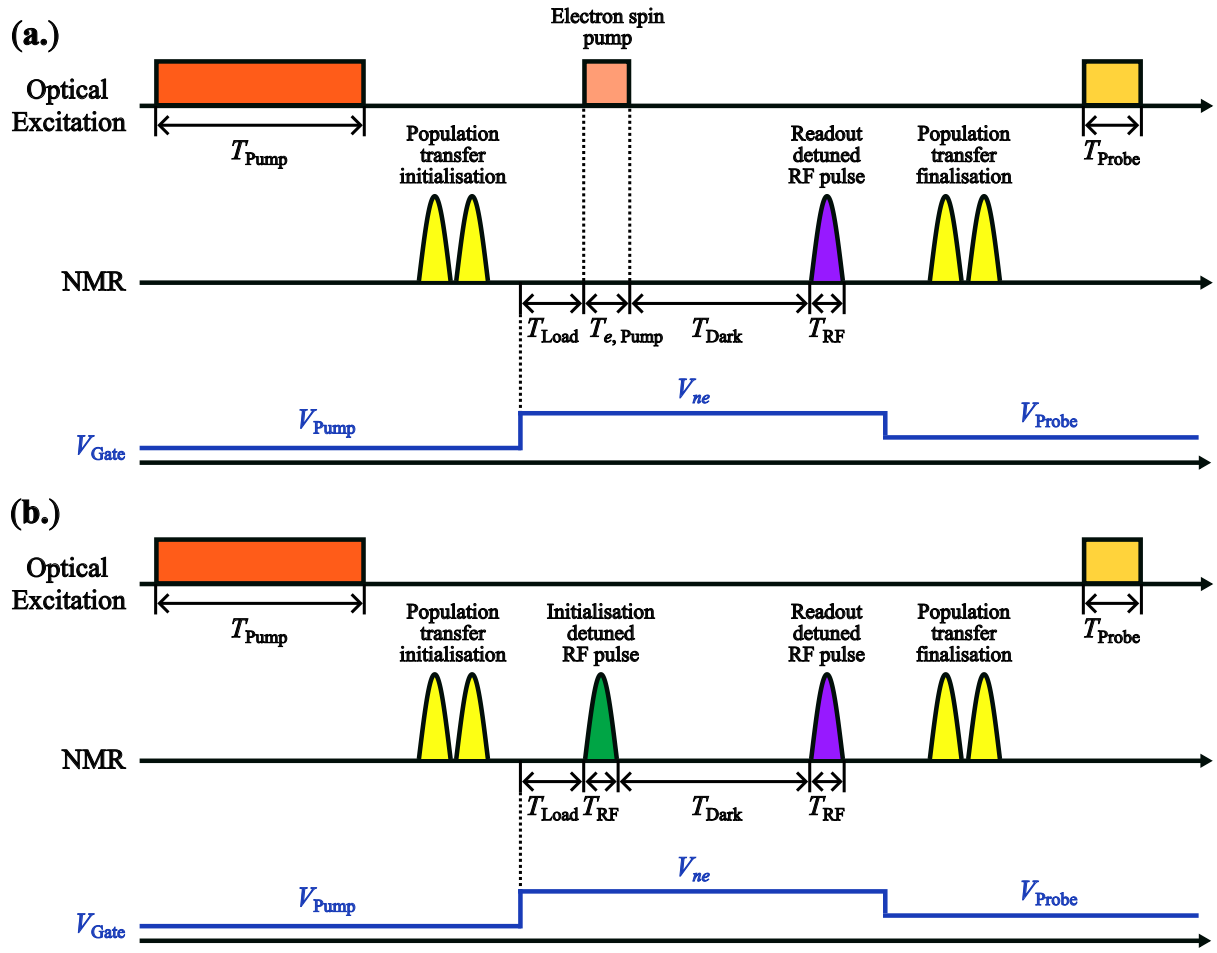


Figure 6.1: (a) Timing diagram for optically initialised electron spin state measurements. First a long ($T_{\text{Pump}} = 3.5 - 5.5$ s) optical pump is used to polarise the QD nuclear spins using circularly polarised light. The bias across the sample is then increased to change the charge state of the QD. The electrons are then left to equilibrate for a short time T_{Load} before a second shorter ($T_{e,\text{Pump}} = 100$ μs) optical pump is produced using an AOM, which can generate electron polarisations of up to $P_e \approx 90\%$. Next the electron is left to evolve in the dark for a variable time T_{Dark} before a detuned RF π pulse is used to encode the electron spin z projection onto the nuclear spins. Typically $T_{\text{RF}} = 10 - 60$ μs. To retrieve the information encoded in the nuclear spin state a short ($T_{\text{Probe}} =$ 40-50 ms) optical probe pulse is used and the nuclear spin state is then obtained through changes in the measured PL splitting. (b) Same as (a) however the electron is initialised through an initial measurement of its z projection before T_{Dark}. The measurement is achieved by applying a detuned RF pulse. A second detuned RF pulse can then be applied either to the same NMR transition or a different isotope, encoding both the initial and final spin z projection of the electron into the nuclei for retrieval via optical probing. If two isotopes are used the number of population transfer pulses is doubled, as pulses need to be applied to both isotopes.

tograms in Figs. 6.2b, c, d and e. In Fig. 6.2b we see that in the absence of optical pumping the two histogram modes corresponding to the two electron spin z projections (labelled on figure) are equal in magnitude, corresponding to the electron being in its equilibrium state with a polarisation degree of $P_e \approx 13\%$. The situation is the same for the $3e$ case where we measure an equilibrium polarisation degree of $P_e \approx 10\%$ (Fig. 6.2c). The result of optically pumping the $1e$ spin state is shown in Fig 6.2d. We see now that the majority of readouts have the electron in the spin down state, while only a small number of spin up readouts occur. The optical pumping has therefore polarised the electron spin into the down state, with a measured polarisation of $P_e \approx -95\%$. We likewise demonstrate that the $3e$ state can also be polarised optically, as we see in Fig 6.2e, where we measure a polarisation degree of $P_e \approx -77\%$. As we are using the same pump laser for the nuclear and electron spin polarisation, electron spin polarisation currently occurs through a quasi-resonant pumping of the p shell state, limiting the achievable polarisation. Values approaching 100 % should be achievable using the spin-shelving technique [30]. Alternatively, in some situations initialisation through optical pumping was insufficient to be measurable. We therefore present an alternate measurement scheme where the initial electron spin z projection is measured using a detuned RF pulse, as seen in Fig. 6.1b. The initial RF pulse can be either applied to the same isotope as the readout pulse or a different one. The use of an additional RF pulse causes additional histogram modes to appear during measurements, which can then be used to measure the polarisation state. This will be discussed in more detail in Section 6.5.

After the electron is initialised, the electron is left to evolve freely in the dark, characterised by the time T_{Dark}, before a single detuned RF pulse burst with raised cosine envelope is applied to one of the nuclear spin transitions in order to perform a QND measurement of the electron spin z projection. Typical T_{RF} times are 10-60 μs. The RF pulses are applied to one of the STs of either ^{75}As or ^{69}Ga in order to minimise spectral overlap between the RF pulse and the other nuclear spin transitions. The choice of which ST to use is dependent on the polarisation of the light used in the nuclear spin pumping. In order to maximise signal the ST that the spins are pumped towards will be used. Additionally, the RF detuning is chosen to maximise the separation between the histogram modes to improve the resolution (see Section 6.4). Rabi oscillation measurements are used to calibrate the required pulse amplitude to perform a π rotation of the nuclei. By varying T_{Dark} we can measure the evolution of P_e over time.

Finally, to retrieve the stored electron spin z projection, the nuclei are probed using a short optical pulse with duration $T_{\text{Probe}} = 40-50$ ms, while the bias is set to generate the desired exciton (both X^0 and X^- were used at different external magnetic fields) and to optimise the QD PL. The entire process above is performed as a single-shot measurement, meaning the PL exposures are not averaged. Instead the measurements are repeated hundreds or thousands of times in order to build up sufficient statistics that an estimate of electron spin polarisation degree can be reliably

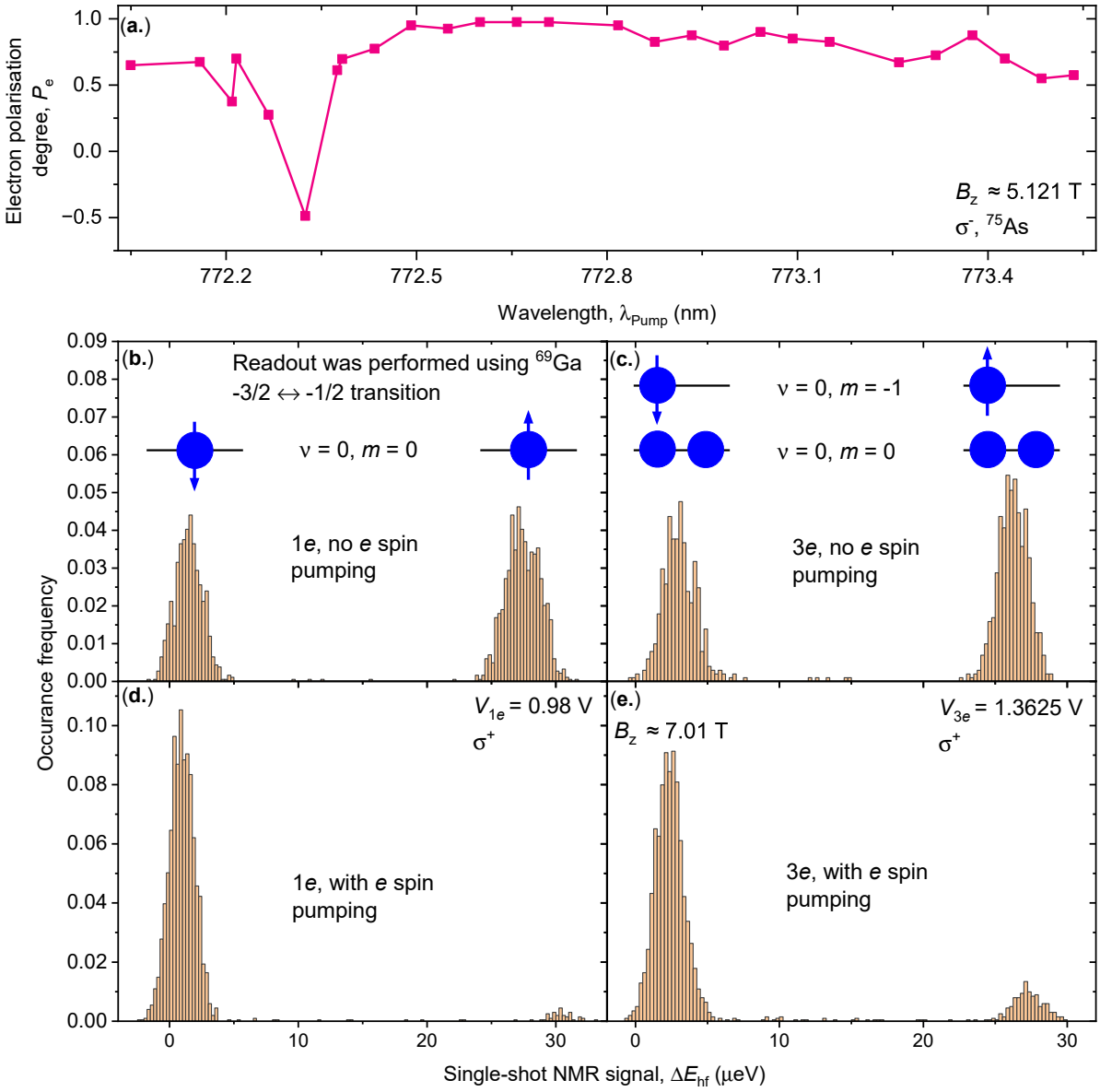


Figure 6.2: (a) Electron pump wavelength calibration measurement, measured using ^{75}As at $B_z \approx 5.121$ T with σ^- pumping. We see that the electron polarisation is relatively stable with respect to the wavelength, with an optimal stable region around $\lambda_{\text{Pump}} \approx 772.6$ nm, giving a polarisation degree of $p_e \approx 97\%$. (b) Histogram showing the single shot statistics of measurements on the one electron z projection in the absence of optical pumping. We observe electron spin polarisation of $P_e \approx 13\%$ meaning that the electron is weakly polarised in the spin up ($s_z = +1/2$) state. (c) Same as (b) but measured on the three electron spin state. Like the one electron state we observe a small equilibrium polarisation of $P_e \approx 10\%$. (d) Measurement of the single electron spin z projection after a short optical pump. Compared to (b) we see a clear difference in the magnitude of the two histogram modes due to the pumping of the electron spin state. The measured polarisation degree is $P_e \approx -95\%$ meaning the electron has been pumped into the spin down state. (e) Same as (d) but measured on the three electron spin state. Again we see the clear effects of the electron spin pumping with a measured polarisation degree of $P_e \approx -77\%$.

determined.

6.3 Deterministic Generation of Charged QD States

To determine the required bias needed to confine an arbitrary number of electrons we need a way to probe the QD charge state. Typically this is done by measuring the capacitance or PL of the QD [55, 79, 84, 85]. Here we instead probe the charge state by its effect on the nuclear spin lifetime $T_{1,N}$ [87]. To measure $T_{1,N}$ the nuclei are optically polarised and are then left to evolve in the dark for time T_{Dark}. The final nuclear spin polarisation is then measured using an optical probe. During T_{Dark} the bias is set to an arbitrary value. By varying T_{Dark} we obtain decay curves like those shown in Fig. 6.3a. The decay curves can be fit with a stretched exponential function in order to obtain $T_{1,N}$. Interestingly, we measure a noticeable difference in the nuclear spin lifetimes for the two biases measured in Fig. 6.3a. We find that for $V_{\text{Gate}} = 0.986$ V the lifetime is $T_{1,N} \approx 237.6$ s, while for $V_{\text{Gate}} = 1.07$ V the lifetime is found to be $T_{1,N} \approx 47.3$ s.

To understand this behaviour we measure the full dependence of $\Gamma_N = 1/T_{1,N}$ on the applied gate bias, obtaining plots like those shown in Fig. 6.3b, where $T_{1,N}$ has been converted into the nuclear spin relaxation rate Γ_N. For the measurements conducted at $B_z \approx 0.982$ T (solid squares) we see that as the bias increases there are several peaks in the relaxation rate for narrow bias regions. These peaks are separated by broader regions where the relaxation rate remains relatively constant. In experiments, observed biases used for optical measurements of the neutral exciton ($V_{\text{Probe}} \approx 0.84$ V) and negative trion ($V_{\text{probe}} \approx 1.06$ V) are found to coincide with the first two stable regions seen in Fig. 6.3b [206]. We therefore infer that these stable regions correspond to the QD being empty ($0e$) and occupied with a single electron ($1e$). We can then extrapolate that the subsequent flat regions correspond to states with an increasing number of electrons, which have been labelled on Fig. 6.3b. The layout of these plateau regions are consistent with the Coulomb blockade structure where the electrons confined within the dot lift the degeneracy of states due to Coulomb repulsion with any electrons being added. Therefore, we see that the $1e$ and $2e$ states occur at different energies. After, the $2e$ region is relatively large compared to the $1e$ case. This is due to the additional energy requirements to load a third electron into the p shell. Finally loading of the $4e$, $5e$ and $6e$ states occurs again at similar intervals as the p shell is filled. The peaks in Γ_N observed in Fig. 6.3b correspond to regions where, due to the applied V_{Gate}, the Fermi energy E_{F} is brought into resonance with the lowest lying unoccupied electron state, greatly enhancing the cotunnelling rate meaning an electron will rapidly tunnel into and out of the QD. The tunnelling electron therefore provides a route for nuclear spin polarisation to be carried out of the QD, explaining the sharp increase in Γ_N [87, 158]. Measurement of the bias dependence of $T_{1,N}$ was conducted at several external magnetic fields B_z; examples are shown in Fig. 6.3b. We observe that

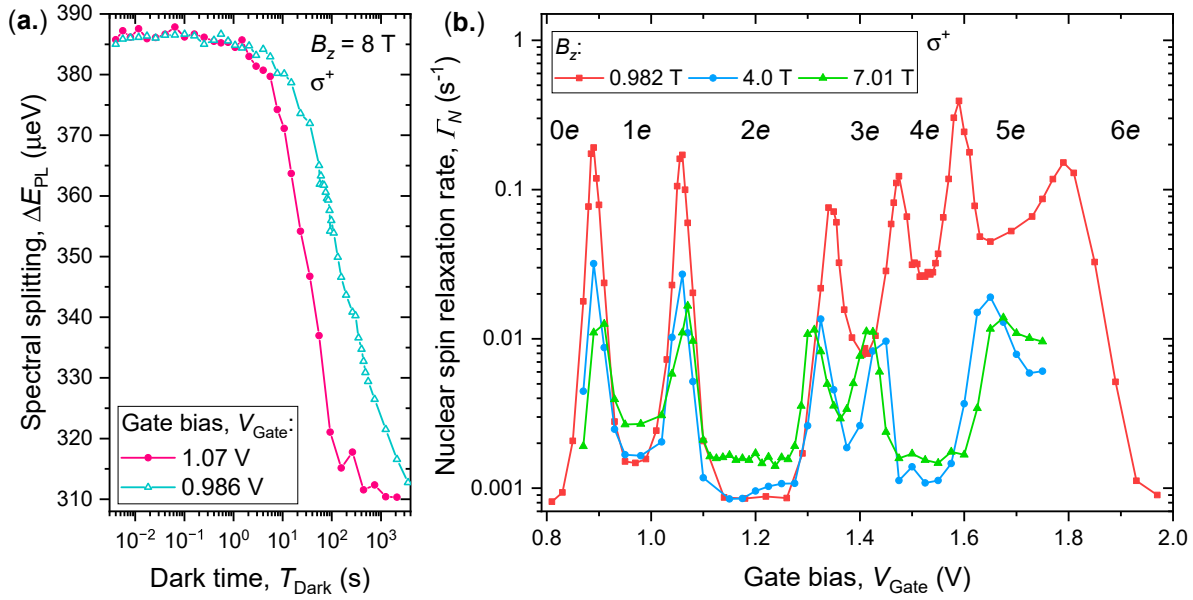


Figure 6.3: (a) Nuclear spin polarisation decay curves measured with external field $B_z = 8$ T applied. The nuclei were optically polarised using σ^+ polarised light. The polarisation is observed to decrease as the dark time T_{Dark} increases. The two shown decay curves were measured on the QD at different gate biases $V_{\text{Gate}} = 1.07$ V (solid circles) and $V_{\text{Gate}} = 0.986$ V (open triangles), where we obtain the nuclear spin lifetimes $T_{1,N} \approx 47.3$ s and $T_{1,N} \approx 237.6$ s respectively. We attribute the change in $T_{1,N}$ to changes in the charge state of the QD. (b) Bias dependence of the nuclear spin relaxation rate $\Gamma_N = 1/T_{1,N}$ measured on the same QD at different external magnetic fields $B_z = 0.982$ T (squares), $B_z = 4.0$ T (circles), and $B_z = 7.01$ T (triangles). At all fields, a pattern of sharp peaks separated by plateau regions emerges as the gate bias V_{Gate} increases. The peaks are attributed to regions where electrons are rapidly tunnelling into and out of the QD, accelerating nuclear spin relaxation. The regions between these spikes are therefore regions where the QD is occupied by a set number of electrons, which have been labelled on the figure. Differences between the relaxation rates at different magnetic fields and in the presence of different numbers of electrons allow the complex spin interactions of the few-electron states to be investigated.

the bias at which each tunnelling peak occurs changes with B_z, meaning that there are changes in the few-electron state energies. However, a full study of this dependence is out of the scope of this work and will be reported on separately [206].

We now analyse the nuclear spin relaxation in the Coulomb blockade regions. In the absence of any electrons, the nuclear spin relaxation is dominated by spin diffusion [116]. The addition of a single electron causes a small increase in the relaxation rate due to the mediation of nuclear spin flip-flops between distant nuclei by the electron [116, 157]. Once a second electron is added, the s shell becomes completely filled with the two electron spins aligned anti-parallel, producing a net spin of zero. Subsequently, the absence of a net electron spin causes Γ_N to return to values comparable with an empty QD. When a third electron is added to the p shell it is unpaired, causing

an expected increase of Γ_N as is the case for $1e$. Interestingly, at low $B_z \approx 0.982$ T, we see the $3e$ state has a higher Γ_N than for the $1e$ state. As we will discuss in Section 6.5 the $3e$ relaxation is dominated by cotunelling, which in turn could accelerate the nuclear spin relaxation [87, 158], explaining the observed result.

Next, looking at the $5e$ and $6e$ cases measured at $B_z = 0.982$ T, we see that in the presence of $5e$ the relaxation rate further increases as expected due to the additional spin dynamics introduced by the fifth electron. Finally, adding a sixth electron fully fills the p shell, meaning all of the electrons are paired and the net spin once again drops to zero, as seen in the measured relaxation rate. While we have discussed potential causes for the spin interaction dynamics measured here, additional measurements and theoretical modelling are required to fully understand them. However as the focus of this chapter is on electron spin lifetimes, these studies are out of the scope of this work and are not discussed any further [206].

6.4 Probing the Knight Field

In order to perform electron spin state readout via the method presented in Chapter 5, the optimal RF pulse detuning needs to be determined to maximise the measurement resolution. Therefore the NMR frequency shift introduced by the electron's Knight field [129] needs to measured. Additionally, such measurements can be used to study the interactions between the electron and nuclear spins, primarily through the hyperfine interaction, which is important for developing ways to exploit the full spin system of a QD where both the electron and nuclear spins can be utilised as quantum resource. It is also important to investigate the broadening of the nuclear spin transition frequencies caused by the electron Knight field, as this can limit the effectiveness of control RF pulses.

We probe the Knight field of the $1e$ and $3e$ states by applying RF pulses detuned from the measured NMR transition frequency, the measurements are performed as single-shot measurements and repeated to collect the required statistics. Histograms of single-shot NMR signals for measurements on a QD loaded with $1e$ are shown by the heat map in Fig. 6.4a. The NMR transition used is the higher ST of ^{75}As (shown by the short dashes) chosen due the transition being favourably pumped by the arbitrarily chosen σ^+ optical pumping. We note that such measurements can also be carried out on the lower ST of ^{75}As as well as both ^{69}Ga STs. At 0 kHz offset we clearly see that there is no NMR signal, in direct contrast with the $0e$ measurement. As the offset increases a bimodal distribution forms, with one mode remaining at $\Delta E_{\text{hf}} \approx 0$ μeV while the other experiences increasing NMR signal as the offset frequency increases, reaching a maximum amplitude of $\Delta E_{\text{hf}} \approx 3$ μeV at an RF offset of $\approx$ 80 kHz. After this, the measured NMR signal for this mode decreases, reaching $\Delta E_{\text{hf}} \approx 0$ μeV at an offset of $\approx$ 230 kHz. This trend is mirrored for

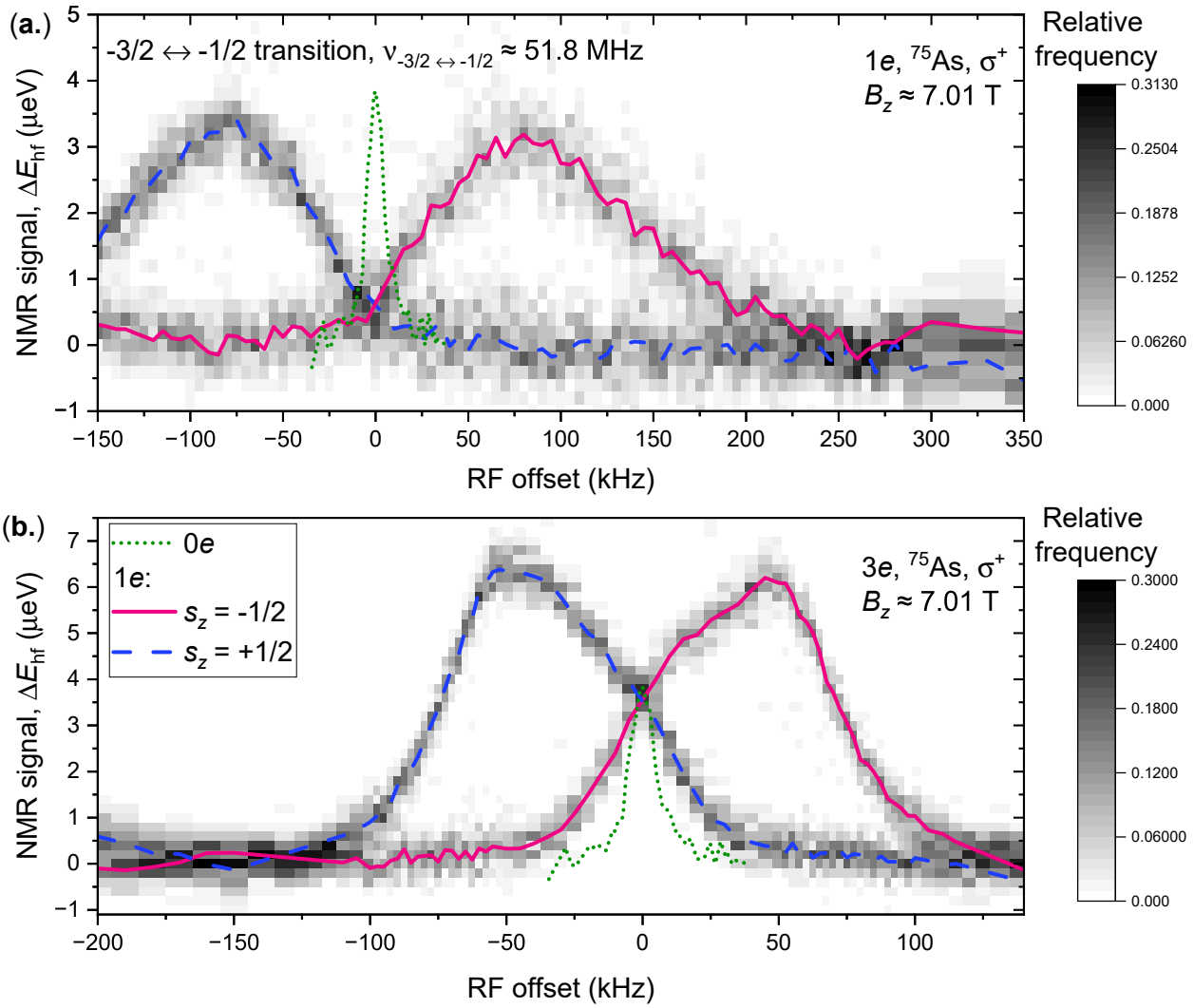


Figure 6.4: (a) Heat map showing results of a series of single-shot QND measurements conducted on the higher ST of ^{75}As ($\nu_{-3/2\leftrightarrow-1/2} \approx 51.8$ MHz) when a single electron ($1e$) is confined within the QD. The $0e$ transition is shown by the dotted line. As the frequency of the RF π pulses is swept relative to the transition frequency a bimodal distribution is observed, corresponding to the Knight shifted NMR transition when the electron is in the spin up ($s_z = +1/2$) or down ($s_z = -1/2$) state, shown by dashed and solid traces respectively. The Knight field for the spin up (down) electron shifts the NMR transition down (up) in frequency, with typical Knight shift $\approx \pm 80$ kHz. Compared to the NMR transition in an empty dot ($0e$) with a FWHM of $\Delta\nu_{-3/2\leftrightarrow-1/2} \approx 12$ kHz, the Knight shifted transitions are significantly broader, with some shifts being up to 250 kHz. (b) Same as (a) this time measured when three electrons ($3e$) are confined within the QD. Again two shifted NMR transitions are observed, corresponding to the Knight field of the unpaired p shell electron. We observe that the p shell electron distributes the nuclear frequencies over a narrower range than the s shell electron with a typical Knight shift $\approx$ 60 kHz, and a maximum offset of $\approx$ 100 kHz. This is due to the larger spatial extent of the p shell electron wavefunction envelope.

negative offsets. The observation of a bimodal distribution in the single shot NMR measurements means there must be two regimes being measured, these being the two electron spin projections ($s_z = \pm 1/2$). Considering a positive offset, NMR signal is only produced if the nuclei are rotated by the RF π pulse, meaning in these cases that the nuclear spins must be resonant with the RF pulse. Therefore when the electron is in the spin down (up) state, the nuclei are shifted up (down) in frequency, causing them to be flipped (not flipped) by the RF pulse [137]. The two modes therefore give the Knight field shifted NMR transitions, traced by the solid and dashed lines for the spin down and up states respectively, which are effectively a convolution of the Knight field and the spectral profile of the raised cosine envelope RF pulses.

From Fig. 6.4a we see that the Knight field of one electron causes a typical Knight shift of $\approx$ 80 kHz away from the $0e$ transition frequency while a small number of nuclei located close to the confined electron are shifted by up to $\approx$ 250 kHz. This means the Knight field causes a significant broadening of the NMR transition, which in the absence of an electron has a FWHM of $\Delta\nu_{-3/2\leftrightarrow-1/2} \approx 12$ kHz making it significantly harder to achieve the so-called hard pulse limit to ensure accurate rotation and control of the nuclei [207, 208]. Additionally the $\approx$ 250 kHz broadening is sufficient that there will be significant overlap between the CT and ST transitions, even with the large ($\nu_Q^{(1),^{75}\mathrm{As}} \approx 255$ kHz and $\nu_Q^{(1),^{69}\mathrm{Ga}} \approx 126$ kHz) first order quadrupolar splitting between the three transitions in this externally strained sample. Therefore the measurement can only be carried out when the Knight field shifts the ST away from the CT frequency. We study the Knight field in the case where three electrons are confined in the dot as shown in Fig. 6.4b. In this case the Knight field produces a typical Knight shift $\approx$ 60 kHz with a maximum offset of $\approx$ 100 kHz. This difference is expected as for the $1e$ case the electron wavefunction has s shell character, while for the $3e$ case the unpaired electron has p shell character. The p shell electron wavefunction envelope overlaps with roughly double the number of nuclei compared to that of an s shell electron, seen from the fact that the nuclear frequency shifts are located in smaller frequency range. This opens up the potential to use the $3e$ state as a qubit, as the smaller broadening of the NMR transitions should make it easier to effectively manipulate the nuclear spins in the presence of the electrons, while also potentially having improved electron coherence, as the electron dephasing scales with $N^{-1/2}$, where N is the number of interacting nuclei [209]. Finally, from Fig. 6.4a and b we extract the optimal RF detuning needed for electron spin readout which, for this field $B_z \approx 7.01$ T, is found to be 80 kHz and 60 kHz for the $1e$ and $3e$ cases respectively.

6.5 Electron Spin Lifetimes

In Section 6.4 we again demonstrate that detuned RF pulses can be used to perform QND measurements of the z projection of a confined electron's spin. The bimodal distributions seen in Fig. 6.4

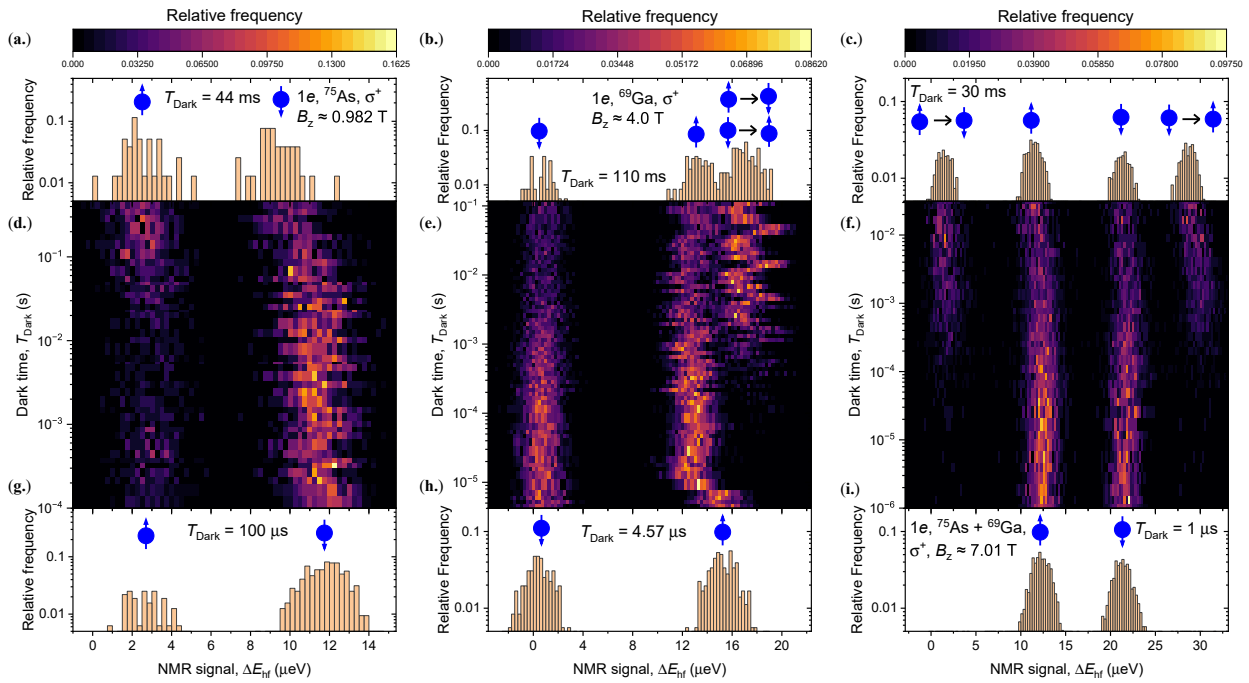


Figure 6.5: (a) Histogram showing statistics of single shot readout measurements conducted on a QD containing a single electron ($1e$). The external field was $B_z = 0.982$ T while readout was performed using ^{75}As initialised using σ^+ polarised light. The readouts are performed at long $T_{\text{Dark}} = 44$ ms where the electron has relaxed into its equilibrium state after being optically polarised, seen in the even distribution of NMR shifts between the two modes (the corresponding electron spin z projections are labelled on the figure). (b) Same as (a) however this time the electron spin is initialised by a detuned RF pulse measurement before T_{Dark}, with readout performed using ^{69}Ga after σ^+ pumping and $B_z = 4$ T. Again at long $T_{\text{Dark}} = 110$ ms the electron is in its equilibrium state and the readouts are evenly distributed between the electron 'spin flip' mode and the two electron 'no flip' modes. (c) Same as (a, b) but this time the initialisation detuned RF pulse is performed on a different isotope (^{75}As) while readout is performed using ^{69}Ga after σ^+ pumping and at $B_z = 7.01$ T. We therefore see four histogram modes, each corresponding to the four possible initial and final spin z projection combinations. Due to the long $T_{\text{Dark}} = 30$ ms the readouts are evenly distributed among the four histogram modes. (d) Heat map of the single shot readout measurements conducted at different T_{Dark} times, we see the electron polarisation decrease as T_{Dark} increases. (e) Same as (d) but measured using the double pulse method, as T_{Dark} increases a third mode appears, corresponding to cases where the electron has undergone a spin flip. (f) Same as (e) but measured using the pulse on two isotopes method, as T_{Dark} increases two additional modes appear, corresponding to cases where the electron has undergone a spin flip. (g) Same as (a) but measured at short $T_{\text{Dark}} = 100$ μs. We find a majority of the NMR shifts are in the electron spin down mode due to the optical initialisation of the electron spin state. (h) Same as (b) but measured at short $T_{\text{Dark}} = 4.57$ μs where the electron does not have sufficient time to undergo a spin flip. We therefore only observe the two modes corresponding to the two electron 'no flip' cases. (i) Same as (c) but measured at short $T_{\text{Dark}} = 1$ μs. Again, the electron has only a small amount of time to undergo a spin flip, meaning that the majority of readouts correspond to the two electron 'no flip' cases.

show that the electron spin z projection can be inferred from which of the two modes a given single-shot readout arises in, due to the fact that the nuclei are flipped (not flipped) only when the RF pulse is in resonance (out of resonance) with the Knight shifted NMR transition [137]. By initialising the electron into an initial state, either through optical pumping or through an initialisation measurement using a detuned RF pulse, and then leaving the electron to evolve for a time T_{Dark}, we can probe the decay of the electron spin polarisation (see timing diagram in Fig. 6.1). At each T_{Dark} a series of single shot readout measurements are performed to produce histograms like those seen in Figs. 6.5a, b, c, g, h and i. Figs. 6.5d, e and f show examples of full sets of histograms over all the measured T_{Dark} values, replotted as a single heat map, the differences in the distributions are caused by the different measurement procedures used for the electron spin readout.

Figs. 6.5a, d and g are obtained from measurements where the electron was polarised optically (Fig. 6.1a). At short times $T_{\mathrm{Dark}} = 100\ \mu$s as seen in Fig. 6.5g we observe an unequal distribution of the modes, suggesting the electron is polarised into the spin down state by the optical pumping. In Fig. 6.5d we see that as T_{Dark} increases the weighting of the two modes equalises, a consequence of the electron undergoing spin flips as it relaxes. Finally, for long $T_{\mathrm{Dark}} = 44$ ms we see in Fig. 6.5a that the magnitude of the two modes are equal, demonstrating that the electron spin has relaxed into its equilibrium state. The distribution of NMR shifts differs from the case in Fig. 6.5d when the optical electron spin polarisation is omitted and two RF pulses are applied. Instead results like those seen in Figs. 6.5b, e and h are obtained. For this case, we now see at short $T_{\mathrm{Dark}} = 4.57\ \mu$s that the NMR shifts are evenly distributed between the two electron z projections, due to the lack of polarisation. Instead these two modes constitute the electron 'no flip' cases as, due to the short T_{Dark}, the electron does not switch z projections between the two detuned RF pulses, meaning the nuclei are either not flipped by either of the pulses (electron spin down) or are flipped by both (electron spin up). It is worth noting that while the two π rotations should produce a full 2π rotation leaving the nuclei in the exact same state as the no nuclear spin flip case, in Fig. 6.5h the NMR shifts are observed to be different. This is due to either pulse amplitude errors or lost spectral overlap due to the broadening caused by the Knight shift. This effect can be seen in the Rabi oscillation measurement in supplementary figure 5, Chapter 5. As T_{Dark} (Fig. 6.5e) increases we now see the amplitude of the two electron 'no flip' modes decrease, while a third mode at $\Delta E_{\mathrm{hf}} \approx 17\ \mu$eV emerges, corresponding to cases where the electron undergoes a spin flip between the two RF pulses meaning the nuclei are only rotated once. Because the nuclei are flipped once it is impossible to distinguish between the two electron spin 'flip' cases. At long $T_{\mathrm{Dark}} = 110$ ms (Fig. 6.5h), the readouts at equilibrium are distributed such that half are the electron 'flip' mode, while the other half are distributed equally between the two electron 'no flip' modes. By measuring the frequency of 'flip' and 'no flip' cases the polarisation can be determined. Finally we present a further modification on the experiment shown in Figs. 6.5b, e and h in which the two RF pulses

are now applied to different isotopes, first ^{75}As then ^{69}Ga. At short $T_{\text{Dark}} = 1\ \mu$s (Fig. 6.5i) we see, like in the one isotope case, the single shot readouts are evenly distributed between the two electron 'no flip' states. However due to how the pulses are implemented both cases now produce an NMR shift as one of the two isotopes will be rotated, which in turn produces different NMR shifts due to the differing populations of nuclei. In Fig. 6.5f we see now that as T_{Dark} increases two new modes appear, which are the two electron 'flip' modes that are now resolvable because the pulses are implemented on two isotopes. We now see for one case the electron spin flip means none of the nuclei are rotated, while for the other both isotopes are flipped. For long $T_{\text{Dark}} = 30$ ms (Fig. 6.5c) we see at equilibrium that the readouts are evenly distributed between the four modes. By comparing the occurrence frequency of the inner two modes against the outer two modes the polarisation can be obtained. All three of the above methods give the same results for electron spin decay, demonstrating the validity of these techniques.

To obtain electron polarisation values from the histograms like those seen in Figs. 6.5a, b, c, g, h and i the number of shots measured for each mode are counted. The middle ΔE_{hf} value between the modes is used to decide the range of NMR shifts corresponding to each mode. The mode populations are then summed based on if they are electron 'no flip' (n_{NoFlip}) or 'flip' (n_{Flip}) cases. The polarisation P_e can then be calculated using the equation:

$$P_e = \frac{n_{\text{Flip}} - n_{\text{NoFlip}}}{n_{\text{Flip}} + n_{\text{NoFlip}}}. \tag{6.1}$$

For a given magnetic field B_z, we can plot the measured P_e values against T_{Dark}, obtaining decay curves like those shown in Fig. 6.5a. We confirm the observations made from the heat maps in Figs. 6.5d, e and f, observing a clear loss in electron spin polarisation overtime. Additionally, we note that for the $1e$ case there appears to be a dependence on the magnetic field, with $T_{1,e}$ decreasing as B_z increases as observed in the measured values. Comparatively, for the two curves measured on the $3e$ state the values of $T_{1,e}$ seen are approximately equal. The $T_{1,e}$ values are obtained by fitting the curves in Fig. 6.5a with a stretched exponential function. The fitted values are then plotted in Fig. 6.5b against B_z. We see, on a log-log scale, a power law dependence between T_1 and B_z for the $1e$ lifetime. As discussed in Section 2.4.3 electron spin relaxation is dominated by two processes. At low external fields relaxation is dominated by electron cotunelling which is itself independent of the external field. For larger magnetic fields the external field dependent phonon-assisted relaxation method instead becomes dominant [87, 137, 155]. As we see a clear change in $T_{1,e}$ with B_z, we ascribe the $1e$ relaxation to the phonon-assisted process where in the high temperature regime $\Delta E_e \gg k_b T$ $T_{1,e}$ is related to B_z by [155, 210, 211]

$$T_{1,e} \propto (k_b T)^{-1} B_z^{-2} \Delta E_e^{-2}, \tag{6.2}$$

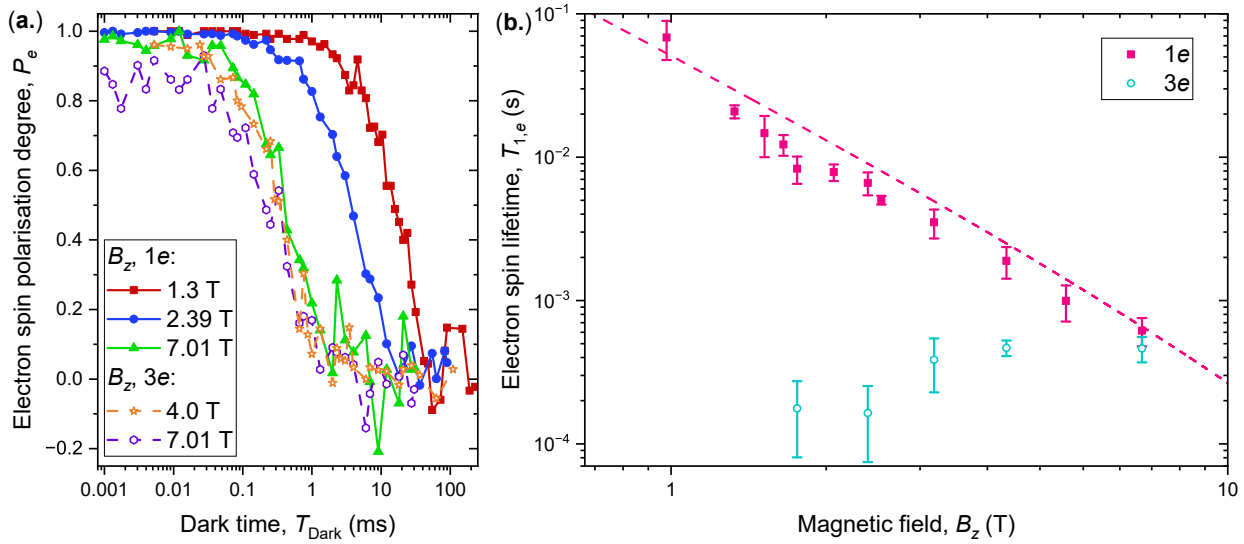


Figure 6.6: (a) Decay curves of the electron spin polarisation measured on the 1e state (solid symbols) and the 3e state (open symbols). For the 1e state we observe that the lifetime decreases with increasing external field B_z, while for the 3e state the lifetime appears to remain constant. (b) Dependence of the fitted $T_{1,e}$ values against the external field strength B_z for the 1e (solid squares, magenta) and 3e states (open circles, cyan). For the 1e case, relaxation is driven by phonon assisted-mechanisms and follows a power law dependence on a log-log scale, which matches the expected $T_{1,e} \propto B_z^{-2}$ relation for these types of QDs, where the Zeeman interaction is small compared to the hyperfine shift. The dashed line shows fitting for the data using Eq. 6.2. For the 3e case the trend is less clear though there is a small increase in $T_{1,e}$ with B_z. It is therefore likely that the 3e states relaxation is dominated by the field independent cotunnelling mechanism.

where $\Delta E_e = \mu_B g_e B_z + \Delta E_{\text{hf}}$ is the total electron spin energy splitting, and ΔE_{hf} is the hyperfine shift produced by optical pumping, which for the measurements in this chapter $\Delta E_{\text{hf}} \approx -50\ \mu$eV. For GaAs QDs the electron g-factor is small [116, 117] ($g_e \approx$ -0.1). This means that ΔE_e is dominated by the hyperfine shift, making $\Delta E_e \approx \Delta E_{\text{hf}}$ and consequently $T_{1,e}$ follows a B_z^{-2} dependence. In comparison, for InGaAs QDs where g_e is large, the Zeeman effect is dominant over the hyperfine shift ($\Delta E_e \approx \mu_B g_e B_z$) and the lifetime is found to have a much stronger dependence on B_z, with $T_{1,e}$ proportional to B_z^{-4} or B_z^{-5} in the high or low temperature regimes respectively [87, 210]. We therefore find that the electron spins in these GaAs QDs are significantly less sensitive to the externally applied magnetic field. To demonstrate that the relaxation is dependent on the phonon-assisted mechanism, we fit the data for 1e in Fig. 6.5b using Eq. 6.2. The fit is shown by the dashed line in Fig. 6.5b where we observe that it follows the data trend relatively well, confirming that the description in Eq. 6.2 is valid. However, in the current range of measured external fields, we do not see clear signs of the electron cotunnelling effect at low B_z that is expected to become dominant over phonon-assisted relaxation mechanisms, though it is likely to begin around the minimum field measured in this work. We therefore report that electron spin lifetimes can be extended up to at

least $T_{1,e} \approx 50$ ms at $B_z \approx 0.982$ T for these GaAs QDs.

Compared to the $1e$ case, the $3e$ lifetimes do not show a clear relation with B_z, though there appears to be a weak increase in $T_{1,e}$ with increasing B_z. This suggests that the relaxation is dominated by the cotunnelling mechanism, which is field independent [87]. Further evidence to support this is seen in Fig. 6.3 where the $3e$ charging plateau is observed to be narrower than the $1e$ plateau. While out of the scope of this work, more detailed measurements of the bias dependence of $T_{1,N}$ reveals that the $3e$ bias plateau becomes even narrower at high magnetic fields which will further increase the electron relaxation rate [206]. This would explain the weak dependence on B_z for the $3e$ state seen in Fig. 6.5b. Additionally, as already mentioned in Section 6.3, the reduced $T_{1,N}$ times compared to the $1e$ case further suggest electron cotunelling as the dominant relaxation mechanism. In both the $1e$ and $3e$ case the upper limit on the electron lifetimes is the field independent cotunnelling. This can be potentially overcome by increasing the thickness of the tunnelling barrier, though this can cause additional issues with Auger recombination [87]. Additionally either reducing the temperature or the lateral size of the QD to increase the electron charging energy may lead to further improvements in the $3e$ lifetimes.

6.6 Summary

In this chapter we have probed the properties of confined multi-electron states in GaAs QDs. We demonstrate the potential of using nuclear spin relaxation measurements to probe both the charge state of a given QD and the intricate spin interactions between the confined electrons, due to their interactions with the nuclei. While out of the scope of this work, such measurements can be extended further and in combination with other experiments, a significant amount of information about the different electron states can be determined [206]. We also expand upon the work conducted in Chapter 5 probing both the Knight field of the $1e$ and $3e$ electron states and the electron spin lifetimes through the use of detuned RF pulses [137]. We demonstrate that the Knight field of the $3e$ state produces a significantly narrower distribution ($\approx$ 100 kHz) of nuclear spin frequencies compared to the $1e$ state ($\approx$ 230 kHz). We attribute this difference to the unpaired electron in the $3e$ state having p shell like character, giving a greater wavefunction envelope spatial extent that overlaps with approximately double the number of nuclei. This could be a route to using both electron and nuclear qubits in the same QD, as the increased overlap with the nuclei should improve the electron coherence time, while the narrower NMR transition should be easier to manipulate with RF pulses.

Additionally, we demonstrate the flexibility of the detuned RF readout protocol by showing that the QND characteristic of the measurement allows multiple readouts to be performed with a single isotope, or two isotopes can be used to improve the measurement resolution. We also demonstrate

that both the 1e and 3e electron states can be initialised both optically or through readout. Finally, measurements of the electron spin lifetimes reveal that the 1e state relaxation is driven by phonon-assisted processes for external fields 1 T < B_z < 8 T, though due to the small electron g-factor for GaAs QDs [116, 117] the dependence follows a B_z^{-2} relation, rather than the B_z^{-4} and B_z^{-5} dependence seen in InGaAs QDs [87]. Finally we observe the 3e states relaxation is dominated by cotunneling at all measured fields, confirmed by the reduced $T_{1,N}$ and narrower bias plateau region compared to the 1e state. The maximum $T_{1,e}$ time measured in this work is approximately 50 ms at $B_z \approx 0.982$ T, though cotunnelling at lower fields is likely to prevent further improvement. Instead the cotunnelling could be minimised by increasing the tunnel barrier layer thickness though this can cause additional issues with Auger recombination which would need to be investigated [87]. For the 3e state further lifetime improvements may be realised through increasing the charge plateau width, either by reducing the temperature or through reducing the QDs lateral size.

Chapter 7

Storing Quantum Coherence in a Quantum Dot Nuclear Spin Ensemble for over 100 Milliseconds

So far we have primarily studied the nuclei as a way to measure and probe the spin of a confined electron. In this chapter we return to studying the nuclei directly. Future quantum computers are likely to be connected together to form quantum networks, allowing the communication of quantum information over long distances [12, 212–214]. A crucial component to these networks will be quantum memories, which are qubits that can store quantum states for sufficiently long enough for them to be distributed over the network. Typically as $T_2 < T_1$ the coherence time is often the limiting factor on storage time and, as a result, numerous systems are being investigated for their long coherence times as quantum memories [15, 32, 215–219]. The actual transmission of quantum information is likely to be implemented through photons. Therefore QDs would be an attractive candidate for a quantum memory, being excellent emitters of single [32] and entangled photons [33] with interfacing of photon and electron qubits having been demonstrated [199]. However, as demonstrated in Chapter 6 the electrons in QDs have millisecond lifetimes, while the coherence times are currently limited to $\approx$ 100 μs [126, 159], too short for a quantum memory.

Comparatively the nuclei are well isolated from their environment possessing long lifetimes ($T_{1,N} \approx 10-20$ s) and coherence times [70, 131, 135]. Currently the coherence time is limited to $\approx$ 1 ms [220] by two interactions, the dipolar interaction between the nuclei, and the quadrupolar interaction between the nuclei and the strain induced EFGs. Both of these processes can be suppressed. Dephasing can be refocused by a π rotation of the nuclei, which is the well known Hahn echo [160] while dipolar interactions can be suppressed by a series of $\pi/2$ rotations, termed the solid echo [163]. Here, we employ the CHASE dynamical decoupling sequence which combines Hahn and solid echoes to suppress both decoherence mechanisms [150]. In previous works studying

the effectiveness of CHASE on InGaAs QDs [150], CHASE has been demonstrated to effectively suppress dechoherence allowing a significant improvement in the nuclear coherence times, though ultimately the maximum achievable improvement is limited by the large inhomogeneous broadening caused by the large internal strain present in InGaAs QDs [150].

In this chapter we implement a new 40 pulse CHASE sequence which improves on previous sequences by removing spin locking effects. Applying it to low strain GaAs/AlGaAs QDs we are able to extend the nuclear coherence time to over 100 ms. In this regime spin transverse relaxation becomes driven by a three nuclear spin process. We find that the narrow central NMR transition is well isolated from the other nuclear spin transitions by the externally applied strain, with effects due to spectral overlap between the RF pulses and the STs only accumulating after hundreds of control pulses are applied. This opens the route to longer coherence times by using strain engineering to further separate the nuclear spin transitions, which combined with recent demonstration of the transfer and retrieval of information between an electron spin qubit and the surrounding nuclear spin bath [136], opens a route to an optically-active and long lived nuclear spin qubit for uses within optical quantum communication.

This work takes the form of a pre-submission manuscript which is currently on ArXiv where I am the first author:

H. E. Dyte, S. Manna, S. F. Covre da Silva, A. Rastelli, E. A. Chekhovich. "Storing quantum coherence in a quantum dot nuclear spin ensemble for over 100 milliseconds". *arXiv:2502.11092* (2025). DOI: https://doi.org/10.48550/arXiv.2502.11092

Storing quantum coherence in a quantum dot nuclear spin ensemble for over 100 milliseconds

Harry E. Dyte,[1] Santanu Manna,[2] Saimon F. Covre da Silva,[2] Armando Rastelli,[2] and Evgeny A. Chekhovich[3,*]

[1] *Department of Physics and Astronomy, University of Sheffield, Sheffield S3 7RH, United Kingdom*
[2] *Institute of Semiconductor and Solid State Physics, Johannes Kepler University Linz, Altenberger Str. 69, 4040 Linz, Austria*
[3] *Department of Physics and Astronomy, University of Sussex, Brighton BN1 9QH, United Kingdom*

(Dated: February 20, 2025)

States with long coherence are a crucial requirement for qubits and quantum memories. Nuclear spins in epitaxial quantum dots are a great candidate, offering excellent isolation from external environments and on-demand coupling to optical flying qubits. However, coherence times are limited to $\lesssim 1$ ms by the dipole-dipole interactions between the nuclei and their quadrupolar coupling to inhomogeneous crystal strain. Here, we combine strain engineering of the nuclear spin ensemble and tailored dynamical decoupling sequences to achieve nuclear spin coherence times exceeding 100 ms. Recently, a reversible transfer of quantum information into nuclear spin ensembles has been demonstrated in quantum dots. Our results provide a path to develop this concept into a functioning solid-state quantum memory suitable for quantum repeaters in optical quantum communication networks.

I. INTRODUCTION

Quantum memories are indispensable in large scale quantum networks, which are expected to enable long distance communication of quantum information [1–4]. Quantum memories have several key requirements [2], a primary figure of merit is the storage time, which is directly related to quantum repeater communication distance. Millisecond-range storage time allows for improvements over direct transmission through an optical fiber [5, 6]. Although entanglement generation rate is currently the main limitation [7], its continuous improvement highlights the need for even longer storage times, exceeding 100 ms, in order to achieve worldwide optical communication.

The storage of a quantum state in a memory is limited by the coherence time T_2. Several material systems offer long T_2, ranging from seconds to hours [8], including trapped atomic ensembles [9, 10], ions [11–16], electron spins [17, 18] and phosphorus nuclear spins [19–21] in silicon, as well as electron and nuclear spins of impurities in diamond [22, 23]. However, long T_2 are often negated by poor optical properties required for a long-distance quantum network. There are promising hybrid approaches, such as combination of transmon qubits with solid-state quantum memories [24], but these often suffer from coupling inefficiencies and bandwidth mismatch [8] (see further discussion in Supplementary Note 4).

Epitaxial quantum dots (QDs) in group III-V semiconductors have high qubit entanglement rates [25] and are excellent on-demand emitters of single [8, 26–28] and entangled photons [29, 30]. At the same time, QDs host material qubits: Electron spin qubits can be interfaced with optical photon qubits [31–33], but the coherence of the electron spin is limited to ≈ 100 μs [34]. The nuclear spins are isolated from external environments, resulting in long lifetimes and coherence times [35–37]. Recently, two-way quantum state transfer between photon and nuclear spins has been demonstrated in a QD, using an electron spin qubit as a mediator [38, 39]. However, since all atoms in group III-V materials have non-zero nuclear spins, the natural nuclear spin coherence is limited to a rather modest ≈ 1 ms range [40]. Extending nuclear spin coherence is thus a key task in achieving quantum memories suitable for quantum repeaters [41, 42].

Here, we achieve nuclear spin coherence of over $T_2 \approx 100$ ms, made possible by applying two concepts: Firstly, elastic strain is used to engineer the spin-3/2 nuclei and spectrally isolate the subspace with $I_z = \pm 1/2$ spin projections. Small inhomogeneity of this subspace allows application of thousands of coherent control operations, thus enabling efficient dynamical decoupling. Secondly, a dedicated 40-pulse decoupling sequence is designed to extend nuclear spin ensemble coherence while overcoming the parasitic spin locking effects encountered in previous decoupling experiments [43, 44]. Analysis shows that residual decoherence is dominated by the finite-pulse effects and the effective three-body nuclear spin interactions, which are often overlooked. We predict that even longer T_2, on the order of ≈ 1 s, is well within reach through larger strains and further advances in dynamical decoupling. The macroscopically long coherence times achieved here do not rely on isotope enrichment, which is available only in group IV material spin qubits [20, 45]. Our demonstration of engineered long coherence unlocks the unrivaled optical properties of group III-V materials for applications in quantum memory devices.

* E.Chekhovich@sussex.ac.uk

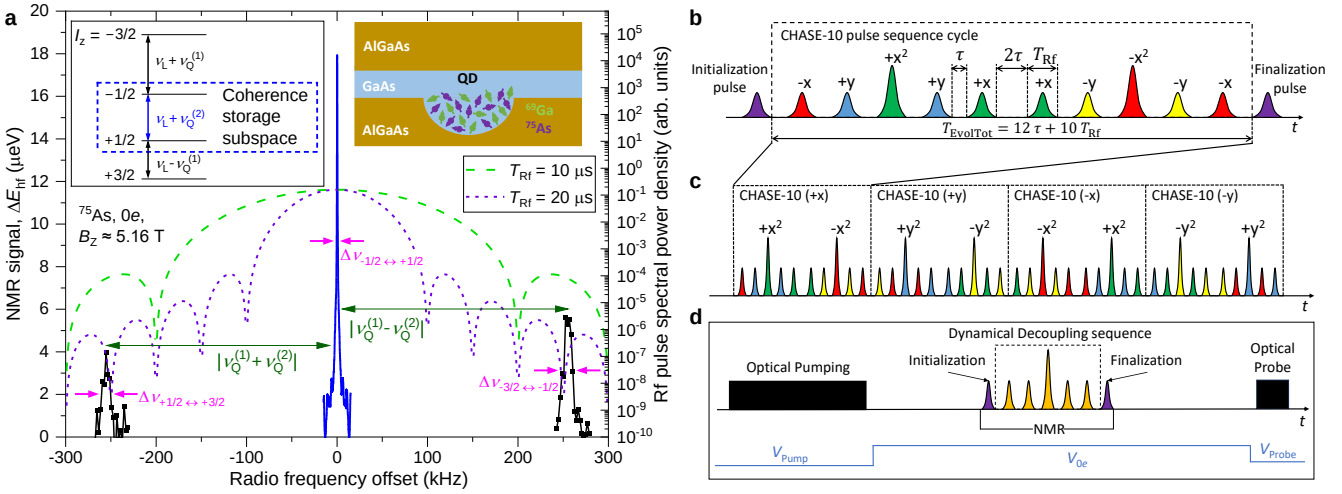


FIG. 1. **Optically detected nuclear magnetic resonance of a single quantum dot. a** Right inset shows schematic diagram of ^{69}Ga and ^{75}As nuclear spins in a GaAs/AlGaAs QD. NMR spectrum of the spin-3/2 ^{75}As nuclei (black and blue solid lines, left scale) in an uncharged ($0e$) QD. Frequency offset is shown with respect to the Larmor frequency $\nu_L \approx 37.981$ MHz arising from the Zeeman splitting at external field of $B_z \approx 5.16$ T (left inset). Out of the three magnetic dipole transitions, the two satellite transitions (STs) undergo a first-order quadrupolar shift $\pm\nu_Q^{(1)}$ (where $\nu_Q^{(1)} \approx 255.1$ kHz), while the central transition (CT) is affected only by the second-order quadrupolar shift $\nu_Q^{(2)} \approx 3.3$ kHz. The CT linewidth ($\Delta\nu_{-1/2\leftrightarrow+1/2} \approx 0.8$ kHz) is much narrower than the ST linewidth ($\Delta\nu_{+1/2\leftrightarrow+3/2} \approx \Delta\nu_{-3/2\leftrightarrow-1/2} \approx 13.8$ kHz). Dashed lines (right scale) show spectral profiles of the Rf pulse bursts with duration $T_{\rm Rf} = 10$ or 20 μs, tuned in resonance with the CT. **b** Schematic diagram of a CHASE-10 sequence cycle, letters and signs denote Rf pulse phases. The pulses are separated by the free-evolution intervals τ. The total nuclear evolution time is $T_{\rm EvolTot} = 10T_{\rm Rf} + 12\tau$, while $T_{\rm FreeEvol} = 12\tau$ is the pure free evolution time for one cycle. **c** The CHASE-40 supercycle constructed of four CHASE-10 steps, with pulse phase incremented by $\pi/2$ in each step. **d** Timing of the ODNMR measurement cycle. Optical pumping creates longitudinal nuclear spin polarization. The initialization $\pi/2$ Rf pulse converts this into transverse (coherent) nuclear polarization in the xy plane. Dynamical decoupling is applied, followed by a finalization $\pi/2$ pulse to rotate the remaining transverse polarization back along the z-axis. Finally, the nuclear polarization is read out using photoluminescence (PL) spectroscopy under an optical probe pulse. The sample bias is pulsed to maximize optical nuclear spin pumping and PL intensity during optical probing.

II. RESULTS

Strain-engineered nuclear spin ensemble. We study the nuclear spin coherence of GaAs/AlGaAs QDs grown by molecular beam epitaxy. The right inset of Fig. 1a sketches the QD nuclear spin system of $N \approx 5 \times 10^4$ nuclei. The three isotopes ^{75}As, ^{69}Ga, and ^{71}Ga all have nuclear spin $I = 3/2$. The sample is cooled to ≈ 4.2 K. A superconducting magnet is used to apply a static magnetic field $B_z \approx 5.16$ T along the sample growth crystal direction [001], lifting the degeneracy of the four nuclear spin states with spin projections $I_z = \pm 1/2, \pm 3/2$ (left inset in Fig. 1a). Optical pumping with circularly polarized light (Faraday geometry) is used to polarize the nuclear spins along the static magnetic field [46]. The nuclear spin lifetime is typically $T_1 > 10$ s [47], significantly longer than the coherence times measured in this work. Nuclear spin polarization is measured via photoluminescence (PL) spectroscopy [48], see examples in Fig. 2a. A copper coil generates oscillating magnetic field perpendicular to B_z, enabling optically detected nuclear magnetic resonance (ODNMR) measurements. Radio frequency (Rf) bursts with raised cosine envelope are used to transfer coherence in and out of the storage nuclear spin subspace $I_z = \pm 1/2$ and to perform its dynamical decoupling.

The sample is stressed uniaxially along the [110] crystal direction, perpendicular to the static magnetic field. The resulting anharmonicity [36, 49], is characterised by the first-order qudrupolar splitting $\nu_Q^{(1)}$. The measured NMR spectrum, shown in Fig. 1a for ^{75}As nuclei in a neutral ($0e$) GaAs/AlGaAs QD, reveals $\nu_Q^{(1)} \approx 255.1$ kHz. This splitting significantly exceeds the linewdiths of the NMR transitions: the full width at half maximum (FWHM) $\Delta\nu_{+1/2\leftrightarrow+3/2} \approx \Delta\nu_{-3/2\leftrightarrow-1/2} \approx 13.8$ kHz of the satellite transitions (STs) $-3/2 \leftrightarrow -1/2$ and $+1/2 \leftrightarrow +3/2$ is dominated by the inhomogeneous qudrupolar broadening, while the FWHM $\Delta\nu_{-1/2\leftrightarrow+1/2} \approx 0.8$ kHz of the central transition $-1/2 \leftrightarrow +1/2$ is controlled by a combination of the second-order quadrupolar inhomogeneity and the dipole-dipole interactions [44, 50]. The small CT linewidth combined with its strain-induced spectral isolation from STs make it an ideal spin subspace for coherence storage. Notably, the lattice-matched GaAs/AlGaAs QDs offer a significant advantage over Stranski-Krastanov QDs where $\Delta\nu_{-1/2\leftrightarrow+1/2} \approx 10 - 40$ kHz [44].

Hamiltonian engineering of a nuclear spin en-

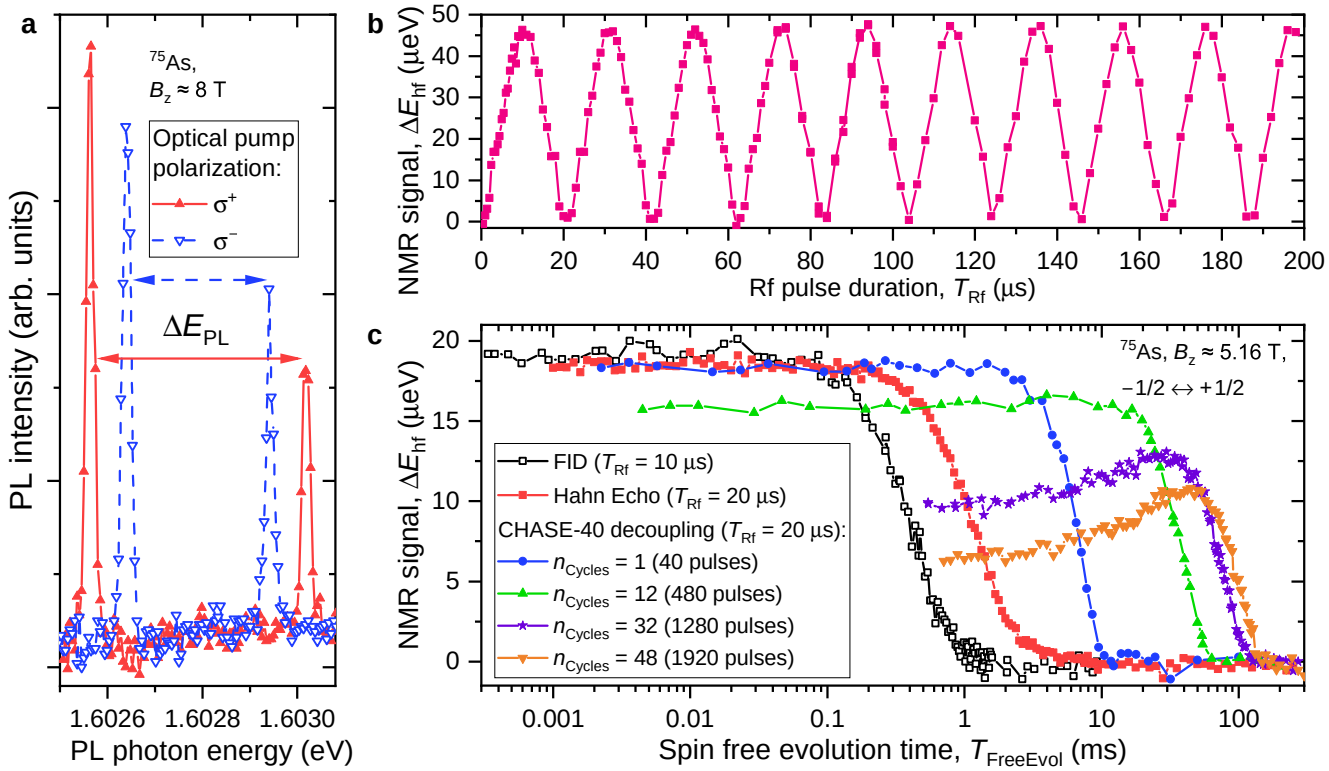


FIG. 2. **Dynamical decoupling of QD nuclear spins.** **a** Two photoluminescence (PL) spectra of a neutral exciton in the same individual QD measured after optical pumping with σ^+ (σ^-) polarized light, which results in negative (positive) nuclear spin polarization. PL spectral splitting $\Delta E_{\rm PL}$ is a sum of the constant Zeeman splitting and the nuclear hyperfine shift $\Delta E_{\rm hf}$, which is derived from the variations of $\Delta E_{\rm PL}$. **b** Rabi oscillations of the nuclear spins in a neutral ($0e$) QD observed under an increasing duration $T_{\rm Rf}$ of an Rf pulse of constant amplitude. **c** Nuclear spin decoherence measured by optically detected nuclear magnetic resonance (ODNMR) under free induction decay (FID, open squares), Hahn echo (solid squares) and an increasing number of CHASE-40 dynamical decoupling cycles $n_{\rm Cycles} = 1 - 48$ (see legend). Rf pulses, with duration $T_{\rm Rf} = 20$ μs are applied to the central spin transition $-1/2 \leftrightarrow +1/2$ in a neutral ($0e$) QD. Nuclear spin polarization is initialized with an x pulse ($\phi = 0$).

semble. Dynamical control of spin interactions is a powerful technique in magnetic resonance [51, 52]. The method is based on applying a sequence of Rf pulses that perform fast coherent rotations of the spins, separated by the free evolution intervals. In the interaction picture (the "toggling" frame of reference) the Rf pulses can be viewed as transformations of the spin-interaction Hamiltonian. The π-pulse rotations invert the sign of the frequency shifts, allowing refocusing of the dephasing [53], which in QDs is caused primarily by inhomogeneous quadrupolar broadening. On the other hand, a sequence of four phase-shifted $\pi/2$-pulses transforms the nuclear spin-spin dipolar interactions in such a way that averages them to zero over the pulse sequence cycle [54]. The average Hamiltonian is the leading (0th order) term in the Magnus expansion of the entire Hamiltonian in the toggling frame. By introducing more complex sequences of pulses it is possible to eliminate the unwanted interactions to higher orders, thus engineering the spin Hamiltonian to have the desired form [52].

Here, we engineer a "time suspension" [55] type of sequence, where the Hamiltonian terms are eliminated as much as possible to preserve an arbitrary coherent state of the nuclear spin ensemble for the longest possible time. As a starting point we use a CHASE-10 cyclic sequence of $\pi/2$ and π pulses [44] shown in Fig. 1b. This sequence eliminates the average (0th order) free-evolution Hamiltonian both for the resonance frequency shifts and the spin-spin interactions. By symmetrizing the sequence, a CHASE-20 supercycle is formed, which further eliminates all the 1st-order terms in the Hamiltonian. The CHASE-20 sequence has been applied to QDs previously, demonstrating its ability to suppress decoherence even under large inhomogeneous resonance broadenings in Stranski-Krastanov InGaAs/GaAs QDs [44]. In low-strain GaAs/AlGaAs QDs, nuclear spin coherence times up to $T_2 \approx 20$ ms have been achieved [36]. However, the π pulses cause spin locking [43, 44] which selectively accelerate decoherence of the spin states polarized along a certain equatorial axis of the Bloch sphere in the rotating frame, while artificially enhancing ("locking") the states polarized along the orthogonal equatorial axis. This be-

haviour is unwanted in quantum memory applications as it may lead to distortion of the state during storage.

Here we use a different approach, where four CHASE-10 cycles are combined into a CHASE-40 supercycle shown in Fig. 1c. The phases of the Rf pulses in each CHASE-10 subcycle are stepped by $\pi/2$. While each subcycle causes spin locking, the preferential direction of the "lock", when viewed in the rotating frame, makes a full rotation around the direction of the static magnetic field (z) over the CHASE-40 supercycle. This four-step "rotating spin lock" eliminates the net spin locking effect for an arbitrary coherent state, as demonstrated through rigorous calculation (See Supplementary Note 5). Furthermore, the leading order residual Hamiltonian of CHASE-40 is twice smaller than in CHASE-20, resulting in extended coherence.

Extended spin coherence under dynamical decoupling. We start by examining experimentally the nuclear spin dynamics under continuous resonant Rf driving. The results shown in Fig. 2b reveal Rabi oscillations, which confirm the coherent nature of spin driving and allow the $\pi/2$ and π Rf pulses to be calibrated for dynamical decoupling (See Supplementary Note 2C). We then apply dynamical decoupling to the isolated $I_z = \pm 1/2$ nuclear spin subspace with two varying parameters: the number of sequence cycles n_{Cycles} and the total free evolution time T_{FreeEvol}. Fig. 2c shows nuclear spin coherence decay measured using ODNMR. In the simplest case of free induction decay (FID), without any dynamical decoupling (open black squares), the dephasing time is $T_2^* \approx 0.46$ ms and is a combined effect of quadrupolar inhomogeneity and dipole-dipole interactions. By using a single π pulse as a decoupling sequence (solid squares), we find the Hahn echo [53] coherence time $T_2^{\mathrm{HE}} \approx 1.38$ ms, which is dominated by the dipole-dipole interactions.

The measured effect of dynamical decoupling with one cycle of CHASE-40 is shown by the circles in Fig. 2c. The decay of the transverse nuclear polarization is plotted as a function of the total free evolution time T_{FreeEvol} (i.e. excluding the duration of the Rf pulses), and reveals a significant extension of the coherence time $T_2^{1\mathrm{xCHASE-40}} \approx 12.3$ ms. With the increasing number of CHASE-40 cycles the coherence time is extended further, reaching $T_2^{48\mathrm{xCHASE-40}} \approx 106.6$ ms for $n_{\mathrm{Cycles}} = 48$ (orange triangles), an improvement by 2 orders of magnitude compared to the bare Hahn echo coherence time. The achieved nuclear spin coherence is also 3 orders of magnitude longer than the coherence of a dynamically decoupled electron spin in these QDs [34]. These results demonstrate the superior properties of the nuclear spins as a coherence-storage medium.

It can be seen from Fig. 2c that under an increasing number of decoupling cycles n_{Cycles} the coherence (the NMR echo signal) is reduced even in the limit of $T_{\mathrm{FreeEvol}} \to 0$. Moreover, the dependence of transverse nuclear spin polarization on T_{FreeEvol} becomes nonmonotonic. These are the indications of nuclear spin decoherence during the finite (nonzero duration) Rf pulses. For quantum memory applications, we are interested in minimising decoherence, whether caused by free evolution or the Rf control pulses. We seek this optimum by replotting the data of Fig. 2c in Fig. 3a, where the normalized nuclear spin coherence is shown as a function of the total evolution (free evolution plus Rf pulses) time T_{EvolTot} (horizontal axis) and the duration T_{Cycle} of one CHASE-40 cycle (vertical axis). The individual decay plots of Fig. 2c measured at fixed n_{Cycles} now appear along the diagonal lines in Fig. 3a. We fit the decay of coherence with an exponential function of T_{EvolTot}: the resulting decay time, which we denote as spin memory time T_{M}, is distinct from coherence time T_2 and is shown as a function of T_{Cycle} by the single solid line in Fig. 3e. The maximum $T_{\mathrm{M}} \approx 136$ ms is achieved not under the fastest possible Rf pulsing, but at $T_{\mathrm{Cycle}} \approx 2$ ms, which is 5 times longer than the minimum $T_{\mathrm{Cycle}} \approx 0.8$ ms achieved at $T_{\mathrm{Rf}} = 20$ μs. This confirms that the finite-pulse effects are the main limitation to extending coherence storage through fast dynamical decoupling.

Decoherence during the Rf pulses can in principle be suppressed by reducing T_{Rf}. However, experiments conducted on the $I_z = \pm 1/2$ spin states with a reduced $T_{\mathrm{Rf}} = 10$ μs yield faster decoherence than under $T_{\mathrm{Rf}} = 20$ μs (see Supplementary Note 3A). This seemingly contradictory result is understood by considering the spectral profiles of the Rf pulses (dashed lines in Fig. 1a). While the unwanted spin decoherence is indeed suppressed under the shorter $T_{\mathrm{Rf}} = 10$ μs pulses, their broader spectral profile results in a stronger overlap with the STs. Such overlap leads to a faster "leakage" of coherence from the storage $I_z = \pm 1/2$ subspace into the $I_z = \pm 3/2$ states. Thus, there is an optimal pulse duration that balances the finite-pulse and the leakage effects. For the studied structure with the strain-induced quadrupolar splitting of $\nu_{\mathrm{Q}}^{(1)} \approx 250$ kHz, this optimum is close to $T_{\mathrm{Rf}} = 20$ μs. Increasing elastic strain from ≈ 0.0025 in the studied sample to the ≈ 0.01 range [56] is a promising route for applying shorter Rf pulses and a further significant improvement of the storage time and fidelity in a QD nuclear spin quantum memory.

CHASE decoupling of an inhomogeneous spin ensemble. In order to demonstrate the importance of isolating the homogeneous $I_z = \pm 1/2$ CT storage subspace, we examine the opposite case of a $I_z = (-3/2, -1/2)$ subspace. The considerably larger inhomogeneous broadening is characterised by the spectral shape of the ST NMR transitions. This is a weighted sum of a visible peak (Fig. 1a) with a linewidth of $\Delta\nu_{+1/2 \leftrightarrow +3/2} \approx \Delta\nu_{-3/2 \leftrightarrow -1/2} \approx 13.8$ kHz (65% weight), and a much broader invisible peak, which was shown previously [34] to stretch to $\approx \pm 100$ kHz (35% weight) and is caused by the atomic-scale strain of the randomly positioned Al and Ga atoms. The measured ST decoherence under CHASE decoupling is shown in Fig. 3b, and the resulting spin memory time T_{M} is shown by the double solid line in Fig. 3e. Unlike with $I_z = \pm 1/2$, the best possible dynamical decoupling of the $I_z = (-3/2, -1/2)$ subspace

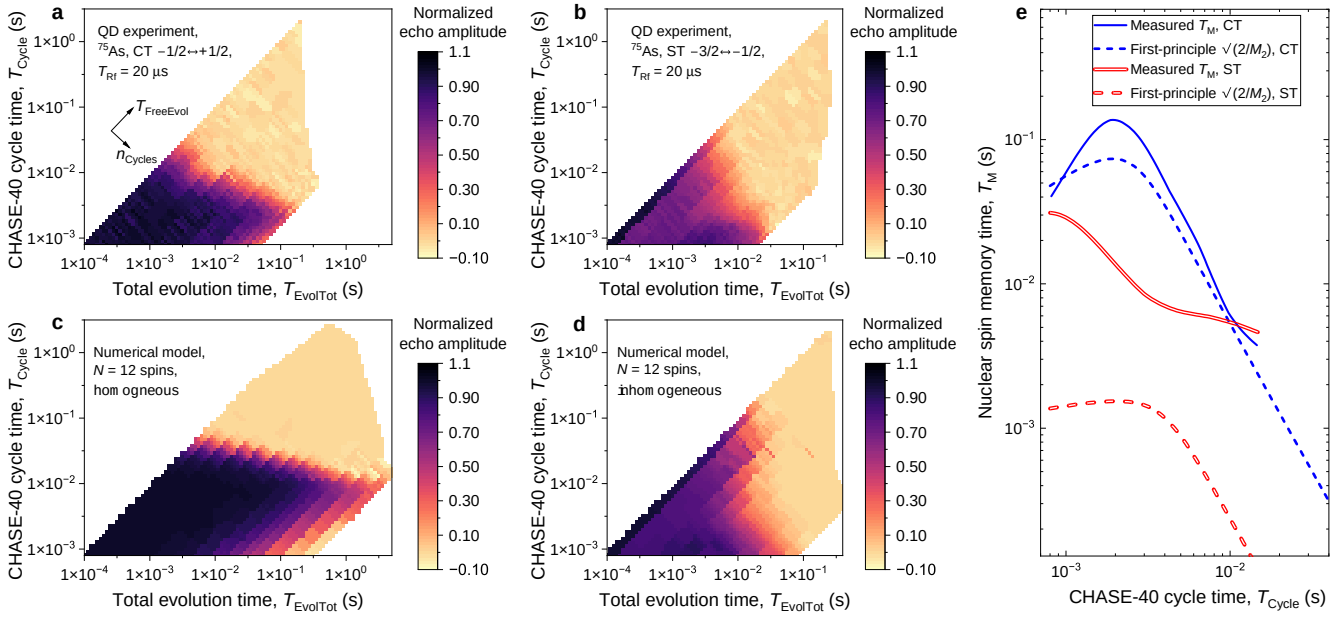


FIG. 3. **Coherence storage in a nuclear spin ensemble under dynamical decoupling. a** Decoherence of the $I_z = \pm 1/2$ subspace of the ^{75}As nuclei measured in a neutral ($0e$) QD under dynamical decoupling with Rf pulse duration of $T_{Rf} = 20$ μs. normalized echo amplitude (colour scale) is shown as a function of the total evolution time $T_{EvolTot} = n_{Cycles} T_{Cycle}$ (free evolution plus Rf pulses, horizontal axis) and the rate of Rf pulsing expressed in terms of the duration $T_{Cycle} = 40T_{Rf} + 48\tau$ of a single CHASE-40 cycle (vertical axis). The axes of the plot correspond to a nonlinear transformation from the variables n_{Cycles} and $T_{FreeEvol} = 40 n_{Cycles} \tau$ used in Fig. 2c. The plot combines data obtained with different numbers of CHASE-40 cycles and with shorter subcycles such as CHASE-10. **b** Decoherence of the $I_z = (-3/2, -1/2)$ subspace of the ^{75}As nuclei measured under dynamical decoupling with $T_{Rf} = 20$ μs. **c** Decoherence under dynamical decoupling derived from first-principles numerical modeling of spin dynamics of a homogeneous ensemble of $N = 12$ nuclei. **d** Numerically modeled decoherence of $N = 12$ nuclei subject to inhomogeneous spectral broadening. **e** Nuclear spin memory time T_M derived from exponential fitting of decoherence measured as a function of $T_{EvolTot}$. Single and double solid lines show results for $I_z = \pm 1/2$ CT and $I_z = (-3/2, -1/2)$ ST subspaces of ^{75}As nuclei, respectively. T_M calculated analytically from the second moment M_2 of the residual Hamiltonian under dynamical decoupling are shown by the single and double dashed lines for $I_z = \pm 1/2$ and $I_z = (-3/2, -1/2)$ subspaces, respectively.

is achieved at the shortest possible T_{Cycle}. Despite this fastest possible Rf pulsing, the maximum achieved memory time is $T_M \approx 31$ ms. Although this storage time is a factor of ≈ 15 improvement over the simple Hahn echo, it is a factor of ≈ 4.4 worse than T_M achieved for the spectrally narrow $I_z = \pm 1/2$ subspace.

The inferior spin memory time for an inhomogeneously broadened spin ensemble demonstrates how CHASE-40, as any other dynamical decoupling protocol, reaches the limit of its performance when the interaction that is being decoupled is no longer a small perturbation. The inhomogeneous broadening of the $I_z = \pm 1/2$ CT subspace is a small perturbation, characterized by $\Delta\nu_{-1/2\leftrightarrow+1/2} T_{Rf} \approx 0.015 \ll 1$. By contrast, the relative broadening of the $I_z = (-3/2, -1/2)$ subspace is comparable to unity for the visible part of the ST NMR peak ($\Delta\nu_{-3/2\leftrightarrow-1/2} T_{Rf} \approx 0.28$) and violates the perturbative approximation ($\Delta\nu_{-3/2\leftrightarrow-1/2} T_{Rf} > 1$) for the broad component of the ST. The large inhomogeneity of the ST exacerbates decoherence through spin evolution during the finite Rf pulses. Moreover, $\Delta\nu_{-3/2\leftrightarrow-1/2} T_{Rf} \gtrsim 1$ means that Rf control pulses become more "soft" (i.e. not infinitely broad spectrally), resulting in imperfect rotations of the nuclear spins [57, 58]. On the other hand, CHASE-40 shows no sign of spin-locking even for the $I_z = (-3/2, -1/2)$ subspace, despite its larger inhomogeneous broadening (See Supplementary Note 3B).

Uniform decoupling of an arbitrary coherent nuclear spin state. An ideal quantum memory must store any given state with equally high fidelity. However, dynamical decoupling can create parasitic spin locking regimes, where storage effectiveness depends on the initial state [43, 44]. We examine the uniformness of the quantum state storage by measuring dynamical decoupling of the homogeneous $I_z = \pm 1/2$ subspace under four cycles of CHASE-40 with different initial states. The phase ϕ of the initialization Rf pulse is varied to prepare transverse nuclear spin polarization along the different axes in the equatorial xy plane of the rotating frame ($\phi = 0$ corresponds to an "+x" Rf pulse and prepares polarization along the $-y$ axis, a "+y" pulse with $\phi = \pi/2$ prepares polarization along the x axis). We further perform a measurement, where the initialization pulse is omitted, corresponding to initial nuclear spin po-

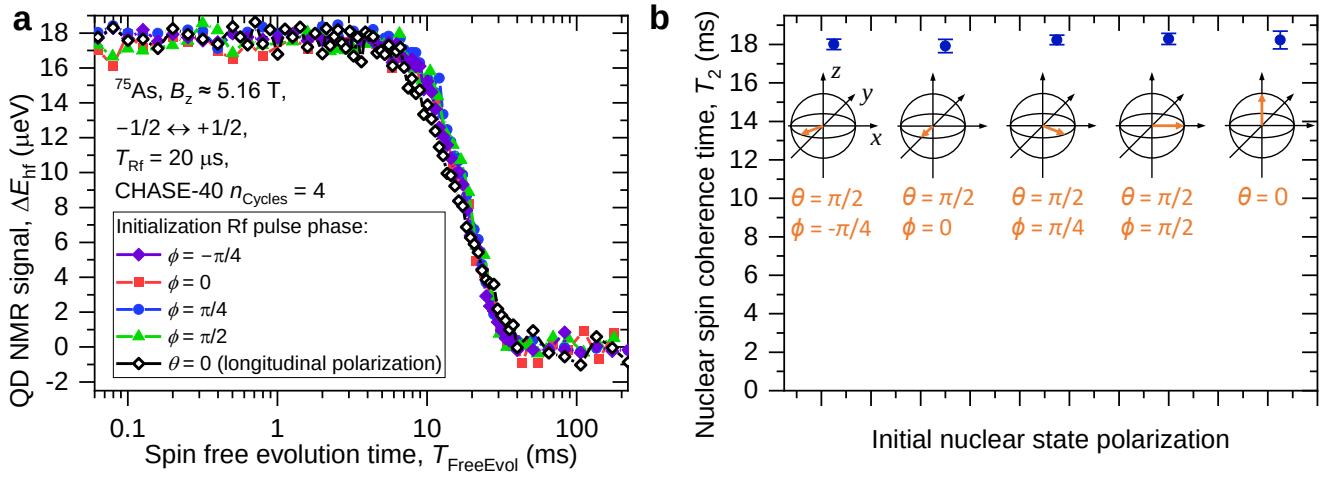


FIG. 4. **Uniform decoupling of an arbitrary coherent nuclear spin state. a** Nuclear spin decoherence measured under 4 cycles of CHASE-40 with different phases ϕ of the initialization Rf pulse, which initializes transverse nuclear polarization along different azimuth angles in the xy plane ($\theta = \pi/2$). The measurement of the longitudinal nuclear spin relaxation under CHASE-40 (without the initialization pulse, $\theta = 0$) is shown by the open diamonds. **b** The nuclear spin decay times T_2 and T_1 obtained from fitting the data in **a**. Schematics show orientation of the nuclei on the Bloch sphere after the initialization pulse, where present.

larization along the strong magnetic field ($\theta = 0$). The measured decay curves are shown in Fig. 4a. The coherence times obtained from fitting are shown in Fig 4b, and are around $T_2 \approx 18$ ms, nearly independent of the initial state.

The uniform dynamical decoupling of different initial states confirms experimentally the design principle of the CHASE-40 supercycle. Cycling of the Rf pulse phases in the four constituent CHASE-10 subcycles can be understood intuitively as a "rotary spin lock": the axis of spin locking is slowly precessing with respect to the rotating frame, with a net effect of removing any preferential spin locking axis over the entire CHASE-40 cycle. Rigorous calculations confirm this result, showing that the symmetry axis of the residual Hamiltonian of CHASE-40 is along the strong static magnetic field (z axis). It is also worth noting that the T_2 decay time of the transverse polarization (measured with an initialization $\pi/2$ pulse) is nearly identical to that of the longitudinal T_1 decay time (measured without any initialization pulse): a well-designed time-suspension sequence eliminates all the leading interaction terms, effectively removing the distinction between the longitudinal (T_1) and transverse (T_2) relaxation timescales.

The rotary spin lock offers a simple and reliable approach for reusing the dynamical decoupling sequences where spin locking is otherwise present [44, 59, 60]. The robustness of CHASE-40 against spin locking is key to achieving long spin memory times $T_M \gtrsim 100$ ms through repeated cycling (up to 2400 pulses).

Predicting dynamical decoupling performance through analytical and numerical modeling. The effective spin Hamiltonian under dynamical decoupling can be calculated as a Magnus expansion series. However, finding the spin dynamics from a known Hamiltonian is still a difficult problem. On the other hand, the exact spin dynamics is related to the exact NMR spectral lineshape through Fourier transform. The NMR lineshape can be approximated as a Gaussian, and its linewidth can be approximated in terms of the second moment M_2, which in turn can be found from the Hamiltonian through direct calculation. The approximate coherent memory time can then be found as $T_M \approx \sqrt{2/M_2}$ [52]. The residual Hamiltonian of CHASE-40 has been computed analytically up to second order: it is too bulky to reproduce in full, a more detailed discussion can be found in Supplementary Note 5. The Hamiltonian depends on two parameters: the magnitude of the dipole-dipole interaction and the quadrupolar inhomogeneity. These are derived from FID and Hahn Echo experimental data, allowing $T_M^{CHASE-40}$ to be calculated up to second order in analytical form and without any fitting parameters. The results are shown by the dashed lines in Fig. 3e. For the homogeneous subspace $I_z = \pm 1/2$ (single dashed line), the analytical model accurately predicts the peak in the spin memory time T_M at $T_{Cycle} \approx 2$ ms. The actual peak value of T_M is underestimated but matches the experiment within a factor of ≈ 2. By contrast, for the inhomogeneous subspace $I_z = (-3/2, -1/2)$, the model underestimates T_M by an order of magnitude. This indicates the limited accuracy of the perturbative Magnus expansion, which breaks down when the inhomogeneous broadening (in frequency units) is no longer small when compared to the reciprocal cycle time $1/T_{Cycle}$. In principle, the analytical model could be improved by extending the Magnus expansion. However, the increasing complexity of the high-order terms makes this approach impractical.

The advantage of the analytical model is that it allows insights into the underlying phenomena. In particular, we find that direct dipole-dipole interactions of the ith and jth spins of the ensemble, characterised by the coupling constant ν_{ij}, is eliminated by CHASE-40 up to second order inclusive. However, the dipolar interaction of the spins i, j remains, but with a coupling constant $\propto \nu_{ik}\nu_{kj}$, where $k \neq i, j$ is any other spin. Such a term can be interpreted as a three-particle coupling, where the interaction of any two spins i and j is mediated by any other spin k. Although often ignored, here we find that the residual decoherence of the homogeneous subspace $I_z = \pm 1/2$ can be explained only by taking into account this effective three-body interaction. The three-body second-order interaction limits T_M under slow dynamical decoupling (long T_{Cycle}). In the oposite limit of fast decoupling (short T_{Cycle}) the memory time T_M is limited by the zero-order dipole-dipole term arising from finite $T_{Rf} > 0$. A combination of these two effects results in a non-monotonic dependence $T_M(T_{Cycle})$ with a maximum in T_M, as shown by the single lines in Fig. 3e. By contrast, the decoherence in the inhomogeneous subspace $I_z = (-3/2, -1/2)$ is dominated by the quadrupolar offset inhomogeneity under finite ($T_{Rf} > 0$) control pulses.

We further conduct numerical modeling of the CHASE dynamical decoupling by solving the exact Schrodinger equation of a system of $N = 12$ spins (see details in Supplementary Note 6). The results for the case of the inhomogeneous subspace $I_z = (-3/2, -1/2)$, are shown in Fig. 3d. Since the decoherence rate is dominated by the quadrupolar offsets, which is a single-particle effect, a good quantitative agreement with the experiment (Fig. 3b) is obtained by using realistic values of the inhomogeneous quadrupolar shifts in the numerical model. The results for the $I_z = \pm 1/2$ subspace, where quadrupolar inhomogeneity is taken to be zero, are shown in Fig. 3c. The numerical model reproduces the main features of the experimental data on the $I_z = \pm 1/2$ subspace (Fig. 3a), in particular the nonmonotonic dependence of the spin memory time T_M on the decoupling sequence cycle time T_{Cycle}. However, the agreement is only within an order of magnitude: the numerically-simulated maximum $T_M \approx 2$ s occurs at $T_{Cycle} \approx 8$ ms, compared to the measured maximum $T_M \approx 0.136$ s at $T_{Cycle} \approx 2$ ms. This discrepancy may seem unexpected, given that the numerically-simulated coherence time under simple Hahn echo $T_2^{HE} \approx 1.4$ ms is very close to the measured $T_2^{HE} \approx 1.38$ ms. However, the decoherence under Hahn echo is governed by the direct (pairwise) dipole-dipole interaction of the nuclear spins, whereas decoherence under CHASE-40 is dominated by the effective three-spin interaction. We therefore ascribe the discrepancy in T_M to the limited number of spins in the numerical model: the number of three-spin combinations contributing to decoherence in an ensemble with $N = 12$ is considerably smaller than in a real crystal lattice of a QD. The discrepancy is also likely to include the small but nonzero quadrupolar inhomogeneity of the $I_z = \pm 1/2$ subspace, which reduces CHASE-40 T_M in a real QD.

III. DISCUSSION

We have demonstrated very long coherence storage times of over 100 ms in a nuclear spin ensemble of an optically-active GaAs semiconductor QD. These QDs are a promising candidate for quantum memory, which integrates the spin qubit with a single photon sources [8], thus avoiding the need for complex hybrid schemes [24]. Long-term preservation of nuclear spin coherence demonstrated here is a key step in bringing the concept of QD-based optical quantum memory [39] to practical implementation. The extended coherence is enabled by strain engineering of the nuclear spin ensemble and the tailored 40-pulse time-suspension decoupling sequences.

We use a three-pronged approach to the design of dynamical decoupling sequences. Numerical modelling can predict the overall performance of a dynamical decoupling protocol, but its accuracy is limited by the small number of spins N, constrained in turn by the exponential scaling of the required computing resources with increasing N. As a result, numerical simulations are time-consuming: full datasets of Figs. 3c, d require many days of computations on a workstation PC, which is comparable to experimental time required for Figs. 3a, b. Analytical calculations provide good predictions in case of small inhomogeneity. However, for a sequences with 40 pulses, derivation of the residual Hamiltonian takes several hours of computer-assisted algebraic derivations and further tedious manual work to analyse the bulky analytical results. Thus, the two modeling approaches encounter their different limitations, leaving experiment as the ultimate verification of the excellent coherence protection achieved with CHASE-40. The sequence is robust against spin locking, errors in control pulses, and is applicable to spin ensembles with a substantial inhomogeneous broadening.

Strain engineering is a key enabling technique, as it allows spectral isolation of the homogeneous $I_z = \pm 1/2$ nuclear spin subspace. A further increase of elastic strain by a factor of ≈ 4 is within the yield strain of GaAs and is feasible using membrane microstructures [56, 61, 62]. This would allow quadrupolar splitting in excess of $\nu_Q^{(1)} \gtrsim 1$ MHz, enabling further improvement in quantum memory storage time and fidelity. More importantly, the MHz-range quadrupolar splitting would be sufficient to exceed the electron-nuclear hyperfine interaction, which is $\lesssim 200$ kHz in the studied GaAs QDs [49]. While dynamical decoupling of nuclear spins in presence of the central electron spin qubit is possible in principle [37], achieving long nuclear spin coherence in presence of electron would require spectral isolation (through increased strain) of the hyperfine-broadened nuclear spin transitions.

The maximum storage time T_M under CHASE-40 decoupling is limited by the finite duration of the control

pulses, which causes a drop in T_M in the limit of frequent Rf pulsing (single lines in Fig. 3e, limit of small T_{Cycle}). By eliminating the effect of finite pulses [51, 63] it should be possible to achieve $T_M \approx 1$ s even at the current level of elastic strain, limited only by the second-order three-particle spin-spin interactions. More broadly, dynamical decoupling can be used to study spin-spin entanglement, thermalization in disordered quantum systems, and many-body localization [64, 65].

ACKNOWLEDGMENTS

Acknowledgements: H.E.D. was supported by an EPSRC doctoral training grant. E.A.C. was supported by a Royal Society University Research Fellowship, the Leverhulme Trust grant RPG-2023-141, and the EPSRC award EP/V048333/1. A.R. acknowledges support of the Austrian Science Fund (FWF) via the Research Group FG5, I 4320, I 4380, I 3762, the Linz Institute of Technology (LIT), and the LIT Secure and Correct Systems Lab, supported by the State of Upper Austria, the European Union's Horizon 2020 research and innovation program under Grant Agreements No. 899814 (Qurope), No. 871130 (Ascent+), the QuantERA II project QD-E-QKD and the FFG (grant No. 891366). A.R. and E.A.C. were supported by the QuantERA award MEEDGARD. *Author contributions:* S.M., S.F.C.S. and A.R. developed, grew and processed the quantum dot samples. H.E.D, conducted the experiments. H.E.D. and E.A.C. analysed the data. H.E.D. and E.A.C. drafted the manuscript with input from all authors. E.A.C. performed numerical modelling and coordinated the project.

[1] Ladd, T. D. *et al.* Quantum computers. *Nature* **464**, 45–53 (2010).
[2] Lvovsky, A. I., Sanders, B. C. & Tittel, W. Optical quantum memory. *Nat. Photon.* **3**, 706–714 (2009).
[3] Pang, X.-L. *et al.* A hybrid quantum memory–enabled network at room temperature. *Sci. Adv.* **6**, eaax1425 (2020).
[4] Bussières, F. *et al.* Quantum teleportation from a telecom-wavelength photon to a solid-state quantum memory. *CLEO: 2014* FTu2A.4 (2014).
[5] Tittel, W. *et al.* Photon-echo quantum memory in solid state systems. *Laser Photonics Rev.* **4**, 244–267 (2010).
[6] Zhao, R. *et al.* Long-lived quantum memory. *Nat. Phys.* **5**, 100–104 (2009).
[7] Yu, Y. *et al.* Entanglement of two quantum memories via fibres over dozens of kilometres. *Nature* **578**, 240–245 (2020).
[8] Neuwirth, J. *et al.* Quantum dot technology for quantum repeaters: from entangled photon generation toward the integration with quantum memories. *Mater. Quantum Technol.* **1**, 043001 (2021).
[9] Treutlein, P., Hommelhoff, P., Steinmetz, T., Hänsch, T. W. & Reichel, J. Coherence in microchip traps. *Phys. Rev. Lett.* **92**, 203005 (2004).
[10] Deutsch, C. *et al.* Spin self-rephasing and very long coherence times in a trapped atomic ensemble. *Phys. Rev. Lett.* **105**, 020401 (2010).
[11] Langer, C. *et al.* Long-lived qubit memory using atomic ions. *Phys. Rev. Lett.* **95**, 060502 (2005).
[12] Bollinger, J., Heizen, D., Itano, W., Gilbert, S. & Wineland, D. A 303-MHz frequency standard based on trapped Be^+ ions. *IEEE Trans. Instrum. Meas.* **40**, 126–128 (1991).
[13] Wang, Y. *et al.* Single-qubit quantum memory exceeding ten-minute coherence time. *Nat. Photon.* **11**, 646–650 (2017).
[14] Wang, P. *et al.* Single ion qubit with estimated coherence time exceeding one hour. *Nat. Commun.* **12**, 233 (2021).
[15] Zhong, M. *et al.* Optically addressable nuclear spins in a solid with a six-hour coherence time. *Nature* **517**, 177–180 (2015).
[16] Bruzewicz, C. D., Chiaverini, J., McConnell, R. & Sage, J. M. Trapped-ion quantum computing: Progress and challenges. *Appl. Phys. Rev.* **6**, 021314 (2019).
[17] Tyryshkin, A. M., Lyon, S. A., Astashkin, A. V. & Raitsimring, A. M. Electron spin relaxation times of phosphorus donors in silicon. *Phys. Rev. B* **68**, 193207 (2003).
[18] Tyryshkin, A. M. *et al.* Electron spin coherence exceeding seconds in high-purity silicon. *Nat. Mater.* **11**, 143–147 (2011).
[19] Morton, J. J. *et al.* Solid-state quantum memory using the ^{31}P nuclear spin. *Nature* **455**, 1085–1088 (2008).
[20] Steger, M. *et al.* Quantum information storage for over 180 s using donor spins in a ^{28}Si "semiconductor vacuum". *Science* **336**, 1280–1283 (2012).
[21] Freer, S. *et al.* A single-atom quantum memory in silicon. *Quantum Sci. Technol.* **2**, 015009 (2017).
[22] Atatüre, M., Englund, D., Vamivakas, N., Lee, S.-Y. & Wrachtrup, J. Material platforms for spin-based photonic quantum technologies. *Nat. Rev. Mater.* **3**, 38–51 (2018).
[23] Stas, P.-J. *et al.* Robust multi-qubit quantum network node with integrated error detection. *Science* **378**, 557–560 (2022).
[24] Kubo, Y. *et al.* Hybrid quantum circuit with a superconducting qubit coupled to a spin ensemble. *Phys. Rev. Lett.* **107**, 220501 (2011).
[25] Stockill, R. *et al.* Phase-tuned entangled state generation between distant spin qubits. *Phys. Rev. Lett.* **119**, 010503 (2017).
[26] Huber, D. *et al.* Highly indistinguishable and strongly entangled photons from symmetric GaAs quantum dots. *Nat. Commun.* **8**, 15506 (2017).
[27] Schweickert, L. *et al.* On-demand generation of background-free single photons from a solid-state source. *Appl. Phys. Lett.* **112**, 093106 (2018).
[28] Arakawa, Y. & Holmes, M. J. Progress in quantum-dot single photon sources for quantum information technologies: A broad spectrum overview. *Appl. Phys. Rev.* **7**, 021309 (2020).
[29] Liu, J. *et al.* A solid-state source of strongly entangled photon pairs with high brightness and indistinguishability. *Nat. Nanotechnol.* **14**, 586–593 (2019).

[30] Rota, M. B. *et al.* A source of entangled photons based on a cavity-enhanced and strain-tuned GaAs quantum dot. *eLight* **4**, 13 (2024).

[31] De Greve, K. *et al.* Quantum-dot spin–photon entanglement via frequency downconversion to telecom wavelength. *Nature* **491**, 421–425 (2012).

[32] Coste, N. *et al.* High-rate entanglement between a semiconductor spin and indistinguishable photons. *Nat. Photon.* **17**, 582–587 (2023).

[33] Laccotripes, P. *et al.* Spin-photon entanglement with direct photon emission in the telecom C-band. *Nat. Commun.* **15**, 9740 (2024).

[34] Zaporski, L. *et al.* Ideal refocusing of an optically active spin qubit under strong hyperfine interactions. *Nat. Nanotechnol.* **18**, 257–263 (2023).

[35] Gillard, G. *et al.* Fundamental limits of electron and nuclear spin qubit lifetimes in an isolated self-assembled quantum dot. *npj Quantum Inf.* **7**, 43 (2021).

[36] Chekhovich, E. A., da Silva, S. F. C. & Rastelli, A. Nuclear spin quantum register in an optically active semiconductor quantum dot. *Nat. Nanotechnol.* **15**, 999–1004 (2020).

[37] Gillard, G., Clarke, E. & Chekhovich, E. A. Harnessing many-body spin environment for long coherence storage and high-fidelity single-shot qubit readout. *Nat. Commun.* **13**, 4048 (2022).

[38] Gangloff, D. A. *et al.* Quantum interface of an electron and a nuclear ensemble. *Science* **364**, 62–66 (2019).

[39] Appel, M. H. *et al.* A many-body quantum register for a spin qubit. *Nat. Phys.* (2025).

[40] Chekhovich, E., Hopkinson, M., Skolnick, M. & Tartakovskii, A. Suppression of nuclear spin bath fluctuations in self-assembled quantum dots induced by inhomogeneous strain. *Nat. Commun.* **6**, 6348 (2015).

[41] Childress, L., Taylor, J. M., Sørensen, A. S. & Lukin, M. D. Fault-tolerant quantum communication based on solid-state photon emitters. *Phys. Rev. Lett.* **96**, 070504 (2006).

[42] Sharman, K., Kimiaee Asadi, F., Wein, S. C. & Simon, C. Quantum repeaters based on individual electron spins and nuclear-spin-ensemble memories in quantum dots. *Quantum* **5**, 570 (2021).

[43] Li, D. *et al.* Intrinsic origin of spin echoes in dipolar solids generated by strong π pulses. *Phys. Rev. B* **77**, 214306 (2008).

[44] Waeber, A. M. *et al.* Pulse control protocols for preserving coherence in dipolar-coupled nuclear spin baths. *Nat. Commun.* **10**, 3157 (2019).

[45] Balasubramanian, G. *et al.* Ultralong spin coherence time in isotopically engineered diamond. *Nat. Mater.* **8**, 383–387 (2009).

[46] Millington-Hotze, P. *et al.* Approaching a fully-polarized state of nuclear spins in a solid. *Nat. Commun.* **15**, 985 (2024).

[47] Millington-Hotze, P., Manna, S., Covre da Silva, S. F., Rastelli, A. & Chekhovich, E. A. Nuclear spin diffusion in the central spin system of a GaAs/AlGaAs quantum dot. *Nat. Commun.* **14**, 2677 (2023).

[48] Urbaszek, B. *et al.* Nuclear spin physics in quantum dots: An optical investigation. *Rev. Mod. Phys.* **85**, 79–133 (2013).

[49] Dyte, H. E. *et al.* Is wave function collapse necessary? explaining quantum nondemolition measurement of a spin qubit within linear evolution. *Phys. Rev. Lett.* **132**, 160804 (2024).

[50] Klauder, J. R. & Anderson, P. W. Spectral diffusion decay in spin resonance experiments. *Phys. Rev.* **125**, 912–932 (1962).

[51] Haeberlen, U. & Waugh, J. S. Coherent averaging effects in magnetic resonance. *Phys. Rev.* **175**, 453–467 (1968).

[52] Mehring, M. *Principles of High Resolution NMR in Solids* (Springer Berlin Heidelberg, 1983).

[53] Hahn, E. L. Spin echoes. *Phys. Rev.* **80**, 580–594 (1950).

[54] Waugh, J. S., Huber, L. M. & Haeberlen, U. Approach to high-resolution NMR in solids. *Phys. Rev. Lett.* **20**, 180–182 (1968).

[55] Cory, D., Miller, J. & Garroway, A. Time-suspension multiple-pulse sequences: applications to solid-state imaging. *J. Magn. Reson. (1969)* **90**, 205–213 (1990).

[56] Huo, Y. H. *et al.* A light-hole exciton in a quantum dot. *Nat. Phys.* **10**, 46–51 (2013).

[57] Khodjasteh, K. & Lidar, D. A. Fault-tolerant quantum dynamical decoupling. *Phys. Rev. Lett.* **95**, 180501 (2005).

[58] Souza, A. M., Álvarez, G. A. & Suter, D. Robust dynamical decoupling. *Philos. Trans. R. Soc. A* **370**, 4748–4769 (2012).

[59] Dementyev, A. E., Li, D., MacLean, K. & Barrett, S. E. Anomalies in the NMR of silicon: Unexpected spin echoes in a dilute dipolar solid. *Phys. Rev. B* **68**, 153302 (2003).

[60] Li, D., Dementyev, A. E., Dong, Y., Ramos, R. G. & Barrett, S. E. Generating unexpected spin echoes in dipolar solids with π pulses. *Phys. Rev. Lett.* **98**, 190401 (2007).

[61] Hjort, K., Soderkvist, J. & Schweitz, J. A. Gallium arsenide as a mechanical material. *J. Micromech. Microeng.* **4**, 1 (1994).

[62] Martín-Sánchez, J. *et al.* Strain-tuning of the optical properties of semiconductor nanomaterials by integration onto piezoelectric actuators. *Semicond. Sci. and Technol.* **33**, 013001 (2017).

[63] Burum, D. P. & Rhim, W. K. Analysis of multiple pulse NMR in solids. III. *J. Chem. Phys.* **71**, 944–956 (1979).

[64] Wei, K. X., Ramanathan, C. & Cappellaro, P. Exploring localization in nuclear spin chains. *Phys. Rev. Lett.* **120**, 070501 (2018).

[65] Lukin, A. *et al.* Probing entanglement in a many-body–localized system. *Science* **364**, 256–260 (2019).

Supplementary Information: Storing quantum coherence in a quantum dot nuclear spin ensemble for over 100 milliseconds

Harry E. Dyte

Department of Physics and Astronomy, University of Sheffield, Sheffield S3 7RH, United Kingdom

Santanu Manna, Saimon F. Covre da Silva, and Armando Rastelli

Institute of Semiconductor and Solid State Physics, Johannes Kepler University Linz, Altenberger Str. 69, 4040 Linz, Austria

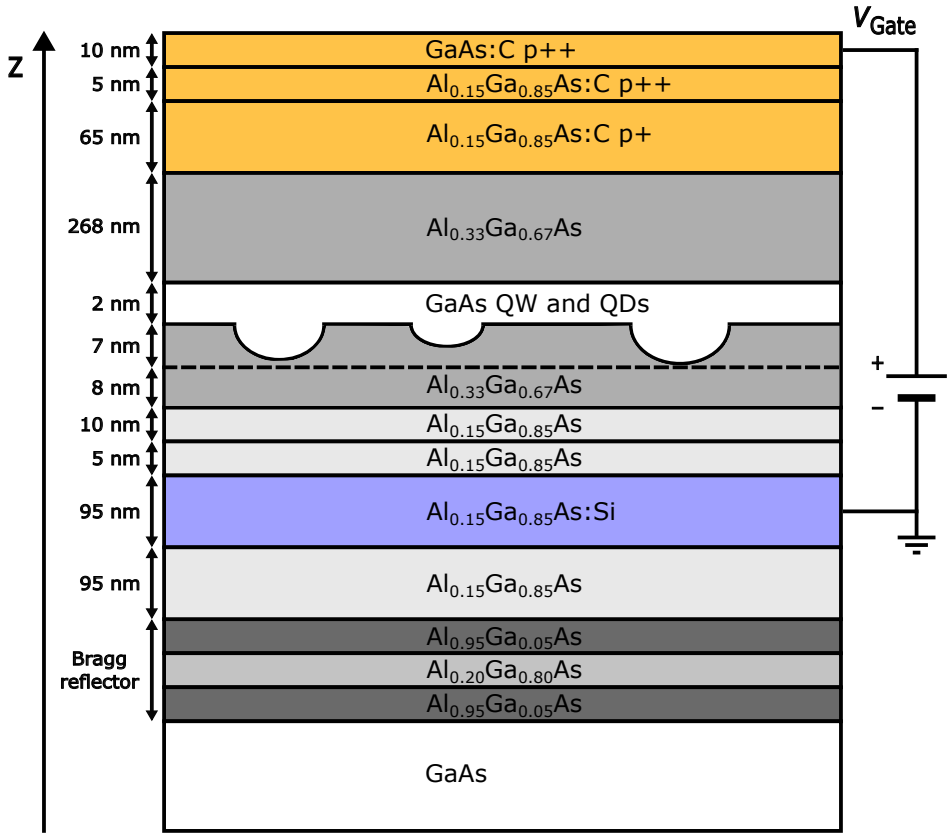
Evgeny A. Chekhovich

Department of Physics and Astronomy, University of Sussex, Brighton BN1 9QH, United Kingdom

(Dated: February 20, 2025)

Supplementary Note 1. SAMPLE STRUCTURE

The sample used for this work is the same as used in Refs. [1–4]. The sample is grown on a semi-insulating GaAs (001) substrate. Supplementary Fig. 1 shows the layer sequence of the semiconductor structure. Growth starts with a layer of $Al_{0.95}Ga_{0.05}As$ followed by a single pair of $Al_{0.2}Ga_{0.8}As$ and $Al_{0.95}Ga_{0.05}As$ layers, which act as a Bragg reflector in optical experiments. A 95 nm thick layer of $Al_{0.15}Ga_{0.85}As$ is then grown followed by a 95 nm thick layer of $Al_{0.15}Ga_{0.85}As$ doped with Si at a volume concentration of 1.0×10^{18} cm^{-3}. The concentration of Al is kept at a low value of 0.15 in the Si doped layer, in order to avoid the formation of the deep DX centers [5–7]. The n-type doped layer is followed by the electron tunnel barrier layers: first a 5 nm thick $Al_{0.15}Ga_{0.85}As$ layer is grown at a reduced temperature of 560 °C to suppress Si segregation, followed by a 10 nm thick $Al_{0.15}Ga_{0.85}As$ and then a 15 nm thick $Al_{0.33}Ga_{0.67}As$ layer grown at 600 °C. Droplets of Aluminium are grown on the surface of the $Al_{0.33}Ga_{0.67}As$ layer and are used to etch the nanoholes [8–10]. Atomic force microscopy shows typical nanoholes have a depth of ≈ 6.5 nm and are ≈ 70 nm in diameter [1]. A 2.1 nm thick layer of GaAs is grown to form QDs by infilling the nanoholes and additionally form the quantum well (QW) layer. Thus, the maximum height of the QDs in the growth z direction is ≈ 9 nm. The GaAs layer is followed by a 268 nm thick $Al_{0.33}Ga_{0.67}As$ barrier layer. Finally, the p-type contact layers doped with C are grown: a 65 nm thick layer of $Al_{0.15}Ga_{0.85}As$ with a 5.0×10^{18} cm^{-3} doping concentration, a 5 nm thick layer of $Al_{0.15}Ga_{0.85}As$ with a 9.0×10^{18} cm^{-3} concentration, and a final 10 nm thick layer of GaAs



Supplementary Figure 1. Schematic of the quantum dot sample structure.

with a 5.0×10^{18} cm^{-3} concentration.

Next, the sample is processed into a *p*-*i*-*n* diode structure. Mesa structures with a height of 250 nm are created by etching away the *p*-doped layers and depositing onto the etched regions the following sequence of layers: Ni(10 nm), AuGe(150 nm), Ni(40 nm), Au(100 nm). The sample is then annealed to enable diffusion of the deposited metals down to the *n*-doped layer to form the ohmic back contact. Depositing Ti(15 nm)/Au(100 nm) on to the *p*-type surface of the mesa areas forms the top gate contact. QD photoluminescence (PL) is excited and collected through the top of the sample. Sample gate bias V_{Gate} is the bias of the *p*-type top contact with respect to the grounded *n*-type back contact. Tunneling of holes is suppressed due to the large thickness of the top $Al_{0.33}Ga_{0.67}As$ layer, whereas tunnel coupling to the *n*-type layer enables deterministic charging of the QDs with electrons by changing V_{Gate}. For this work however, we leave the QD uncharged by applying reverse bias.

To allow the quadrupolar components of the nuclear magnetic resonance (NMR) spectra to be

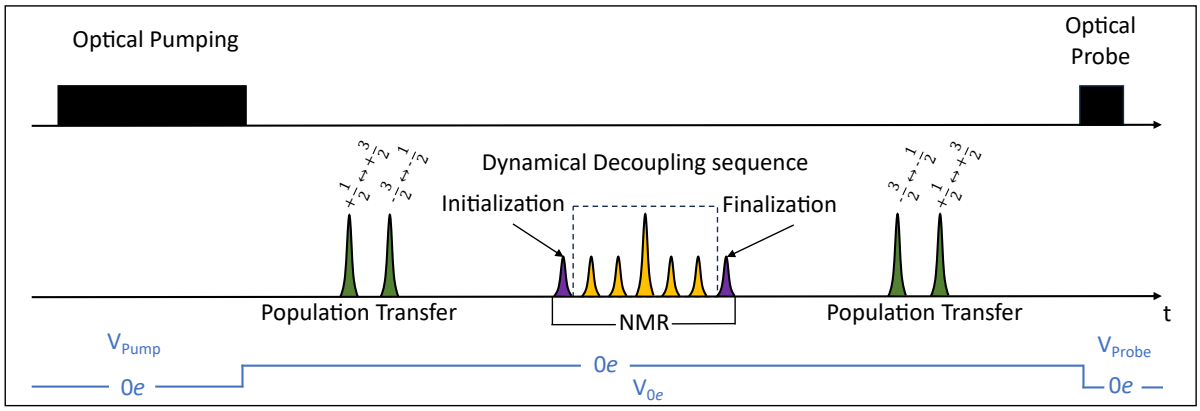
resolved, the semiconductor sample used in this work is subjected to uniaxial mechanical stress. To this end, the semiconductor wafer is first cleaved into a small piece with a rectangular surface area of 0.7 mm×2.35 mm. The edges of the rectangular profile are aligned along the [110] and [1$\bar{1}$0] crystallographic directions. The sample thickness along the [001] growth direction is 0.35 nm. Thus, the sample is a parallelepiped. The sample is then inserted into a home-made stress cell. This is done in such a way that the two 0.7 mm×0.35 mm surfaces of the sample are contacted to the flat titanium surfaces of the stress cell bracket. Finally, a titanium screw is directed along the 2.35 mm long edge of the sample in order to apply compressive stress [4].

Supplementary Note 2. EXPERIMENTAL TECHNIQUES

The sample is placed in a bath-cryostat and cooled using liquid He to $\approx$ 4.2 K. An inbuilt superconducting coil is used to apply a static magnetic field B_z up to 8 T along the z-axis parallel to the sample growth direction [001] and the optical axis (Faraday geometry). Therefore, the applied mechanical stress is perpendicular to the field and optical axis. Optical measurements are conducted using a confocal microscopy configuration. An aspheric lens with a focal distance of 1.45 mm and NA = 0.58 is used as an objective for optical excitation of the QD and for collection of photoluminescence (PL). The excitation laser is focused into a spot with a diameter of ≈ 1 μm. A two-stage Czerny-Turner spectrometer is used to analyze the collected PL. The light is collimated and directed to a plane diffraction grating at each stage. Upon dispersion, the light is focused by a mirror with a 1 m focal length. After the spectrometer, a pair of achromatic lens doublets transfer the spectral image onto a charge-coupled device (CCD) photo-detector with a magnification of 3.75. The changes in the spectral splitting, determined from the PL spectra of a neutral exciton X^0, allow measurement of the hyperfine shifts E_{hf}, which is proportional to the nuclear spin polarization degree (Fig. 2a of the main text). Both the pump and probe laser pulses are formed using mechanical shutters. One more mechanical shutter is used to block the input of the spectrometer during the optical pumping.

A. Optical pumping of nuclear spin polarization

Supplementary Fig. 2 shows the full timing diagram for the NMR measurements used in this work. In the first part of the measurement cycle dynamical nuclear spin polarization is created by optically pumping the QD with a tunable single-mode circularly polarized diode laser. This is a well



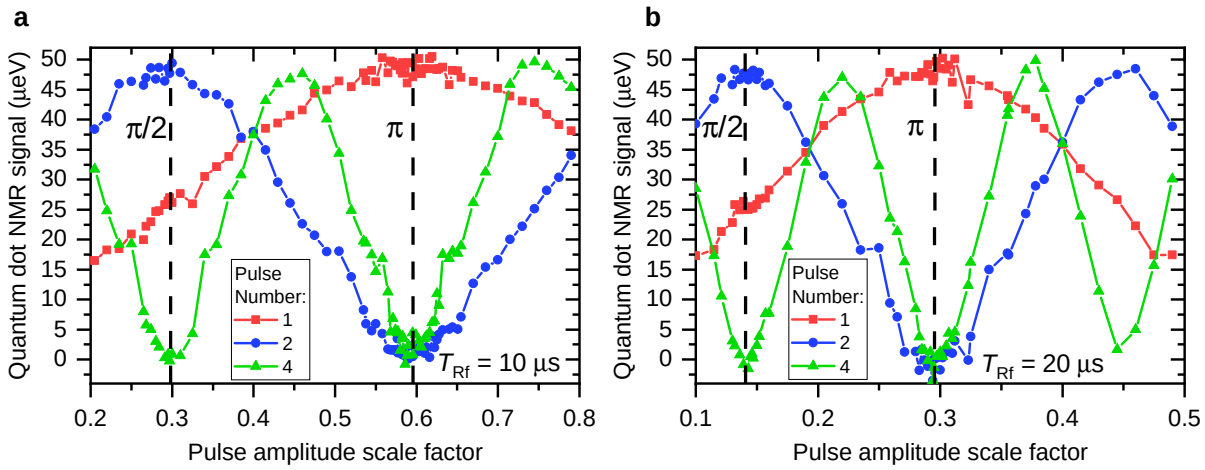
Supplementary Figure 2. Full timing diagram of pulsed dynamical decoupling experiments.

established technique and allows nuclear spin polarization greater than 50% to be reached [11–16]. The process is cyclic with three stages. First, optical excitation creates a spin polarized electron, a process enabled by the selection rules in III-V semiconductors allowing spin-polarized electron-hole pairs to be formed from the conversion of circularly polarized light. Secondly, the flip-flop term of the electron-nuclear hyperfine Hamiltonian allows the electron to exchange its spin with a single nuclei. Finally, electron-hole recombination removes the flipped electron allowing another polarized electron to be created in the dot and the process repeats, building-up polarization of the ensemble of nuclei. The pump laser pulse is typically 5 s long, afterwards, a 10 ms delay is added to ensure that the mechanical shutter has fully closed. The pump power ≈ 1 mW is three orders of magnitude greater than the ground-state PL saturation power, with typical photon energy $\approx 5-10$ meV above the X^0 PL energy. To ensure the QD is unoccupied during the pump process, a large reverse bias is applied $V_{\mathrm{Gate}} = -2.4$ V.

B. Nuclear magnetic resonance (NMR)

A copper wire coil is used to generate the magnetic field $B_x \perp z$ needed to carry out NMR experiments. The coil is positioned ≈ 0.5 mm from the QD sample. The coil is made of 10 turns of a 0.1 mm diameter enamelled copper wire wound on a ≈ 0.4 mm diameter spool in 5 layers, with 2 turns in each layer. A class-AB radiofrequency (Rf) amplifier (Tomco BT01000-AlphaSA rated up to 1000 W) is used to drive the coil, fed by the output of an arbitrary waveform generator (Keysight M8190).

The timing of NMR experiments proceeds as shown in Fig. 2. First, two Rf pulses are used to



Supplementary Figure 3. **a** Rabi oscillations of the nuclear spins under Rf pulse bursts of increasing amplitude with fixed pulse duration $T_{\mathrm{Rf}} = 10$ μs. Increasing the pulse amplitude increases the degree of rotation of the spins. The first peak in the oscillation (solid squares, red, one pulse) corresponds to a π rotation. We obtain the required amplitude of a $\pi/2$ rotation from the first peak for the oscillation driven by two pulses (solid circles, blue). Additionally we conduct measurements with 4, 8 and 16 pulses to improve the accuracy of the acquired amplitudes. Only the 4 pulse measurement (solid triangles, green) is shown for clarity. **b** Same as **a** but for pulses with $T_{\mathrm{Rf}} = 20$ μs.

increase the NMR signal by transferring the nuclear spin population into the optimal configuration [4, 17]. Consider the case where the dot is pumped with σ^+ light leaving the $I_z = -3/2$ nuclear spin states the most populated [3], while the $I_z = +3/2$ states are nearly unpopulated. By maximising the population change we maximize the NMR signal. For measurements performed on the central transition the population difference between the $I_z = -1/2$ and $I_z = +1/2$ states needs to be maximized. To this end we apply two π pulses to transfer the nuclear spin populations. First, a pulse is applied to the $+1/2 \leftrightarrow +3/2$ transition, exchanging their populations leaving $I_z = +1/2$ as the least populated state. Then, after a short delay, a second pulse is applied to the $-3/2 \leftrightarrow -1/2$ transition leaving $I_z = -1/2$ as the most populated state. A similar process can be applied in the case one of the satellite transitions is being investigated.

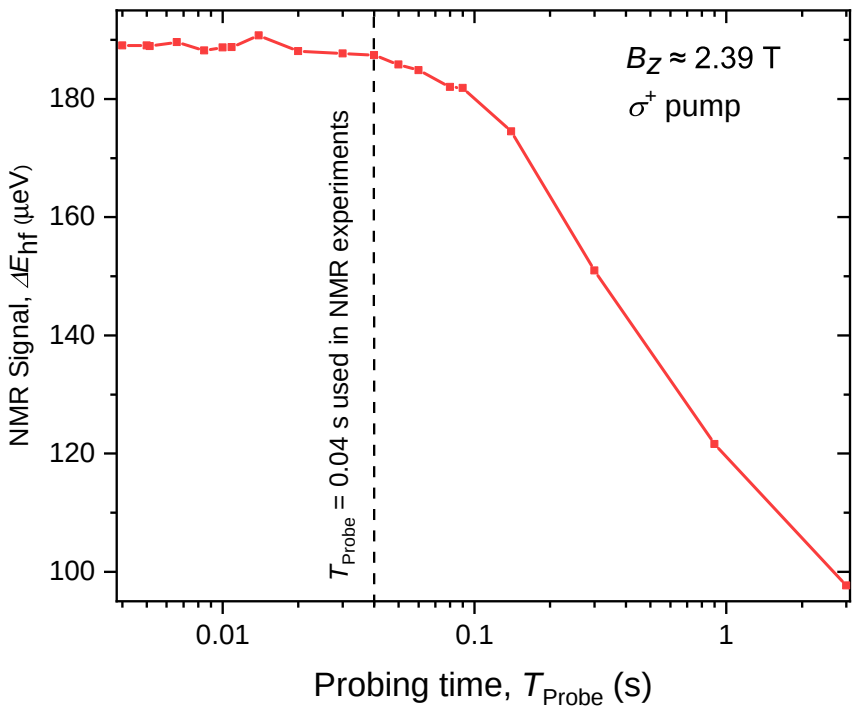
Next, the optically generated nuclear spin polarization needs to be converted from longitudinal polarization to transverse polarization. This is so the spins begin to decohere and the coherence time can be measured. We achieved this simply by using a single $\pi/2$ Rf pulse. The phase of the pulse can be varied to allow control over the initial orientation of the nuclear spins in the xy plane. Dynamical decoupling is then applied. The pulses for a given sequence are applied in a way that they are equally spaced by time τ, this means that while T_{FreeEvol} is increased the time τ

between each pair of adjacent pulses increases uniformly. Due to hardware limitations, the minimal interpulse delay achievable is $\tau \approx 0.3$ μs. This places a lower limit on the free evolution time that could be measured for a given dynamical decoupling sequence, based on the sequences number of pulses. Finally, a $\pi/2$ pulse is used to rotate the nuclei back along the z axis for optical readout. Again, the phase of finalization pulse can be varied. If the phase of the finalization pulse is the same as the initialization pulse, the nuclei are rotated such that their populations are antiparrallel compared to before the initialization pulse. Comparatively, if the finalization pulse is π out of phase with the initialization pulse, then the nuclear spins are aligned parallel to the orientation before initialization. All measurements use initialization and finalization pulses with π phase difference, as this allows us to avoid the range of nuclear polarizations where electron-nuclear bistability [18] accelerates the nuclear spin dynamics.

Before optical readout we again transfer the spin populations, this allows us to multiply the NMR signal by exploiting the entire $I = 3/2$ Hilbert space. The process is the reverse of the process described above. First, a π pulse is applied to the $-3/2 \leftrightarrow -1/2$ transition followed by another π pulse on the $+1/2 \leftrightarrow +3/2$ transition. The reason for this is that after application of the dynamical decoupling sequence, the remaining nuclear spin polarization is encoded in the $-1/2 \leftrightarrow +1/2$ states. Assuming a π phase difference between initial and final pulses, the $I_z = -1/2$ state will be most populated, while the $I_z = +1/2$ state will be least populated. The reverse population transfer means the $I_z = -3/2$ and $I_z = +3/2$ become the most and least populated states respectively, encoding the NMR signal into the $I_z = \pm 3/2$ subspace, approximately tripling the NMR signal measured optically. During NMR a bias of $V_{\mathrm{Gate}} = -1.5$ V is applied to the sample to ensure that there are no resident electrons.

C. Rf pulse calibration

Dynamical decoupling requires that precise rotations of the nuclei are performed. For some of the measurements in this work, as many as 2400 Rf pulses were applied to drive rotations of the nuclear spins, any inaccuracy in the rotations would therefore worsen the coherence of the nuclear spin polarization. To this end, we performed Rabi oscillation measurements to calibrate the π and $\pi/2$ Rf pulses. The Rf pulses are produced by modulating the Rf carrier with a raised cosine envelope function of total duration T_{Rf} between the two zero-amplitude points. For a desired T_{Rf}, the amplitude of the applied pulses was increased and the resulting NMR signal measured, Supplementary Fig. 3a shows the Rabi oscillations observed for $T_{\mathrm{Rf}} = 10$ μs pulse duration. From



Supplementary Figure 4. Calibration measurement for the optical probe duration. Hyperfine shift measured under different duration optical probing after being polarized with σ^+ optical pumping. The time (T_{Probe}) used for coherence measurements and nuclear spin decoupling is shown by the dashed line. Measurement was conducted with external magnetic field $B_z = 2.39$ T.

this the power required for a π pulse is obtained by locating the first peak in the oscillation. The power needed for a $\pi/2$ Rf pulse is found by applying two separate pulses. Here, the first peak now gives the amplitude needed for a $\pi/2$ pulse, as this corresponds to a total rotation of nuclei by π meaning each of the two pulses will have rotated the nuclei by $\pi/2$. Finally, to improve the accuracy of these calibrations we conducted measurements with an increasing number of pulses: 4, 8, and 16. The Rabi oscillations were collectively fitted to obtain the power scaling factors. Supplementary Fig. 3b shows the same calibrations but for $T_{\mathrm{Rf}} = 20$ μs pulses.

D. Optical probing of nuclear spins

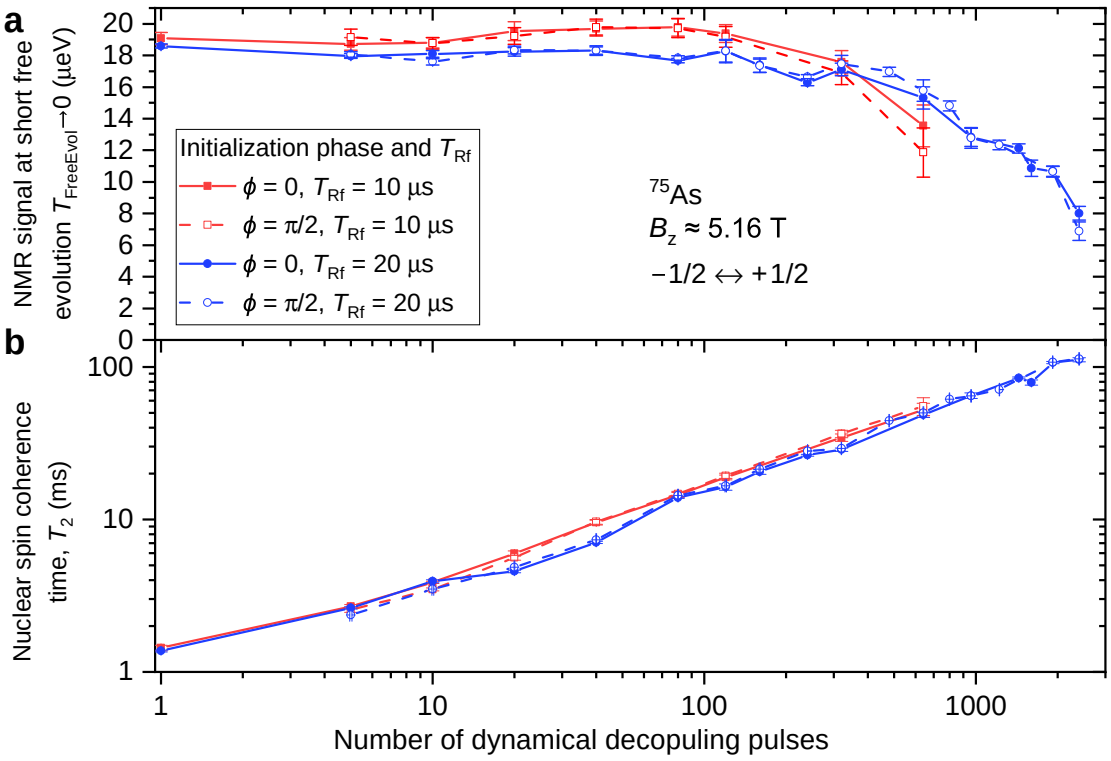
Measurement of the nuclear spin polarization is conducted using optical probing. The probe power and the bias during the probe ($V_{\mathrm{Gate}} = +0.9$ V) are chosen to maximize (saturate) the intensity of the ground neutral exciton (X^0) state PL. There is a 10 ms delay between the bias switching and the mechanical shutter activating, forming the probe pulse. This delay ensures that the charge state of the quantum dot is in its steady state when the optical probe pulse is applied.

An example PL spectra is shown in Fig. 2a of the main text. The PL is generated by recombination of the electron-hole pairs. Under optical excitation the spin of the electron is random, meaning light is emitted from both bright exciton spin states. The PL is accumulated over millisecond timescales allowing both exciton states to be observed in the same PL spectrum. The applied magnetic field splits the two PL lines, these can be further shifted by the nuclear polarization via the hyperfine interaction. The shifts can be seen when the nuclei are polarized with different circularly polarized light. Injection of optically excited electrons into the dot leads to spin flip-flops between the electron spin and nuclei which will progressively depolarize the nuclei. A probe pulse duration measurement is shown in Supplementary Fig. 4 for external magnetic field of $B_z = 2.39$ T. As the probe time is increased the nuclear polarization decreases, seen in the reduction of PL splitting. Similar results are observed in a wide range of magnetic fields $B_z = 1 - 8$ T. Based on such calibration results we use a probe time of $T_{\mathrm{Probe}} = 0.04$ s maximizing the collected signal from the optical excitation without a significant loss in nuclear spin polarization due to spin flip-flops.

Supplementary Note 3. ADDITIONAL EXPERIMENTAL RESULTS

A. Optimal Rf pulse duration in dynamical decoupling

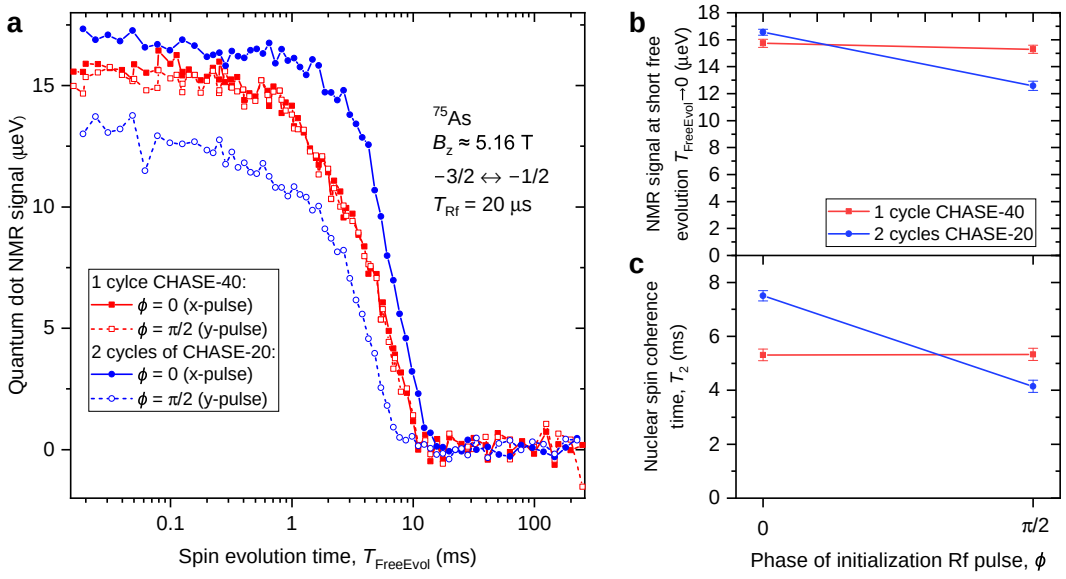
Ideally, nuclear spin rotations would be carried out instantaneously, minimising decoherence due to unwanted evolution of the nuclear spin ensemble during the rotation. As we are limited to using finite time Rf pulses, one may expect that shorter T_{Rf} times would yield better coherence storage performance. Yet, as discussed in the main text, we find that when using short $T_{\mathrm{Rf}} = 10$ μs pulses we see a drop in performance for high pulse number sequences (≈ 640 pulses) compared to when longer $T_{\mathrm{Rf}} = 20$ μs pulses are used. Here were present experimental results that reveal these counterintuitive observations. Nuclear spin decoherence measurements, such as shown in Fig. 2c of the main text, have been conducted both with $T_{\mathrm{Rf}} = 10$ μs and $T_{\mathrm{Rf}} = 20$ μs on the $I_z = \pm 1/2$ nuclear spin subspace. In each such measurement, the total free evolution time T_{FreeEvol} is varied while keeping a constant number of pulses in the dynamical decoupling sequence. The resulting dependence of the spin echo NMR signal is fitted with a stretched exponential function of T_{FreeEvol}. From the fit we derive the NMR signal in the limit of short free evolution $T_{\mathrm{FreeEvol}} \to 0$ and the characteristic nuclear spin coherence time T_2. These results are shown in Figs. 5a and b, respectively. The values are shown as a function of the total number of pulses in Hahn echo (1 pulse), CHASE-5 (5 pulses), CHASE-10 (10 pulses), CHASE-20 (20 pulses), and a varying



Supplementary Figure 5. **a** NMR signal (spin echo amplitude) at short free evolution time $T_{\rm FreeEvol} \to 0$ plotted as a function of the number of Rf pulses in the dynamical decoupling sequence. The data is shown for Rf pulse durations of $T_{\rm Rf} = 10$ μs (squares) and $T_{\rm Rf} = 20$ μs (circles). Measurements are conducted with initial nuclear polarization along the $-y$ axis (solid symbols, initialization Rf pulse phase $\phi = 0$) and the x axis ($\phi = \pi/2$, open symbols) of the rotating frame. **b** Dependence of the nuclear spin coherence time T_2 on the number of Rf pulses.

number of CHASE-40 cycles (all points with ≥ 40 pulses). The results are shown for two different orientations of the initial nuclear spin polarization in the equatorial plane of the rotating frame (initialization pulse phase $\phi = 0$ and $\phi = \pi/2$).

From Supplementary Fig. 5a we find that for short pulse sequences ($\lesssim 100$ pulses) the short-evolution NMR signal is somewhat better (larger) for short pulses ($T_{\rm Rf} = 10$ μs, squares), as these are better approximation to instantaneous spin Hamiltonian transformations than the $T_{\rm Rf} = 20$ μs pulses (circles) pulses. However, for longer sequences (640 pulses) the short-evolution spin echo under short pulses ($T_{\rm Rf} = 10$ μs) becomes worse than under long pulses ($T_{\rm Rf} = 20$ μs). Supplementary Fig. 5b shows that the coherence time T_2, which is a measure of decoherence during free evolution, is nearly independent of the Rf pulse duration $T_{\rm Rf}$. This allows us to conclude that the reduced short-evolution NMR signal (i.e. reduced fidelity of coherence storage) at $T_{\rm Rf} = 10$ μs



Supplementary Figure 6. **a** Decoherence measured on the $I_z = (-3/2, -1/2)$ nuclear spin subspace. Two cycles of CHASE-20 (squares) are compared to a single CHASE-40 cycle (circles) both when initializing the nuclear spin polarization along the $-y$ axis of the rotating frame (solid symbols, $\phi = 0$ Rf pulse phase) and along the x axis (open symbols, $\phi = \pi/2$). **b** NMR signal (spin echo amplitude) at short free evolution time $T_{\mathrm{FreeEvol}} \to 0$ plotted as a function of the phase ϕ of the initialization Rf pulse for two cycles of CHASE-20 (squares) and one cycle of CHASE-40 (circles). The values are obtained from fitting the decay curves in (**a**). **c** Same as (**b**) but for nuclear spin decoherence time T_2.

is a result of undesired spin evolution during the pulses, rather than pure decoherence during free evolution between the pulses. In particular, we attribute the reduced performance of the $T_{\mathrm{Rf}} = 10$ μs pulses to parasitic leakage of the stored state to the two nuclear satellite transitions, owing to the broader spectral profile of the pulses, as shown by the dashed lines in Fig. 1a of the main text.

B. Comparison of pulsed spin locking in CHASE-20 and CHASE-40 decoupling sequences

Pulsed spin locking is observed in various dynamical decoupling techniques. The simplest example is the Carr-Purcell sequence, where a train of π Rf pulses of the same phase is applied. The spin locking can be understood intuitively as an effective transverse magnetic field in the rotating frame that arises from repeated rotations of the nuclear spins around a preferential equatorial axis of the rotating frame [19]. If the coherent nuclear polarization, created by the initial $\pi/2$ Rf pulse, is parallel to this effective transverse magnetic field, the nuclear state becomes "locked" and its

decay is suppressed. In other words, the transverse (T_2) coherence decay is replaced by a decay that is akin to longitudinal (T_1) relaxation in the rotating frame. By contrast, the initial state polarized orthogonal to the effective locking field undergoes precession and accelerated decoherence. In the case of the CHASE-10 cycle, shown in Fig. 1b of the main text, the two π rotations (labeled $+\mathrm{x}^2$ and $-\mathrm{x}^2$) create a preferential direction in the rotating frame, whereas the four $\pi/2$ rotation pulses labeled as $\pm$x are balanced by four $\pm$y Rf pulses rotating the spins around the orthogonal axis in the rotating frame.

The CHASE-40 sequence is designed to be resilient against pulsed spin locking, by combining four CHASE-10 subsequences, where the phase of all Rf pulses is stepped in each block by $\pi/2$, as shown in Fig. 1c of the main text. Here we perform direct comparison of CHASE-40 with a sequences of pulses, where such phase stepping is omitted. To this end we use two cycles of CHASE-20 sequences, where each CHASE-20 block is a combination of CHASE-10 and its mirror copy, where all Rf pulses are applied in reverse [20]. Thus, both the CHASE-40 and 2 cycles of CHASE-20 differ only by the phases of the Rf pulses. In the case of CHASE-20, all the π rotations ($+\mathrm{x}^2$ and $-\mathrm{x}^2$) are around the same equatorial axis of the rotating frame.

The experiments are performed on the $I_z = (-3/2, -1/2)$ subspace of the ^{75}As nuclear spins. The resulting decays of nuclear spin echo with the increasing free evolution time T_{FreeEvol} are shown in Supplementary Fig. 6a. The decay curves are fitted with stretched exponentials to derive the NMR signal in the limit of short free evolution $T_{\mathrm{FreeEvol}} \to 0$ (shown in Supplementary Fig. 6b) and the characteristic nuclear spin coherence time T_2 (shown in Supplementary Fig. 6c). In the case of CHASE-40 (squares in Supplementary Fig. 6a) the decoherence (characterized by $T_2 \approx 5.3$ ms) does not depend on the direction of the initial transverse nuclear spin polarization. This is also in agreement with the data of Fig. 4 of the main text obtained for the $I_z = -1/2, +1/2$ nuclear spin subspace. These results confirm that CHASE-40 effectively eliminates the pulsed spin locking.

For the two cycles of CHASE-20 (circles in Supplementary Fig. 6a) we observe a pronounced difference in decoherence, depending on the initial nuclear spin state. For the spin state polarized along the $-y$ axis of the rotating frame (solid circles, $\phi = 0$) the decay is slowed down ($T_2 \approx 7.5$ ms), revealing the pulsed spin locking effect. (With the convention used here, the pulse labeled as "+x" in the sequence definition of Figs. 1b, c of the main text corresponds to $\phi = 0$. This pulse produces Rf magnetic field along the x axis of the rotating frame and initializes nuclear polarization along the $-y$ axis of the rotating frame. For the "−x" pulse the Rf phase is $\phi = \pi$. The "+y" pulse corresponds to $\phi = \pi/2$ and initializes the nuclear spin state along the x axis. The $\pm\mathrm{x}^2$ Rf pulses have the same phase as $\pm$x, and so on).

For the case of CHASE-20 decoupling with an initial nuclear spin polarization along the x axis ($\phi = 0$), there is a pronounced reduction both in the nuclear spin echo amplitude at short free evolution $T_{\mathrm{FreeEvol}} \to 0$ and in $T_2 \approx 4.1$ ms, characterizing decoherence during free evolution. In the context of quantum memories, this can be interpreted as the worst case scenario, which is an inevitable side effect of the pulsed spin locking. This is why elimination of spin locking, such as achieved with CHASE-40, is important for operating nuclear spins as a quantum memory, which is generally expected to preserve an arbitrary coherent state.

C. Details on Measurement of Nuclear Spin Transitions

The NMR Spectra of the ^{75}As nuclei used in Fig. 1a of the main text were obtained using two seperate measurment techniques. For the $-1/2 \leftrightarrow +1/2$ central transition (blue in Fig. 1a) the spectrum was obtained from a Fourier transform of the measured free induction decay. The free induction decay was measured using $T_{\mathrm{Rf}} = 10\ \mu s$. The $-3/2 \leftrightarrow -1/2$ and $+1/2 \leftrightarrow +3/2$ satellite transitions (black in Fig. 1a) were measured using the inverse NMR measurement technique [21].

Supplementary Note 4. DISCUSSION OF QUANTUM MEMORY APPLICABILITY FOR QUANTUM REPEATERS

Quantum repeaters are a necessary component for the realization of long distance communication of quantum information. The implementation of such devices will enable the secure communication of information, paving the way for the quantum internet [22–24]. The need for quantum repeaters stems from the limitations on information transfer distance in optical fibers. Photons are superb 'flying' qubits that can be used for long distance communication of quantum states owing to their long coherence times. Yet modern optical fibers can only be used to transmit photons for distances of $\approx 20 - 100$ km due to attenuation. One solution to this problem is to transmit the quantum information via satellites, removing the issue of losses due to fiber attenuation. Such systems have been demonstrated, enabling quantum teleportation over distances of up to 1400 km, yet issues such as sensitivity to atmospheric turbulence and the requirement for direct line of sight with the satellite remain [25]. Another alternative is to use quantum repeaters, which seek to get around this limitation by splitting the full communication distance into several shorter channels connected by quantum repeater nodes, by entangling all of the nodes, entanglement swapping can then be used to transmit information between the two end nodes over distances greater than those

possible by direct photon transmission [22–24, 26]. This simplified approach requires that entanglement generation occurs on every repeater node simultaneously, which significantly limits the chance of success. By using a quantum memory qubit which possess a long coherence time T_2, the entangled states can be stored for time T_2 allowing multiple attempts at generating entanglement. Therefore, by using time multiplexing, the chance of successful entanglement swapping can be increased [24, 27].

The storage time of the memory required to achieve the transfer of information over a useful distance varies significantly depending on the quantum repeater protocol. In particular, the required communication time can be reduced by introducing more complexity to the system, such as multiplexing [28, 29]. Therefore the memory time needed for a $\approx$ 1000 km channel can vary from 1000 s down to 1 ms [22, 23, 30]. Fundamentally, the maximum distance achievable for a given memory time is tied to the speed of light, therefore memories of 1 ms are sufficient to beat direct photon transmission [23] while 5 ms is sufficient to reach distances of 1000 km, a commonly used benchmark in the literature [22]. Therefore, using this approach, we estimate that a quantum memory based on nuclear spins with $T_{\mathrm{M}} \approx 100$ ms would be able to store a given state for long enough to send a message over a distance greater than half the Earth's circumference, meaning it would be sufficient for world wide communication. However, photon transmission time is not the only limitation of a quantum repeater [30, 31]. Other limiting factors include: light-matter entanglement generation [32–34], state transfer to the nuclei [35, 36], entanglement swapping [37], and state measurement [38]. While all these building blocks have been demonstrated for QDs, they would all consume time, reducing the amount of time for generating entanglement. Out of the factors listed above, the generation of entanglement is the main limitation on communication distance. In the above discussion we assumed a unity fidelity of entanglement generation. In reality this is not the case and the photon transmission process needs to be repeated multiple times until the entanglement is established, which significantly limits the achievable distances for quantum repeaters [39]. For QDs, entanglement generation rates as high as 7.3 kHz have been demonstrated [37]. We can therefore estimate, using the equations and parameters reported in Ref. [39], that with the current memory storage time of $T_{\mathrm{M}} \approx 100$ ms it should be possible to achieve quantum repeater communication distances of ≈ 13.4 km. Assuiming a link efficiency of 0.34, as used in [39] leads to a more favorable estimate of ≈ 39.4 km, making nuclear spin based memories competitive with the atomic ensemble systems used in Ref. [39], as well as matching communication distances achievable with direct fiber transmission of photons.

Although current nuclear spin memory times do not yet match those achievable in certain solid

state or atomic systems [40–42], the III-V semiconductor quantum dots benefit from superior optical properties such as efficient generation of single [43–46] and entangled photons [47, 48], which are also required for quantum communication. QDs also benefit from the well established semiconductor fabrication techniques, offering a path for scalability. The storage times demonstrated here for nuclear spins, combined with the high optical entanglement generation rates mean that QDs should be able to compete with other existing approaches to quantum repeaters [37, 39]. Finally, by using multiplexing or alternatively, by extending the coherence time to $T_2 = 1$ s as discussed in the main text, it should be possible to extend the possible communication distance to $500 - 1000$ km, sufficient to outperform direct photon transmission and enable quantum repeater channels that, for example, connect major cities [28, 30].

Supplementary Note 5. AVERAGE HAMILTONIAN THEORY APPLIED TO DESIGN OF CHASE DYNAMICAL DECOUPLING SEQUENCES

A. Nuclear spin interactions

The Zeeman term accounts for the coupling of the QD nuclear spins $\mathbf{I}_k$ to the static magnetic field B_z directed along the z axis. In the laboratory frame it can be written as

$$\mathcal{H}_{\mathrm{Z,N}} = -\sum_{k=1}^{N} \hbar\gamma_k B_\mathrm{z} \hat{I}_{\mathrm{z},k}, \tag{S1}$$

where the summation goes over all individual nuclei $1 \leq k \leq N$, $\hbar = h/(2\pi)$ is the reduced Planck's constant, γ_k is the gyromagnetic ratio of the k-th nuclear spin and $\hat{\mathbf{I}}_k$ is a vector of spin operators with Cartesian components $(\hat{I}_{\mathrm{x},k}, \hat{I}_{\mathrm{y},k}, \hat{I}_{\mathrm{z},k})$. The result of the Zeeman term alone is a spectrum of equidistant single-spin eigenenergies $-I_\mathrm{z}\hbar\gamma_k B_\mathrm{z}$. These $2I+1$ states are also the eigenstates of the $\hat{I}_\mathrm{z}$ spin projection operator with eigenvalues I_z satisfying $-I \leq I_\mathrm{z} \leq +I$.

The interaction of the nuclear electric quadrupolar moment with the electric field gradients is described by the term (Ch. 10 in Ref. [49]):

$$\mathcal{H}_{\mathrm{Q,N}} = \sum_{k=1}^{N} \frac{q_k}{6}[3\hat{I}^2_{\mathrm{z}',k} - I_k^2 + \eta_k(\hat{I}^2_{\mathrm{x}',k} - \hat{I}^2_{\mathrm{y}',k})], \tag{S2}$$

where q_k and η_k describe the magnitude and asymmetry of the electric field gradient tensor, whose principal axes are $x'y'z'$. The strain is inhomogeneous within the QD volume, so that q_k and η_k vary between the individual nuclei. The axes $x'y'z'$ are different for each nucleus and generally do not coincide with crystallographic axes or magnetic field direction. For the as-grown (unstrained)

GaAs/AlGaAs QDs the typical quadrupolar shift is around $|q_k|/h \approx 24$ kHz for ^{75}As [1, 11]. The full width at half maximum of the $|q_k|/h$ distribution is ≈ 14 kHz. For a small fraction of arsenic nuclei, adjacent to aluminium atoms, the shifts are as large as $|q_k|/h \approx 200$ kHz [2]. In the strained sample structure, q_k are dominated by the extrinsic uniaxial stress, with the typical values $|q_k|/h \approx 250$ kHz for ^{75}As in the present work. All experiments are conducted under sufficiently strong magnetic fields, where $|\hbar\gamma_k B_z| \gg |q_k|$ and quadrupolar effects can be treated perturbatively. In this perturbative regime, the main effect of the quadrupolar shifts is the anharmonicity of the nuclear spin eigenenergies and the resulting quadrupolar NMR multiplet of $2I$ magnetic-dipole transitions, split by $\nu_\mathrm{Q} \approx q_k/h$. The $I_\mathrm{z} = \pm 1/2$ projection states of a half-integer nuclear spin are influenced by quadrupolar effects only in the second order. These second order shifts scale as $\propto \nu_\mathrm{Q}^2/\nu_\mathrm{N}$, where $\nu_\mathrm{N} = \gamma B_\mathrm{z}/(2\pi)$ is the nuclear spin Larmor frequency.

Since we apply dynamical decoupling only to the two-level subspaces of the spin 3/2 four-level Hilbert space, we can use the standard rotating frame representation. For the $I_\mathrm{z} = \pm 1/2$ subspace the reference frequency of the frame is set to the Larmor frequency ν_N, while for the satellite subspaces the reference frequency is set to $\nu_\mathrm{N} \pm \nu_\mathrm{Q}$ to match the NMR frequency of the corresponding satellite transition. The rotating frame transformation in the following effective Zeeman Hamiltonian term

$$\mathcal{H}'_{\mathrm{Z,N}} = -\sum_{k=1}^{N} h\Delta\nu_k \hat{I}_{\mathrm{z},k}, \tag{S3}$$

where $\Delta\nu_k$ is the resonance offset of the kth nucleus. In the case of the $I_\mathrm{z} = \pm 1/2$ spin subspace, $\Delta\nu_k$ represents the inhomogeneous second order quadrupolar shifts, which are within $\lesssim 1$ kHz. For the $I_\mathrm{z} = (-3/2, -1/2)$ satellite transition subspace the set of $\Delta\nu_k$ describes the distribution of the first order quadrupolar shifts which arise from inhomogeneous strain within the QD volume and range from tens to hundreds of kHz for the individual ^{75}As nuclei.

Direct interaction between the nuclei is described by the dipole-dipole Hamiltonian:

$$\mathcal{H}_\mathrm{DD} = \sum_{1\le j<k\le N} b_{j,k}\left(3\hat{I}_{\mathrm{z},j}\hat{I}_{\mathrm{z},k} - \hat{\mathbf{I}}_j\cdot\hat{\mathbf{I}}_k\right),$$
$$b_{j,k} = \frac{\mu_0\hbar^2}{4\pi}\frac{\gamma_j\gamma_k}{2}\frac{1-3\cos^2\theta_{j,k}}{r_{j,k}^3} \tag{S4}$$

Here, $\mu_0 = 4\pi\times 10^{-7}$ N A^{-2} is the magnetic constant and $r_{j,k}$ denotes the length of the vector, which forms an angle θ with the z axis and connects the two spins j and k. The Hamiltonian of Supplementary Eq. S4 has been truncated to eliminate all spin non-conserving terms – this is justified for static magnetic field exceeding $\gtrsim 1$ mT. The spin-spin interaction constants can be

written in frequency units $\nu_{jk} = b_{j,k}/h$. The typical magnitude of the interaction constants for the nearby nuclei in GaAs is $\max|\nu_{jk}| \approx 100$ Hz. Consequently, the typical timescales of the decoherence driven by the many-body dipole-dipole interactions are on the order of $T_2 \approx 1$ ms. The dipole-dipole interaction does not change its form under rotating frame transformation.

B. Average Hamiltonian theory

The basics of average Hamiltonian theory can be found in relevant textbooks [50]. Here we briefly outline the key points. The effect of the Rf pulses can be viewed as transformation of the many-body nuclear spin Hamiltonian. In the limit of short and strong Rf pulses, we can treat the Hamiltonian in a toggling reference frame as a piece-wise function of time, which remains constant in between the Rf pulses. After the first pulse, the Hamiltonian can be written as:

$$\mathcal{H}_1 = P_1^{-1}\mathcal{H}_0 P_1, \tag{S5}$$

where $\mathcal{H}_0 = \mathcal{H}'_{\mathrm{Z,N}} + \mathcal{H}_{\mathrm{DD}}$ is the initial Hamiltonian in the rotating frame and P_1 is the unitary transformation operator. After the second and third Rf pulses, the Hamiltonian is:

$$\mathcal{H}_2 = (P_2P_1)^{-1}\mathcal{H}_0 P_2P_1, \tag{S6}$$

$$\mathcal{H}_3 = (P_3P_2P_1)^{-1}\mathcal{H}_0 P_3P_2P_1, \tag{S7}$$

and so on for the subsequent pulses. The evolution of the spin ensemble can in principle be calculated using the Hamiltonians, such as in equations S5, S7, to derive the unitary propagators in each time segment. However, for long pulse sequences this quickly becomes impractical. Instead, we want to find the propagator over the entire pulse sequence cycle T_{Cycle}

$$U(T_{\mathrm{Cycle}}) = \exp\left(-iT_{\mathrm{Cycle}}\mathcal{H}_{\mathrm{eff}}\right), \tag{S8}$$

where $\mathcal{H}_{\mathrm{eff}}$ is some effective Hamiltonian describing spin interactions in the toggling frame over the pulse sequence cycle. Such an effective Hamiltonian can indeed be found in the form of a Magnus expansion

$$\mathcal{H}_{\mathrm{eff}} = \mathcal{H}^{(0)} + \mathcal{H}^{(1)} + \mathcal{H}^{(2)}..., \tag{S9}$$

where the first terms of the expansion are

$$\mathcal{H}^{(0)} = \frac{1}{T_{\text{Cycle}}} \int_0^{T_{\text{Cycle}}} \tilde{\mathcal{H}}(t) \mathrm{d}t \ , \tag{S10}$$

$$\mathcal{H}^{(1)} = \frac{-i}{2T_{\text{Cycle}}} \int_0^{T_{\text{Cycle}}} \mathrm{d}t_2 \int_0^{t_2} \mathrm{d}t_1 \left[\tilde{\mathcal{H}}(t_2), \tilde{\mathcal{H}}(t_1)\right] \ , \tag{S11}$$

$$\mathcal{H}^{(2)} = \frac{1}{6T_{\text{Cycle}}} \int_0^{T_{\text{Cycle}}} \mathrm{d}t_3 \int_0^{t_3} \mathrm{d}t_2 \int_0^{t_2} \mathrm{d}t_1 \Big(\left[\tilde{\mathcal{H}}(t_1), \left[\tilde{\mathcal{H}}(t_2), \tilde{\mathcal{H}}(t_3)\right]\right] + \left[\tilde{\mathcal{H}}(t_3), \left[\tilde{\mathcal{H}}(t_2), \tilde{\mathcal{H}}(t_1)\right]\right] \Big) \ . \tag{S12}$$

The $\mathcal{H}^{(0)}$ term is the average Hamiltonian over the pulse sequence cycle. In all CHASE sequences it is eliminated $\mathcal{H}^{(0)} = 0$ in the limit of short Rf control pulses $T_{\text{RF}} \to 0$. For the term $\mathcal{H}^{(n)}$, the integration volume scales as $\propto T_{\text{Cycle}}^{n+1}$. Thus, as long as $\mathcal{H}^{(0)} = 0$, one can ensure the convergence of the effective Hamiltonian to zero $\mathcal{H}_{\text{eff}} \to 0$ in the limit of a short cycle $T_{\text{Cycle}} \to 0$ (i.e. in the limit of fast dynamical decoupling). This is the main goal of the time-suspension dynamical decoupling. As a general rule, one seeks to eliminate the lowest order terms in the expansion, in order to achieve faster convergence of the effective Hamiltonian.

C. Average Hamiltonians of the CHASE cycles

We have calculated average Hamiltonian terms of the CHASE sequences up to the second order in Magnus expansion, inclusive. We take into account the finite (nonzero duration, $T_{\text{Rf}} > 0$) Rf pulses, which represent the time segments within the sequence cycle where the toggling frame Hamiltonian depends explicitly on time. For simplicity, we only treat Rf pulses with rectangular envelope function. Although this is different from the raised cosine pulses used in experiment, the rectangular pulses are sufficient to derive the main effect of the finite control pulses on the average Hamiltonian terms.

We start with the CHASE-10 sequence cycle. The leading term appears in the average Hamiltonian $\mathcal{H}^{(0)}$ under finite pulses $T_{\text{Rf}} > 0$. This Hamiltonian term has the form of a dipole-dipole interaction (Equation S4) but with an effective quantization axis along the y direction (i.e. $3\hat{I}_{\text{z},j}\hat{I}_{\text{z},k}$ is replaced with $3\hat{I}_{\text{y},j}\hat{I}_{\text{y},k}$):

$$\mathcal{H}^{(0)}_{\text{CHASE}-10} = h\frac{T_{\text{Rf}}}{T_{\text{Cycle}}} \sum_{i<j} \nu_{ij}(3I_{i,y}I_{j,y} - \mathbf{I}_i \cdot \mathbf{I}_j). \tag{S13}$$

This interaction causes preferential spin locking of the nuclear spin states polarized along the y axis of the rotating frame. There are also non-zero first and second order terms in the Magnus expansion of the CHASE-10 effective Hamiltonian. The exact expressions can be derived, but

are bulky. These higher order terms can be neglected, since they appear only for finite Rf pulses $T_{\mathrm{Rf}} > 0$ and are dominated by the zero order term $\mathcal{H}^{(0)}$ in the practically useful limit of a short cycle time T_{Cycle}.

The expression for the dominant zero order term of CHASE-20 is twice that of CHASE-10 (Eq. S13). However, since T_{Cycle} appears in denominator of Eq. S13 and is twice longer for CHASE-20, the resulting zero order average Hamiltonian is the same as for CHASE-10. CHASE-20 is a symmetrised version of CHASE-10, i.e. it consists of a CHASE-10 subcycle and second CHASE-10 subcycle where all pulses are applied in reverse order. Symmetrisation leads to cancellation of the first order Magnus term, as well as all other terms with odd orders.

We now consider CHASE-40, the new sequence implemented in this work. The zero order (average) Hamiltonian term appears only under finite pulses $T_{\mathrm{Rf}} > 0$ and has the following form

$$\mathcal{H}^{(0)}_{\mathrm{CHASE-40}} = -2h\frac{T_{\mathrm{Rf}}}{T_{\mathrm{Cycle}}}\sum_{i<j}\nu_{ij}(3I_{i,z}I_{j,z} - \mathbf{I}_i \cdot \mathbf{I}_j) \tag{S14}$$

Compared to Eq. S13, there is an additional factor of 2, but T_{Cycle} in the denominator is 4 times larger. Thus the $\mathcal{H}^{(0)}_{\mathrm{CHASE-40}}$ term is twice smaller in magnitude compared to $\mathcal{H}^{(0)}_{\mathrm{CHASE-10}}$. Moreover, the symmetry axis of $\mathcal{H}^{(0)}_{\mathrm{CHASE-40}}$ coincides with the external magnetic field (z axis). Thus, there is no preferential direction in the equatorial plane of the rotating frame, explaining the absence of spin locking.

CHASE-40 is not symmetric, so the first order Magnus term is not canceled. However, for all physically relevant parameters the first order term is found to be dominated, either by the zero order term (at short T_{Cycle}) or by the second order term discussed below (for long T_{Cycle}). The small first order term is not a major issue since it can be easily eliminated with an 80-pulse symmetrised supercycle [50, 51].

The second order term of CHASE-40 is present even for ideal Rf pulses $T_{\mathrm{Rf}} \to 0$. Thus we only consider this limit of delta-pulses and ignore all the corrections arising from finite pulses $T_{\mathrm{Rf}} > 0$. Even then, the expression for the second order term of CHASE-40 is rather bulky. There are different types of contributions. In particular there are the so called cross terms which appear only in presence of both the resonance offset of the individual spins ($\Delta\nu_k \neq 0$) and the dipole-dipole interactions between the spins ($\nu_{jk} \neq 0$). These cross terms play an important role for the $I_z = (-3/2, -1/2)$ spin subspace subject to a considerable first order quadrupolar broadening, leading to $\Delta\nu_k$ on the order of tens of kHz. For the homogeneous $I_z = \pm 1/2$ subspace, affected only by the second order quadrupolar shifts, the resonance offsets $\Delta\nu_k$, and hence the cross term in $\mathcal{H}^{(2)}_{\mathrm{CHASE-40}}$, can be made arbitrarily small, for example by increasing the static magnetic field,

which increases the nuclear Larmor frequency ν_{N}. But even in the absence of any resonance offsets $\Delta\nu_k = 0$, there remains a second order Magnus term of the following form

$$\mathcal{H}^{(2)}_{\mathrm{CHASE-40}} = h\frac{T^2_{\mathrm{Cycle}}}{110592}\sum_{i<j}\Big[\big(3\sum_{k\neq i,j}(\nu_{ik}+\nu_{jk})(\nu_{ik}\nu_{jk}+\nu_{ij}\nu_{ik}+\nu_{ij}\nu_{jk})\big)+ \\ +8\nu_{ij}(\Delta\nu_i^2+\Delta\nu_i\Delta\nu_j+\Delta\nu_j^2)\Big](3I_{i,z}I_{j,z}-\mathbf{I}_i\cdot\mathbf{I}_j) \qquad \text{(S15)}$$

This term has a form of an effective dipolar coupling between spins i and j, summed over all unique pairs $i<j$. Such interaction can arise from the direct dipole-dipole interaction of spins i and j in presence of a resonance offset for at least one of the spins from the pair (the $8\nu_{ij}(\Delta\nu_i^2+\Delta\nu_i\Delta\nu_j+\Delta\nu_j^2)$ term). However, the interaction remains even if all $\Delta\nu_k = 0$, but requires dipolar coupling to some third spin k. Such interaction can be interpreted as a three particle effect, where the effective interaction of spins i and j is mediated by all other spins $k \neq i, j$. There are some further second order terms that appear only under non-zero resonance offsets, but these are small and are omitted in Eq. S15.

The $\mathcal{H}^{(2)}_{\mathrm{CHASE-40}}$ term of Eq. S15 dominates the residual toggling-frame Hamiltonian of CHASE-40 in the limit of large T_{Cycle}. It is responsible for the quadratic growth of the decoherence rate T_{M}^{-1} with increasing T_{Cycle} at large $T_{\mathrm{Cycle}} \gtrsim 2$ ms, as observed in Fig. 3e of the main text for the measurement on the CT subspace $I_{\mathrm{z}} = \pm 1/2$. The zero order term $\mathcal{H}^{(0)}_{\mathrm{CHASE-40}}$ (Eq. S14) is negligible at large T_{Cycle} due to the small ratio $T_{\mathrm{Rf}}/T_{\mathrm{Cycle}}$, but becomes dominant in the limit of fast dynamical decoupling (when most of the sequence cycle is taken up by the control pulses, corresponding to $T_{\mathrm{Rf}}/T_{\mathrm{Cycle}} \approx 1/40$). The zero order term $\mathcal{H}^{(0)}$ is responsible for the growth of the decoherence rate T_{M}^{-1} with reducing T_{Cycle} at small $T_{\mathrm{Cycle}} \gtrsim 2$ ms, as observed in Fig. 3e of the main text for the measurement on the CT subspace $I_{\mathrm{z}} = \pm 1/2$. The slowest decoherence (the longest spin memory time T_{M}) is achieved when the contributions of the zero and second order terms are comparable. This observation allows us to estimate the maximum T_{M} that would be achieved if the effect of finite pulses was eliminated [51, 52]. Assuming the second order term would be unaffected, we can extrapolate the measured power-law dependence of T_{M} on T_{Cycle} at large $T_{\mathrm{Cycle}} \gtrsim 2$ ms into the range of small T_{Cycle}. This yields an expected $T_{\mathrm{M}} \approx 1$ s for the shortest possible $T_{\mathrm{Cycle}} = 0.8$ ms of a CHASE-40 cycle at $T_{\mathrm{RF}} = 20$ μs used in this work. This prediction shows that another order of mangitude improvement in the quantum memory storage time might be within reach with the existing material parameters (such as strain) and using only pulse sequence design techniques [51, 52].

Even once the effective Hamiltonian (Eq. S9) is known, finding the spin dynamics is still a

difficult problem. Formally, the relaxation function of the transverse nuclear spin polarization can be written as an infinite power series over time, where the coefficients are the moments of the NMR spectral lineshape (Ch. 6 in [53]). In practice, only the second (M_2) and the fourth (M_4) moments can be calculated [54], making the power series rather inaccurate. It is more practical to approximate the lineshape with a function, such as Gaussian, and use the second moment M_2 as a linewidth parameter. The approximate coherent memory time can then be found as

$$T_{\mathrm{M}} \approx \sqrt{2/M_2}. \tag{S16}$$

For nuclear spin polarization along the x axis of the rotating frame, the second moment can be caclualted as

$$M_2 = -\mathrm{Tr}\left\{[\mathcal{H}_{\mathrm{eff}}, \sum_{k=1}^{N} \hat{I}_{\mathrm{x},k}]^2\right\} / \mathrm{Tr}\left\{\left(\sum_{k=1}^{N} \hat{I}_{\mathrm{x},k}\right)^2\right\} \tag{S17}$$

The second moments can be calculated for an arbitrary orientation of the nuclear spin polarization by substituting the corresponding spin operators (e.g. $\hat{I}_{\mathrm{y},k}$) in Eq. S17.

For practical calculations, Eq. S17 is applied to a system of 3 nuclear spins, assuming the same dipolar coupling ν_{DD} between each spin pair, and the resonance offsets of $0, +\Delta\nu, -\Delta\nu$. The effective Hamiltonians are calculated for free induction decay (FID, no dynamical decoupling), Hahn echo (single π refocusing pulse), and CHASE-40, and are substituted into Eqns. S16, S17 to derive the spin memory times. The values for FID and Hahn echo are equated to the measured T_2 values (the difference between T_2 and T_{M} is negligible if there is at most one refocusing pulse). This allows the coupling parameters ν_{DD} and $\Delta\nu$ to be extracted and then used to calculate the spin memory time T_{M} for the CHASE-40 sequence. The resulting $T_{\mathrm{M}}^{\mathrm{CHASE-40}}$ is shown by the dashed lines as a function of T_{Cycle} in Fig. 3e of the main text and is discussed therein.

Supplementary Note 6. NUMERICAL MODELING OF NUCLEAR SPIN DECOHERENCE AND DYNAMICAL DECOUPLING

We perform exact numerical modeling on an ensemble of N spin-1/2 nuclei coupled through dipole-dipole interactions (Supplementary Eq. S4). The Zeeman effect of the strong static magnetic field is eliminated through rotating frame transformation. This leaves the Zeeman offset Hamiltonian (Supplementary Eq. S3), where $\Delta\nu_k$ is the resonance frequency shift of the k-th nucleus, which includes the inhomogeneous nuclear qaudrupolar effects and chemical shifts.

During the Rf pulses, the time-dependent Hamiltonian is added:

$$\mathcal{H}_{\mathrm{rf,N}} = -h \sum_k \nu_1(t) \left(\cos(\phi) \hat{I}_{\mathrm{x},k} - \sin(\phi) \hat{I}_{\mathrm{y},k} \right), \tag{S18}$$

where the summation goes over all nuclei, $\nu_1(t)$ is the slowly-varying Rf pulse envelope, and ϕ describes the phase of the Rf carrier and the corresponding orientation of the transverse magnetic field in the equatorial plane of the rotating frame. The envelope function has a raised cosine profile $\nu_1(t) \propto (1 - \cos(2\pi(t - t_0)/T_{\mathrm{Rf}}))/2$, where t_0 is the starting time of the Rf pulse burst.

Most of the numerical modeling is carried out for a system of $N = 12$ ^{75}As nuclear spins. The $\{x, y, z\}$ coordinates of the nuclei in units of nm are as follows:

$$\begin{aligned}
&\{0., 0., 0.\},\\
&\{0.282393, 0.282393, 0.\},\\
&\{0.282393, 0., 0.282393\},\\
&\{0.282393, -0.282393, 0.\},\\
&\{0.282393, 0., -0.282393\},\\
&\{0., 0.282393, 0.282393\},\\
&\{-0.282393, 0.282393, 0.\},\\
&\{0., 0.282393, -0.282393\},\\
&\{-0.282393, 0., 0.282393\},\\
&\{0., -0.282393, 0.282393\},\\
&\{-0.282393, -0.282393, 0.\},\\
&\{-0.282393, 0., -0.282393\}.
\end{aligned} \tag{S19}$$

The unitary evolution of the system is simulated through numerical propagation of the Schrödinger equation from an initial wave function state ψ_{Init}. The computation is carried out using the software package Wolfram Mathematica 13.2 and the Python QuTiP 4.7.3 package [55]. We chose ψ_{Init} as eigenstates of the time-independent Hamiltonian, which is a sum of Supplementary Eq. S4 and Supplementary Eq. S3. We typically use 16 different initial states, spanning the whole range of the total spin z projections from $-N/2$ to $+N/2$. The same initial states are used through when sweeping the parameters of the Rf pulse sequence. Once the spin evolution is calculated for a particular Rf pulse sequence, we use the final wavefunction ψ_{Fin} to calculate the final nuclear spin polarization $I_{\mathrm{z,Fin}} = \langle \psi_{\mathrm{Fin}} | \sum_{k=1}^{N} \hat{I}_{\mathrm{z},k} | \psi_{\mathrm{Fin}} \rangle$. Each final polarization value is normalized by the sign

of the initial polarization $I_{\mathrm{z,Init}}$, and these normalized values are then averaged over all the initial states ψ_{Init}. Such averaging over multiple initial states helps to eliminate the oscillations that arise due to the small number of spins N in the model. This averaging also mimics the experimental conditions, where the initial optically-induced nuclear polarization is subject to fluctuations due to fluctuations and drifts of various experimental parameters (e.g. optical pump power).

When modeling the nuclear spin dynamics of the homogeneous $I_{\mathrm{z}} = \pm 1/2$ subspace we set all resonance offsets to be zero $\Delta\nu_k = 0$. For the $I_{\mathrm{z}} = (-3/2, -1/2)$ satellite transition subspace we model the resonance offset of each nuclear spin k as $\Delta\nu_k = \Delta\nu_0(k-1) + \mathrm{N}(0, 0.2\Delta\nu_0/(2\sqrt{2\ln 2}))$, where $\mathrm{N}(\mu, \sigma)$ stands for a normal distribution with the mean μ and standard deviation σ. This model ensures that the resonance frequency of each nucleus is detuned from the nearest frequency of another nucleus by $\Delta\nu_0$, on average. Each resonance shift is randomly varied (by a $\approx 20\%$ fraction of $\Delta\nu_0$) to avoid periodic recurrences and oscillations. Once the set of randomized $\Delta\nu_k$ is generated, it is fixed and used throughout the different modeling runs. We have used three sets with $\Delta\nu_0 = 0.8$ kHz, $\Delta\nu_0 = 1.2$ kHz, and $\Delta\nu_0 = 1.6$ kHz. The calculated final nuclear spin polarizations $I_{\mathrm{z,Fin}}$ are averaged over these three sets, once again to combat the oscillations that arise from the small number of spins N in the model.

The numerical modeling closely follows the experiments: the total free evolution time T_{FreeEvol} and the number of cycles n_{Cycles} of the dynamical decoupling sequence are varied, to calculate the final nuclear spin polarization $I_{\mathrm{z,Fin}}$, averaged over initial states and resonance offsets as described above. The dependencies on T_{FreeEvol} yield decay curves that are similar to the experimental curves shown in Fig. 2c of the main text. Alternatively, the same data can be plotted as a function of the total evolution time T_{EvolTot} and the decoupling sequence period T_{Cycle}, such as shown in Figs. 3c, d of the main text. The numerically modeled values of the final nuclear polarization $I_{\mathrm{z,Fin}}$ shown in Figs. 3c, d of the main text are normalized by the initial nuclear polarization $I_{\mathrm{z,Init}}$ averaged over all the initial states. This way, the normalized values are limited to the $[-1, +1]$ range, with $+1$ corresponding to no decay of the nuclear spin polarization (i.e. complete preservation through dynamical decoupling). The values close to 0 can be interpreted as complete decoherence, whereas the negative values of the normalized nuclear spin echo amplitude are a sign of recurrences in the dynamics of a small nuclear spin ensemble. The corresponding experimental data, shown in Figs. 3a, b of the main text, is also normalized, but using the amplitude of the simple Hahn echo decoupling measured at short T_{FreeEvol}, which approximates the initial nuclear spin polarization

with good accuracy.

---

[1] Millington-Hotze, P., Manna, S., Covre da Silva, S. F., Rastelli, A. & Chekhovich, E. A. Nuclear spin diffusion in the central spin system of a GaAs/AlGaAs quantum dot. *Nat. Commun.* **14**, 2677 (2023).

[2] Zaporski, L. *et al.* Ideal refocusing of an optically active spin qubit under strong hyperfine interactions. *Nat. Nanotechnol.* **18**, 257–263 (2023).

[3] Millington-Hotze, P. *et al.* Approaching a fully-polarized state of nuclear spins in a solid. *Nat. Commun.* **15**, 985 (2024).

[4] Dyte, H. E. *et al.* Is wave function collapse necessary? explaining quantum nondemolition measurement of a spin qubit within linear evolution. *Phys. Rev. Lett.* **132**, 160804 (2024).

[5] Oshiyama, A. & Ohnishi, S. DX center: Crossover of deep and shallow states in Si-$Al_xGa_{1-x}As$. *Phys. Rev. B* **33**, 4320–4323 (1986).

[6] Mooney, P. M. Deep donor levels (DX centers) in III-V semiconductors. *J. Appl. Phys.* **67**, R1–R26 (1990).

[7] Zhai, L. *et al.* Low-noise GaAs quantum dots for quantum photonics. *Nat. Commun.* **11**, 4745 (2020).

[8] Heyn, C. *et al.* Highly uniform and strain-free GaAs quantum dots fabricated by filling of self-assembled nanoholes. *Appl. Phys. Lett.* **94**, 183113 (2009).

[9] Atkinson, P., Zallo, E. & Schmidt, O. G. Independent wavelength and density control of uniform GaAs/AlGaAs quantum dots grown by infilling self-assembled nanoholes. *J. Appl. Phys.* **112**, 4745 (2012).

[10] Huo, Y. H., Rastelli, A. & Schmidt, O. G. Ultra-small excitonic fine structure splitting in highly symmetric quantum dots on GaAs (001) substrate. *Appl. Phys. Lett.* **102**, 152105 (2013).

[11] Ulhaq, A. *et al.* Vanishing electron g factor and long-lived nuclear spin polarization in weakly strained nanohole-filled GaAs/AlGaAs quantum dots. *Phys. Rev. B* **93**, 165306 (2016).

[12] Gammon, D. *et al.* Electron and nuclear spin interactions in the optical spectra of single GaAs quantum dots. *Phys. Rev. Lett.* **86**, 5176–5179 (2001).

[13] Eble, B. *et al.* Dynamic nuclear polarization of a single charge-tunable InAs/GaAs quantum dot. *Phys. Rev. B* **74**, 081306 (2006).

[14] Skiba-Szymanska, J. *et al.* Overhauser effect in individual InP/$Ga_xIn_{1-x}P$ dots. *Phys. Rev. B* **77**, 165338 (2008).

[15] Ragunathan, G. *et al.* Direct measurement of hyperfine shifts and radio frequency manipulation of nuclear spins in individual CdTe/ZnTe quantum dots. *Phys. Rev. Lett.* **122**, 096801 (2019).

[16] Urbaszek, B. *et al.* Nuclear spin physics in quantum dots: An optical investigation. *Rev. Mod. Phys.* **85**, 79–133 (2013).

[17] Chekhovich, E., Hopkinson, M., Skolnick, M. & Tartakovskii, A. Suppression of nuclear spin bath

fluctuations in self-assembled quantum dots induced by inhomogeneous strain. *Nat. Commun.* **6**, 6348 (2015).

[18] Braun, P.-F. *et al.* Bistability of the nuclear polarization created through optical pumping in $In_{1-x}Ga_xAs$ quantum dots. *Phys. Rev. B* **74**, 245306 (2006).

[19] Li, D. *et al.* Intrinsic origin of spin echoes in dipolar solids generated by strong π pulses. *Phys. Rev. B* **77**, 214306 (2008).

[20] Waeber, A. M. *et al.* Pulse control protocols for preserving coherence in dipolar-coupled nuclear spin baths. *Nat. Commun.* **10**, 3157 (2019).

[21] Chekhovich, E. A. *et al.* Structural analysis of strained quantum dots using nuclear magnetic resonance. *Nat. Nanotechnol.* **7**, 646–650 (2012).

[22] Zhao, R. *et al.* Long-lived quantum memory. *Nat. Phys.* **5**, 100–104 (2009).

[23] Tittel, W. *et al.* Photon-echo quantum memory in solid state systems. *Laser Photonics Rev.* **4**, 244–267 (2010).

[24] Azuma, K. *et al.* Quantum repeaters: From quantum networks to the quantum internet. *Rev. Mod. Phys.* **95**, 045006 (2023).

[25] Ren, J.-G. *et al.* Ground-to-satellite quantum teleportation. *Nature* **549**, 70–73 (2017).

[26] Briegel, H.-J., Dür, W., Cirac, J. I. & Zoller, P. Quantum repeaters: The role of imperfect local operations in quantum communication. *Phys. Rev. Lett.* **81**, 5932–5935 (1998).

[27] Duan, L.-M., Lukin, M. D., Cirac, J. I. & Zoller, P. Long-distance quantum communication with atomic ensembles and linear optics. *Nature* **414**, 413–418 (2001).

[28] Collins, O. A., Jenkins, S. D., Kuzmich, A. & Kennedy, T. A. B. Multiplexed memory-insensitive quantum repeaters. *Phys. Rev. Lett.* **98**, 060502 (2007).

[29] Jiang, L., Taylor, J. M. & Lukin, M. D. Fast and robust approach to long-distance quantum communication with atomic ensembles. *Phys. Rev. A* **76**, 012301 (2007).

[30] Sharman, K., Kimiaee Asadi, F., Wein, S. C. & Simon, C. Quantum repeaters based on individual electron spins and nuclear-spin-ensemble memories in quantum dots. *Quantum* **5**, 570 (2021).

[31] Langenfeld, S., Thomas, P., Morin, O. & Rempe, G. Quantum repeater node demonstrating unconditionally secure key distribution. *Phys. Rev. Lett.* **126**, 230506 (2021).

[32] De Greve, K. *et al.* Quantum-dot spin–photon entanglement via frequency downconversion to telecom wavelength. *Nature* **491**, 421–425 (2012).

[33] Coste, N. *et al.* High-rate entanglement between a semiconductor spin and indistinguishable photons. *Nat. Photon.* **17**, 582–587 (2023).

[34] Laccotripes, P. *et al.* Spin-photon entanglement with direct photon emission in the telecom C-band. *Nat. Commun.* **15**, 9740 (2024).

[35] Gangloff, D. A. *et al.* Quantum interface of an electron and a nuclear ensemble. *Science* **364**, 62–66 (2019).

[36] Appel, M. H. *et al.* A many-body quantum register for a spin qubit. *Nat. Phys.* (2025).

[37] Stockill, R. *et al.* Phase-tuned entangled state generation between distant spin qubits. *Phys. Rev. Lett.* **119**, 010503 (2017).

[38] Atatüre, M. *et al.* Quantum-dot spin-state preparation with near-unity fidelity. *Science* **312**, 551–553 (2006).

[39] Yu, Y. *et al.* Entanglement of two quantum memories via fibres over dozens of kilometres. *Nature* **578**, 240–245 (2020).

[40] Wang, Y. *et al.* Single-qubit quantum memory exceeding ten-minute coherence time. *Nat. Photon.* **11**, 646–650 (2017).

[41] Wang, P. *et al.* Single ion qubit with estimated coherence time exceeding one hour. *Nat. Commun.* **12**, 233 (2021).

[42] Atatüre, M., Englund, D., Vamivakas, N., Lee, S.-Y. & Wrachtrup, J. Material platforms for spin-based photonic quantum technologies. *Nat. Rev. Mater.* **3**, 38–51 (2018).

[43] Neuwirth, J. *et al.* Quantum dot technology for quantum repeaters: from entangled photon generation toward the integration with quantum memories. *Mater. Quantum Technol.* **1**, 043001 (2021).

[44] Huber, D. *et al.* Highly indistinguishable and strongly entangled photons from symmetric GaAs quantum dots. *Nat. Commun.* **8**, 15506 (2017).

[45] Schweickert, L. *et al.* On-demand generation of background-free single photons from a solid-state source. *Appl. Phys. Lett.* **112**, 093106 (2018).

[46] Arakawa, Y. & Holmes, M. J. Progress in quantum-dot single photon sources for quantum information technologies: A broad spectrum overview. *Appl. Phys. Rev.* **7**, 021309 (2020).

[47] Liu, J. *et al.* A solid-state source of strongly entangled photon pairs with high brightness and indistinguishability. *Nat. Nanotechnol.* **14**, 586–593 (2019).

[48] Rota, M. B. *et al.* A source of entangled photons based on a cavity-enhanced and strain-tuned GaAs quantum dot. *eLight* **4**, 13 (2024).

[49] Slichter, C. P. *Principles of Magnetic Resonance* (Springer, 1990).

[50] Mehring, M. *Principles of High Resolution NMR in Solids* (Springer Berlin Heidelberg, 1983).

[51] Burum, D. P. & Rhim, W. K. Analysis of multiple pulse NMR in solids. III. *J. Chem. Phys.* **71**, 944–956 (1979).

[52] Haeberlen, U. & Waugh, J. S. Coherent averaging effects in magnetic resonance. *Phys. Rev.* **175**, 453–467 (1968).

[53] Cowan, B. *Nuclear Magnetic Resonance and Relaxation* (Cambridge University Press, 1997).

[54] Van Vleck, J. H. The dipolar broadening of magnetic resonance lines in crystals. *Phys. Rev.* **74**, 1168–1183 (1948).

[55] Johansson, J., Nation, P. & Nori, F. Qutip 2: A Python framework for the dynamics of open quantum systems. *Comput. Phys. Commun.* **184**, 1234–1240 (2013).

Chapter 8

Conclusions

As we discussed in Chapter 1, QDs display many of the desired properties for a usable spin qubit. While interactions with the nuclear spin bath are problematic for a working QD electron spin qubit, the studies in this thesis build on previous works demonstrating the potential of nuclear spins as an additional resource for quantum computing and communication [70]. This work is enabled by the samples used. The combination of the low internal strain found in GaAs/AlGaAs QDs and externally applied uniaxial strain, create an ideal nuclear spin system where the NMR transitions are narrow, minimising dephasing effects, while also spectrally separate enough to allow each transition to be resolvable by RF control pulses. We identify that further strain engineering, as well as alterations to the dot structure may lead to improvements in the state longevity for both the nuclear spins and electron spin leading to a new generation of devices composed of optically active electron spin qubits with a combined nuclear spin memory within the same QD. We now summarise the key findings of this thesis.

In Chapter 4 inverse NMR techniques are used to measure the nuclear spin transitions over a range of external magnetic fields. From these spectra we observe a clear increase in the first order quadrupolar splitting caused by the externally applied strain, with measured $\nu_Q^{(1),^{75}\mathrm{As}} \approx 255.6$ kHz and $\nu_Q^{(1),^{69}\mathrm{Ga}} \approx 124.8$ kHz which is an $\approx$ 10 times increase over values measured in unstrained samples. From these measurements we estimate the peak biaxial strain $\varepsilon_b \approx 0.2789\%$. We measure the value of S_{44}/S_{11} for GaAs by analysing the second order quadrupolar shift. The obtained value $S_{44}/S_{11} \approx 2.053 \pm 0.014$ matches well with previous measurements [181, 186]. We also identify issues with the generation of sufficient DNP at small B_z due to the increase in the quadrupolar field strength caused by the applied strain. This issue can potentially be resolved in future works by using biaxial rather than uniaxial strain.

In Chapter 5 we demonstrate that the large quadrupolar splitting between the NMR transitions due to the externally applied uniaxial stress allows the NMR STs to remain resolvable in the

presence of the Knight field produced by a confined electron. Due to the sensitivity of the NMR frequencies to the projection of the electron spin via the hyperfine interaction, we implement electron spin readout through detuned RF pulses applied to the nuclei. We are able to perform repeated readouts of the electron spin z projection, demonstrating the QND nature of the measurement while the measurement can also be performed single-shot. By accumulating readout statistics we measure a readout fidelity of $F \approx 99.85\%$ which is comparable to other state of the art readout techniques [192–196]. Simulations are used to confirm the small back action exerted on the electron by the nuclei and to rule out the nuclei as a cause of electron spin flips, which are instead attributed to phonons [87]. Finally the QND nature of the measurement, which is a criteria for a working qubit [12], also poses questions about the nature of quantum measurements. The lack of necessity for a wavefunction collapse to describe the experiment may provide evidence for certain interpretations of quantum mechanics, such as Quantum Darwinism [197, 198].

Next in Chapter 6, we implement the above electron spin readout protocol to measure the electron spin lifetime. We probe the Knight field of the $1e$ and the $3e$ states, observing that the Knight shifted NMR transitions are narrower for the $3e$ state, which could be a route to improved electron spin coherence [209]. Probing the lifetimes we observe that relaxation for the $1e$ state is dominated by phonon-assisted processes while the $3e$ states relaxation is dominated by cotunnelling for the measured external field range $B_z \approx 1-8$ T. We obtain a maximum $T_{1,e} \approx 50$ ms for the $1e$ state at $B_z \approx 0.982$ T, though further improvements at lower B_z is likely to be limited by cotunnelling. Additionally, improvements to $T_{1,e}$ could be achieved by increasing the tunnelling barrier thickness to suppress cotunnelling [87], while $T_{1,e}$ for the $3e$ state could be improved by increasing the QD lateral size or reducing the temperature. Finally nuclear spin relaxation measurements are used to provide insight on the QDs charge state and multi-electron spin dynamics, further demonstrating the versatility of the nuclei as a measurement probe.

Finally in Chapter 7 we return to studying the nuclear spins. We implement a new 40 pulse CHASE [150] sequence to dynamically decouple the nuclear spins from quadrupolar and dipole interaction decoherence effects. The applied strain isolates the $-1/2 \leftrightarrow +1/2$ subspace, which due to the low internal strain has a narrow linewidth making it an ideal system for the storage of coherence. Therefore the CHASE sequence is able to effectively suppress decoherence, allowing the coherence time to be extended to over 100 ms. The design of the CHASE sequence also ensures spin locking effects are not observed. Further improvements in the coherence time are limited by three spin nuclear dipole interactions and coherence leakage due to unwanted driving of the STs. Through further strain engineering quadrupolar splitting values of $\nu_Q^{(1)} \approx 1$ MHz should be achievable yielding further improvements in $T_{2,N}$ due to reduced spectral overlap between the applied RF pulses and the STs. Long storage times, combined with the superb optical properties of QDs [32, 33], and recent demonstrations of transmission and retrieval of information between

an electron and the nuclei in a QD [136], makes these nuclear spin systems an attractive quantum memory for quantum communication devices.

A direction for potential future work will be to study the effectiveness of CHASE sequences in the presence of confined electrons as this has been found previously to seriously limit the improvement in coherence (for InGaAs QDs) [131]. However, with these strain engineered low internal strain GaAs samples we have demonstrated that certain NMR transitions remain resolvable even when an electron is present (Chapter 6); meaning that CHASE may still be effective in these scenarios. Additionally further increasing the strain, as discussed in Chapter 7, to achieve $\nu_Q^{(1)} \approx 1$ MHz would allow all of the NMR transitions to remain resolvable in a charged QD, which may allow for further improvements in $T_{2,N}$. An alternative direction of study would be to investigate biaxially strained samples. As the first order quadrupolar splitting is directly dependent on ε_b it should be possible to increase the splitting using lower values of strain. Therefore using biaxial strain may alleviate some of the issues discussed in this thesis for uniaxially strained samples. Finally, the recent demonstration of nuclear spin polarisations approaching 100 % is a major improvement in nuclear spin initialisation fidelity [148], this may allow for further improvements in the nuclear coherence times if these techniques were combined with the CHASE sequences implemented in Chapter 7.

Bibliography

[1] M. Born and P. Jordan. “Zur Quantenmechanik”. *Z. Phys.* 34 (1925), 858–888. DOI: 10.1007/BF01328531.

[2] P. Benioff. “The computer as a physical system: A microscopic quantum mechanical Hamiltonian model of computers as represented by Turing machines”. *J. Stat. Phys.* 22 (1980), 563–591. DOI: 10.1007/BF01011339.

[3] R. P. Feynman. “Simulating Physics with Computers”. *Int. J. Theor. Phys.* 21 (1982), 467–488. DOI: 10.1007/BF02650179.

[4] P. Benioff. “Quantum mechanical hamiltonian models of turing machines”. *J. Stat. Phys.* 29 (1982), 515–546. DOI: https://doi.org/10.1007/BF01342185.

[5] D. Deutsch and R. Penrose. “Quantum theory, the Church–Turing principle and the universal quantum computer”. *Proc. R. Soc. Lond. A: Mathematical and Physical Sciences* 400 (1985), 97–117. DOI: 10.1098/rspa.1985.0070.

[6] R. P. Feynman. “Quantum mechanical computers”. *Found. Phys.* 16 (1986), 507–531. DOI: 10.1007/BF01886518.

[7] D. Deutsch and R. Jozsa. “Rapid solution of problems by quantum computation”. *Proc. R. Soc. Lond. A: Mathematical and Physical Sciences* 439 (1992), 553–558. DOI: 10.1098/rspa.1992.0167.

[8] L. K. Grover. “A fast quantum mechanical algorithm for database search”. STOC ’96 (1996), 212–219. DOI: 10.1145/237814.237866.

[9] P. W. Shor. “Polynomial-Time Algorithms for Prime Factorization and Discrete Logarithms on a Quantum Computer”. *SIAM J. Computing* 26 (1997), 1484–1509. DOI: 10.1137/S0097539795293172.

[10] F. Arute et al. “Quantum supremacy using a programmable superconducting processor”. *Nature* 574 (2019), 505–510. DOI: 10.1038/s41586-019-1666-5.

[11] D. P. DiVincenzo. “The Physical Implementation of Quantum Computation”. *Fortschr. Phys.* 48 (2000), 771–783. DOI: https://doi.org/10.1002/1521-3978(200009)48:9/11<771::AID-PROP771>3.0.CO;2-E.

[12] T. D. Ladd et al. “Quantum computers.” *Nature* 464 (2010), 45–53. DOI: https://doi.org/10.1038/nature08812.

[13] J. I. Cirac and P. Zoller. “Quantum Computations with Cold Trapped Ions”. *Phys. Rev. Lett.* 74 (1995), 4091–4094. DOI: 10.1103/PhysRevLett.74.4091.

[14] R. Blatt and D. Wineland. “Entangled states of trapped atomic ions”. *Nature* 453 (2008), 1008–1015. DOI: 10.1038/nature07125.

[15] C. D. Bruzewicz et al. “Trapped-ion quantum computing: Progress and challenges”. *Appl. Phys. Reviews* 6 (2019), 021314. DOI: 10.1063/1.5088164.

[16] C. Monroe et al. “Demonstration of a Fundamental Quantum Logic Gate”. *Phys. Rev. Lett.* 75 (1995), 4714–4717. DOI: 10.1103/PhysRevLett.75.4714.

[17] M. H. devoret and J. M. Martinis. “Implementing Qubits with Superconducting Integrated Circuits”. *Quantum Information Processing* 3 (2004), 163–203. DOI: 10.1007/s11128-004-3101-5.

[18] J. Koch et al. “Charge-insensitive qubit design derived from the Cooper pair box”. *Phys. Rev. A* 76 (2007), 042319. DOI: 10.1103/PhysRevA.76.042319.

[19] P. Krantz et al. “A quantum engineer’s guide to superconducting qubits”. *Appl. Phys. Rev.* 6 (2019), 021318. DOI: 10.1063/1.5089550.

[20] M. Kjaergaard et al. “Superconducting Qubits: Current State of Play”. *Annu. Rev. Condens. Matter Phys* 11 (2020), 369–395. DOI: https://doi.org/10.1146/annurev-conmatphys-031119-050605.

[21] B. E. Kane. “A silicon-based nuclear spin quantum computer”. *Nature* 393 (1998), 133–137. DOI: 10.1038/30156.

[22] R. Vrijen et al. “Electron-spin-resonance transistors for quantum computing in silicon-germanium heterostructures”. *Phys. Rev. A* 62 (2000), 012306. DOI: 10.1103/PhysRevA.62.012306.

[23] J. C. McCallum, B. C. Johnson, and T. Botzem. “Donor-based qubits for quantum computing in silicon”. *Appl. Phys. Rev.* 8 (2021), 031314. DOI: 10.1063/5.0060957.

[24] S. Pezzagna and J. Meijer. “Quantum computer based on color centers in diamond”. *Appl. Phys. Reviews* 8 (2021), 011308. DOI: 10.1063/5.0007444.

[25] J. Wrachtrup, S. Ya. Kilin, and A. P. Nizovtsev. "Quantum computation using the ^{13}C nuclear spins near the single NV defect center in diamond". *Opt. Spectrosc.* 91 (2001), 429–437. DOI: 10.1134/1.1405224.

[26] D. Loss and D. P. DiVincenzo. "Quantum computation with quantum dots". *Phys. Rev. A* 57 (1998), 120–126. DOI: 10.1103/PhysRevA.57.120.

[27] R. Hanson et al. "Spins in few-electron quantum dots". *Rev. Mod. Phys.* 79 (2007), 1217–1265. DOI: 10.1103/RevModPhys.79.1217.

[28] G. Burkard et al. "Semiconductor spin qubits". *Rev. Mod. Phys.* 95 (2023), 025003. DOI: 10.1103/RevModPhys.95.025003.

[29] S. Wehner, D. Elkouss, and R. Hanson. "Quantum internet: A vision for the road ahead". *Science* 362 (2018), eaam9288. DOI: 10.1126/science.aam9288.

[30] M. Atatüre et al. "Quantum-Dot Spin-State Preparation with Near-Unity Fidelity". *Science* 312 (2006), 551–553. DOI: 10.1126/science.1126074.

[31] M. Kroner et al. "Optical Detection of Single-Electron Spin Resonance in a Quantum Dot". *Phys. Rev. Lett.* 100 (2008), 156803. DOI: 10.1103/PhysRevLett.100.156803.

[32] J. Neuwirth et al. "Quantum dot technology for quantum repeaters: from entangled photon generation toward the integration with quantum memories". *Mater. Quantum Technol.* 1 (2021), 043001. DOI: 10.1088/2633-4356/ac3d14.

[33] J. Liu et al. "A solid-state source of strongly entangled photon pairs with high brightness and indistinguishability". *Nat. Nanotechnol.* 14 (2019), 586–593. DOI: 10.1038/s41565-019-0435-9.

[34] R. Stockill et al. "Phase-Tuned Entangled State Generation between Distant Spin Qubits". *Phys. Rev. Lett.* 119 (2017), 010503. DOI: 10.1103/PhysRevLett.119.010503.

[35] A. L. Efros and L. E. Brus. "Nanocrystal Quantum Dots: From Discovery to Modern Development". *ACS Nano* 15 (2021), 6192–6210. DOI: 10.1021/acsnano.1c01399.

[36] L. Esaki and R. Tsu. "Superlattice and Negative Differential Conductivity in Semiconductors". *IBM J. Res. Dev.* 14 (1970), 61–65. DOI: 10.1147/rd.141.0061.

[37] R. Dingle, W. Wiegmann, and C. H. Henry. "Quantum States of Confined Carriers in Very Thin $Al_xGa_{1-x}As$-GaAs-$Al_xGa_{1-x}As$ Heterostructures". *Phys. Rev. Lett.* 33 (1974), 827–830. DOI: 10.1103/PhysRevLett.33.827.

[38] A.I. Ekimov and A.A. Onushchenko. "Quantum size effect in three-dimensional microscopic emiconductor crystals". *Sov. J. of Experimental and Theoretical Phys. Lett.* 34 (1981), 363.

[39] R. Rossetti, S. Nakahara, and L. E. Brus. “Quantum size effects in the redox potentials, resonance Raman spectra, and electronic spectra of CdS crystallites in aqueous solution”. *J. Chem. Phys.* 79 (1983), 1086–1088. DOI: 10.1063/1.445834.

[40] A.I. Ekimov and A.A. Onushchenko. “Size quantization of the electron energy spectrum in a microscopic semiconductor crystal”. *Jetp. Lett.* 118 (2023), S12–S14. DOI: https://doi.org/10.1134/S0021364023130027.

[41] R. Rossetti et al. “Excited electronic states and optical spectra of ZnS and CdS crystallites in the ≈15 to 50 Å size range: Evolution from molecular to bulk semiconducting properties”. *J. Chem. Phys.* 82 (1985), 552–559. DOI: 10.1063/1.448727.

[42] C. B. Murray, D. J. Norris, and M. G. Bawendi. “Synthesis and characterization of nearly monodisperse CdE (E = sulfur, selenium, tellurium) semiconductor nanocrystallites”. *J. Am. Chem. Soc* 115.19 (1993), 8706–8715. DOI: 10.1021/ja00072a025.

[43] M. A. Cotta. “Quantum Dots and Their Applications: What Lies Ahead?” *ACS Appl. Nano Mater.* 3.6 (2020), 4920–4924. DOI: 10.1021/acsanm.0c01386.

[44] M. Grundmann. *The Physics of Semiconductors an Introduction Including Devices and Nanophysics*. Springer, 2010.

[45] F. C. Frank, J. H. van der Merwe, and N. F. Mott. “One-dimensional dislocations. I. Static theory”. *Proc. R. Soc. Lond. A. Mathematical and Physical Sciences* 198 (1949), 205–216. DOI: 10.1098/rspa.1949.0095.

[46] M. Volmer and A. Weber. “Keimbildung in übersättigten Gebilden”. *Z. Phys. Chem* 119U (1926), 277–301. DOI: doi:10.1515/zpch-1926-11927.

[47] I. N. Stranski and L. Krastanow. “Zur Theorie der Orientierten Ausscheidung von Ionenkristallen Aufeinander”. *Monatsh. Chem* 71 (1937), 351–364. DOI: 10.1007/bf01798103.

[48] O. Gywat, J. Berezovsky, and H. J. Krenner. *Spins in Optically Active Quantum Dots Concepts and Methods*. Wiley-VCH Verlag, 2009.

[49] Ch. Heyn et al. “Highly uniform and strain-free GaAs quantum dots fabricated by filling of self-assembled nanoholes”. *Appl. Phys. Lett.* 94 (2009), 183113. DOI: 10.1063/1.3133338.

[50] Zh. M. Wang et al. “Nanoholes fabricated by self-assembled gallium nanodrill on GaAs(100)”. *Appl. Phys. Lett.* 90 (2007), 113120. DOI: 10.1063/1.2713745.

[51] Ch. Heyn, A. Stemmann, and W. Hansen. “Nanohole formation on AlGaAs surfaces by local droplet etching with gallium”. *J. Cryst. Growth* 311 (2009), 1839–1842. DOI: https://doi.org/10.1016/j.jcrysgro.2008.11.001.

[52] A. Stemmann et al. “Local droplet etching of nanoholes and rings on GaAs and AlGaAs surfaces”. *Appl. Phys. Lett.* 93 (2008), 123108. DOI: 10.1063/1.2981517.

[53] P. Atkinson, E. Zallo, and O. G. Schmidt. “Independent wavelength and density control of uniform GaAs/AlGaAs quantum dots grown by infilling self-assembled nanoholes”. *J. Appl. Phys.* 112 (2012), 054303. DOI: 10.1063/1.4748183.

[54] M. Gurioli et al. “Droplet epitaxy of semiconductor nanostructures for quantum photonic devices”. *Nat. Mater.* 18 (2019), 799–810. DOI: 10.1038/s41563-019-0355-y.

[55] R. J. Warburton et al. “Optical emission from a charge-tunable quantum ring”. *Nature* 405 (2000), 926–929. DOI: 10.1038/35016030.

[56] F. Langer et al. “Single photon emission of a charge-tunable GaAs/Al0.25Ga0.75As droplet quantum dot device”. *Appl. Phys. Lett.* 105 (2014), 081111. DOI: 10.1063/1.4894372.

[57] L. Bouet et al. “Charge tuning in [111] grown GaAs droplet quantum dots”. *Appl. Phys. Lett.* 105 (2014), 082111. DOI: 10.1063/1.4894174.

[58] H. G. Babin et al. “Charge Tunable GaAs Quantum Dots in a Photonic n-i-p Diode”. *Nanomaterials* 11 (2021), 2703. DOI: 10.3390/nano11102703.

[59] C. Schneider et al. “Single site-controlled In(Ga)As/GaAs quantum dots: growth, properties and device integration”. *NanoTechnol.* 20 (2009), 434012. DOI: 10.1088/0957-4484/20/43/434012.

[60] V. Zolatanosha and D. Reuter. “Site-controlled droplet epitaxy of GaAs quantum dots by deposition through shadow masks”. *J. Vac. Sci. Technol.* 36 (2018), 02D105. DOI: 10.1116/1.5013650.

[61] F. Bloch. “On the quantum mechanics of electrons in crystal lattices”. *Z. Phys.* 52 (1929), 555–600. DOI: 10.1007/bf01339455.

[62] J. S. Blakemore. “Semiconducting and other major properties of gallium arsenide”. *J. Appl. Phys.* 53 (1982), R123–R181. DOI: 10.1063/1.331665.

[63] P. Harrison. *Quantum Wells, Wires and Dots: Theoretical and Computational Physics of Semiconductor Nanostructures*. John Wiley & Sons, 2005.

[64] R. J. Elliott. “Intensity of Optical Absorption by Excitons”. *Phys. Rev.* 108 (1957), 1384–1389. DOI: 10.1103/PhysRev.108.1384.

[65] S. A. Lourenço et al. “Temperature dependence of optical transitions in AlGaAs”. *J. Appl. Phys.* 89 (2001), 6159–6164. DOI: 10.1063/1.1367875.

[66] M. B. Panish and Jr. Casey H. C. “Temperature Dependence of the Energy Gap in GaAs and GaP”. *J. Appl. Phys.* 40 (1969), 163–167. DOI: 10.1063/1.1657024.

[67] J. L. Shay. “Temperature Dependence of the Energy Gap in GaAs”. *Phys. Rev. B* 4 (1971), 1385–1386. DOI: 10.1103/PhysRevB.4.1385.

[68] S. L. Chuang. *Physics of optoelectronic devices*. John Wiley & Sons, 1995.

[69] Y. Sun, S. E. Thompson, and T. Nishida. “Physics of strain effects in semiconductors and metal-oxide-semiconductor field-effect transistors”. *J. Appl. Phys.* 101 (2007), 104503. DOI: 10.1063/1.2730561.

[70] E. A. Chekhovich, S. F. Covre da Silva, and A. Rastelli. “Nuclear spin quantum register in an optically active semiconductor quantum dot”. *Nat. Nanotechnol.* 15 (2020), 999–1004. DOI: 10.1038/s41565-020-0769-3.

[71] E. A. Chekhovich et al. “Structural analysis of strained quantum dots using nuclear magnetic resonance”. *Nat. Nanotechnol.* 7 (2012), 646–650. DOI: 10.1038/nnano.2012.142.

[72] M. Yamagiwa et al. “Confined electronic structure in GaAs quantum dots”. *J. Lumin.* 108 (2004), 379–383. DOI: https://doi.org/10.1016/j.jlumin.2004.01.080.

[73] Hao Lee, Weidong Yang, and Peter C. Sercel. “Temperature and excitation dependence of photoluminescence line shapein InAs/GaAs quantum-dot structures”. *Phys. Rev. B* 55 (1997), 9757–9762. DOI: 10.1103/PhysRevB.55.9757.

[74] L. Brusaferri et al. “Thermally activated carrier transfer and luminescence line shape in self-organized InAs quantum dots”. *Appl. Phys. Lett.* 69 (1996), 3354–3356. DOI: 10.1063/1.117304.

[75] B. Urbaszek et al. “Temperature-dependent linewidth of charged excitons in semiconductor quantum dots: Strongly broadened ground state transitions due to acoustic phonon scattering”. *Phys. Rev. B* 69 (2004), 035304. DOI: 10.1103/PhysRevB.69.035304.

[76] M. C. Löbl et al. “Excitons in InGaAs quantum dots without electron wetting layer states”. *Commun. Phys.* 2 (2019), 93. DOI: 10.1038/s42005-019-0194-9.

[77] S. Das and S. Dhar. “Exciton binding energy in GaAsBiN spherical quantum dot heterostructures”. *Superlattices and Microstructures* 103 (2017), 145–150. DOI: https://doi.org/10.1016/j.spmi.2017.01.030.

[78] K. L. Jahan et al. “Magnetic field effect on the energy levels of an exciton in a GaAs quantum dot: Application for excitonic lasers”. *Sci. Rep.* 8 (2018), 5073. DOI: 10.1038/s41598-018-23348-9.

[79] R. J. Warburton et al. “Coulomb interactions in small charge-tunable quantum dots: A simple model”. *Phys. Rev. B* 58 (1998), 16221–16231. DOI: 10.1103/PhysRevB.58.16221.

[80] A. V. Kuhlmann et al. “A dark-field microscope for background-free detection of resonance fluorescence from single semiconductor quantum dots operating in a set-and-forget mode”. *Rev. Sci. Instrum.* 84 (2013), 073905. DOI: 10.1063/1.4813879.

[81] A. Kiraz, M. Atatüre. “Quantum-dot single-photon sources: Prospects for applications in linear optics quantum-information processing”. *Phys. Rev. A* 69 (2004), 032305. DOI: 10.1103/PhysRevA.69.032305.

[82] C. Matthiesen, A. N. Vamivakas, and M. Atatüre. “Subnatural Linewidth Single Photons from a Quantum Dot”. *Phys. Rev. Lett.* 108 (2012), 093602. DOI: 10.1103/PhysRevLett.108.093602.

[83] A. V. Kuhlmann et al. “Charge noise and spin noise in a semiconductor quantum device”. *Nat. Phys.* 9 (2013), 570–575. DOI: 10.1038/nphys2688.

[84] M. Ediger et al. “Controlled generation of neutral, negatively-charged and positively-charged excitons in the same single quantum dot”. *Appl. Phys. Lett.* 86 (2005), 211909. DOI: 10.1063/1.1937996.

[85] J. J. Finley et al. “Observation of multicharged excitons and biexcitons in a single InGaAs quantum dot”. *Phys. Rev. B* 63 (2001), 161305. DOI: 10.1103/PhysRevB.63.161305.

[86] A. S. Bracker, D. Gammon, and V. L. Korenev. “Fine structure and optical pumping of spins in individual semiconductor quantum dots”. *Semicond. Sci. Technol.* 23 (2008), 114004. DOI: 10.1088/0268-1242/23/11/114004.

[87] G. Gillard et al. “Fundamental limits of electron and nuclear spin qubit lifetimes in an isolated self-assembled quantum dot”. *npj Quantum Inf.* 7 (2021), 032305. DOI: 10.1038/s41534-021-00378-2.

[88] M. Bayer et al. “Fine structure of neutral and charged excitons in self-assembled In(Ga)As/(Al)GaAs quantum dots”. *Phys. Rev. B* 65 (2002), 195315. DOI: 10.1103/PhysRevB.65.195315.

[89] H. Tong and M. W. Wu. “Theory of excitons in cubic III-V semiconductor GaAs, InAs and GaN quantum dots: Fine structure and spin relaxation”. *Phys. Rev. B* 83 (2011), 235323. DOI: 10.1103/PhysRevB.83.235323.

[90] H. W. van Kesteren et al. “Fine structure of excitons in type-II GaAs/AlAs quantum wells”. *Phys. Rev. B* 41 (1990), 5283–5292. DOI: 10.1103/PhysRevB.41.5283.

[91] E. Blackwood et al. “Exchange interaction of excitons in GaAs heterostructures”. *Phys. Rev. B* 50 (1994), 14246–14254. DOI: 10.1103/PhysRevB.50.14246.

[92] D. Gammon et al. “Fine Structure Splitting in the Optical Spectra of Single GaAs Quantum Dots”. *Phys. Rev. Lett.* 76 (1996), 3005–3008. DOI: 10.1103/PhysRevLett.76.3005.

[93] P. W. Fry et al. “Inverted Electron-Hole Alignment in InAs-GaAs Self-Assembled Quantum Dots”. *Phys. Rev. Lett.* 84 (2000), 733–736. DOI: 10.1103/PhysRevLett.84.733.

[94] F. Hofbauer et al. “Electrically probing photonic bandgap phenomena in contacted defect nanocavities”. *Appl. Phys. Lett.* 91 (2007), 201111. DOI: 10.1063/1.2812576.

[95] A Laucht et al. “Electrical control of spontaneous emission and strong coupling for a single quantum dot”. *New J. Phys.* 11 (2009), 023034. DOI: 10.1088/1367-2630/11/2/023034.

[96] R. B. Patel et al. “Two-photon interference of the emission from electrically tunable remote quantum dots”. *Nat. Photonics* 4 (2010), 632–635. DOI: 10.1038/nphoton.2010.161.

[97] S. M. Thon et al. “Independent electrical tuning of separated quantum dots in coupled photonic crystal cavities”. *Appl. Phys. Lett.* 99 (2011), 161102. DOI: 10.1063/1.3651491.

[98] F. Pagliano et al. “Dynamically controlling the emission of single excitons in photonic crystal cavities”. *Nat. Commun.* 5 (2014), 5786. DOI: 10.1038/ncomms6786.

[99] C. P. Dietrich et al. “GaAs integrated quantum photonics: Towards compact and multi-functional quantum photonic integrated circuits”. *Laser Photonics Rev.* 10 (2016), 870–894. DOI: https://doi.org/10.1002/lpor.201500321.

[100] A. Högele et al. “Spin-selective optical absorption of singly charged excitons in a quantum dot”. *Appl. Phys. Lett.* 86 (2005), 221905. DOI: 10.1063/1.1940733.

[101] Abbarchi M. et al. “Diamagnetic coefficient of excitonic complexes in GaAs/Al0.3Ga0.7As quantum dots”. *J. Phys. Conf. Ser.* 210 (2010), 012012. DOI: 10.1088/1742-6596/210/1/012012.

[102] K. Peng et al. “Probing the Dark-Exciton States of a Single Quantum Dot Using Photocurrent Spectroscopy in a Magnetic Field”. *Phys. Rev. Appl.* 8 (2017), 064018. DOI: 10.1103/PhysRevAppl..8.064018.

[103] B. Urbaszek et al. “Nuclear spin Physics in quantum dots: An optical investigation”. *Rev. Mod. Phys.* 85 (2013), 79–133. DOI: 10.1103/RevModPhys.85.79.

[104] T. Takagahara. “Theory of exciton doublet structures and polarization relaxation in single quantum dots”. *Phys. Rev. B* 62 (2000), 16840–16855. DOI: 10.1103/PhysRevB.62.16840.

[105] I. A. Merkulov, Al. L. Efros, and M. Rosen. “Electron spin relaxation by nuclei in semiconductor quantum dots”. *Phys. Rev. B* 65 (2002), 205309. DOI: 10.1103/PhysRevB.65.205309.

[106] P.-F. Braun et al. “Direct Observation of the Electron Spin Relaxation Induced by Nuclei in Quantum Dots”. *Phys. Rev. Lett.* 94 (2005), 116601. DOI: 10.1103/PhysRevLett.94.116601.

[107] R. J. Warburton. “Single spins in self-assembled quantum dots”. *Nat. Mater.* 12 (2013), 483–493. DOI: 10.1038/nmat3585.

[108] O. Krebs and P. Voisin. “Giant Optical Anisotropy of Semiconductor Heterostructures with No Common Atom and the Quantum-Confined Pockels Effect”. *Phys. Rev. Lett.* 77 (1996), 1829–1832. DOI: 10.1103/PhysRevLett.77.1829.

[109] T. Belhadj et al. “Impact of heavy hole-light hole coupling on optical selection rules in GaAs quantum dots”. *Appl. Phys. Lett.* 97 (2010), 051111. DOI: 10.1063/1.3473824.

[110] E. A. Chekhovich et al. “Element-sensitive measurement of the hole–nuclear spin interaction in quantum dots”. *Nat. Phys.* 9 (2013), 74–78. DOI: 10.1038/nphys2514.

[111] B. Eble et al. “Hole-Nuclear Spin Interaction in Quantum Dots”. *Phys. Rev. Lett.* 102 (2009), 146601. DOI: 10.1103/PhysRevLett.102.146601.

[112] B. Lax et al. “Cyclotron Resonance in Indium Antimonide at High Magnetic Fields”. *Phys. Rev.* 122 (1961), 31–35. DOI: 10.1103/PhysRev.122.31.

[113] Craig E. Pryor and Michael E. Flatté. “Landé g Factors and Orbital Momentum Quenching in Semiconductor Quantum Dots”. *Phys. Rev. Lett.* 96 (2006), 026804. DOI: 10.1103/PhysRevLett.96.026804.

[114] M. J. Snelling et al. “Magnetic g factor of electrons in GaAs/$Al_xGa_{1-x}As$ quantum wells”. *Phys. Rev. B* 44 (1991), 11345–11352. DOI: 10.1103/PhysRevB.44.11345.

[115] A V Shchepetilnikov et al. “Electron g-factor in GaAs/AlGaAs quantum wells of different width and barrier Al concentrations”. *Journal of Physics: Conference Series* 456 (2013), 012035. DOI: 10.1088/1742-6596/456/1/012035.

[116] P. Millington-Hotze et al. “Nuclear spin diffusion in the central spin system of a GaAs/AlGaAs quantum dot”. *Nat. Commun.* 14 (2023), 2677. DOI: 10.1038/s41467-023-38349-0.

[117] A. Ulhaq et al. “Vanishing electron g factor and long-lived nuclear spin polarization in weakly strained nanohole-filled GaAs/AlGaAs quantum dots”. *Phys. Rev. B* 93 (2016), 165306. DOI: 10.1103/PhysRevB.93.165306.

[118] L. Childress et al. “Coherent Dynamics of Coupled Electron and Nuclear Spin Qubits in Diamond”. *Science* 314 (2006), 281–285. DOI: 10.1126/science.1131871.

[119] A. M. Tyryshkin et al. “Electron spin coherence exceeding seconds in high-purity silicon”. *Nat. Mater.* 11 (2011), 143–147. DOI: 10.1038/nmat3182.

[120] R. K Harris et al. “NMR Nomenclature: Nuclear Spin Properties and Conventions for Chemical Shifts: IUPAC Recommendations 2001”. *Solid State Nucl. Magn. Reson.* 22 (2002), 458–483. DOI: https://doi.org/10.1006/snmr.2002.0063.

[121] A. Abragam. *The principles of Nuclear Magnetism*. Vol. 69. Clarendon Press, 1961.

[122] D. Paget. “Optical detection of NMR in high-purity GaAs: Direct study of the relaxation of nuclei close to shallow donors”. *Phys. Rev. B* 25 (1982), 4444–4451. DOI: 10.1103/PhysRevB.25.4444.

[123] W. A. Coish and J. Baugh. “Nuclear spins in nanostructures”. *Phys. Status Solidi b* 246 (2009), 2203–2215. DOI: https://doi.org/10.1002/pssb.200945229.

[124] E. A. Chekhovich et al. “Dynamics of optically induced nuclear spin polarization in individual InP/$Ga_xIn_{1-x}P$ quantum dots”. *Phys. Rev. B* 81 (2010), 245308. DOI: 10.1103/PhysRevB.81.245308.

[125] C. P. Slichter. *Principles of Magnetic Resonance*. Vol. 69. Springer, 1989.

[126] L. Zaporski et al. “Ideal refocusing of an optically active spin qubit under strong hyperfine interactions”. *Nat. Nanotechnol.* 18 (2023), 257–263. DOI: 10.1038/s41565-022-01282-2.

[127] E. R. Andrew, A. Bradbury, and R. G. Eades. “Nuclear Magnetic Resonance Spectra from a Crystal rotated at High Speed”. *Nature* 182 (1958), 1659. DOI: 10.1038/1821659a0.

[128] A. W. Overhauser. “Polarization of Nuclei in Metals”. *Phys. Rev.* 92 (1953), 411–415. DOI: 10.1103/PhysRev.92.411.

[129] W. D. Knight. “Nuclear Magnetic Resonance Shift in Metals”. *Phys. Rev.* 76 (1949), 1259–1260. DOI: 10.1103/PhysRev.76.1259.2.

[130] A. Bechtold et al. “Three-stage decoherence dynamics of an electron spin qubit in an optically active quantum dot”. *Nat. Phys.* 11 (2015), 1005–1008. DOI: 10.1038/nphys3470.

[131] G. Gillard, E. Clarke, and E. A. Chekhovich. “Harnessing many-body spin environment for long coherence storage and high-fidelity single-shot qubit readout”. *Nat. Commun.* 13 (2022), 4048. DOI: 10.1038/s41467-022-31618-4.

[132] D. Paget et al. “Low field electron-nuclear spin coupling in gallium arsenide under optical pumping conditions”. *Phys. Rev. B* 15 (1977), 5780–5796. DOI: 10.1103/PhysRevB.15.5780.

[133] B. Eble et al. “Dynamic nuclear polarization of a single charge-tunable InAs/GaAs quantum dot”. *Phys. Rev. B* 74 (2006), 081306. DOI: 10.1103/PhysRevB.74.081306.

[134] S.W. Brown, T.A. Kennedy, and D. Gammon. "Optical NMR from single quantum dots". *Solid State Nucl. Magn. Reson.* 11 (1998), 49–58. DOI: https://doi.org/10.1016/S0926-2040(97)00095-7.

[135] D. A. Gangloff et al. "Quantum interface of an electron and a nuclear ensemble". *Science* 364.6435 (2019), 62–66. DOI: 10.1126/science.aaw2906.

[136] M. H. Appel et al. "A many-body quantum register for a spin qubit". *Nat. Phys.* 21 (2025), 368–373. DOI: 10.1038/s41567-024-02746-z.

[137] H. E. Dyte et al. "Is Wave Function Collapse Necessary? Explaining Quantum Nondemolition Measurement of a Spin Qubit within Linear Evolution". *Phys. Rev. Lett.* 132 (2024), 160804. DOI: 10.1103/PhysRevLett.132.160804.

[138] D. Gammon et al. "Electron and Nuclear Spin Interactions in the Optical Spectra of Single GaAs Quantum Dots". *Phys. Rev. Lett.* 86 (2001), 5176–5179. DOI: 10.1103/PhysRevLett.86.5176.

[139] E. A. Chekhovich et al. "Measurement of the spin temperature of optically cooled nuclei and GaAs hyperfine constants in GaAs/AlGaAs quantum dots". *Nat. Mater.* 16 (2017), 982–986. DOI: 10.1038/nmat4959.

[140] D. N. Krizhanovskii et al. "Individual neutral and charged $In_xGa_{1-x}As-GaAs$ quantum dots with strong in-plane optical anisotropy". *Phys. Rev. B* 72 (2005), 161312. DOI: 10.1103/PhysRevB.72.161312.

[141] X. Xu et al. "Fast Spin State Initialization in a Singly Charged InAs-GaAs Quantum Dot by Optical Cooling". *Phys. Rev. Lett.* 99 (2007), 097401. DOI: 10.1103/PhysRevLett.99.097401.

[142] J. Dreiser et al. "Optical investigations of quantum dot spin dynamics as a function of external electric and magnetic fields". *Phys. Rev. B* 77 (2008), 075317. DOI: 10.1103/PhysRevB.77.075317.

[143] J. Skiba-Szymanska et al. "Overhauser effect in individual $InP/Ga_xIn_{1-x}P$ dots". *Phys. Rev. B* 77 (2008), 165338. DOI: 10.1103/PhysRevB.77.165338.

[144] E. A. Chekhovich et al. "Pumping of Nuclear Spins by Optical Excitation of Spin-Forbidden Transitions in a Quantum Dot". *Phys. Rev. Lett.* 104 (2010), 066804. DOI: 10.1103/PhysRevLett.104.066804.

[145] G. Ragunathan et al. "Direct Measurement of Hyperfine Shifts and Radio Frequency Manipulation of Nuclear Spins in Individual CdTe/ZnTe Quantum Dots". *Phys. Rev. Lett.* 122 (2019), 096801. DOI: 10.1103/PhysRevLett.122.096801.

[146] A. Imamoğlu et al. “Optical Pumping of Quantum-Dot Nuclear Spins”. *Phys. Rev. Lett.* 91 (2003), 017402. DOI: 10.1103/PhysRevLett.91.017402.

[147] P. Maletinsky et al. “Nonlinear dynamics of quantum dot nuclear spins”. *Phys. Rev. B* 75 (2007), 035409. DOI: 10.1103/PhysRevB.75.035409.

[148] P. Millington-Hotze et al. “Approaching a fully-polarized state of nuclear spins in a solid”. *Nat. Commun.* 15 (2024), 032305. DOI: 10.1038/s41467-024-45364-2.

[149] I. I. Rabi et al. “A New Method of Measuring Nuclear Magnetic Moment”. *Phys. Rev.* 53 (1938), 318–318. DOI: 10.1103/PhysRev.53.318.

[150] A. M. Waeber et al. “Pulse control protocols for preserving coherence in dipolar-coupled nuclear spin baths”. *Nat. Commun.* 10 (2019), 3157. DOI: 10.1038/s41467-019-11160-6.

[151] G.P. Flinn et al. “Optically detected nuclear magnetic resonance in semiconductor quantum wells”. *J. Lumin.* 45 (1990), 218–220. DOI: https://doi.org/10.1016/0022-2313(90)90150-A.

[152] D. Press et al. “Complete quantum control of a single quantum dot spin using ultrafast optical pulses”. *Nature* 456 (2008), 218–221. DOI: 10.1038/nature07530.

[153] F. Bloch, W. W. Hansen, and M. Packard. “Nuclear Induction”. *Phys. Rev.* 69 (1946), 127–127. DOI: 10.1103/PhysRev.69.127.

[154] B. Cowan. *Nuclear Magnetic Resonance and Relaxation*. Vol. 69. Cambridge University Press, 2009.

[155] A. V. Khaetskii and Y. V. Nazarov. “Spin-flip transitions between Zeeman sublevels in semiconductor quantum dots”. *Phys. Rev. B* 64 (2001), 125316. DOI: 10.1103/PhysRevB.64.125316.

[156] Xiayu Linpeng et al. “Longitudinal spin relaxation of donor-bound electrons in direct band-gap semiconductors”. *Phys. Rev. B* 94 (2016), 125401. DOI: 10.1103/PhysRevB.94.125401.

[157] D. J. Reilly et al. “Exchange Control of Nuclear Spin Diffusion in a Double Quantum Dot”. *Phys. Rev. Lett.* 104 (2010), 236802. DOI: 10.1103/PhysRevLett.104.236802.

[158] C. Latta, A. Srivastava. “Hyperfine Interaction-Dominated Dynamics of Nuclear Spins in Self-Assembled InGaAs Quantum Dots”. *Phys. Rev. Lett.* 107 (2011), 167401. DOI: 10.1103/PhysRevLett.107.167401.

[159] G. N. Nguyen et al. “Enhanced Electron-Spin Coherence in a GaAs Quantum Emitter”. *Phys. Rev. Lett.* 131 (2023), 210805. DOI: 10.1103/PhysRevLett.131.210805.

[160] E. L. Hahn. “Spin Echoes”. *Phys. Rev.* 80 (1950), 580–594. DOI: 10.1103/PhysRev.80.580.

[161] H. Y. Carr and E. M. Purcell. “Effects of Diffusion on Free Precession in Nuclear Magnetic Resonance Experiments”. *Phys. Rev.* 94 (1954), 630–638. DOI: 10.1103/PhysRev.94.630.

[162] S. Meiboom and D. Gill. “Modified Spin-Echo Method for Measuring Nuclear Relaxation Times”. *Rev. Sci. Instrum.* 29 (1958), 688–691. DOI: 10.1063/1.1716296.

[163] J. S. Waugh, L. M. Huber, and U. Haeberlen. “Approach to High-Resolution nmr in Solids”. *Phys. Rev. Lett.* 20 (1968), 180–182. DOI: 10.1103/PhysRevLett.20.180.

[164] A. Oshiyama and S. Ohnishi. “DX center: Crossover of deep and shallow states in Si-doped $Al_xGa_{1-x}As$”. *Phys. Rev. B* 33 (1986), 4320–4323. DOI: 10.1103/PhysRevB.33.4320.

[165] P. M. Mooney. “Deep donor levels (DX centers) in III-V semiconductors”. *J. Appl. Phys.* 67 (1990), R1–R26. DOI: 10.1063/1.345628.

[166] L. Zhai et al. “Low-noise GaAs quantum dots for quantum photonics”. *Nat. Commun.* 11 (2020), 4745. DOI: 10.1038/s41467-020-18625-z.

[167] E. Muñoz et al. “Techniques to minimize DX center deleterious effects in III-V device performance”. *J. Appl. Phys.* 73 (1993), 4988–4997. DOI: 10.1063/1.353818.

[168] A. Franzen. *ComponentLibrary*. Accessed 2025-02-24. Used under Creative Commons Attribution-NonCommercial 3.0 Unported License. URL: https://www.gwoptics.org/ComponentLibrary/..

[169] A. Abragam and W. G. Proctor. “Spin Temperature”. *Phys. Rev.* 109 (1958), 1441–1458. DOI: 10.1103/PhysRev.109.1441.

[170] P.-F. Braun et al. “Bistability of the nuclear polarization created through optical pumping in $In_{1-x}Ga_xAs$ quantum dots”. *Phys. Rev. B* 74 (2006), 245306. DOI: 10.1103/PhysRevB.74.245306.

[171] P. Maletinsky et al. “Nonlinear dynamics of quantum dot nuclear spins”. *Phys. Rev. B* 75 (2007), 035409. DOI: 10.1103/PhysRevB.75.035409.

[172] A. I. Tartakovskii et al. “Nuclear Spin Switch in Semiconductor Quantum Dots”. *Phys. Rev. Lett.* 98 (2007), 026806. DOI: 10.1103/PhysRevLett.98.026806.

[173] A. M. Waeber et al. “Few-second-long correlation times in a quantum dot nuclear spin bath probed by frequency-comb nuclear magnetic resonance spectroscopy”. *Nat. Phys.* 12 (2016), 688–693. DOI: 10.1038/nphys3686.

[174] D. M. Pozar. *Microwave Engineering*. Vol. 107. John Wiley & Sons, 2011.

[175] H. E. Dyte et al. *Storing quantum coherence in a quantum dot nuclear spin ensemble for over 100 milliseconds*. (2025). arXiv: 2502.11092. URL: https://arxiv.org/abs/2502.11092.

[176] M. Munsch et al. "Manipulation of the nuclear spin ensemble in a quantum dot with chirped magnetic resonance pulses". *Nat. Nanotechnol.* 9 (2014), 671–675. DOI: 10.1038/nnano.2014.175.

[177] D. P. Franke et al. "Interaction of Strain and Nuclear Spins in Silicon: Quadrupolar Effects on Ionized Donors". *Phys. Rev. Lett.* 115 (2015), 057601. DOI: 10.1103/PhysRevLett.115.057601.

[178] S. Seidl et al. "Effect of uniaxial stress on excitons in a self-assembled quantum dot". *Appl. Phys. Lett.* 88 (2006), 203113. DOI: 10.1063/1.2204843.

[179] X. Yuan et al. "GaAs quantum dots under quasiuniaxial stress: Experiment and theory". *Phys. Rev. B* 107 (2023), 235412. DOI: 10.1103/PhysRevB.107.235412.

[180] E. A. Chekhovich et al. "Cross calibration of deformation potentials and gradient-elastic tensors of GaAs using photoluminescence and nuclear magnetic resonance spectroscopy in GaAs/AlGaAs quantum dot structures". *Phys. Rev. B* 97 (2018), 235311. DOI: 10.1103/PhysRevB.97.235311.

[181] I. M. Griffiths et al. "Complete characterization of GaAs gradient-elastic tensors and reconstruction of internal strain in GaAs/AlGaAs quantum dots using nuclear magnetic resonance". *Phys. Rev. B* 99 (2019), 125304. DOI: 10.1103/PhysRevB.99.125304.

[182] D. M. Grant and R. K. Harris. *Encyclopedia of Nuclear Magnetic Resonance*. Vol. 107. Chichester, England: John Wiley & Sons, 2002.

[183] R. V. Pound. "Nuclear Electric Quadrupole Interactions in Crystals". *Phys. Rev.* 79 (1950), 685–702. DOI: 10.1103/PhysRev.79.685.

[184] R. J. Harrison and P. L. Sagalyn. "Trace Relations for Tensors Relating Electric Fields and Elastic Strains to Nuclear Quadrupole Effects". *Phys. Rev.* 128 (1962), 1630–1631. DOI: 10.1103/PhysRev.128.1630.

[185] S. Adachi. *Properties of Semiconductor Alloys: Group-IV, III–V and II–VI Semiconductors*. Vol. 107. Wiley-Blackwell, 2009.

[186] R. K. Sundfors. "Experimental gradient-elastic tensors and chemical bonding in III-V semiconductors". *Phys. Rev. B* 10 (1974), 4244–4252. DOI: 10.1103/PhysRevB.10.4244.

[187] A. N. Vamivakas et al. “Observation of spin-dependent quantum jumps via quantum dot resonance fluorescence”. *Nature* 467 (2010), 297–300. DOI: 10.1038/nature09359.

[188] A. Delteil et al. “Observation of Quantum Jumps of a Single Quantum Dot Spin Using Submicrosecond Single-Shot Optical Readout”. *Phys. Rev. Lett.* 112 (2014), 116802. DOI: 10.1103/PhysRevLett.112.116802.

[189] N. O. Antoniadis et al. “Cavity-enhanced single-shot readout of a quantum dot spin within 3 nanoseconds”. *Nat. Commun.* 14 (2023), 3977. DOI: 10.1038/s41467-023-39568-1.

[190] J. Yoneda et al. “Quantum non-demolition readout of an electron spin in silicon”. *Nat. Commun.* 11 (2020), 1144. DOI: 10.1038/s41467-020-14818-8.

[191] T. C. Ralph et al. “Quantum nondemolition measurements for quantum information”. *Phys. Rev. A* 73 (2006), 012113. DOI: 10.1103/PhysRevA.73.012113.

[192] B. Hensen et al. “A silicon quantum-dot-coupled nuclear spin qubit”. *Nat. Nanotechnol.* 15 (2020), 13–17. DOI: 10.1038/s41565-019-0587-7.

[193] M. Raha et al. “Optical quantum nondemolition measurement of a single rare earth ion qubit”. *Nat. Commun.* 11 (2020), 1605. DOI: 10.1038/s41467-020-15138-7.

[194] R. E. Evans et al. “Photon-mediated interactions between quantum emitters in a diamond nanocavity”. *Science* 362 (2018), 662–665. DOI: 10.1126/science.aau4691.

[195] M. K. Bhaskar et al. “Experimental demonstration of memory-enhanced quantum communication”. *Nature* 580 (2020), 60–64. DOI: 10.1038/s41586-020-2103-5.

[196] Q. Zhang et al. “High-fidelity single-shot readout of single electron spin in diamond with spin-to-charge conversion”. *Nat. Commun.* 12 (2021), 1529. DOI: 10.1038/s41467-021-21781-5.

[197] W. H. Zurek. “Quantum Darwinism”. *Nat. Phys.* 5 (2009), 181–188. DOI: https://doi.org/10.1038/nphys1202.

[198] W. H. Zurek. “Quantum theory of the classical: quantum jumps, Born’s Rule and objective classical reality via quantum Darwinism”. *Philos. Trans. R. Soc. A: Mathematical, Physical and Engineering Sciences* 376 (2018), 20180107. DOI: 10.1098/rsta.2018.0107.

[199] K. De Greve et al. “Quantum-dot spin–photon entanglement via frequency downconversion to telecom wavelength”. *Nature* 491 (2012), 421–425. DOI: 10.1038/nature11577.

[200] N. Coste et al. “High-rate entanglement between a semiconductor spin and indistinguishable photons”. *Nat. Photon.* 17 (2023), 582–587. DOI: 10.1038/s41566-023-01186-0.

[201] P. Laccotripes et al. “Spin-photon entanglement with direct photon emission in the telecom C-band”. *Nat. Commun.* 15 (2024), 9740. DOI: 10.1038/s41467-024-53964-1.

[202] D. Huber et al. “Highly indistinguishable and strongly entangled photons from symmetric GaAs Quantum Dots”. *Nat. Commun.* 8 (2017), 15506. DOI: 10.1038/ncomms15506.

[203] L. Schweickert et al. “On-demand generation of background-free single photons from a solid-state source”. *Appl. Phys. Lett.* 112 (2018), 093106. DOI: 10.1063/1.5020038.

[204] Y. Arakawa and M. J. Holmes. “Progress in quantum-dot single photon sources for quantum information technologies: A broad spectrum overview”. *Appl. Phys. Reviews* 7 (2020), 021309. DOI: 10.1063/5.0010193.

[205] M. B. Rota et al. “A source of entangled photons based on a cavity-enhanced and strain-tuned GaAs quantum dot”. *eLight* 4 (2024), 13. DOI: 10.1186/s43593-024-00072-8.

[206] Peter Millington-Hotze et al. *Few-electron spin qubits in optically active GaAs quantum dots*. (2025). arXiv: 2504.19257. URL: https://arxiv.org/abs/2504.19257.

[207] A. M. Souza, G. A. Álvarez, and D. Suter. “Robust dynamical decoupling”. *Philos. Trans. R. Soc. A: Mathematical, Physical and Engineering Sciences* 370 (2012), 4748–4769. DOI: 10.1098/rsta.2011.0355.

[208] K. Khodjasteh and D. A. Lidar. “Fault-Tolerant Quantum Dynamical Decoupling”. *Phys. Rev. Lett.* 95 (2005), 180501. DOI: 10.1103/PhysRevLett.95.180501.

[209] R. C. C. Leon et al. “Coherent spin control of s-, p-, d- and f-electrons in a silicon quantum dot”. *Nat. Commun.* 11 (2020), 797. DOI: 10.1038/s41467-019-14053-w.

[210] M. Kroutvar et al. “Optically programmable electron spin memory using semiconductor quantum dots”. *Nature* 432 (2004), 81–84. DOI: 10.1038/nature03008.

[211] L. C. Camenzind et al. “Hyperfine-phonon spin relaxation in a single-electron GaAs quantum dot”. *Nat. Commun.* 9 (2018), 3454. DOI: 10.1038/s41467-018-05879-x.

[212] A. I. Lvovsky, B. C. Sanders, and W. Tittel. “Optical quantum memory”. *Nat. Photon.* 3 (2009), 706–714. DOI: https://doi.org/10.1038/nphoton.2009.231.

[213] X-L. Pang et al. “A hybrid quantum memory–enabled network at room temperature”. *Sci. Adv.* 6 (2020), eaax1425. DOI: 10.1126/sciadv.aax1425.

[214] F. Bussières et al. “Quantum teleportation from a telecom-wavelength photon to a solid-state quantum memory”. Vol. 107. 2014, FTu2A.4. DOI: 10.1364/CLEO_QELS.2014.FTu2A.4.

[215] P. Treutlein et al. “Coherence in Microchip Traps”. *Phys. Rev. Lett.* 92 (2004), 203005. DOI: 10.1103/PhysRevLett.92.203005.

[216] C. Langer et al. “Long-Lived Qubit Memory Using Atomic Ions”. *Phys. Rev. Lett.* 95 (2005), 060502. DOI: 10.1103/PhysRevLett.95.060502.

[217] A. M. Tyryshkin et al. “Electron spin relaxation times of phosphorus donors in silicon”. *Phys. Rev. B* 68 (2003), 193207. DOI: 10.1103/PhysRevB.68.193207.

[218] J. J. Morton et al. “Solid-state quantum memory using the ^{31}P nuclear spin”. *Nature* 455 (2008), 1085–1088. DOI: 10.1038/nature07295.

[219] M. Atatüre et al. “Material platforms for spin-based photonic quantum technologies”. *Nat. Rev. Mater.* 3 (2018), 38–51. DOI: 10.1038/s41578-018-0008-9.

[220] E.A. Chekhovich et al. “Suppression of nuclear spin bath fluctuations in self-assembled quantum dots induced by inhomogeneous strain”. *Nat. Commun.* 6 (2015), 6348. DOI: 10.1038/ncomms7348.